Mechanism of metal uptake by clay minerals — X-ray spectroscopy and molecular modelling study

Inauguraldissertation
der Philosophisch-naturwissenschaftlichen Fakultät
der Universität Bern

vorlegt von

Annamária Gabriella Kéri
von Budapest, Ungarn

Leiter der Arbeit:
Prof. Dr. Sergey V. Churakov
(Institut für Geologie, Universität Bern)
(Laboratory for Waste Management, Paul Scherrer Institute)

Co-Leiter der Arbeit:
Dr. Rainer Dähn
(Laboratory for Waste Management, Paul Scherrer Institute)

Co-Leiter der Arbeit:
Dr. Matthias Krack
(Laboratory for Scientific Computing and Modelling, Paul Scherrer Institute)

Koreferent:
Prof. Dr. Jeffrey G. Catalano
(Department of Earth and Planetary Sciences, Washington University in St. Louis)

source: https://doi.org/10.48549/4927 | downloaded: 13.7.2025

Original document saved on the web server of the University Library of Bern

This work is licensed under a Creative Commons Attribution-Non-Commercial-No derivative works 2.5 Switzerland license. To see the license go to http://creativecommons.org/licenses/by-nc-nd/2.5/ch/deed.en or write to Creative Commons, 171 Second Street, Suite 300, San Francisco, California 94105, USA.

Mechanism of metal uptake by clay minerals — X-ray spectroscopy and molecular modelling study

Inauguraldissertation
der Philosophisch-naturwissenschaftlichen Fakultät
der Universität Bern

vorlegt von

Annamária Gabriella Kéri
von Budapest, Ungarn

Leiter der Arbeit:
Prof. Dr. Sergey V. Churakov
(Institut für Geologie, Universität Bern)
(Laboratory for Waste Management, Paul Scherrer Institute)

Co-Leiter der Arbeit:
Dr. Rainer Dähn
(Laboratory for Waste Management, Paul Scherrer Institute)

Co-Leiter der Arbeit:
Dr. Matthias Krack
(Laboratory for Scientific Computing and Modelling, Paul Scherrer Institute)

Koreferent:
Prof. Dr. Jeffrey G. Catalano
(Department of Earth and Planetary Sciences, Washington University in St. Louis)

Von der Philosophisch-naturwissenschaftlichen Fakultät angenommen.

Bern, 19.04.2019

Der Dekan:
Prof. Dr. Zoltán Balogh

Copyright Notice

Copyright Notice

This document is licensed under the Creative Commons Attribution-Non-Commercial-No derivative works 2.5 Switzerland.
http://creativecommons.org/licenses/by-nc-nd/2.5/ch/deed.en

You are free:

 to copy, distribute, display, and perform the work**.**

Under the following conditions:

 **Attribution**. You must give the original author credit.

 **Non-Commercial**. You may not use this work for commercial purposes.

 **No derivative works**. You may not alter, transform, or build upon this work.

For any reuse or distribution, you must take clear to others the license terms of this work.

Any of these conditions can be waived if you get permission from the copyright holder.

Nothing in this license impairs or restricts the author's moral rights according to Swiss law.

The detailed license agreement can be found at:
http://creativecommons.org/licenses/by-nc-nd/2.5/ch/legalcode.de (only in German)

Acknowledgements

For the contribution of many people:

The present thesis would not have been possible and would be much more difficult to finalize without the help and support of numerous people.

First of all, I would like to thank to my supervisors, who has given me the chance to work on this PhD project, encouraged me, at the same time gave me sufficient freedom to learn and test new approaches. I would like to say special thanks to **Prof. Dr. Sergey Churakov,** my main supervisor ("Doktorvater"), for his continuous support during my doctoral studies. He guided me in this wonderful interdisciplinary world of the mixture of physics, chemistry and geology. The helpful discussions with him has not only given answers to current issues but he also broadened my scientific view. I would like to thank to **Dr. Rainer Dähn,** my PSI supervisor, who encouraged me at the most critical points of the PhD project. His help was essential to properly interpret the results derived from the comparison of the calculated and the measured XAS spectra. I would like to thank also to **Dr. Matthias Krack,** my supervisor, for his concise introduction to *ab initio* calculations, in addition, his friendly guidance in the finalization of this thesis.

I would like to thank to **all the colleagues at the Laboratory for Waste Management (LES) Paul Scherrer Institute (PSI)** for creating me an inspiring and friendly work environment. I would like to say special thanks to **Dr. Marie Marques Fernandez** for providing me XAS spectra from iron sorption experiments and her essential help in the interpretation of the spectroscopic results. I am grateful to **Dr. Bart Baeyens**, my group leader, for his support both in professional and administrative issues. I would like to say special thanks to **Dr. Enzo Curti**, who gave me standards and advices to essentially participate at a XAS measurement. I am grateful to **Dr. Dan Miron** for explaining me the application of sensitivity analysis and raising up several interesting (scientific) topics during lunchtimes. A special thank goes to **Dr. Ravi Patel** for his friendly guidance and who was always open-minded to discuss any (scientific) question. I am also grateful to **Dr. Dimitri Kulik** who aroused my interest in geology (and in many other Swiss related topics, we discussed). I would thank to **my office mates** (Ravi, Guomin, Alina, Amir, Bruno, Jenna and Louis) for their collegiality.

I would like to thank to the **colleagues from University of Bern** (Rene, Georgia) their hospitality and helpfulness during my stays at the university. I thank to my **colleagues at the MTA EK** (Dr. Szabina Török, Dr. János Osán, Dr. Margit Fábián) for their patience during the finalization of this thesis and the opportunity to participate at a synchrotron XAS experiment.

I would like to thank "**LES Jüngster**" (Leonardo, Philip, Latina and many others), "**ClayBikers**" (especially Elmo) and the **PSI volleyball team** (Eberhard, Adolf and many others) that my PhD also contained leisure activities. I would like to thank **my friends** (especially to Lilla, Gergő, Soumya, Joel) for making my stay in Switzerland unforgettable.

Last but not least, many thanks to **my parents and sister,** who always helped and supported me from far away and I would certainly never have gotten here without the love and support of **András**.

For the financial supports and grants

Results present in CHAPTER 2 was financed by the **Swiss–Hungarian Cooperation Program** through Project no SH/7/2/11, while the research leading to the results in CHAPTER 3, CHAPTER 4, CHAPTER 5 and CHAPTER 6 has received funding from the **Swiss National Science Foundation (SNSF)** through project number SNF-200021_156412 (2015-2018). The work was supported by grants from the **Swiss National Supercomputing Centre (CSCS)** under project ID "*s620*", "*s750*", "*psi*" and "*psi12*". The use of computer resources of the **Merlin 4 Cluster,** Paul Scherrer Institute and the **UBELIX** the HPC cluster at the University of Bern (www.id.unibe.ch/hpc) gratefully acknowledged.

Abstract

Clay minerals play essential roles in argillaceous rock formations since they are strong sorbents for transition and heavy metals. Iron is one of the most abundant redox-active element which may participate in redox interactions at the edge surface of clay minerals. It is expected to adsorb as various surface species on clay minerals, moreover, Fe can also be incorporated into the structure of the clay layer. Structural iron might participate in redox-reactions influencing the relative stability of the sorbed surface species. The accurate description of clay structures and the quantification of Fe^{2+}, radionuclide uptake capacity and mechanism is essential to understand the fate of heavy metals and radioactive contaminants in subsurface environments.

In this thesis, several microanalytical techniques, mathematical methods and atomistic modelling approaches were combined to comprehend sorption processes of transition metals and radionuclides on clay minerals. The uptake capabilities of mineral phases present in argillaceous rock were estimated by applying multivariate methods (factor analysis, positive matrix factorization, cluster analysis) on combined micro-XRF (microscopic X-ray fluorescence) and SEM/EDX (scanning electron microscopy energy dispersive X-ray analysis) data sets. In Boda Claystone Formation (Hungary), the clayey matrix – containing phyllosilicates (mainly illite), fine grained albite, rutile and nanocrystalline hematite – was identified as mineral phases with the highest Nd uptake capability. Almost the same amount of Nd was found to bind to calcite, while the ion uptake capability of dolomite was orders of magnitude lower.

The structural properties of natural clay minerals, the sorption mechanism of Fe and UO_2^{2+} on them were studied by combining *ab initio* and XAS (X-ray absorption spectroscopy) approaches. Relax structure and molecular dynamics (MD) calculations based on density functional theory (DFT+U) were applied as basis to calculate EXAFS (extended X-ray absorption fine structure) and XANES (X-ray absorption near edge structure) spectra. A good agreement between the *ab initio* simulated and the measured XAS spectra demonstrates the robustness of the employed simulation approach.

The results suggest that iron in smectites is preferentially incorporated as Fe^{3+} (ferric iron) into the octahedral sheet and there is no preferential occupation of *cis*- or *trans*-sites. Natural smectites with similar structure originating from different mines have distinct arrangement of isomorphic substitutions (individual iron or Fe–Fe, Fe–Mg clusters). The structural differences might explain the distinct extent and efficiency of redox reactions happen at the clay edge surfaces. The relaxed structure calculation of several different clay structures with substituted Fe^{2+}/Fe^{3+} in the bulk or at surface sites show that the energetically preferred position for ferrous iron is in the bulk, while for ferric iron is at the edge site. The spectroscopic calculations show that strong- and weak-site complexation has different characteristics. The quantitative interpretation of the atomistic modelling based XAS spectra measured on samples with distinct Fe loadings indicates particularly complex behaviour of iron.

The energy comparison of the relaxed structures of various bidentate uranyl surface complexes revealed that the structural parameters of the uranyl species are essentially determined by the placement of surface chemical groups (e.g. OH^{-}) forming the adsorption site. Structural Fe^{3+} in the octahedral sheet of montmorillonite at the surface site increases the stability of bidentate uranium species.

Table of Content

Copyright Notice ..... **I**
Acknowledgements ..... **III**
Abstract ..... **V**
Table of Content ..... **VII**

CHAPTER 1: Introduction **1**
1. Motivation of this study 3
1.1. Research objectives 4
1.2. Host rock 5
1.3. Bentonite buffer 10
2. Experimental techniques 13
2.1. Microanalytical methods 13
2.2. X-ray absorption spectroscopy (XAS) 16
3. Analytical techniques and modelling approaches 19
3.1. Correlation analysis and multivariate methods 19
3.2. *Ab initio* calculations 22
3.3. EXAFS and XANES calculations 25
4. Outline of the thesis 27
5. References 31

CHAPTER 2: Experimental study: Combined X-ray microanalytical study of the Nd uptake capability of argillaceous rocks **39**
Abstract 41
1. Introduction 41
2. Materials and methods 43
2.1. Samples 43
2.2. SEM/EDX and micro-XRF measurements 44
2.3. Interleaving of micro-XRF and SEM/EDX data sets 45
2.4. Micro-XRD 46
2.5. Multivariate methods 47
3. Results and discussion 48
3.1. Elemental concentration maps 48
3.2. Multivariate methods 50
3.3. Micro-XRD results 55
4. Conclusion 57
5. References 57

CHAPTER 3: Theoretical study: Combined XAFS spectroscopy and *ab initio* study on the characterization of iron incorporation by montmorillonite 63
Abstract 65
1. Introduction 65
2. Materials and methods 67
2.1. Modeling setup 67
2.2. *Ab initio* calculations 68
2.3. Calculations of EXAFS and XANES spectra 69
2.4. XAFS experiments 70
3. Results and discussion 71
3.1. EXAFS spectra 71
3.2. XANES spectra 74
3.3. Structural position of Fe in bulk montmorillonite 77
4. Implication of the theoretical study in the interpretation of XAFS 78
5. References 78
6. Supporting Information 1: Choice of the Hubbard U_{eff} parameter 83
7. Supporting Information 2: Determination of the XANES convolutional parameters ... 88
CHAPTER 4: Theoretical study: Characterization of structural iron in smectites — an *ab initio* based XAS study 95
Abstract 97
1. Introduction 97
2. Materials and methods 99
2.1. Modeling setup 99
2.2. *Ab initio* calculations 102
2.3. Calculations of EXAFS spectra 102
2.4. XAS experiments 103
3. Results and discussion 104
3.1. EXAFS spectra 104
3.2. Distribution of iron in low Fe-content montmorillonites 107
4. Implication of the structural position of Fe in bulk montmorillonite 111
5. References 112
6. Supporting Information 1 117
7. Supporting Information 2 120

CHAPTER 5: Theoretical study: Iron adsorption on clays inferred from atomistic simulations and XAS spectroscopy 129
Abstract 131
1. Introduction 131
2. Materials and methods 133
2.1. Modeling setup 133
2.2. *Ab initio* calculations 136
2.3. Calculations of EXAFS and XANES spectra 137
2.4. XAFS experiments 139
3. Results and discussion 139
3.1. Preferred position of Fe^{2+} and Fe^{3+} in montmorillonite 139
3.2. EXAFS spectra 144
3.3. XANES spectra 147
4. Implication of the oxidative sorption of iron by montmorillonite 149
5. References 149
CHAPTER 6: Theoretical study: First-principles study of uranyl adsorption on montmorillonite edge surfaces 155
Abstract 157
1. Introduction 157
2. Materials and methods 158
2.1. Modelling setup 158
2.2. *Ab initio* calculations 161
2.3. XAS measurements 161
3. Results and discussion 162
3.1. Uranyl complexation on montmorillonite edge surfaces 162
3.2. Impact of structural iron on the uranium complexation 167
4. Implication of uranium adsorption on montmorillonite 172
5. References 174
CHAPTER 7: Conclusions and Outlook 179
Declaration of consent 187
Curriculum Vitae ..... Hiba! A könyvjelző nem létezik.

CHAPTER 1:
Introduction

1. Motivation of this study

The safe disposal of spent fuel (SF) arising from the operation of nuclear power plants and vitrified high-level waste (HLW) from reprocessing is one of the most difficult and complex challenges for the modern society, which needs to be solved to maintain a sustainable use of resources and to protect natural environments[1]. The deep geological disposal of radioactive waste is internationally considered as the safest option for the radioactive waste management[1,2]. The approach is based on a defense-in-depth concept which relies on an assembly of independent passive engineered and natural geological barriers[1,3,4]. In the Swiss concept for a HLW repository (Figure 1), the SF and the HLW matrices will be encapsulated in thick walled (0.25m) steel casks, which will be surrounded by compacted bentonite and placed into an argillaceous host rock formation[5]. All access tunnels will be backfilled and sealed to reduce the release of radionuclides and to prevent any unwanted human intrusion and misuse of the radioactive materials[1,5].

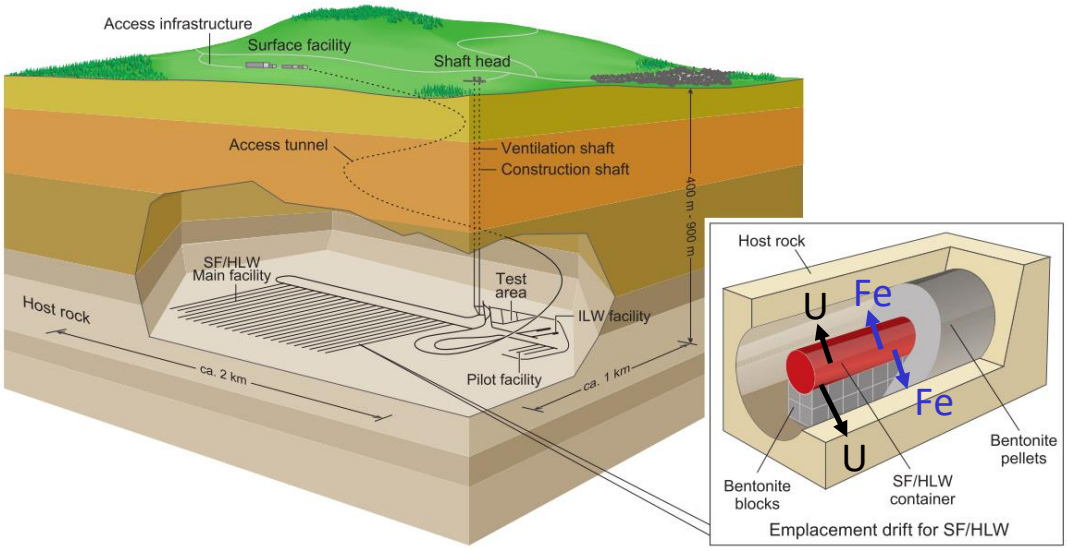

Figure 1. Concept of the Swiss HLW disposal site[5]

After the closure of the repository, the bentonite buffer will be re-saturated and the corrosion of the steel casks under anoxic conditions will start[5,6]. Although, the steel casks are expected to maintain integrity and retain radionuclides for at least 10'000 years, the corrosion processes will immediately take place after emplacement and will contribute to the changes of the geochemical environment in the repository near-field[1,6]. For example, the anoxic corrosion of the steel is expected to result in the release of hydrogen gas and Fe^{2+} (ferrous iron) according to Equation (1):[5,6]

$$Fe^0+2H_2O \rightarrow Fe^{2+}+H_2+2OH^- \quad (1)$$

New iron phases such as magnetite and siderite will be formed[6]. Dissolved Fe^{2+} will be transported by pore water and it will influence the geochemical environment in the near field[6]. In particular, Fe^{2+} is expected to adsorb on clay minerals and thus it will reduce the effective sorption capacity of buffer material with respect to the radionuclides uptake[7].

A complete confinement cannot be provided over the relevant time scale for the radionuclide decay (circa 1 million year), as the failure of the casks is expected up to 10'000 years post disposal[6]. After the breaching of disposal casks, radionuclides will slowly be released from the spent fuel assemblies and the vitrified HLW[6]. The bentonite buffer and the host rocks should retard the migration of radionuclides to the biosphere[5]. The transport of radionuclide ions $\left(\text{e.g. } Cs^{+}, Ni^{2+}, Nd^{3+}, UO_2^{2+}\right)$ towards the surface environment will be attenuated by a number of processes (e.g. dilution, precipitation, sorption)[1]. In the near field, the most relevant mechanism is the sorption of radionuclides on minerals, which greatly depends on the geochemical environment (e.g. nature of mineral phases, pH) in the bentonite buffer and in the host rock formation[1,6]. Therefore, the detailed study on the engineered and geological barrier is a crucial issue in the safety assessment of the HLW repository's long-term evolution.

1.1. Research objectives

The current study represents an important contribution for investigations concerning the safety assessment of the radioactive waste disposal sites for SF (and HLW). The uptake capacity of the clay minerals from an argillaceous rock formation and the sorption process of iron and uranium on smectites representing the bentonite buffer were investigated.

The aims of this thesis can be summarized in terms of the following scientific questions:

- What are the radionuclide uptake capacities of the main mineral phases in an argillaceous rock formation?
- What is the preferred oxidation state and occupational site of iron in bulk montmorillonite? Is there any (and if yes, what are the) differences in the structural iron distribution for variant montmorillonite types?
- Is the oxidative sorption of Fe^{2+} ion energetically favored on Fe-bearing montmorillonites? How does the ferrous iron (sorbent) concentration influence the sorption process?
- Which are the most stable uranium complexes formed at the relevant edge surfaces of montmorillonite? Has structural iron any impact on the uranium uptake?

This multidisciplinary work combines several microanalytical techniques, mathematical methods and atomistic modelling approaches to comprehend sorption processes of transition metals and radionuclides on clay minerals in the near field. For a better understanding, a general overview of the applied experimental, analytical and modelling techniques will be given in the next sections.

1.2. Host rock

The suitable choice of the host rock is a key question. The process of selecting the appropriate deep final repository requires many stages and it is in progress at different status in several countries (who have SF and/or HLW). Investigations often start with selection of the potential host rock formation considering exclusion criteria (e.g. tectonic and seismic activity of the formation)[8]. In a well-defined stepwise procedure, the few potential formations with several different siting area are narrowed to one disposal site[8,9]:

Stage 1: Selection of the potential host rock formation(s) and (5–10) possible geological siting areas in the country based on pre-defined safety criteria (e.g. engineering feasibility, location from human settlement);

Stage 2: Identification of at least one suitable site for HLW disposal based on structural, textural and mineralogical properties of the investigated areas (e.g. structural homogeneity of the formation at the site, mineralogical composition);

Stage 3: Narrowing the number of disposal sites for detailed studies.

To demonstrate disposal feasibility, the potential site should have the following properties[1]:

- the siting area is tectonically stable over the relevant timescales, with a low rate of uplift and associated erosion;
- geological environment is simple, with predictable structural, hydrogeological and geochemical properties.

Argillaceous formations are foreseen as potential host rocks for HLW waste disposal in many countries (e.g. Switzerland[1], Hungary[10]) as they possess several physical and chemical properties advantageous for the safe disposal of radioactive wastes (e.g. low hydraulic conductivity, high swelling pressure and radionuclide sorption capability)[1,4,5,11].

In Switzerland, three potential sites “Jura Ost”, “Nördlich Lägern” and “Zürich Nordost” have been approved in 2018 for detailed investigation (Figure 2)[12]. These three sites belong to the same argillaceous formation, Opalinus Clay, which was identified as the priority host rock option based on a comprehensive, three-decades long geological and mineralogical study investigating crystalline and sedimentary rock formations in the country[12]. The formation consists of a monotonous sequence of dark grey, silty, micaceous clays and sandy shales that were deposited around 174 million years ago[13]. Opalinus Clay reached a burial depth of about 1000m during the Cretaceous (~65–120 million years ago)[1,13]. The last major tectonic events affected the region in the Miocene when the Rhine Graben was rifted in the mid-Tertiary (~25–40 million years ago) followed by down-warping and burial under late-Tertiary sediments (~10–20 million years ago)[1,13]. From about 10 million years ago, Alpine uplift and erosion brought the Opalinus Clay progressively up to its present burial depth of about 600m in the region of interest[1,13]. The most recent stage of the orogeny involved the thrusting and folding of the Jura Mountains, which along with the uplift of the Alps, continues today[1,13]. Therefore, the formation is overlain by a succession of sandy limestones, shales and oolitic ironstones of Early Bajocian age[1,13].

Based on detailed geological studies of Opalinus Clay, the formation has several advantageous properties for SF and HLW disposal[1]:

- the sediments overlying the basement and the basement rocks themselves in the region of interest are not considered to have any significant natural resource potential;
- expected effectively stable geochemical environment over several million years in the formation;
- beneficial geochemical (reducing, slightly alkaline and moderately saline) conditions;
- reasonable engineering properties allowing small, unlined tunnels and larger, lined tunnels to be constructed at depths of several hundred meters;
- low hydraulic conductivity due to high self-sealing capacity (solute movement through the formation is predominantly by diffusion rather than advection).

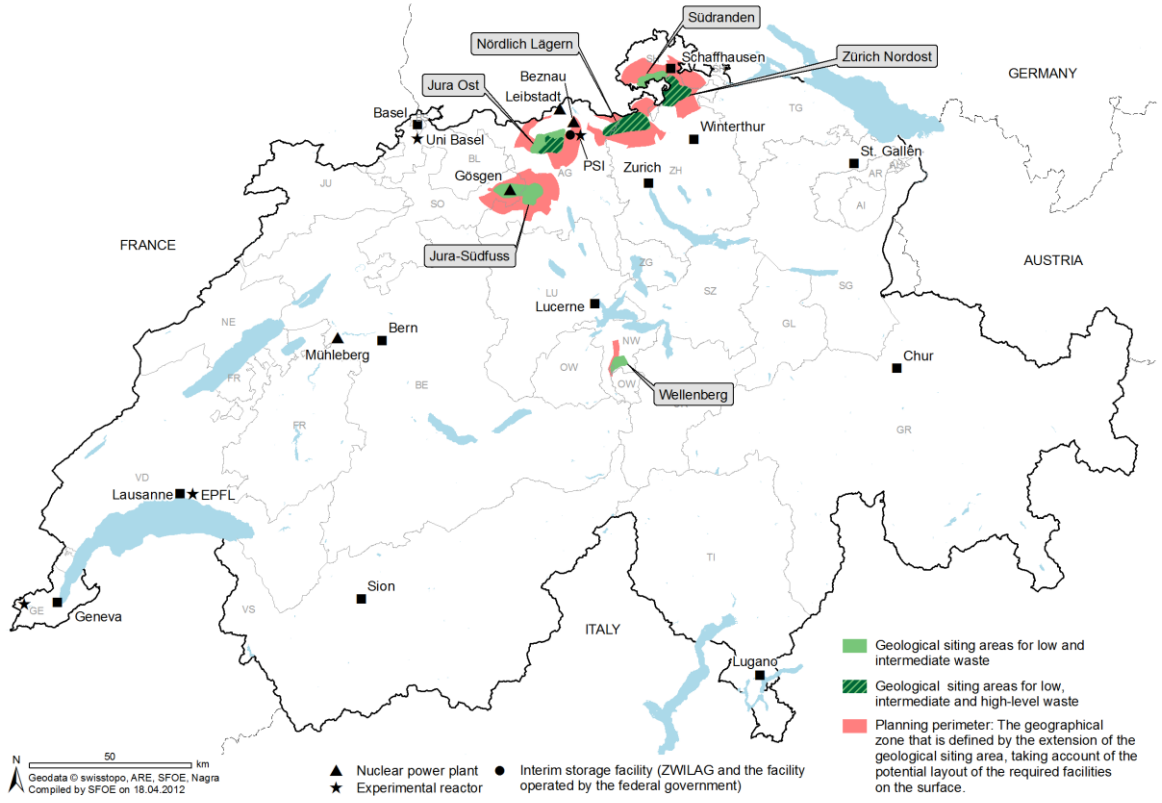

Figure 2. Siting regions for a deep geological repository for SF and HLW in Switzerland investigated in the Stage 2[14].

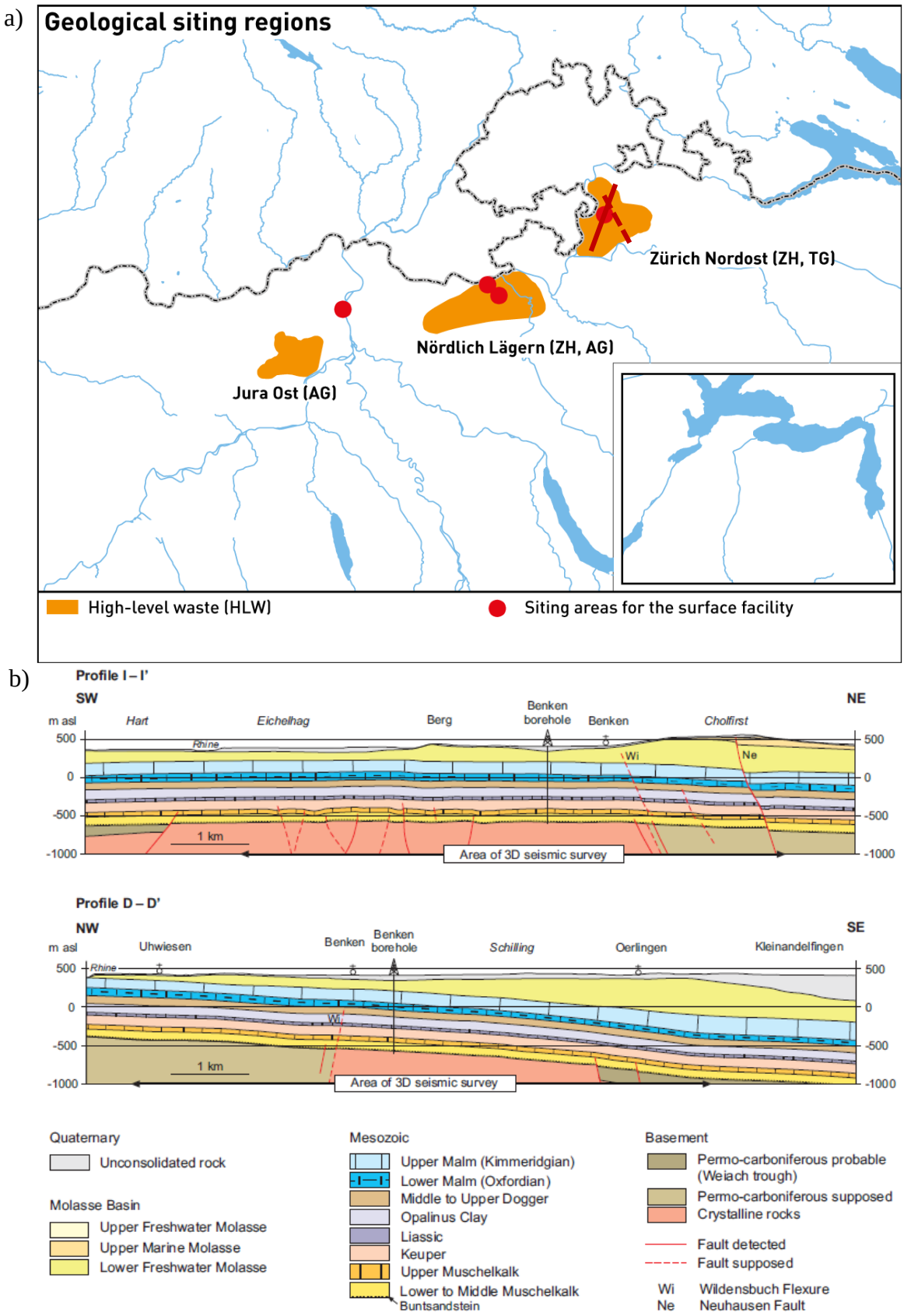

Figure 3. Siting regions for a deep geological repository for SF and HLW in Switzerland selected for further investigation in Stage 3 (panel a)[12]. Red lines represent the measurement areas of geological profiling (panel b) from SW to NE (top) and NW to SE (bottom) through the sedimentary rocks in "Zürcher Weinland"[1].

Large effort has been made to identify the most suitable disposal site for SF and HLW in Switzerland, however, the feasibility and the scientific understanding of the argillaceous system evolution requires further investigations[1]. It is beneficial to compare the results of the study on Opalinus Clay with similar argillaceous rock formation. The comparative analysis might shed light how the small geological and mineralogical differences of the three potential siting area effect the radionuclide uptake capabilities of the rock.

For instance, Boda Claystone Formation (BCF) in Hungary was selected as the potential host rock formation for SF disposal[10]. (HLW arises from the reprocessing of the Hungarian spent fuel, which was performed in the Soviet Union, later on in Russian Federation. According to a bilateral agreement, this waste will remain in the Russian Federation[14]. Furthermore, there are no reprocessing capabilities in the country and there are no plans to develop any[14].) The mineralogical content of BCF is similar to Opalinus. Both host rocks consist largely (up to 30%) of minerals from the class of phyllosilicates. The rock of the BCF is however highly heterogeneous on the microscale with two major constituents: the clayey matrix (~50wt.% illite–muscovite, chlorite, kaolinite, mixed structure clay minerals, albite/analcime cement, hematite flanks) and the fracture fillings (hematite grains, quartz, calcite, dolomite)[16]. The predominantly red and reddish brown color of BCF is given by the hematite flanks and it reflects the oxidizing nature of the depositional and early diagenetic environments[10]. This argillaceous rock formation located in the Western Mecsek Mountains in a 150km^2 large area of 700–900m thickness (Figure 4) was deposited in a shallow-water salt lake environment surrounded by dry to saline mudflat, under semi-arid to arid climatic conditions during the Upper Permian, approximately 260 million years ago[4,10,15-17].

Two possible sites of the Boda Claystone Formation are studied (Figure 4): the perianticlinal structure of the West-Mecsek Anticline Block (WMAB) and the Gorica-block (GB)[4,10]. (The annotation of WMAB changed to Boda-block in 2016, however, CHAPTER 2 as

a manuscript was submitted before the altering. For the sake of clarity, only the old annotation is used in this thesis.) The two sites belong to the same formation based on the structural and textural properties, but their mineral content differs significantly[10]. The two sites have different amount of phyllosilicates, quartz, albite, analcime, calcite and dolomite (Table 1)[18]. The different mineralogical compositions can be explained by the variant diagenesis degree. The process can be quantified by the Kübler-index (postulating the Scherrer-equation) that represents the crystallinity of illite and chlorite phases[19]. The Kübler-index of the two sites differs: it is lower in GB than in WMAB (Table 1), thus the degree of the diagenesis was higher at the latter site[20]. Radionuclide retention capacities of the different BCF areas may significantly be influenced by the distinct mineralogy of the sites, therefore it should be studied in detail.

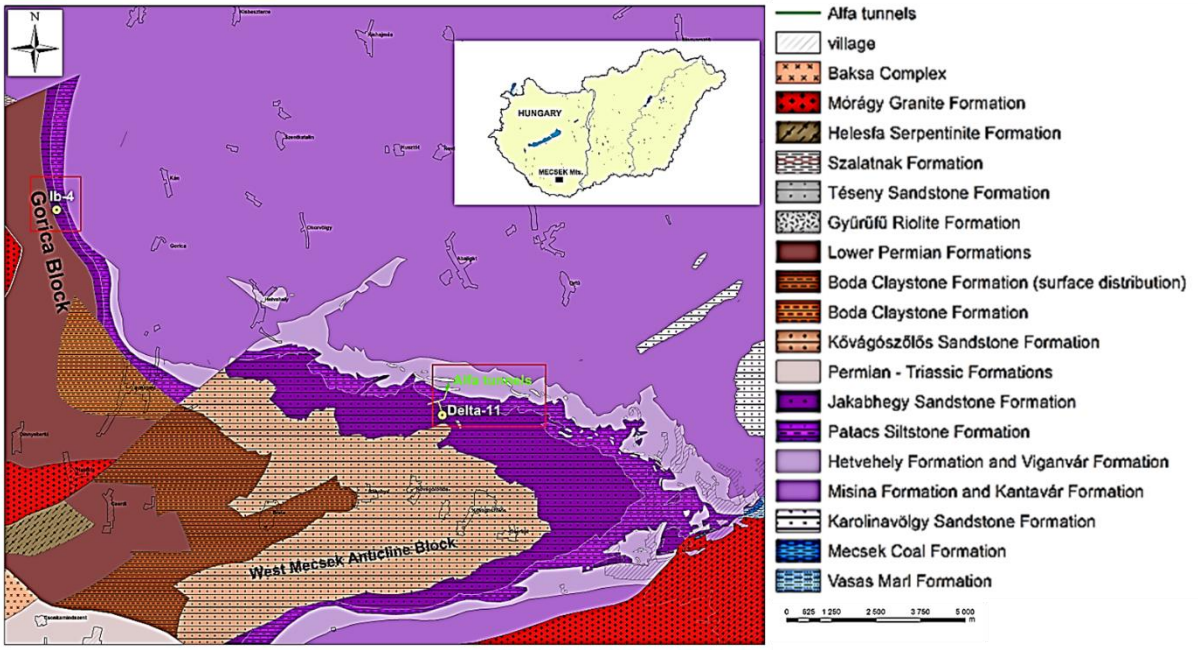

Figure 4. Location of Mecsek Mountains in Hungary and its geological map of the potential repository sites in the Boda Claystone Formation (BCF)[18]. (Delta-11 in the Alpha-tunnel and Ib-4 are boreholes representing West-Mecsek Anticline Block and Gorica Block, respectively[18].)

Table 1. Semi-quantitative mineral composition [wt.%] of bulk samples originating from Opalinus Clay (OPA)[21] and the two (WMAB, GB) sites of Boda Claystone Formation[18]

Sample **Depth** [m]			**OPA** ca. 600	**WMAB** ca. 1000	**GB** 540
Semi-quantitative mineral composition [wt.%]	**Pyrophillite**	Illite	24	38	50
		Illite/smectite mixed layer	9		
		Smectite	<1		
		Chlorite	9	<1	<1
	Feldspar	Albite	<1	45	17
		K-feldspar	2	<1	<1
	Silicate	Quartz	20	<1	8
		Kaolinite	18	<1	<1
		Plagioclase	<1	<1	<1
	Carbonate	Calcite	13	3	8
		Dolomite	<1		
		Ankerite		6	<1
		Siderite	4	<1	<1
	Sulfide	Pyrite	1	<1	<1
Kübler-index			—	0.676	0.387

The primary studies on a potential HLW disposal site mainly consists of geological and mineralogical studies of the host rock formation that are necessary but insufficient for the safety assessment of the radioactive waste repository. To demonstrate the feasibility of the HLW disposal site, the quantification of the radionuclide retention capabilities are essential[1]. However, the determination of these physico-chemical parameters is challenging due to the usually high heterogeneity of the host rock on the microscale.

1.3. Bentonite buffer

The investigations of the HLW repository so far demonstrated the feasibility of the safe construction and operation with current technologies as well as the achievability of the long-term safety[5]. However, the evolution of the geochemical environment in the nearfield needs further studies to reduce the uncertainties and to optimize the repository design[1]. In the near field, the bentonite buffer plays a particularly important role to ensure a stable and suitable chemical environment[5]. The unaltered bentonite backfill predominantly consists of clay minerals which determine the several advantageous properties (e.g. high swelling pressure, low hydraulic conductivity, high radionuclide sorption capacity) of the engineer barrier[22]. During the long-term evolution of the HLW repository, large quantities of ferrous iron in the interstitial pore water (arising from the corrosion of the steel casks) will prevail in the near field[5]. The large amount of Fe^{2+} released into the pore water interacts with the clay minerals, thus ferrous iron will have a substantial effect on the physical and chemical properties of the bentonite buffer[5,23–25].

It has been shown experimentally that ferrous iron influences the uptake characteristics of other divalent ions on Fe-bearing clay minerals[7]. The investigations demonstrated competitive interaction effects between Fe^{2+} and Zn^{2+} (representing Ni^{2+} key radionuclide) on montmorillonite, the main (65–90wt.%) constituent of bentonite when ferrous iron was added in excess[1,7,22]. The results indicated that the sorption of ferrous iron at montmorillonite surfaces are substantially enhanced by structural ferric iron due to surface induced redox processes[7,24]. Although, this effect is known from the interaction between ferrous iron and iron oxides (e.g. hematite[26]) as well as nontronite (the iron rich end-member of the clay minerals)[27], much less attention was focused on low Fe-bearing clay minerals. The studies so far performed suggest that the extent of ferrous iron uptake is much more complex and clay-specific than previously considered[25]. A recent investigation demonstrated that oxidative sorption does not exclusively alter with the Fe^{2+} concentration, but also slightly depends on the type of montmorillonite (originating from different mining sites)[24]. The results may be explained by the differences in the lattice structure of the clay mineral, however, the exact explanation requires further research.

Montmorillonite is a 2:1 dioctahedral smectite (aluminosilicate) of which ideal layer consists of two sheets of siloxane tetrahedra with a pseudohexagonally ordered alumina octahedral sheet in between (Figure 5)[3,28,29]. Two thirds of the cation sites in the octahedral layer have *cis*-symmetry and one-third have *trans*-symmetry with respect to the hydroxyl (OH^-) groups (Figure 5)[28,29]. As a dioctahedral smectite, only two of the three octahedral positions are filled yielding two distinct structural models[28,30,31]. In one model, all *trans*-octahedra are occupied and half of the *cis*-octahedra are vacant (*cv*-model)[28,30,31]. In the second model, all *trans*-octahedra are vacant and *cis*-octahedra are occupied (*tv*-model)[28,30,31]. Natural montmorillonites can be found in both, *cis*- and *trans*–vacant form (Figure 5)[28,30,31]. Natural clay minerals (montmorillonites and illites) contain isomorphic substitutions of Al^{3+} for Fe^{2+}, Fe^{3+}, Mg^{2+} in the octahedral sheet or to a lesser extent substitutions of Si^{4+} for Al^{3+} and Fe^{3+} in tetrahedral sheet (Figure 5)[3,30]. The structural characteristics of clay minerals (*cis*- or *trans*-occupational vacant forms), type and concentration of the substituted cations and their distribution in the octahedral and tetrahedral sheets (e.g. *cis*- or *trans*-position, extent of Fe—Fe clustering) depend on the mining site[30]. Furthermore, even for similar elemental compositions, the distribution of cations can be very different, especially in the octahedral sheet[30]. The structural chemistry of the Fe bearing montmorillonites from different locations (e.g. Milos-, Wyoming-, Texas-) is currently under debate[30,32,33]. Meanwhile, geological studies attempt to determine and to quantify parameters influencing the isomorphic substitution of cations into a montmorillonite layer (e.g. extent of diagenesis, type of mother rock)[30,32,33].

The oxidation state of iron in the crystal lattice structure of montmorillonite may profoundly alter the physicochemical properties of the clay mineral[34]. Macroscopic sorption experiments combined with extended X-ray absorption fine structure (EXAFS) and Mössbauer spectroscopy indicated the oxidative sorption of ferrous iron at the edge surface of Fe-bearing clay minerals[24]. This redox process is generally known from the iron uptake behavior of clay minerals exhibiting with high structural iron content (e.g. nontronite)[27,35]. The results showed that the oxidation of the sorbed Fe^{2+} is mainly caused by an electron transfer to the structural ferric iron[27,35]. Recent studies also investigated ferrous iron uptake behavior on low Fe-bearing clay minerals (various montmorillonites)[24,35,36]. The investigations revealed that the redox capacity of the clay mineral depends on multiple parameters (e.g. total iron content)[24,35]. The studies indicated that there is a difference in the accessibility of structural ferric iron for the different types of montmorillonite (e.g. structural iron in Texas-montmorillonite is less accessible than in Wyoming-montmorillonite) possibly because of their distinct Fe distribution in the clay lattice structure (e.g. random Fe distribution or Fe—Fe clustering)[24]. Although, these studies generally indicated an increased ferrous iron sorption on most Fe-bearing clay minerals (also with low Fe-content), the current sorption models significantly underscore their importance as iron sinks[37]. Furthermore, the presence of high amounts of sorbed ferrous iron may significantly influence the retardation of other metal and radioactive contaminants (e.g. nickel, uranium) through competitive sorption effects in radioactive waste repositories[7].

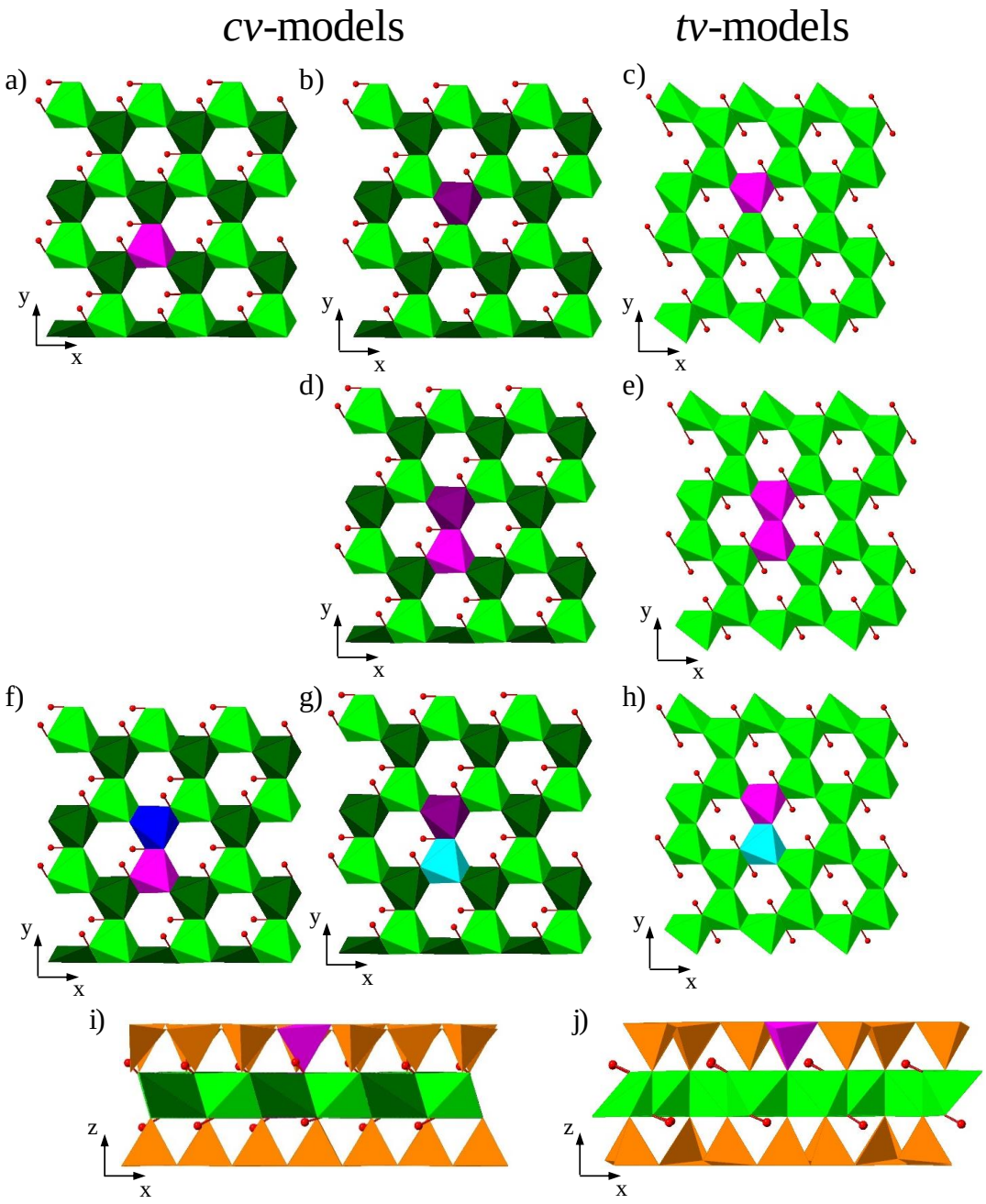

Figure 5. Schematic views of smectite models with different distribution of structural iron[2]. Panels a-h indicate only the octahedral sheet for the sake of clarity. The structures with single iron atom per supercell corresponding to a random distribution are shown in panels a-c, configurations with Fe–Fe clustering are represented in panels d-e, while Mg–Fe clustering is in panels f-h. The tetrahedral incorporation of iron is shown in panels i-j. *cv*-models correspond to panels a-b, d, f-g and i, while *tv*-models are shown in panels c,e,h,j. Orange color corresponds to silica tetrahedra, Mg and Al octahedra are shown with blue and green colors, respectively. Structural Fe incorporation is marked with pink color. *Cis*-octahedra are represented with lighter, while *trans*-octahedra are shown with darker colors. The different occupational sites can be distinguished by the different relative position of the hydroxyl (OH^-) groups shown with red spheres.

In the safety assessment of the HLW disposal site, the retention of uranium has superior significance through sorption and/or (co)precipitation on montmorillonite surfaces to avoid contact with the biosphere[1]. Uranium may form outer-sphere surface complexes on the basal planes and inner-sphere complexes at the edge sites of the clay mineral[38]. The stability of the uranium retention mechanism and the exact nature of the sorption complexes however remained unclear[38]. In addition, iron (as a transition metal) may influence the formation of these surface species[1]. Therefore, the uranium uptake behavior on relevant montmorillonite edge surfaces and the impact of structural and sorbed iron on the uptake mechanism.

2. Experimental techniques

2.1. Microanalytical methods

Natural samples are usually highly heterogeneous on the microscale and contaminants with minor or trace elemental concentrations as well as oxidation states have to be determined from microscopic volumes[39]. Different microanalytical methods are used to perform this task. One of them is the microscopic X-ray fluorescence (micro-XRF). It became widespread due to its capability to simultaneously detect multiple chemical elements. Measurements requiring high element specific sensitivity and/or high lateral spatial resolution (e.g. low or trace element concentrations in microscopic volumes) are often carried out at the micro-XRF beamlines in a synchrotron storage ring because of the several advantages of synchrotron radiation[17,40]:

- monoenergetic beams can be produced in a wide energy range allowing excitation of specific elements;
- scattering background is low due to the highly polarized radiation;
- the beam can be focused onto a small area due to the good and natural vertical collimation, as well as its high intensity and brightness.

Elements present in a sample can be identified by the energy of peaks occurring in the spectra[40,41]. After the identification of the elements, the net characteristic peak areas and their background values can be determined[40,41]. Concentrations can be calculated from the characteristic intensities obtained as the results of the fit with the least squares method[40,41]. The dependence of the concentration on the intensity of the element i with the corresponding X-ray line with the energy E_i in a homogenous sample volume with of thickness d can be calculated based on Equation (2)[40,41].

$$I_i(E_i) = \frac{d\Omega_1 d\Omega_2}{4\pi} \frac{\varepsilon(E_i)}{\sin(\psi_0)} C_i \cdot \omega_{X_i} \cdot J_{X_i} \cdot p_i \cdot \tau_i(E_0) \cdot \frac{1 - \exp\left[-\rho d \left(\frac{\mu_s(E_0)}{\sin(\psi_0)} + \frac{\mu_s(E_1)}{\sin(\psi_1)}\right)\right]}{\frac{\mu_s(E_0)}{\sin(\psi_0)} + \frac{\mu_s(E_1)}{\sin(\psi_1)}} I_0(E_0) \quad (2)$$

where $I_i(E_i)$ is the number of characteristic photons with energy E_i measured in a unit solid angle during a unit time, $d\Omega_1$ and $d\Omega_2$ are the differential solid angles of the excitation and the outgoing X-ray radiation, $\varepsilon(E_i)$ is the detection efficiency of the photon with energy E_i, C_i is the concentration of element i in the sample, ω_{X_i} is the fluorescence yield related to the electron shell X of element i and J_{X_i} is the jump ratio for the same shell, p_i is the intensity ratio within shell X, $\tau_i(E_0)$ is the photoelectric mass absorption coefficient of element i at energy E_0, ψ_0 and ψ_1 are the incidence and detection angles measured from the plane of the sample, $\mu_s(E)$ is the mass absorption coefficient of the sample excited with energy E, $I_0(E_0)$ is the intensity of the excitation radiation at energy E_0[40].

As shown in Equation (2), the total characteristic X-ray intensity of a selected element depends nonlinearly on the concentrations of other elements located in the sample as the total mass absorption coefficient (μ_s) is determined by all elements in the sample[41]. To determine the concentration of the elements, different quantitative methods are used among which the fundamental parameter method is nowadays the most widespread[41,42]. In this mathematical method, a few reference sample with known elemental concentration is still required to determine parameters (e.g. geometric factors), which would otherwise be difficult to calculate[41]. The method also requires an estimation of element content without a detectable characteristic X-ray line in the measured spectra (the so-called dark matrix), which can be estimated in different ways[41]:

- If the composition of the dark matrix is completely unknown, the average atomic number of the dark matrix can be determined from the intensity ratio between the coherent and incoherent scattering. This is the initial approximation of the iterative calculation of the mass absorption correction, however, the less accurate method.
- If the mass ratios between the elements of the dark matrix are known, the measurement of an independent standard is necessary to determine the (initial) intensity I_0 of the excitation radiation. This approach is sufficient, if the mass fraction of the dark matrix is low and it is not needed for the further studies.
- If the concentration of the elements of the dark matrix are known, the concentrations of the measured elements can be calculated using a simple iterative method.

In the latter case, the missing additional information can be obtained, for example, with the elemental mapping of the same sample area using micro-XRF in a modified setup (e.g. lower excitation energy in vacuum mode)[41]. However, it is usually faster and more accurate to apply other microanalytical techniques more sensitive for phases with light elements: microscopic X-ray diffraction (micro-XRD) and scanning electron microscopy energy dispersive X-ray analysis (SEM/EDX)[41].

Micro-XRD is a widely used, non-destructive X-ray based microanalytical approach for phase analysis in a heterogeneous environmental sample[39]. XRD patterns (diffractograms) are routinely produced from powder samples based on the constructive interference of a monochromatic X-ray beam[43]. The peak position in a diffractogram provides information on the structure, crystallographic orientations and structural (e.g. lattice) parameters of each mineral phase[43]. Micro-XRD requires a finely focused (few μm size spatial resolution) excitation X-ray beam with sufficiently high intensity, which can be obtained only at synchrotron beamlines[43]. Micro-XRD diffractograms are usually measured at several selected positions of interest inferred from the micro-XRF elemental maps. A combined micro-XRF and micro-XRD approach allows in the best cases the visualization of the distribution of chemical elements and the associated crystalline phases in complex, heterogeneous materials[44,45]. However, the long measurement time of micro-XRD makes it (almost) impossible to perform a complete thin section (rock) sample analysis.

To determine the concentration of light elements, SEM/EDX measurements should be applied. In these experiments, the sample is irritated by a finely focused electron beam and the emitted characteristic X-ray spectrum is measured with a semiconductor energy dispersive X-ray spectrometer (EDX)[46]. The measured X-ray spectrum in each small excited volume (corresponding pixels in 2D elemental maps) is used to identify and to quantify the distribution of light elements in a heterogeneous sample[46]. Quantitative analysis is challenging because the intensity of each element is influenced by all other constituents present in the excited volume through their influence on the electron scattering and retardation ("atomic number", absorption, "secondary fluorescence" matrix effects) [46]. Furthermore, mutual peak interferences especially when the peaks of major constituents interfere with the peaks of minor or trace constituents may cause issues[46]. The complex physics of the matrix corrections has been rendered into algorithms by a combined theoretical and empirical approach, a standardless iterative method based on Monte Carlo simulations of electrons[46].

In this way, SEM/EDX is capable to detect and to quantify major elements (e.g. Al, Si) of an argillaceous rock sample, but it is insufficient to determine the exact mineral phases and their concentration. The average mineral composition of the sample from micro-XRD measurements gives sufficient additional information to calculate the ratio of the mineral phases in each pixel[44]. Another disadvantage of SEM/EDX is that elements representing key radionuclides with high atomic numbers and low concentration cannot be detected in clay samples because of their lower cross-section for electron excitation. It can be overcome by combining micro-XRF and SEM/EDX measurement results. The interleaving of the concentration based elemental maps obtained by the latter two measurements allows in the best cases for quantifying the radionuclide sorption capacity of the mineral phases present in the sample[47,48]. Even the combination of these three microanalytical methods is insufficient to determine the sorption complex formed at the edge sites of the main mineral phases because of their spatial resolution limits (few μm instead of few Å). Furthermore, information about the structural differences among the same mineral phases (e.g. properties of iron substitution), which may cause differences in the uptake capabilities, cannot be obtained.

2.2. X-ray absorption spectroscopy (XAS)

X-ray absorption spectroscopy (XAS) is one of the most widely applied technique in molecular environmental science to gain structural information at the mineral/water interface[39]. It has several advantageous properties (e.g. in-situ, non-destructivity, element specificity), furthermore, the sample is not required to have long-range order even at low concentration level of the absorbing element[49]. In the best case, the average local structure (types and numbers of neighboring atoms, bond distances) around atoms of the absorbing elements can be determined[49]. The approach is based on the examination of the absorption coefficient around a given absorption edge of the specified element[49–51].

The studies can be divided into two different analysis approaches of a given spectrum based on the energy dependence of the absorption coefficient (Figure 6)[49–51]:

- X-ray absorption near edge structure (XANES) spectroscopy investigates the absorption edge from approximately 50eV below the absorption edge.
- Extended X-ray absorption fine structure (EXAFS) spectroscopy based on the studies beyond ~100eV above the absorption edge.

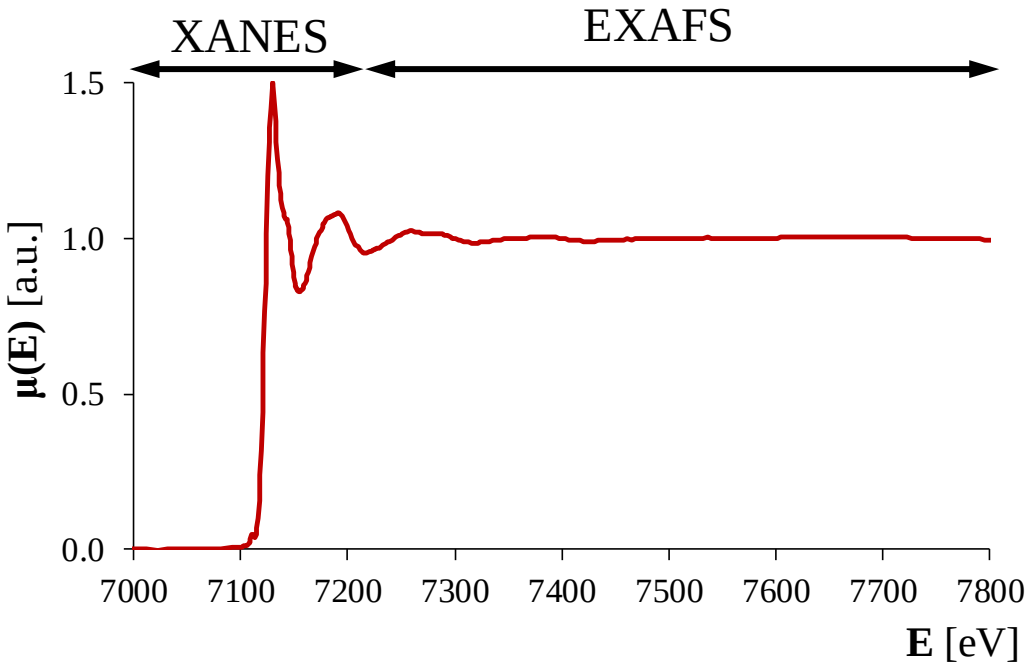

Figure 6. Fe^0 absorption coefficient as the function of energy with marked XANES and EXAFS energy regions

The most common way to interpret XANES spectra is the 'fingerprinting' approach: the comparison of the observed features in unknown samples with features of standards[50]. In the best case, the average oxidation state of the element present in the unknown sample can be identified based on the energy and the intensity of the absorption edge as well as features (e.g. shoulders) in the pre- and/or post-edge regions[50]. A XANES spectrum is easy to measure

and it is inevitably scanned during the attainment of an EXAFS spectrum. Despite these advantages, relatively little use has been made of XANES beyond qualitative comparisons of the unknown spectrum to reference spectra[50]. If the element is present in a mixed chemical state or it is difficult to prepare stable standard(s) of the given chemical state of the element, the measured XANES spectrum can hardly be interpreted. Despite strong efforts made to theoretically predict XANES spectra in the last decade, these calculations are complex and computationally expensive[50]. Therefore, most of the XAS studies focus on the EXAFS region as its evaluation has become nearly a routine.

The standard data analysis of an EXAFS spectrum can determine the local environment of the studied structural element or the nature of surface complexes formed at mineral edges[39]. The approach is based on the examination of the oscillations in the EXAFS region caused by the backscattering of the photoelectron on neighboring atoms as it is determined in Equation (3)[49–51,53]:

$$\chi(E) = \frac{\mu(E) - \mu_0(E)}{\Delta\mu_0} \qquad (3)$$

where $\mu(E)$ is the energy dependent absorption coefficient, $\mu_0(E)$ is the 'background' absorption coefficient if the atom would be isolated and $\Delta\mu_0$ is the magnitude of the absorption edge. $\mu_0(E)$ can be approximated by the fitting of an appropriate function to the smooth part of the EXAFS region (often splined polynomial functions)[50,51].

For the further extraction of the EXAFS spectrum, its energy dependence should be converted to Fourier-space (Equation (4))[49,50,53].

$$k = \sqrt{\frac{2m_e}{\hbar^2} \cdot (E - E_0)} \qquad (4)$$

where k is the wavelength, m_e is the electron rest mass $\left(m_e = 9.109 \cdot 10^{-31}\text{kg}\right)$, $\hbar^2$ is the reduced Planck-constant $\left(\hbar = \frac{h}{2\pi} = 1.055 \cdot 10^{-34}\text{Js}\right)$, E and E_0 are the energies of the incident photon and the absorption edge, respectively. E_0 could be determined by finding the first peak of the first derivative in the $\mu(E)$ spectrum[49,50,53].

EXAFS spectroscopy has the advantage that a spectrum can be fitted by Equation (5) based on the description of the interference between the outgoing photoelectron and the backscattered waves[39,49–51]. The first exponential accounts for finite elastic mean free paths of photoelectrons which limits the distance range that can be sampled by EXAFS[49]. The second damping term is the so-called Debye–Waller factor reflecting destructive interferences due to fluctuations of distances describing structural and/or thermal disorder (under the assumption of small displacements and Gaussian distributions of distances)[49,51]. The main consequence of the damping terms is that the EXAFS information is limited to atoms in the near vicinity of the absorber (approximately 5–10Å from the absorbing atom)[49].

$$\chi(k) = \sum_i \frac{N_i A_i(k) S_0^2}{k R_i^2} \cdot \mathrm{e}^{\frac{-2R_i}{\lambda(k)}} \cdot \mathrm{e}^{-2\sigma_i^2 k^2} \cdot \sin[2kR_i + \varphi_i(k)] \qquad (5)$$

where N_i is the coordination number, $A_i(k)$ is the backscattering amplitude function, S_0^2 is the amplitude reduction factor, R_i is the absorber–scatter distance, σ_i^2 is the mean square average displacement from the mean bond length, $\varphi_i(k)$ is the total phase shift and $\lambda(k)$ is the mean free path length of the photoelectron[49–51]. The sum is over each coordination shell j up to the n^{th} coordination shell typically up to distances of 5Å[50].

In spite of its simplicity and robustness, standard EXAFS analysis has several limitations. The number of scattering atoms (N_i) and the absorber–scatterer distance (R_i) are the parameters of principal interest for coordination chemistry, however, a variety of other parameters (e.g. S_0^2) must also be determined or be assumed[49]. Furthermore, structural parameters obtained by standard EXAFS analyses are highly correlated making definite conclusion sometimes difficult[39]. For example, large uncertainties of R_i and/or N_i are a direct result of their correlation with the structural disorder[51,54].

To transform each sinusoidal component into a separate peak, a Fourier transformation (FT) of the $\chi(k)$ spectrum from Fourier- (k) to real space (R) is required[49,50]. In simple cases, when the FT moduli are well separated from each other and they are determined by only one distance, it is possible to obtain direct information on the interatomic distance[49]. The reciprocal space explored by EXAFS is however limited, the discrimination of atomic shells separated by less than 0.10Å…0.15 Å (typically the case for clay minerals) is practically impossible[51]. For example, X-ray absorbing atoms of the octahedral sheet are surrounded by neighboring atoms from the octahedral and tetrahedral sheets at R = 3.00Å…3.10Å and R = 3.13Å…3.28Å, respectively[31]. This local structure results in a strong overlap of scattering contributions from the octahedral and tetrahedral cations making any definitive structural interpretation of powder EXAFS data for clay minerals with the standard approach difficult[55].

Ab initio simulations of EXAFS and XANES spectra based on atomistic simulations becomes more and more common thanks to significant advances in the modelling algorithm and computer performance. In the best case, the data analysis of XAS spectra allows determining the local environment and the oxidation state of the studied element, unequivocally. Thus, information about the nature of structural iron and surface complexes formed at clay mineral edge sites can be obtained at the same time.

3. Analytical techniques and modelling approaches

3.1. Correlation analysis and multivariate methods

The statistical relationship between two (measured) variables can be indicated by the correlation coefficient (r)[56]. The correlation coefficient varies in the interval [-1,+1], the lower bound represents strong negative, while the upper bound indicates strong positive linear relationship between the variables[56]. Positive values correspond to correlation, while negative values indicate an anticorrelation[56]. If the linear relationship is weak (or there is no), the absolute value of r will be close to 0 (or it will be 0)[56]. Several types of correlation coefficients exist, among which the Pearson correlation coefficient (Equation (6)) is the one that does not require theoretically expected values and deviations[56,57].

$$r = \frac{\sum_{i=1}^{N}(x_i y_i - \overline{xy})}{\sqrt{\frac{\sum_{i=1}^{N}(x_i - \bar{x})^2}{N} \cdot \frac{\sum_{i=1}^{N}(y_i - \bar{y})^2}{N}}} \quad (6)$$

where N is the number of observations, x_i and y_i are the values of the x and y variable during observation i, $\bar{x}$ and $\bar{y}$ are the average values of variable x and y, respectively[56].

The value of the correlation coefficient is insufficient to unambiguously conclude (anti)correlation except in very special cases (e.g. multivariate normal distribution)[56,58]. The appropriate mode to represent the two variables is to plot them in a scatter diagram in which the related values of the variables are represented as a point set[56,58]. This simple plot can give information whether a relationship exists between the variables in the data set, how strict it is and what function describes it[56].

Multivariate methods are used in several areas in environmental research to handle large data matrices. The aim of their application in environmental data analysis is to reduce the large number of observed and multi-correlated variables to a few (new) inherent latent variable to reveal new relationships[58]. From several known multivariate methods, standard factor analysis (FA), positive matrix factorization (PMF) and cluster analysis (CA) were used in this study.

3.1.1. Standard factor analysis

Standard factor analysis (FA) is one of the most widely used multivariate methods to statistically analyze results of chemical analysis. The approach reduces the dimension of the original data matrix based on the multicollinearity between the measured variables[58]. It introduces new, latent variables, so-called factors, which are the linear combination of the original (measured) variables. Factors are chosen to represent the maximum possible fraction of the variability contained in the original data set as the multiplication of two matrices with the best approximation (Equation (7))[58].

$$\boldsymbol{X}_{mxn} = \boldsymbol{G}_{mxp}\boldsymbol{F}_{pxn} + \boldsymbol{E}_{mxn} = \boldsymbol{X}^{(p)}_{mxn} + \boldsymbol{E}_{mxn} \quad (7)$$

where $\boldsymbol{X}_{mxn}$ and $\boldsymbol{X}^{(p)}_{mxn}$ are the original and the FA approximated matrices with m number of observation point and n number of original variables, respectively. $\boldsymbol{G}$ and $\boldsymbol{F}$ are the factor loading and distribution matrices containing a number of p factors, respectively. $\boldsymbol{E}$ is the residual matrix of the approximation[58].

The original (measured environmental) variables (e.g. concentrations) of the original data matrix may appear in different order of magnitude. In FA evaluations, the first *p* components are determined by the variables with the highest values, therefore it is essential to (auto)scale these components to the same order of magnitude[58]:

$$z_{ij} = \frac{x_{ij} - \bar{x}_j}{s_j} \quad (8)$$

where z_{ij} represents the scaled values, x_{ij} the i^{th} (measured) value and $\bar{x}_j$ is the average value and s_j is the standard deviation of the j^{th} original variable, respectively[58].

Factors expressed by the original variables may also contain negative values indicating anticorrelation[58]. However, it might be necessary to assign the composition of the new variables (factors) to the measurement points in the case of data matrices obtained as the result of environmental measurements, which can hardly be interpreted. Therefore, in such cases other multivariate methods should be applied.

3.1.2. Positive matrix factorization

Positive matrix factorization (PMF) is a special type of FA, which decomposes the data matrix into two nonnegative matrices[59]. The best PMF decomposition can be obtained by Equation (9), through several nontrivial elemental rotations of the decomposed matrices[59]. The most common approach to determine the factors is nowadays the multistep iterative method, which rotates the several initial pseudorandomly decomposed matrices into numerous coherent $\boldsymbol{G}$ and $\boldsymbol{F}$ (so-called factor contribution and factor loading) matrices with nonnegative values[59].

$$\boldsymbol{X} = \boldsymbol{GF} + \boldsymbol{E} = \boldsymbol{GTT}^{-1}\boldsymbol{F} + \boldsymbol{E} = \overline{\boldsymbol{G}}\,\overline{\boldsymbol{F}} + \boldsymbol{E} \quad (9)$$

where the new factors are $\overline{\boldsymbol{F}} = \boldsymbol{T}^{-1}\boldsymbol{F}$ and $\overline{\boldsymbol{G}} = \boldsymbol{GT}$[59].

The best PMF decomposition can be obtained by minimizing the target function *Q* as in Equation (10). Factors in PMF are not orthogonal to each other (standard FA) that may result in several local solutions as the currently known iterative methods only allow for finding the local minima of the target function[59].

$$Q = \sum_{i=1}^{m}\sum_{j=1}^{n}\left(\frac{\boldsymbol{X}_{ij} - \sum_{k=1}^{p}\boldsymbol{G}_{ik}\boldsymbol{F}_{kj}}{\boldsymbol{\sigma}_{ij}}\right)^2 \quad (10)$$

where $\boldsymbol{X_{ij}}$ is the (measured) value i of the variable j, σ_{ij} is the uncertainty for this data point, $\boldsymbol{G_{ik}}$ is the value i of the variable (factor) k in the factor contribution matrix, $\boldsymbol{F_{kj}}$ is the value j of the variable (factor) k in the factor loading matrix. m is the number of measurement points, n is the number of variable and p is the number of factors.

A wrongly specified factor number (p) may cause convergence problems during the evaluation[59]. If the analysis is performed with a too high p value, one or multiple factors will describe the noise of the matrix[59]. While the evaluation is performed with a too low value of p, the solution will not describe the matrix properly (e.g. too high value of the residual matrix element)[59]. In the best cases, the value of p can be determined from standard factor analysis.

The method uses the uncertainty of the measured values for the proper weighting of the data matrix, thus allowing the separate treatment of the matrix elements. Consequently, values measured under the detection limit can also be included into the data set, thus data loss is avoidable[59].

3.1.3. Cluster analysis

Cluster analysis (CA) is a multivariate method that classifies the measurement points into different groups called clusters based on the measure of the distance in the multidimensional space. Two types of cluster analysis can be distinguished. In the hierarchical approach, the new clusters are subsequently formed from the existing ones in an iterative manner. In the non-hierarchical approach all the cluster are defined at once.

Non-hierarchical cluster analytical methods are used to handle data matrices containing a large number of (measurement) points and to determine whether there is a correlation between the (measured) variables[60]. The most widely used non-hierarchical clustering approach is the K-means method[60]. The algorithm classifies every object into one of the K number of different clusters, where first the value of K should be determined by the user. The problem in this case is similar to that in PMF, when the incorrect factor/cluster number lead to improper results. Therefore, the value of K is often based on the results of other multivariate method (e.g. standard factor analysis)[60]. The second step is to set randomly or manually K initial clusters (or their centroids). Thereafter, the algorithm proceeds as follows[60]:

1) Computation of the centroids for each cluster and the distances between each object and each cluster centroid;
2) Replacement of every object, which is not in the cluster with the closest centroid;
3) Check of the convergence criteria. If they are not fulfilled, go back to the first step, otherwise stop the iteration.

In this study, the segmentation of the data set could be performed applying cluster analysis based on the similarity (distance) of the measurement point in the abstract space defined by elemental concentrations. After the cluster determination, the average elemental concentration and the distribution of the cluster points of each cluster should be compared to the elemental maps for the further interpretation.

3.2. *Ab initio* calculations

The application of theoretical quantum chemistry (or quantum mechanical calculations) for the quantitative interpretation of experimental data is becoming more and more widespread. *Ab initio* (or first-principles) methods enable us to meticulously describe the electronic structure of fluids, solids or mineral surfaces[61]. Furthermore, the evolution of the atomic and electronic structure in time can be simulated using *ab initio* based molecular dynamics (MD). Density functional theory (DFT) became a widely applied *ab initio* approach to simulate the mechanism of ion adsorption on the edge surfaces of minerals[35,62,63] The recently improved DFT based methods have been proven to accurately predict the electronic structure of transition metals and actinides in condensed phase[64].

The MD method relies on the Newtonian equation of motion (Equation (11)), which relates the acceleration of a particle and the force exerted on it at each instance of time. The value of the force is the derivative of the interaction potential of the particles[65]:

$$m_i \frac{\mathrm{d}^2 \boldsymbol{r}_i(t)}{\mathrm{dt}^2} = \boldsymbol{f}_i(\boldsymbol{r}_1, \boldsymbol{r}_2, \dots, \boldsymbol{r}_N, t) = -\frac{\partial V(\boldsymbol{r}_1, \boldsymbol{r}_2, \dots, \boldsymbol{r}_N, t)}{\partial \boldsymbol{r}_i(t)} \qquad (11)$$

where m_i is the (constant) mass of the particle (atom) and $\boldsymbol{r_i}(t)$ is the position vector of the i^{th} particle, $\boldsymbol{f_i}(\boldsymbol{r}_1, \boldsymbol{r}_2, \dots, \boldsymbol{r}_N, t)$ is the force vector acting on the i^{th} particle at time t. $V(\boldsymbol{r}_1, \boldsymbol{r}_2, \dots, \boldsymbol{r}_N, t)$ describes the interaction potential of the particles, N is the total number of particles in the system $(i = 1; \dots; N)$.

A discretization of the Equation (11) by adopting a finite time step Δt allows for a numerical integration (velocity Verlet algorithm)[65]:

$$\boldsymbol{r}_i(t + \Delta t) = \boldsymbol{r}_i(t) + \Delta t \cdot \boldsymbol{v}_i(t) + \frac{(\Delta t)^2}{2m_i} \cdot \boldsymbol{f}_i(\boldsymbol{r}_1, \boldsymbol{r}_2, \dots, \boldsymbol{r}_N, t) \qquad (12)$$

$$\boldsymbol{v}_i(t + \Delta t) = \boldsymbol{v}_i(t) + \frac{\Delta t}{2m_i} \cdot [\boldsymbol{f}_i(\boldsymbol{r}_1, \boldsymbol{r}_2, \dots, \boldsymbol{r}_N, t) + \boldsymbol{f}_i(\boldsymbol{r}_1, \boldsymbol{r}_2, \dots, \boldsymbol{r}_N, t + \Delta t)] \qquad (13)$$

where $\boldsymbol{r_i}(t)$ and $\boldsymbol{r_i}(t + \Delta t)$ are the position vectors of particle i at time t and $t + \Delta t$, respectively. $\boldsymbol{v_i}(t)$ is the velocity vector of particle i (which can be calculated based on Equation (13)). t is the beginning time and Δt is the time step. In this way, the time evolution of each particle in a system can be simulated.

The consistency of the physical model defined by Equation (11) with the physical system is fully determined by the quality of the interaction potential $V(\boldsymbol{r}_1, \boldsymbol{r}_2, \ldots, \boldsymbol{r}_N, t)$. The interaction potential either can be parametrized for an empirical model or obtained by quantum mechanical calculations. In *ab initio* calculations, the forces between particles are obtained by solving the time-independent Schrödinger equation (Equation (14)).

$$\widehat{H}(\boldsymbol{r}, \boldsymbol{R}) \mid \Psi(\boldsymbol{r}, \boldsymbol{R})\rangle = E \mid \Psi(\boldsymbol{r}, \boldsymbol{R})\rangle \tag{14}$$

where $\widehat{H}(\boldsymbol{r}, \boldsymbol{R})$ is the Hamiltonian operator, $\Psi(\boldsymbol{r}, \boldsymbol{R})$ is the wavefunction and E is the energy of the system.

Equation (14) is solved by employing the Born–Oppenheimer (BO) approximation, which separates the motion of the nuclei and electrons. The approach treats an atomic nucleus as a classical particle and the electrons adiabatically follow the nuclei instantaneously. Therefore, Equation (14) simplifies to:

$$\widehat{H_{\mathrm{e}}}(\boldsymbol{r})\varphi_i(\boldsymbol{r}) = E \cdot \varphi_i(\boldsymbol{r}) \tag{15}$$

where $\widehat{H_{\mathrm{e}}}(\boldsymbol{r})$ is the electronic Hamiltonian, $\varphi_i(\boldsymbol{r})$ is the electronic state (eigenvector) of electron i and E is the corresponding energy eigenvalue. The electronic states have to meet the orthonormality (Equation (16)) and normalization condition to match the $\rho(\boldsymbol{r})$ electronic density (Equation (17)).

$$\left\langle \varphi_i(\boldsymbol{r}) \mid \varphi_j(\boldsymbol{r}) \right\rangle = \delta_{ij} \tag{16}$$

$$\rho(\boldsymbol{r}) = \sum_i f(i) |\varphi_i(\boldsymbol{r})|^2 \tag{17}$$

where $f(i)$ is the factor of orbital occupation of electron i.

Equation (14) can be solved analytically only for a few, very simple cases (e.g. for a single hydrogen atom). Many-electron systems have to rely on approximative methods for determining the ground state. Nowadays, the most widely applied approach is density functional theory (DFT). According to Hohenberg and Kohn, the ground state of an electron system in an external field (columbic potential of the nuclei) can be defined by a universal functional of the electron density and an external potential[66]. In this approach, the exchange–correlation energy is expressed as in Equation (18) where the total energy has a minimum when $\rho(\boldsymbol{r})$ coincides with the true electronic charge density distribution in $V(\boldsymbol{r})$[66].

$$E = \int V(\boldsymbol{r})\rho(\boldsymbol{r})d\boldsymbol{r} + F[\rho(\boldsymbol{r})] \tag{18}$$

where $V(\boldsymbol{r})$ is the external potential, $\rho(\boldsymbol{r})$ is the electronic density and $F[\rho(\boldsymbol{r})]$ is a universal functional of the electronic density independent of the external potential.

Although, the existence of a unique $F[\rho(\boldsymbol{r})]$ function was proved, the exact mathematical expression for such a functional is unknown. Kohn and Sham have approximated Equation (18) by introducing independent single particle electron orbitals $|\varphi_i(\boldsymbol{r})\rangle$[67]:

$$F[|\varphi_i(\boldsymbol{r})\rangle, \boldsymbol{R}] = T[|\varphi_i(\boldsymbol{r})\rangle] + U[\rho(\boldsymbol{r}), \boldsymbol{R}] + E_{\mathrm{xc}}[\rho(\boldsymbol{r})] \quad (19)$$

where $T[|\varphi_i(\boldsymbol{r})\rangle]$ is the kinetic energy functional for single particle electron orbitals (Equation (20)), $U[\rho(\boldsymbol{r}), \boldsymbol{R}]$ is the Coulomb-interaction functional expressed in Equation (21), $E_{\mathrm{xc}}[\rho(\boldsymbol{r})]$ is the exchange–correlation energy functional expounded in Equation (22).

$$T[|\varphi_i(\boldsymbol{r})\rangle] = \frac{1}{2}\sum_i \nabla_i^2 \quad (20)$$

$$U[\rho(\boldsymbol{r}), \boldsymbol{R}] = \sum_j \frac{Z_j}{|\boldsymbol{r} - \boldsymbol{R_j}|} \quad (21)$$

$$E_{\mathrm{xc}}[\rho(\boldsymbol{r})] = \int \rho(\boldsymbol{r})\varepsilon_{\mathrm{xc}}\big(\rho(\boldsymbol{r})\big)d\boldsymbol{r} \quad (22)$$

where Z_j is the charge and $\boldsymbol{R}_j$ is the position vector of atomic nucleus j. $\varepsilon_{\mathrm{xc}}\big(\rho(\boldsymbol{r})\big)$ is the exchange–correlation energy. In the so-called local density approximation (LDA) $\varepsilon_{\mathrm{xc}}\big(\rho(\boldsymbol{r})\big)$ is evaluated based on the properties of the homogenous electron gas for a given charge density. Variables are written in atomic units.

LDA based DFT is a suitable choice that accurately treats exchange and correlation functional by acting some effective potential on the electrons[68]. Equation (22) expresses that the exchange-correlation energy value of the homogeneous electron gas of the charge density at local point $\boldsymbol{r}'$ is used[68]. LDA works best for metallic systems since it has been derived from the uniform electron gas usually reproducing the ground-state charge density to within a few percent[68]. An improvement of LDA is the generalized gradient approximation (GGA), which takes into account not only the electron density $\big(\rho(\boldsymbol{r})\big)$ but also its gradient $\big(\nabla\rho(\boldsymbol{r})\big)$. GGA substantially improves performance of LDA for the systems with ionic and covalent bounding[68].

The accurate description of the strong correlation of the *d*- and *f*-electrons present in transition metals and actinides (e.g. iron and uranium) in the plain DFT calculations applying GGA had been a challenge for a long time[69]. To improve the accuracy of the electronic structure predictions, the so-called DFT+U method is applied which introduces the Hubbard-term (or Mott-Hubbard contribution)[69]:

$$E_{\mathrm{DFT+U}} = E_{\mathrm{DFT}} + \frac{U-J}{2}\sum_{\sigma}\mathrm{Tr}[\rho^{\sigma} - \rho^{\sigma}\rho^{\sigma}] \qquad (23)$$

where E_{DFT} is the total energy of the system calculated by using the conventional DFT method, $\frac{U-J}{2}$ is the so-called effective Hubbard parameter (hereinafter U_{eff}) and ρ^{σ} is the on-site *d*- or *f*-orbital occupation matrix with spin-up (σ). The U_{eff} can be determined as the difference of the value of the on-site Coulomb repulsion (U), which is characterized by a spherically averaged energy required for adding an extra *d*- or *f*-electron to a particle, while the *J* parameter represents the screened exchange energy[69].

The additional term in Equation (23) introduces an energy penalty for the delocalized *d*- and *f*-electrons and forces them to localize. Conventional DFT is recovered, if U_{eff} = 0.0eV $(E_{\mathrm{DFT+U}} = E_{\mathrm{DFT}})$. As DFT+U is a semi empirical approach, the appropriate value of U_{eff} depends on the implementations. It can be derived from theoretical calculations based on LSDA (local spin density approximation, which is the extension of LDA with spin description)[3], but its calibration is usually based on the comparison of the calculated and the measured electronic density of states (eDOS). The band gap (the energy difference between the lowest unoccupied and the highest occupied eDOS) serves as a basis of the testing as it can clearly be determined from calculations and experiments, respectively[3,64].

The described DFT+U method has successfully been demonstrated on challenging bulk systems like iron and uranium oxides[64,70–72]. Hence, it allowed the extension of its application: since then several studies have been performed on iron complexes formed at different edge surface sites of nontronite (the Fe-rich end member of clay minerals)[27,35]. These calculations often based only on the energy comparison of the different structures, from which the energetically favored surface complex can be determined, but it is insufficient to quantify the contribution of the different complexes at different environmental conditions (e.g. variant pH).

3.3. EXAFS and XANES calculations

Only a few studies have applied atomistic simulations for the interpretation of XAS data of cations in aqueous solutions and of species adsorbed on clay mineral surfaces[28,73], the approach is very promising. The theoretical description of the XAS spectra significantly progressed in the last decades allowing to perform structural refinement of the sorption complexes based on quantum mechanical calculations, which serve as accurate input models for the XAS calculations[28,73,74].

The most widely applied EXAFS codes (e.g. FEFF) nowadays relies on the self-consistent real space multiple-scattering (RSMS) method. The computation of RSMS is based on cluster calculations of real space Green's function approach. It is a quasiparticle theory that replaces the independent but interacting electron system with non-interacting quasiparticles.

Whereas the modelling of the EXAFS spectra has nearly become a routine, the theoretical simulation of XANES spectra for complex systems is still rare due to the complexity and challenges in their theoretical prediction. Although, XANES spectra can be calculated using RSMS, the approach is insensitive to multi-atom correlation functions (i.e. RSMS cannot properly describe the backscattering of the outgoing photoelectron near the absorption edge energy into all directions) leading to false spectra[3]. Therefore, *ab initio* calculations of the electronic structure were applied to overcome the limitations of the simplified models of many-body effects as it is implemented in the density functional theory – local spin-density approximation (DFT-LSDA) method[75]. Recent advances of the computational algorithms of DFT-LSDA made it possible to obtain several accurate XANES spectra thus allowing the calculation based on MD trajectories[75].

The structural and thermal disorder can be considered in "direct" or "indirect" ways:

- In the direct case, the XAS calculations are based on the MD trajectory of a modelled structure. Several (or all) "snapshots" from the trajectory are considered and XAS spectra are computed based on the obtained atomic coordinates. The result is the average of the calculated XAS spectra.
- In the indirect case, a single structure is taken and the XAS spectrum is calculated by applying the Debye-Waller term.

The advantage of the latter approach is that one atomic configuration is enough for the calculations making the investigation faster. However, Debye-Waller term has only very little effect in XANES region and it gives only a general broadening to the EXAFS spectrum avoiding element specific deviations. Furthermore, the Debye-Waller factor is a semi-empirical parameter. Thus it has to be calibrated by a measured sample.

The calculated EXAFS and XANES spectra were used as a basis in the interpretation of the experimental data. Comparing the modeled spectra one-by-one to the experimental results would provide only qualitative analysis. It has been demonstrated that the quantitative description of metal-uptake by clay minerals can be achieved by the linear combination fit of the calculated spectra to the experimental one based on Equation (24)[3,28].

$$Q = \left\| \sum_i (a_i^2 f_i) - f^{\exp} \right\|^2 \qquad (24)$$

where f_i are the calculated and $f^{\exp}$ is the experimental XAS spectra (in case of EXAFS $f = \chi(k)$, while $f = \mu(E)$ for XANES), a_i^2 are the fitting parameters (contribution of the different structures). A fit is generally accepted when the features in the XAS spectra match and the Q (indicates the fitting quality) shows a global minimum for the given a_i^2 parameters.

4. Outline of the thesis

This PhD thesis is organized into a series of individual chapters. Chapter 1 introduces the general topic covered by the thesis. Chapters 2-7 present the results of the PhD work, which are published, accepted or will be submitted in international peer reviewed journals. Chapter 8 provides a summary and an outlook of the PhD work. The contributions of the individual co-authors to the articles submitted in co-authorship will be specified below.

CHAPTER 1:
Introduction
Kéri, A.

This chapter defines the objectives and basic research questions to be addressed by this thesis. An overview about the applied experimental techniques and modelling approaches are provided as well as an outline of the analytical techniques.

CHAPTER 2:
Experimental study:
Combined X-ray microanalytical study of the Nd uptake capability of argillaceous rocks
Kéri, A.; Osán, J.; Fábián, M.; Dähn, R.; Török, S.

In this chapter, studies about the physico-chemical properties describing the retention capability of the possible host rock formation for the Hungarian high-level radioactive waste repository (Boda Claystone Formation) were performed. The examinations were focused on the Nd^{3+} ion uptake capability of the micrometer size mineral phases occurring in the argillaceous Boda Claystone. Microscopic X-ray fluorescence (micro-XRF) combined with scanning electron microscopy energy dispersive X-ray analysis (SEM/EDX) was performed on thin sections of the rock samples subjected to sorption experiment. Multivariate methods (factor analysis, positive matrix factorization, non-hierarchical cluster analysis) were applied on the elemental maps to infer the mineral phases with the highest Nd^{3+} uptake capability. The results were verified by microscopic X-ray diffraction (micro-XRD) measurements.
The chapter results from a collaboration between Laboratory for Waste Management, Paul Scherrer Institute (PSI LES) and Environmental Physics Department, Hungarian Academy of Sciences Centre for Energy Research (MTA EK). The first author prepared and interleaved all the micro-XRF and SEM/EDX elemental maps, while J. Osán carried out the sample preparation and the micro-XRF and SEM/EDX measurements. A. Kéri applied the multivariate analysis on the combined data sets. A. Kéri wrote the main part of a first version of the manuscript, only paragraphs in the article about measurement techniques and results of the micro-XRD were written by M. Fábián. R. Dähn (supervisor) and Sz. Török provided logistical and advisory scientific help as well as they assisted with the preparation of the final manuscript.

CHAPTER 3:

Theoretical study: Combined XAFS spectroscopy and *ab initio* study on the characterization of iron incorporation by montmorillonite

Kéri, A.; Dähn, R.; Krack, M.; Churakov, S. V.

This chapter is devoted to specify the preferred oxidation state and occupational site of structurally incorporated iron in bulk montmorillonite. Molecular dynamics (MD) calculations based on density functional theory (DFT+U) were applied on four different atomic model. The trajectories obtained from *ab initio* MD calculations served as a basis for the Fe K-edge extended X-ray absorption fine structure (EXAFS) and X-ray absorption near edge structure (XANES) calculations. The calculated EXAFS and XANES spectra were compared to measurement results to interpret the oxidation state and occupational site of structurally incorporated iron in bulk montmorillonite.

The first author performed all the *ab initio,* EXAFS and XANES calculations. A. Kéri also compared the calculated and the measurement results. The second author carried out all the experiments, while the third and the fourth authors helped in the setup of the *ab initio* simulations. A. Kéri wrote the main part of a first version of the manuscript, only paragraph in the article about measurements was written by R. Dähn. The second, third and fourth authors (supervisors) provided advisory scientific help and they assisted with the preparation of the final manuscript.

CHAPTER 4:

Theoretical study: Characterization of structural iron in smectites — an *ab initio* based XAS study

Kéri, A.; Dähn, R.; Krack, M.; Churakov, S. V.

This chapter comprises the distribution of iron in different types of bulk montmorillonites. The incidence of tetrahedral iron as well as Fe–Fe and Mg–Fe clustering in the octahedral sheet was studied by comparing *ab initio* based EXAFS and XANES spectra with measurement results.

The first author prepared all the atomistic model structures and she performed all the *ab initio,* EXAFS and XANES calculations. The second author carried out all the EXAFS and XANES experiments, while A. Kéri compared the calculated and the measurement results. A. Kéri wrote the main part of the manuscript, only paragraph in the article about measurements was written by R. Dähn. The second, third and fourth authors (supervisors) provided advisory scientific help and they assisted with the preparation of the final manuscript.

CHAPTER 5:

Theoretical study:

Iron adsorption on clays inferred from atomistic simulations and XAS spectroscopy

Kéri, A.; Dähn, R.; Marques Fernandes, M.; Krack, M.; Scheinost, A.; Churakov, S. V.

This chapter is about iron adsorption on montmorillonite. The study was performed using *ab initio* calculations and X-ray absorption spectroscopy (XAS). 56 different atomistic models were prepared representing structural and surface sorbed ferrous and ferric iron in clay minerals. Their relaxed structures and relative energies were calculated to determine the energetically preferred position of the two ions and to verify oxidative surface complexation. Theoretical extended X-ray absorption fine structure (EXAFS) and X-ray absorption near edge structure (XANES) spectra were calculated based on molecular dynamics (MD) studies on strong- and weak-site complexation models. The obtained XAS spectra were compared to experimental XAS data of montmorillonite with different iron loadings to investigate the effect of the concentration of dissolved ferrous iron in the electrolyte.

The first author prepared all the atomistic model structures and she performed all the *ab initio* structure relaxations and MD as well as the EXAFS and XANES calculations. The third author performed all the sorption measurements and she obtained the EXAFS and XANES spectra at ESRF (Grenoble, France) together with A. Scheinost, while A. Kéri performed the comparison of the calculated and the experimental spectra. A. Kéri wrote the main part of the manuscript, only the paragraph in the article about measurements was written by M. Marques Fernandes. R. Dähn (supervisor), M. Krack (supervisor), S. V. Churakov (supervisor) provided advisory scientific help and they assisted with the preparation of the final manuscript.

CHAPTER 6:

Theoretical study:

First-principles study of uranyl adsorption on montmorillonite edge surfaces

Kéri, A.; Dähn, R.; Krack, M.; Churakov, S. V.

This chapter is a first-principle study about the uptake mechanism of uranyl ion at montmorillonite edge surfaces. The energy comparison of the relaxed structures of various (12) bidentate uranyl surface complexes was performed to determine the most stable structures. In addition, ferric iron $\left(Fe^{3+}\right)$ was incorporated into the octahedral sheet at the edge surface of the clay layer to study the effect of structural Fe^{3+} on the bidentate uranium species. The structural parameters (interatomic distances and coordination numbers) of the relaxed structures were compared with experimental results obtained from the conventional fit of extended X-ray absorption fine structure (EXAFS) measurements.

The first author obtained the relaxed structures of the different uranyl complexation models (with and without structural Fe^{3+}) and she calculated the structural parameters. The second author performed all the sorption measurements, he obtained the EXAFS spectra and he performed the conventional EXAFS fit on them. The third author helped in the setup of the *ab initio* parameters. A. Kéri wrote the main part of the manuscript, only paragraph in the article about measurements was written by R. Dähn. R. Dähn, M. Krack, and S. V. Churakov (supervisors) provided advisory scientific help and they assisted with the preparation of the final manuscript.

CHAPTER 7:
Conclusions and Outlook

Kéri, A.

This chapter is a summary of the combined results of the thesis and outlines future research perspectives.

5. References

(1) *Technical Report 02-05: Project Opalinus Clay Safety Report: Demonstration of Disposal Feasibility for Spent Fuel, Vitrified High-Level Waste and Long-Lived Intermediate-Level Waste (Entsorgungsnachweis)*. Wettingen, Switzerland, **2002**.

(2) *IAEA Safety Standards for Protecting People and the Environment (SSR-5). Disposal of Radioactive Waste.* Vienna, Austria, **2011**.

(3) Kéri, A.; Dähn, R.; Krack, M.; Churakov, S. V. Combined XAFS Spectroscopy and *Ab Initio* Study on the Characterization of Iron Incorporation by Montmorillonite. *Environ. Sci. Technol.* **2017**, *51(18)*, 10585–10594.

(4) Lázár, K.; Máthé, Z. Claystone as a Potential Host Rock for Nuclear Waste Storage. In *Clay Minerals in Nature – Their Characterization, Modification and Application*. (Eds.: Valaskova, M., Martynková, G. S.) Budapest, Hungary, **2012**.

(5) Leupin, O. X.; Birgersson, M.; Karnland, O.; Korkeakoski, P.; Sellin, P.; Mader, U.; Wersin, P. *Technical Report 14-12: Montmorillonite Stability under near-Field Conditions*. Wettingen, Switzerland, **2014**.

(6) Bradbury, M. H.; Berner, U.; Curti, E.; Hummel, W.; Kosakowski, G.; Thoenen, T. *Technical Report 12-01: The Long Term Geochemical Evolution of the Nearfield of the HLW Repository*. Wettingen, Switzerland, **2014**.

(7) Soltermann, D.; Marques Fernandes, M.; Baeyens, B.; Miehé-Brendlé, J.; Dähn, R. Competitive Fe(II)–Zn(II) Uptake on a Synthetic Montmorillonite. *Environ. Sci. Technol.* **2013**, *48(1)*, 190–198.

(8) McEwen, T. Site Selection and Characterisation. In *Deep Geological Waste Disposal*, (Eds.: Alexander, W. R., McKinley, L. E.) Melton Mowbray, UK, **2007**; vol. 9, pp. 77–111.

(9) Albert, W.; Deplazes, G.; Gautschi, A.; Gribi, P.; Hertrich, M.; Madritsch, H.; Müller, H.; Ruff, M.; Schneider, J.; Schnellmann, M.; et al. *Technical Report 14-01: Sicherheitstechnischer Bericht Zu SGT Etappe 2*. Wettingen, Switzerland, **2014**.

(10) Németh, T.; Máthé, Z.; Pekker, P.; Dódony, I.; Kovács-Kis, V.; Sipos, P.; Cora, I.; Kovács, I. Clay Mineralogy of the Boda Claystone Formation (Mecsek Mts., SW Hungary). *Open Geosci.* **2016**, *8(1)*, 259–274.

(11) Mazurek, M.; Gautschi, A.; Marschall, P.; Vigneron, G.; Lebon, P.; Delay, J. Transferability of Geoscientific Information from Various Sources (Study Sites, Underground Rock Laboratories, Natural Analogues) to Support Safety Cases for Radioactive Waste Repositories in Argillaceous Formations. *Phys. Chem. Earth* **2008**, *33*, S95–S105.

(12) Nationale Genossenschaft für die Lagerung radioaktiver Abfälle (NAGRA) http://www.nagra.ch/.

(13) Nussbaum, C.; Bossart, P.; Amann, F.; Aubourg, C. Analysis of Tectonic Structures and Excavation Induced Fractures in the Opalinus Clay, Mont Terri Underground Rock Laboratory (Switzerland). *Swiss J. Geosci.* **2011**, *104(2)*, 187–210.

(14) Country Nuclear Power Profile (CNPP) of International Atomic Energy Agency (IAEA) cnpp.iaea.org.

(15) Konrád, G.; Sebe, K.; Halász, A.; Babinszki, E. Sedimentology of a Permian Playa Lake: The Boda Claystone Formation, Hungary. *Geologos* **2010**, *16(1)*, 27–41.

(16) Varga, A. R.; Szakmány, G.; Raucsik, B.; Máthe, Z. Chemical Composition, Provenance and Early Diagenetic Processes of Playa Lake Deposits from the Boda Siltstone Formation (Upper Permian), SW Hungary. *Acta Geol. Hungarica* **2005**, *48(1)*, 49–68.

(17) West, M.; Ellis, A. T.; Potts, P. J.; Streli, C.; Vanhoof, C.; Wegrzynek, D.; Wobrauschek, P. Atomic Spectrometry Update-X-Ray Fluorescence Spectrometry. *J. Anal. At. Spectrom.* **2011**, *26(10)*, 1919–1963.

(18) Breitner, D.; Osán, J.; Fábián, M.; Zagyvai, P.; Szabó, C.; Dähn, R.; Marques Fernandes, M.; Sajó, I. E.; Máthé, Z.; Török, S. Characteristics of Uranium Uptake of Boda Claystone Formation as the Candidate Host Rock of High Level Radioactive Waste Repository in Hungary. *Environ. Earth Sci.* **2014**, *73(1)*, 209–219.

(19) Kübler, B. Evaluation Quantitative Du Metamorphisme Par La Cristallinite de l'illite. *Clay Miner.* **1968**, *2(2)*, 385–397.

(20) Árkai, P.; Balogh, K.; Máthé, Z.; Demény, A.; Fórizs, I.; Nagy, G. Composistion, Diagenatic and Post-Diagenetic Alterations of a Possible Radioactive Waste Repository Site: The Boda Albitic Claystone Formaton, Southern Hungary. *Acta Geol. Hungaria* **2000**, *43(4)*, 351–378.

(21) Baeyens, B.; Thoenen, T.; Bradbury, M. H.; Marques Fernandes, M. *Technical Report 12-04: Sorption Data Bases for Argillaceous Rocks and Bentonite for the Provisional Safety Analyses for SGT-E2*. Villigen PSI, Switzerland, **2014**.

(22) Bradbury, M. H.; Baeyens, B. *Technical Report 01-08: Porewater Chemistry in Compacted Re-Saturated MX-80 Bentonite: Physico-Chemical Characterisation and Geochemical Modelling.* Wettingen, Switzerland, **2002**.

(23) Stucki, J. W. Properties and Behaviour of Iron in Clay Minerals. In *Handbook of Clay Science*; **2006**; vol. 1, pp. 423–475.

(24) Soltermann, D.; Marques Fernandes, M.; Baeyens, B.; Dähn, R.; Joshi, P. A.; Scheinost, A. C.; Gorski, C. A. Fe(II) Uptake on Natural Montmorillonites. I. Macroscopic and Spectroscopic Characterization. *Environ. Sci. Technol.* **2014**, *48(15)*, 8688–8697.

(25) Soltermann, D.; Marques Fernandes, M.; Baeyens, B.; Dähn, R.; Miehé-Brendlé, J.; Wehrli, B.; Bradbury, M. H. Fe(II) Sorption on a Synthetic Montmorillonite. A Combined Macroscopic and Spectroscopic Study. *Environ. Sci. Technol.* **2013**, *47(13)*, 6978–6986.

(26) Kerisit, S.; Rosso, K. M. Computer Simulation of Electron Transfer at Hematite Surfaces. *Geochim. Cosmochim. Acta* **2006**, *70(8)*, 1888–1903.

(27) Alexandrov, V.; Neumann, A.; Scherer, M. M.; Rosso, K. M. Electron Exchange and Conduction in Nontronite from First-Principles. *J. Phys. Chem. C* **2013**, *117(5)*, 2032–2040.

(28) Churakov, S. V.; Daehn, R. Zinc Adsorption on Clays Inferred from Atomistic Simulations and EXAFS Spectroscopy. *Environ. Sci. Technol.* **2012**, *46(11)*, 5713–5719.

(29) Guggenheim, S.; Adams, J. M.; Bain, D. C.; Bergaya, F.; Brigatti, M. F.; Drits, V. A.; Formosso, M. L. L.; Galan, E.; Kogure, T.; Stanjek, H. Summary of Recommendations of Nomenclature Committees Relevant to Clay Mineralogy: Report of the Association Internationale Pour l'Etude Des Argiles (AIPEA) Nomenclature Committee for 2006. *Clays Clay Miner.* **2006**, *54(6)*, 761–772.

(30) Vantelon, D.; Montarges-Pelletier, E.; Michot, L. J.; Pelletier, M.; Thomas, F.; Briois, V. Iron Distribution in the Octahedral Sheet of Dioctahedral Smectites. An Fe K-Edge X-Ray Absorption Spectroscopy Study. *Phys. Chem. Miner.* **2003**, *30(1)*, 44–53.

(31) Tsipursky, S. I.; Drits, V. A. The Distribution of Octahedral Cations in the 2:1 Layers of Dioctahedral Smectites Studied by Oblique-Texture Electron Diffraction. *Clay Miner.* **1984**, *19(2)*, 177–193.

(32) Kaufhold, S.; Kremleva, A.; Krüger, S.; Rösch, N.; Emmerich, K.; Dohrmann, R. Crystal-Chemical Composition of Dicoctahedral Smectites: An Energy-Based Assessment of Empirical Relations. *ACS Earth Sp. Chem.* **2017**, *1(10)*, 629–636.

(33) Kaufhold, S.; Stucki, J. W.; Finck, N.; Steininger, R.; Zimina, A.; Dohrmann, R.; Ufer, K.; Pentrák, M.; Pentráková, L. Tetrahedral Charge and Fe Content in Dioctahedral Smectites. *Clay Miner.* **2017**, *52(1)*, 51–65.

(34) Stucki, J. W.; Lee, K.; Zhang, L.; Larson, R. A. Effects of Iron Oxidation State on the Surface and Structural Properties of Smectites. *Pure Appl. Chem.* **2002**, *74(11)*, 2081–2094.

(35) Alexandrov, V.; Rosso, K. M. Insights into the Mechanism of Fe(II) Adsorption and Oxidation at Fe – Clay Mineral Surfaces from First-Principles Calculations. *J. Phys. Chem. C* **2013**, *117(44)*, 22880–22886.

(36) Latta, D. E.; Neumann, A.; Premaratne, W. A. P. J.; Scherer, M. M. Fe(II)–Fe(III) Electron Transfer in a Clay Mineral with Low Fe Content. *ACS Earth Sp. Chem.* **2017**, *1(4)*, 197–208.

(37) Soltermann, D.; Baeyens, B.; Bradbury, M. H.; Marques Fernandes, M. Fe(II) Uptake on Natural Montmorillonites. II. Surface Complexation Modeling. *Environ. Sci. Technol.* **2014**, *48(15)*, 8698–8705.

(38) Schlegel, M. L.; Descostes, M. Uranium Uptake by Hectorite and Montmorillonite: A Solution Chemistry and Polarized EXAFS Study. *Environ. Sci. Technol.* **2009**, *43(22)*, 8593–8598.

(39) Bergaya, F.; Lagaly, G. *Handbook of Clay Science Part B: Techniques and Applications*. Oxford, UK, **2013**.

(40) Iida, A. Synchrotron Radiation X-Ray Fluorescence Spectrometry. In *Encyclopedia of Analytical Chemistry*. (Eds.: Meyers, R. A.) Hoboken, New Jersey, USA, **2013**.

(41) Szalóki, I.; Lewis, D. G.; Bennett, C. A.; Kilic, A. Application of the Fundamental Parameter Method to the in Vivo X-Ray Fluorescence Analysis of Pt. *Phys. Med. Biol.* **1999**, *44(5)*, 1245–1255.

(42) Piorek, S. Alloy Identification and Analysis with a Field-Portable XRF Analyser. In *Portable X-ray fluorescence spectrometry: Capabilities for in situ analysis*, **2008**, pp. 110–114.

(43) Moore, D. M.; Reynolds, R. C. Jr. *X-Ray Diffraction and the Identification and Analysis of Clay Minerals*, New York, USA, **1997**.

(44) Denecke, M. A.; Somogyi, A.; Janssens, K.; Simon, R.; Dardenne, K.; Noseck, U. Microanalysis (Micro-XRF, Micro-XANES, and Micro-XRD) of a Tertiary Sediment Using Microfocused Synchrotron Radiation. *Microsc. Microanal.* **2007**, *13(3)*, 165–172.

(45) De Nolf, W.; Janssens, K. Micro X-Ray Diffraction and Fluorescence Tomography for the Study of Multilayered Automotive Paints. *Surf. Interface Anal.* **2010**, *42(5)*, 411–418.

(46) Goldstein, J. I.; Newbury, D. E.; Michael, J. R.; Ritchie, N. W. M.; Scott, J. H. J.; Joy, D. C. *Scanning Electron Microscopy and X-Ray Microanalysis*, New York, New York State, USA, **2018**.

(47) Osán, J.; Kéri, A.; Breitner, D.; Fábián, M.; Dähn, R.; Simon, R.; Török, S. Microscale Analysis of Metal Uptake by Argillaceous Rocks Using Positive Matrix Factorization of Microscopic X-Ray Fluorescence Elemental Maps. *Spectrochim. Acta Part B At. Spectrosc.* **2014**, *91*, 12–23.

(48) Kéri, A.; Osán, J.; Fábián, M.; Dähn, R.; Török, S. Combined X-Ray Microanalytical Study of the Nd Uptake Capability of Argillaceous Rocks. *X-Ray Spectrom.* **2016**, *45(1)*, 54–62.

(49) Vlaic, G.; Olivi, L. EXAFS Spectroscopy : A Brief Introduction. *Croat. Chem. Acta* **2004**, *77(3)*, 427–433.

(50) Denecke, M. A. Actinide Speciation Using X-Ray Absorption Fine Structure Spectroscopy. *Coord. Chem. Rev.* **2006**, *250(7–8)*, 730–754.

(51) Teo, B. K. *EXAFS: Basic Principles and Data Analysis*; **1986**.

(52) Chemistry LibreTexts: chem.libretexts.org.

(53) Ravel, B.; Newville, M. ATHENA , ARTEMIS , HEPHAESTUS : Data Analysis for X-Ray Absorption Spectroscopy Using IFEFFIT. *J. Synchrotron Radiat.* **2005**, *12(4)*, 537–541.

(54) Koningsberger, D. C.; Prins, R. Relationships between Smectite Redox and Structural Properties. In *Redox properties of structural Fe in clay minerals*; **1988,** pp. 211–253.

(55) Manceau, A. Distribution of Cations among the Octahedra of Phyllosilicates: Insight from EXAFS. *Can. Mineral.* **1990**, *28*, 321–328.

(56) Wilks, D. S. Empirical Distributions and Exploratory Data Analysis. In *Statistical Methods in the Atmospheric Sciences*. (Eds.: Dmowska, R., Hartmann, D., Rossby, T. H.) Oxford, UK, **2011**; vol. 100, pp. 23–70.

(57) Rodgers, J. L.; Nicewander, W. A. Thirteen Ways to Look at the Correlation Coefficient. *Am. Stat.* **1988**, *42(1)*, 59–66.

(58) Eriksson, L.; Johansson, E.; Kettaneh-Wold, N.; Wold, S. *Multi- and Megavariate Data Analysis*; Umea, Sweden, **2001**.

(59) Paatero, P.; Tapper, U. Positive Matrix Factorization: A Non-Negative Factor Model with Optimal Utilization of Error Estimates of Data Values. *Environmetrics* **1994**, *5(2)*, 111–126.

(60) Wilks, D. S. Cluster Analysis. In *Statistical Methods in the Atmospheric Sciences*; (Eds.: Dmowska, R., Hartmann, D., Rossby, T. H.) Oxford, UK, **2011**, vol. 100, pp. 603–616.

(61) Ohno, K.; Esfarjani, K.; Kawazoe, Y. *Computational Materials Science - From Ab Initio to Monte Carlo Methods*. Berlin, Germany, **2018**.

(62) Liu, X.; Lu, X.; Wang, R.; Zhou, H. Effects of Layer-Charge Distribution on the Thermodynamic and Microscopic Properties of Cs-Smectite. *Geochim. Cosmochim. Acta* **2008**, *72(7)*, 1837–1847.

(63) Liu, X.; Lu, X.; Wang, R.; Zhou, H.; Xu, S. Surface Complexes of Acetate on Edge Surfaces of 2:1 Type Phyllosilicate: Insights from Density Functional Theory Calculation. *Geochim. Cosmochim. Acta* **2008**, *72(24)*, 5896–5907.

(64) Krack, M. On the Ground State Electronic Structure of Uranium Dioxide. *Phys. Scr.* **2015**, *90(9)*, 094014.

(65) Verlet, L. Computer "Experiments" on Classical Fluids. I. Thermodynamical Properties of Lennard-Jones Molecules. *Phys. Rev.* **1967**, *159*, 98–103.

(66) Hohenberg, P.; Kohn, W. Inhomogeneous Electron Gas. *Phys. Rev. B* **1964**, *136(3B)*, 864–871.

(67) Kohn, W.; Sham, L. J. Self-Consistent Equations Including Exchange and Correlation Effects. *Phys. Rev.* **1965**, *140(4A)*, A1133–A1138.

(68) Tran, F.; Blaha, P.; Schwarz, K.; Novák, P. Hybrid Exchange-Correlation Energy Functionals for Strongly Correlated Electrons: Applications to Transition-Metal Monoxides. *Phys. Rev. B* **2006**, *74(15)*, 155108.

(69) Anisimov, V. I.; Zaanen, J.; Andersen, O. K. Band Theory and Mott Insulators: Hubbard *U* Instead of Stoner *I*. *Phys. Rev. B* **1991**, *44(3)*, 943–954.

(70) Dorado, B.; Amadon, B.; Freyss, M.; Bertolus, M. DFT+U Calculations of the Ground State and Metastable States of Uranium Dioxide. *Phys. Rev. B - Condens. Matter Mater. Phys.* **2009**, *79*, 235125.

(71) Rabone, J.; Krack, M. A Procedure for Bypassing Metastable States in Local Basis Set DFT+U Calculations and Its Application to Uranium Dioxide Surfaces. *Comput. Mater. Sci.* **2013**, *71*, 157–164.

(72) Alexandrov, V.; Rosso, K. M. Electron Transport in Pure and Substituted Iron Oxyhydroxides by Small-Polaron Migration. *J. Chem. Phys.* **2014**, *140(23)*, 234701.

(73) Chillemi, G.; D'Angelo, P.; Pavel, N. V.; Sanna, N.; Barone, V. Development and Validation of an Integrated Computational Approach for the Study of Ionic Species in Solution by Means of Effective Two-Body Potentials. The Case of Zn^{2+}, Ni^{2+}, and Co^{2+} in Aqueous Solutions. *J. Am. Chem. Soc.* **2002**, *124(9)*, 1968–1976.

(74) Aimoz, L.; Taviot-Guého, C.; Churakov, S. V.; Chukalina, M.; Dähn, R.; Curti, E.; Bordet, P.; Vespa, M. Anion and Cation Order in Iodide-Bearing Mg/Zn–Al Layered Double Hydroxides. *J. Phys. Chem. C* **2012**, *116(9)*, 5460–5475.

(75) Bunau, O.; Joly, Y. Self-Consistent Aspects of X-Ray Absorption Calculations. *J. Phys. Condens. Matter* **2009**, *21(34)*, 345501.

CHAPTER 2:
Experimental study:
Combined X-ray microanalytical study of the Nd uptake capability of argillaceous rocks

This chapter has been published as "Kéri, A.; Osán, J.; Fábián, M.; Dähn, R.; Török, S. Combined X-ray microanalytical study of the Nd uptake capability of argillaceous rocks. *X-Ray Spectrometry*, **2016**, *45*, 54-62."

The article in the format of the journal can be downloaded from DOI:10.1002/xrs.2656

Abstract

Argillaceous rocks are considered as suitable host rock formation to isolate the high-level radioactive waste from the biosphere for thousands of years. Boda Claystone Formation, the possible host rock formation for the Hungarian high-level radioactive waste repository, has geologically and mineralogically been studied in detail, but its physico-chemical parameters describing the retention capability of the rock needed further examinations. Studies were performed on thin sections subjected to 72h sorption experiments using inactive Nd(III). Nd(III) has been used as a chemical analogue for transuranium elements of the radioactive waste to examine the ion uptake capability of the micrometre size mineral phases occurring in the rock. The elemental mapping of synchrotron radiation-based microscopic X-ray fluorescence (micro-XRF) combined with scanning electron microscopy energy dispersive X-ray analysis (SEM/EDX) has sufficient sensitivity to study the uptake capability of the different mineral phases on the microscale without the necessity of applying radioactive substances. Elemental maps were recorded on several thousand pixels using micrometre magnitude spatial resolution. By interleaving micro-XRF and SEM/EDX data sets from the same sample area and applying multivariate methods, calcite and clay minerals could be identified as the main mineral phases responsible for Nd(III) uptake without using additional microscopic X-ray diffraction mapping. It should be highlighted that the ion uptake capability of dolomite containing calcium and magnesium could be distinguished from the characteristics of calcite only by the interleaving of micro-XRF and SEM/EDX data sets. The presence of minerals was verified by applying microscopic X-ray diffraction point measurements.

1. Introduction

In Hungary, deep geological disposal was found to be the most suitable placement for high-level radioactive waste that is consistent with the international recommendations[1]. The storage site can be placed into several different formations of mineralogical origin (crystalline, clay and salt rock)[2]. In most of the radioactive waste management research programmes, clay formations were found to be suitable for high-level radioactive waste storage[3–5]. It is known that argillaceous rocks have several suitable properties of which the most advantageous are the homogeneity, the chemical buffering capacity, the low groundwater flow, the self-healing capability by crack swelling and the radionuclide retardation related to sorption[3,4]. The main goal of these experiments is to determine the partition coefficient (R_d) between the mobile phase (dissolved in water) and the sedentary (solid) phase[4,6–8]. These bulk experiments are necessary but inadequate to describe the sorption process in detail; thus, sorption experiments involving thin sections and microscopic studies are needed.

In microscopic studies, the samples are treated with different solutions containing key radionuclides in order to study the sorption capability of the different mineral phases present in the rock. The key radionuclides, represent transuranium elements, fission and corrosion

products, are not present in the rock. They can be substituted with their inactive or natural analogues without requiring high-activity radioisotopes. The chemical conditions present at the depth of the planned repository as the concentrations of the elements of interest in the solutions involved should be sufficiently low in order to avoid precipitation. Therefore, the element of interest will be present in minor or trace concentration level heterogeneously distributed in the sample after the sorption experiment[9,10]. Nd(III) was used as a chemical analogue for trivalent transuranium elements of the radioactive waste to examine the ion uptake capability of the micrometre size mineral phases occurring in the rock. Petrographic thin sections are prepared from the geological samples. After treatment, these highly heterogeneous samples are most often studied with microscopy techniques[11]. Microscopic X-ray fluorescence (micro-XRF) spectroscopy is a suitable tool to detect simultaneously the distribution of the sorbed elements and the main elements corresponding to the rock-forming minerals[12]. Although, it has several advantageous properties, micro-XRF performed in air is not capable to detect major light elements (e.g. Na and Mg); therefore, it is inadequate to ascertain the mineral phases containing elements only with low atomic number (e.g. dolomite and albite)[9,12]. The missing additional information can be obtained with the elemental mapping of the same sample area using micro-XRF in vacuum mode or with a helium flush around the sample to avoid its damage. However, in order to excite the major light elements effectively, a modified setup employing lower excitation energy is necessary. Another measurement technique that can be applied is scanning electron microscopy energy dispersive X-ray analysis (SEM/EDX) employing a laboratory-size equipment. SEM/EDX is a well-suited measurement technique for detecting the major elements of mineral phases, but it is inappropriate to detect the elements representing key radionuclides because of their usually high atomic numbers and low concentrations.

Although the differently measured data sets can be treated individually; more accurate information can be obtained if the data sets of different measurements are combined[13,14]. The interleaving of existing data sets of light element concentrations determined from SEM/EDX measurements as well as minor and trace element concentrations obtained from micro-XRF can be applied for this purpose.

Multivariate methods such as factor analysis (FA) and positive matrix factorization (PMF) are used to handle large data matrices. Although, the result of FA is explicit, the expression of factors in the original variables (factor loadings) can contain negative values expressing anticorrelation with original variables (concentrations of chemical elements)[15]. This problem can be overcome by application of PMF, commonly used in air pollution studies, where the factors should contain only non-negative values[16,17]. PMF was successfully applied to process three-dimensional data sets answering questions related to other topics[9,18]. However, no applications of PMF on combined micro-XRF and SEM/EDX data sets have been reported to date. Segmentation of the data set can be performed using cluster analysis based on the similarity (distance) of the pixels in the abstract space defined by elemental concentrations. The most commonly used method is the non-hierarchical K-means clustering algorithm[19–21].

The aim of the present study was to obtain quantitative information on the sorption capacity of the mineral phases responsible for the uptake of Nd(III). Because of the heterogeneity of the rock, microscopic studies (micro-XRF and SEM/EDX measurements) were necessary on the representative geological samples. Multivariate methods were applied on the interleaved data set to handle the large data matrix. Micro-XRF spectroscopy combined with microscopic X-ray diffraction (micro-XRD)[12,22] was applied at selected representative positions to verify the results.

2. Materials and methods

2.1. Samples

The petrographic thin sections were prepared from geochemically characterized cores from drillings of Boda Claystone Formation (BCF). The Upper Permian sedimentary sequence of the BCF, which is the possible formation for high-level radioactive waste repository in Hungary, is located in Western Mecsek Mountains, SW Hungary. The sediments of the BCF are dominantly red and reddish brown in color reflecting the oxidizing nature of the depositional and early diagenetic environments. BCF was deposited in a shallow water salt lake environment surrounded by dry to saline mudflat, under semi-arid to arid climatic conditions[1,23,24]. Two distribution areas of BCF are known in West Mecsek Mountains: the perianticlinal structure of the West Mecsek Anticline (WMA) Block and the Gorica Block (GB)[25].

The rocks are highly heterogeneous on the microscale; two major regions can be distinguished, the clayey matrix and the fracture infillings. The clayey matrix is formed by high amount of clay minerals (around 50m/m% illite, chlorite, kaolinite and mixed structure clay minerals) as well as albite cement (and analcime cement for G Block)[23–25]. The most important clay mineral is illite containing potassium and iron. Nanometre size hematite crystals are wedged between the illite plates[26]. The fracture infillings consist of mostly authigenic albite (or analcime for G Block), carbonate minerals (calcite and dolomite) and authigenic potassium feldspar. The absolute dominant rock type of the formation is albitic claystone in the WMA Block and albite-bearing and analcime bearing claystone in the GB[25]. In previous studies, the differences in the ion uptake of G Block and WMA Block have been examined[24–26]. The results pointed out that only in WMA Block, a new mineral phase was formed with high ion binding capability for the case of uranium and neodymium treated samples[9]. Therefore, hereinafter, only samples from WMA Block will be discussed[9]. Small pieces of the selected core samples were ground and mounted onto 350μm-thick high purity silicon wafers and polished by 0.25μm diamond paste. The samples were reacted for 72h with Nd(III) in porewater and a 0.1M NaCl solution as background electrolyte. The ionic strength of this latter solution was similar to the porewater, while the pH was set to 7.0 to avoid precipitation of Nd phases. Hereinafter, only samples treated with NaCl solution will be discussed, because this electrolyte ensured a sufficient loading of the element of interest to

match the sensitivity of micro-XRF while avoiding precipitation in the solution itself[9]. The concentrations of the key element to be applied for the sorption experiments based on the sorption isotherms were measured and modelled for Eu(III) on illite, taking into account the clay content of the BCF samples (around 40%) as well as the solid-to-liquid ratio[7]. The applied Nd(III) initial concentrations were $3.6 \cdot 10^{-6}$–$3.6 \cdot 10^{-5}$M, resulting in equilibrium concentrations of 10^{-6}—10^{-5}M.[7]

2.2. SEM/EDX and micro-XRF measurements

A JEOL JSM-5600LV scanning electron microscope equipped with an Oxford Si(Li) energy dispersive detector with atmospheric thin window was employed for the SEM/EDX measurements. The system allowed the detection of light elements down to carbon. A 25kV accelerating voltage and a 1nA beam current were used for the measurements. Although, the scanning electron microscope was operated in high-vacuum mode, no conductive coating was necessary for the examinations. Elemental maps of 128×95 pixels were collected with a resolution of $4.5 \times 4.8 \mu m^2$. In order to decrease sample damage due to the electron beam, the area was scanned ten times with a 150ms dwell time at each position.

Because all major elements except hydrogen could be detected using the SEM/EDX method, the concentrations of major elements were determined for each pixel of the elemental maps using a standardless iterative method based on Monte Carlo simulations for electrons[27].

The micro-XRF experiments were performed at the FLUO beamline of ANKA. The white beam of a bending magnet was monochromatized by a W/Si multilayer double monochromator (energy resolution $\Delta E/E = 10^{-2}$). Because of the high iron content of the rock sections, micro-XRF elemental mapping was performed at an energy of 7.1keV below the Fe Kα-absorption edge. A Fresnel zone plate was used as focusing element, providing a $3 \times 8 \mu m^2$ spot size. A silicon-drift detector was applied to collect fluorescence spectra. Characteristic X-ray intensity maps were recorded for the adsorbed element (Nd-Lα) as well as for the major and minor elements of the rock (e.g. K-Kα, Ca-Kα and Mn-Kα) using a 5μm step size and 4–10s counting time per pixel[9]. The net characteristic X-ray intensities were determined by processing the full X-ray spectra collected at each pixel using AXIL software[28].

2.3. Interleaving of micro-XRF and SEM/EDX data sets

First, the interleaving of micro-XRF and SEM/EDX data sets was prepared for further evaluation. Potassium and calcium micro-XRF as well as SEM/EDX elemental maps had sufficiently good statistics for the basis of the interleaving. The micro-XRF and SEM/EDX measurements were not carried out at the same time; therefore, small deviation could be seen on the elemental maps representing the distribution of the same element. The obvious differences were corrected, comparing the potassium and calcium elemental maps measured by micro-XRF and SEM/EDX, respectively. The relatively rotated and/or slipped maps were combined, taking into account only the overlapping area after the rotation and shift. The two measurement methods had different lateral distribution; therefore, the better one was resized with interpolation. This resulted that the corresponding pixels on the elemental maps indicated the same area on the sample (Figure 1).

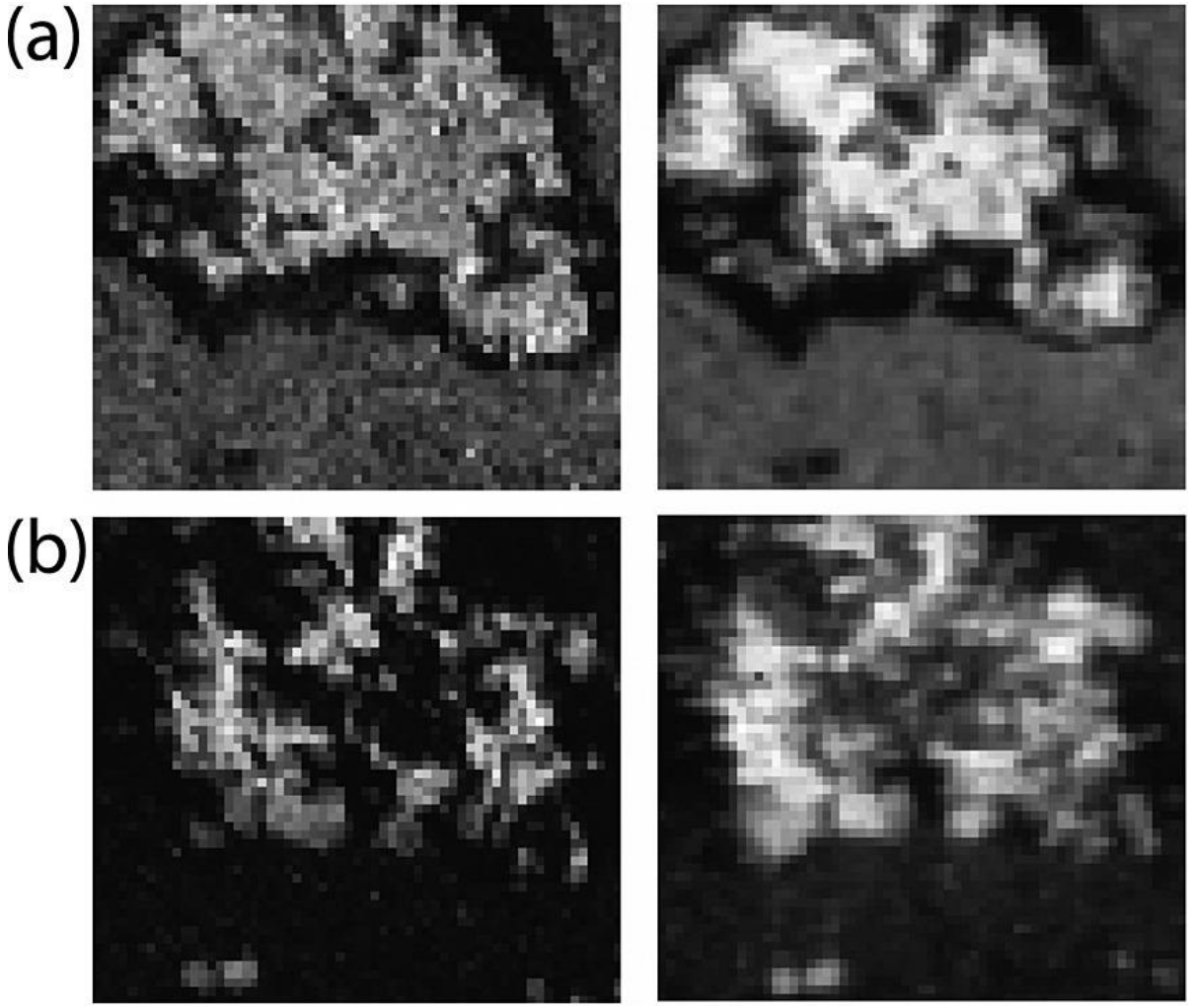

Figure 1. Potassium (a and b) and calcium (c and d) elemental concentration maps from an area of $0.3 \times 0.27 mm^2$ on a thin section measured by scanning electron microscopy energy dispersive X-ray analysis (a and c) and microscopic X-ray fluorescence (b and d). The elemental maps are presented as max–min normalized, where black representing the minimum and white the maximum intensity.

Afterwards, the minor and trace elemental concentrations were calculated for each pixel in the interleaved data set based on the micro-XRF net characteristic X-ray intensities. Standardless fundamental parameter method[29] was used for the calculations, which takes into account the absorption of the exciting X-ray beam, the production of fluorescence in the sample and the absorption of the outgoing fluorescence X-rays as they propagate towards the detector. This mathematical method requires an accurate energy spectrum of the exciting radiation and geometric factors in order to reach reliable quantification. Because monochromatic excitation was applied, the geometric factors, the XRF production cross sections and the detector efficiency could be cancelled out through the measurement of a standard reference material (NIST SRM613)[30,31]. The method also requires a relevant estimation of the composition of elements without a detectable characteristic X-ray line in the measured spectra (the so-called dark matrix). The X-ray spectra Micro-XRD measurements recorded in air and 7.1keV excitation energy do not contain information about elements with lower atomic number than that of silicon. Therefore, the composition of the dark matrix was obtained from the SEM/EDX measurements. The thickness of the sample was 50μm, and the average density of the rock was 2.7g/cm^3. Higher order interactions were not considered for the calculations.

2.4. Micro-XRD

The micro-XRD experiments were performed at the FLUO beamline of ANKA. At several selected positions of interest, micro-XRD images were collected by a 130mm diameter charged coupled device detector using a modified setup applying a 17.5keV excitation energy. In this case, a compound refractive lens was used as the focusing element, providing a 2×5μm^2 spot size. The calibration for the micro-XRD measurements was performed by measuring of standards (corundum, silicon and $PbCO_3 \cdot Pb(OH)_2$). The beam position on the XRD images was determined using the XRDUA software[32]. The least-distorted circular rings were obtained using the parameters of -5° tilt and 25° rotation. XDB software[33,34], which allows full interpretation of a sample diffractogram and helps generate initial concentrations of identified minerals based on a standardless approach, was applied for the phase identification and quantification. Because of the increased width of reflection lines as a result of the low energy resolution of the multilayer monochromator and the existence of large crystallites compared with that of the beam size, only semi-quantitative information could be obtained on the mineral phases. XDB software helped refine the final phase composition applying the mass balance procedure. After the phase identification, the quantitative phase composition was calculated based on the reference intensity method. The phase proportions were derived from the weight parameters of the profile fit corrected with their respective reference intensity – I/I_c – coefficient. The calculated phase proportions, depended on the particle size of the components and the absolute amounts (phase percentages), are normalized to the sum of the phases, while the reliability of the results greatly depended on the distribution of the intensities to the identified phases.

2.5. Multivariate methods

Multivariate data analyses are usually used in environmental chemistry to handle large-scale data matrices. The aim of their application in this study was to obtain new information from the estimation of the number and composition of factors (latent variables) describing the original data set. For this reason, FA, PMF and cluster analysis (CA) were found to be the most suitable methods. As these mathematical methods can treat only 2D matrices (variables–observations), the 2D elemental maps for each element (variable) were unfolded into 1D vectors. The resulting factor or cluster maps were created after refolding the resulting data into 2D matrices.

Standard FA employing varimax rotation was performed using the IDAS software package[35]. The number of factors present in the data set was determined using the 95% limit of the explained variance. The concentration values were scaled using autoscaling (Equation (1)) in order to take the variables into consideration with similar weights but assigning higher weight to data with smaller statistical error[36].

$$z_{ij} = \frac{x_{ij} - \bar{x}_j}{s_j} \tag{1}$$

where $\bar{x}_j$ is the average of the measurement results connected to the given variable j and s_j is the corresponding standard deviation.

Positive matrix factorization decomposes the data matrix into two non-negative matrices in the following way:

$$e_{ij} = x_{ij} - \sum_{k=1}^{p} g_{ik} f_{kj} \tag{2}$$

where e_{ij} is the element of the residual matrix, x_{ij} is the element of the input data matrix at sampling point i, variables j, g_{ik} and f_{kj} are the elements of the left and right factor matrices and p is the number of factors[37].

The objective function should be minimized based on Equation (3), retaining the elements of the factor matrices positive to obtain the best PMF decomposition.

$$Q = \sum_{i=1}^{m} \sum_{j=1}^{n} \left(\frac{x_{ij} - \sum_{k=1}^{p} g_{ik} f_{kj}}{\sigma_{ij}} \right)^2 \tag{3}$$

where σ_{ij} is the uncertainty of each data point and variable[37].

In the weighting of the data matrix, the uncertainty of the data points is also utilized, allowing the separate treatment of the matrix elements (Equation (3)). As a consequence, values measured under the detection limit can also be taken into the data set, avoiding data loss. In this work, the EPA PMF 3.0 software package was used to perform calculations on the interleaved data set. The PMF problem is solved by using multistage iteration method

starting from pseudorandom initial values. The number of runs and factors had to be given as input parameters, which were assumed from the FA results of the same set of elemental maps. Elements could be categorized into three different groups based on the signal/noise ratio of their concentrations. Elements with high signal-to-noise ratio were categorized as 'strong' including every element that could possibly be a component of the mineral phases occurring in the sample (Na, Mg, Al, Si, K, Ca, Ti, Mn and Fe), as well as the element added in the sorption experiment (Nd). Elements with small intensities and high uncertainties (e.g. Ba) were in the group of 'weak'. Oxygen was also classified to this group not to create a separate factor. The output factor profiles were calculated by the software considering that the average factor contribution is equal to unity. The output factor profiles were normalized to their maximum because in the present case, the factor contribution cannot be higher than at the measured pixel. Non-hierarchic CA is generally applied for data matrices containing numerous measurement points[38]. In this work, the k-means algorithm was used, which classifies every object (measurement point) to a cluster whose centroid is the closest to the given object. CA was performed using the built-in routine of PAST software[39].

3. Results and discussion

3.1. Elemental concentration maps

The elemental concentration maps (Figure 2) themselves already bear information on the distribution of minerals on the microscale, based on the mineral phase composition of the corresponding crushed bulk sample determined by powder XRD[9,26]. The regions, where K and Fe were present together, were considered as clayey matrix. This mineral aggregation contains phyllosilicates (mainly illite with 6% K, 1.5% Fe, 1.9% Mg, 9% Al and 25.3% Si), ilmenite ($FeTiO_3$), nanocrystalline (<200nm) hematite (Fe_2O_3), fine-grained albite ($NaAlSi_3O_8$) and rutile (TiO_2)[23,26]. As it can be seen on the K map (bottom and top-right regions), the clayey matrix contains medium concentration of K (~6wt.%) homogeneously distributed. The correlation between K and Fe was reduced because of the presence of micrometer size (1–10μm^2) hematite grains, which could be separated by SEM/EDX[9,23,26]. The studied scanned area was selected such a way that it contained fracture infilling regions in addition to the clayey matrix regions. Pixels on the elemental maps with high K, Al and Si concentrations could be related to the fracture infilling potassium feldspar ($KAlSi_3O_8$)[9,23,26]. Fracture infilling carbonate may be present as calcite ($CaCO_3$), dolomite ($CaMg(CO_3)_2$) and different phase Mn-carbonate, respectively[9,23,26].

Comparing of the concentration distribution maps of major elements and Nd (Figure 2), a homogeneous distribution of Nd was obtained at the clayey matrix regions, while enhanced Nd concentrations were observed at or around Ca-rich phases. Figure 3 shows that a good correlation $(r = 0.68)$ was observed between K and Nd concentrations when only the clayey matrix region was selected, while the concentrations of the two elements were practically uncorrelated $(r = 0.04)$ when all pixels of the scanned area were considered.

Thus, the role of the clayey matrix in the Nd uptake could be highlighted using elemental concentration maps and interelemental correlations. However, the application of multivariate methods and micro-XRD was necessary in order to obtain quantitative information about the sorption capacity of the clayey matrix and the identification of additional mineral phases responsible for the uptake.

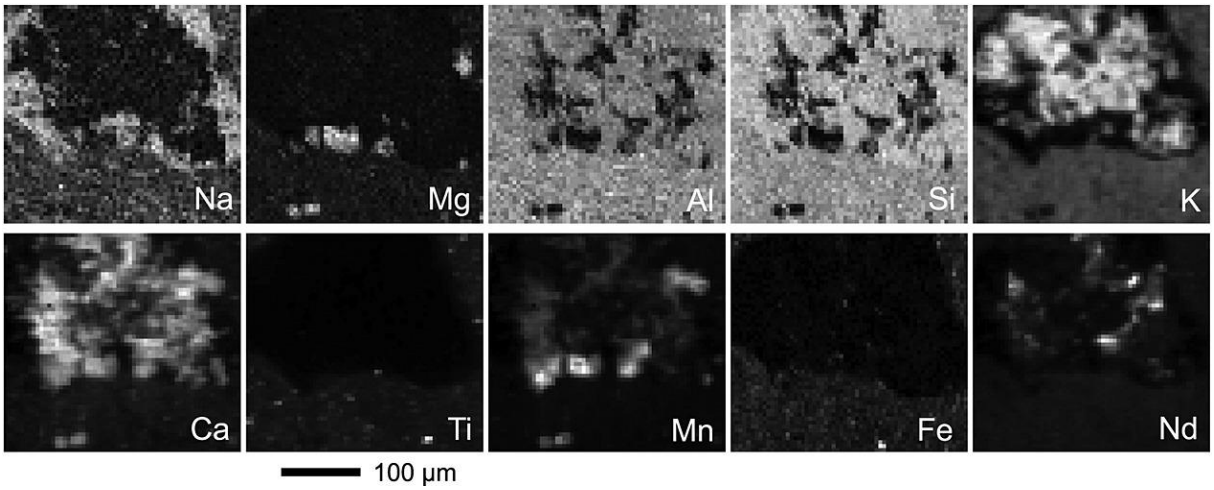

Figure 2. Elemental concentration maps from a $0.3 \times 0.27 mm^2$ scanned area. The elemental maps are presented as max–min normalized, where black representing the minimum and white the maximum concentration. Concentration maps of Na, Mg, Al, Si and Fe were generated from scanning electron microscopy energy dispersive X-ray analysis, while those of K, Ca, Ti, Mn and Nd were based on microscopic X-ray fluorescence data sets.

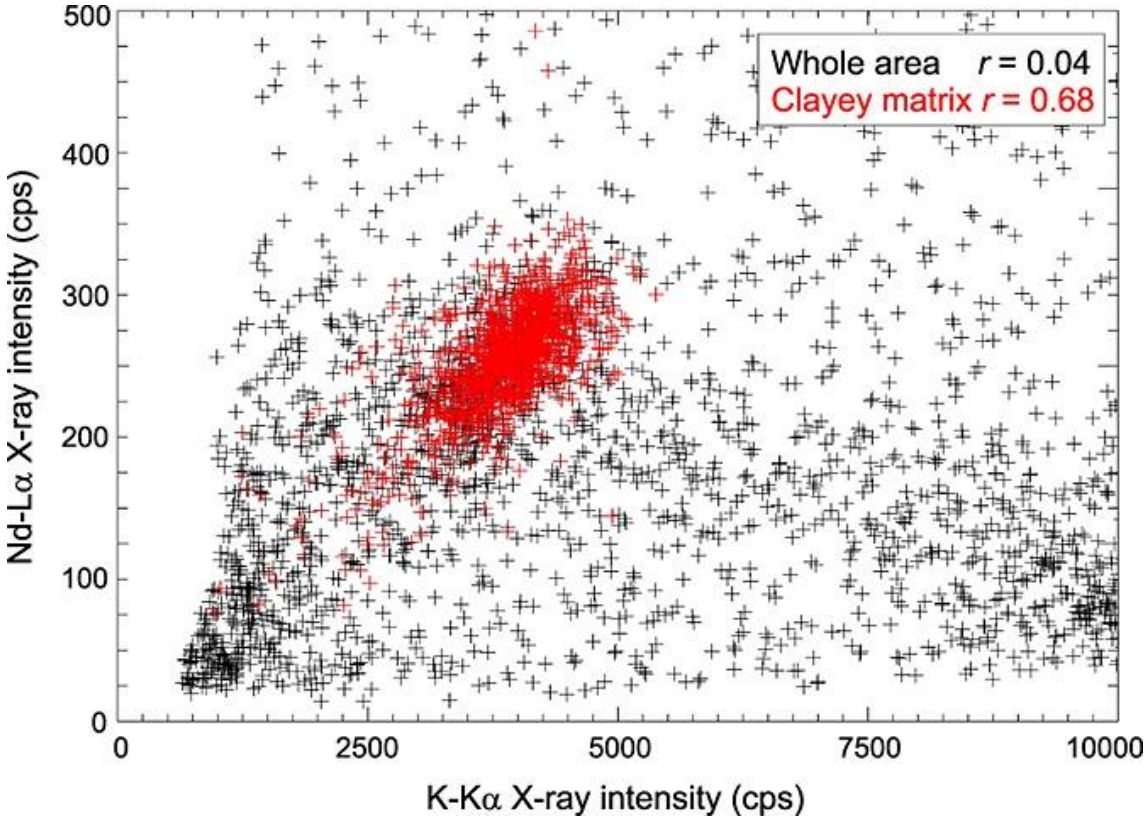

Figure 3. Scatter plot of K and Nd concentrations for all pixels (black) and pixels belonging to the clayey matrix (red).

3.2. Multivariate methods

Based on the 95% limit of the explained variance, six factors (latent variables) were found to describe the interleaved data set of SEM/EDX and micro-XRF concentrations by FA. According to the diagram of factor loadings (correlation of factors with the elemental concentrations; Figure 4), strong correlation was observed between elements present in the same mineral phases, e.g. Ca and Mn (Factor 1) in carbonates, Ti and Fe (Factor 2) mostly in the clayey matrix and Al and Si (Factor 5) as aluminosilicates. A strong anticorrelation was observed between Na and K (Factor 3) as albite and K-feldspar are separated in the fracture infilling regions. A separate factor (Factor 4) was formed for the element of interest Nd with a complete anticorrelation indicating that its distribution was different from that of the main rock-forming minerals. The determination of ion binding capability of the mineral phases would need quantitative information about the elements present together with Nd. FA provides negative loading values (Figure 4); therefore, multivariate methods with non-negativity constraint are needed for quantitativity[40]. However, the application of FA is necessary in order to provide the appropriate number of factors describing the data set.

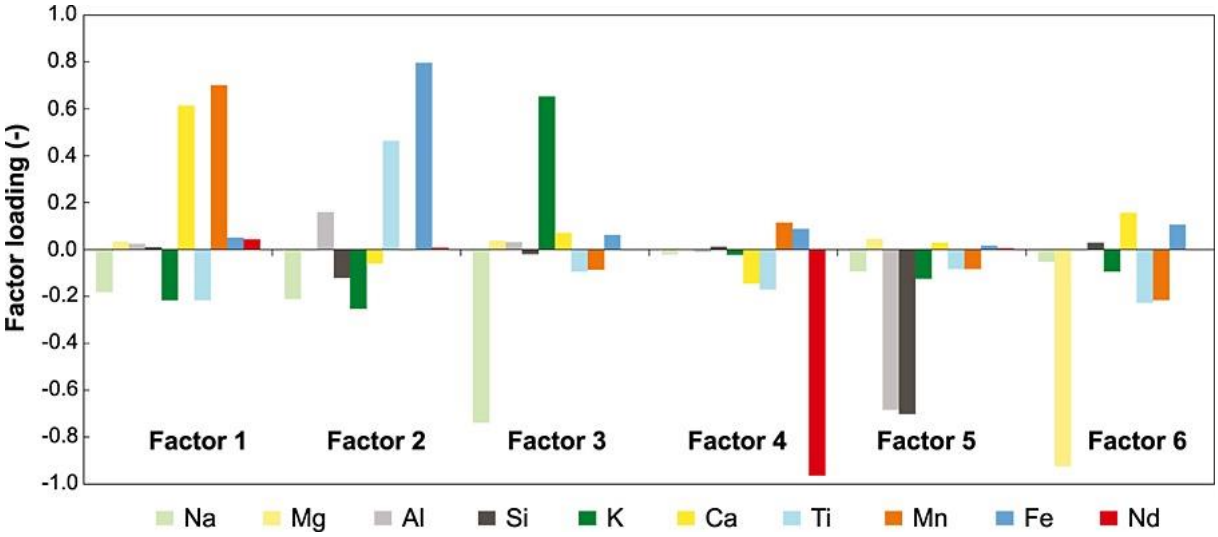

Figure 4. Factor loadings of the interleaved scanning electron microscopy energy dispersive X-ray analysis and microscopic X-ray fluorescence data set representing correlations between the factors and the elemental concentrations. The results were obtained using factor analysis on elementally maximum normalized and autoscaled concentrations.

Positive matrix factorization was performed on the interleaved data set of the maximum normalized elemental concentration measured by SEM/EDX and micro-XRF to identify the mineral phases and to estimate their ion binding capability. From the result of the PMF evaluation (***G*** and ***F*** matrices), the composition of the factors expressed as elemental concentrations (factor profiles) and the values of the factors at each measured pixel (factor contributions) could be created, the latter ones visualized as factor distribution maps (Figure 5a). From the factor profiles expressed in elemental concentrations (Figure 5b) and from the comparison of the factor distribution maps (Figure 5a) with the elemental maps (Figure 2), information on the mineral phases present could be obtained despite the fact that factors could not be identified as single mineral phases.

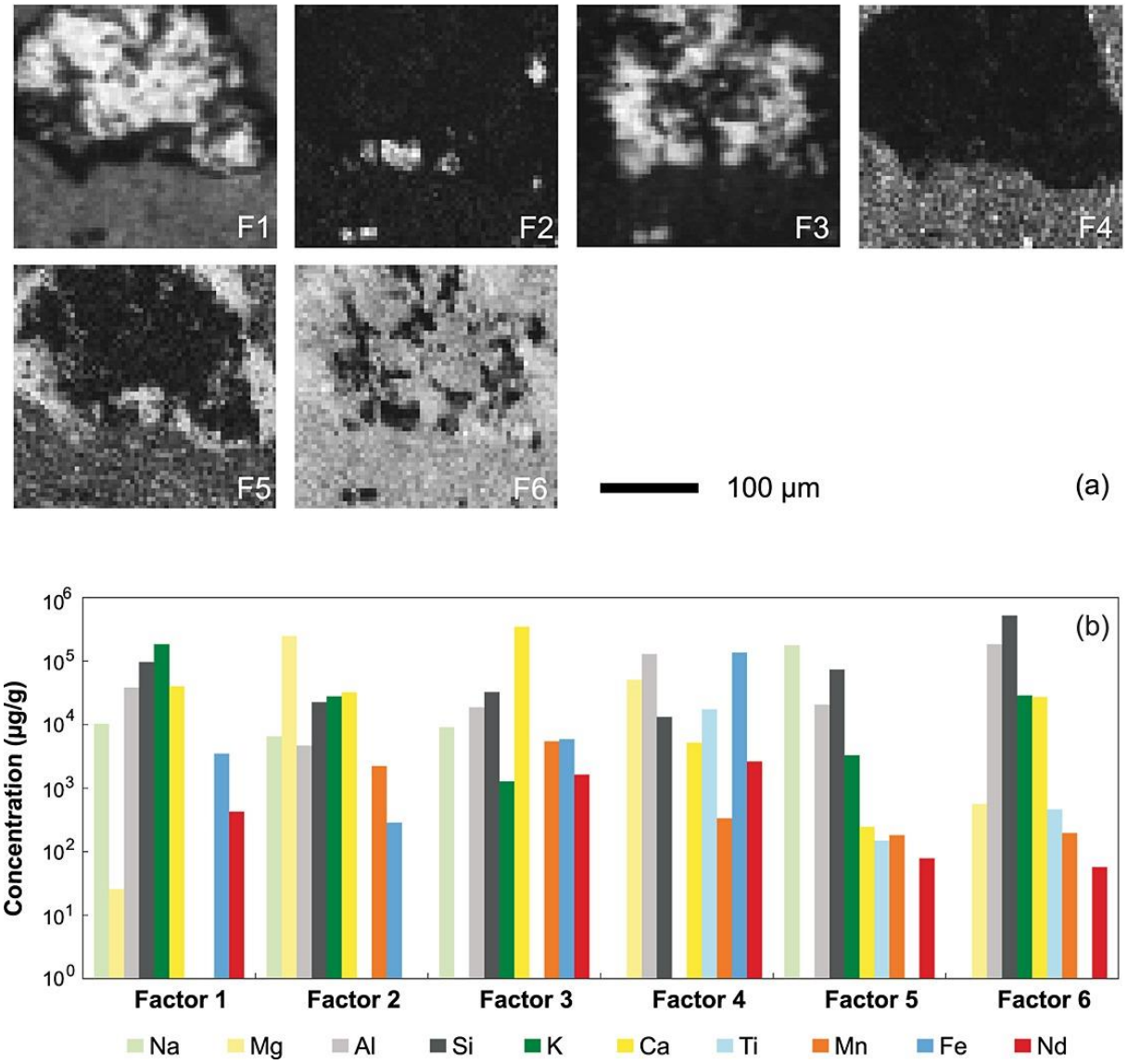

Figure 5. Factor contribution maps (a) and profiles expressed as elemental concentrations (b). The factor contribution maps are presented as max–min normalized, where black representing the minimum and white the maximum contribution. The results were obtained using positive matrix factorization on maximum normalized elemental concentrations from interleaved microscopic X-ray fluorescence and scanning electron microscopy energy dispersive X-ray analysis results taking into account the corresponding standard deviation in each pixel.

The highest Nd uptake capability could be evaluated as 1200µg/g in Factor 4 (Figure 5b) representing the clayey matrix based on its Al, Si and Fe content. Almost the same amount of Nd (1100µg/g) was bound to a calcium-rich mineral phase representing calcite (Factor 3), while the ion uptake capability of dolomite (Factor 2) was orders of magnitude lower. It should be highlighted that the ion uptake capability of dolomite, containing calcium and magnesium, could be distinguished from the very diverse characteristics of calcite only by the interleaving of micro-XRF and SEM/EDX data sets. For both mineral phases, non-negligible but different amount of manganese was bound, corresponding to the two-phase manganese-carbonate.

As multiple mineral phases or chemical elements can be present together, several factors can contribute to the composition at the same pixel. It was a reason applying PMF for relation of abstract factors to mineral phases. CA is a different approach, where one pixel can only belong to one cluster based on the main mineral phase present in the given pixel. It means that CA is capable to provide information on ion uptake capacities of different main mineral phases.

Cluster analysis was carried out on the interleaved micro-XRF and SEM/EDX data set, taking into account only those elements that were dominant in the factors obtained as the result of PMF. The number of clusters was chosen as the number of factors, because the number of separable mineral phases and mineral aggregations (clayey matrix) is the same for both cases as the same data set was studied. Before carrying out CA, every variable was normalized to its maximum to contribute with the same weight defined by the concentration of the chemical elements in the calculation of the distance between the objects. As a result, the assignment of pixels to each of the six clusters is presented as cluster maps (Figure 6). The representative average composition of each cluster could be determined from the average of the elemental concentration of the pixels classified to it. The average Nd and Ca concentrations of the clusters are tabulated into Table 1.

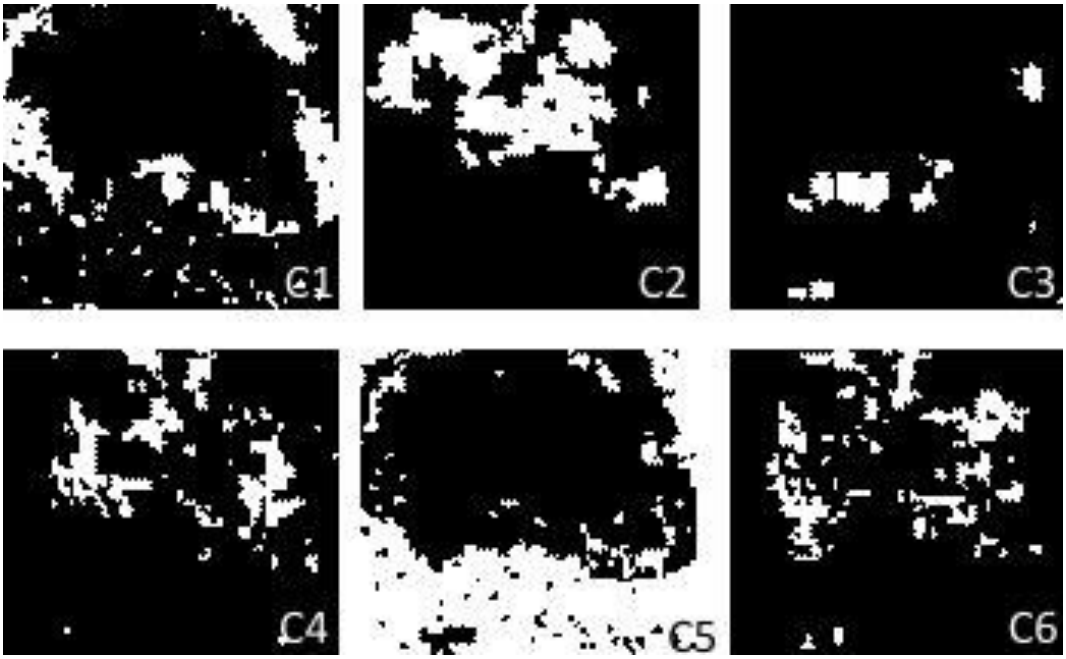

Figure 6. Cluster maps based on the result of interleaved, maximum normalized scanning electron microscopy energy dispersive X-ray analysis and microscopic X-ray fluorescence concentrations; white pixels are assigned to the given cluster.

Table 1. Neodymium concentrations related to the clusters.

Cluster number	**Number of pixels**	**Ca concentration** [wt.%]	**Nd concentration** [μg/g]
1	542	3.96	399
2	671	7.92	681
3	144	13.71	683
4	377	13.15	1140
5	1288	3.41	704
6	394	17.91	1457
Total/Average	3416	7.56	785

The main mineral phases and mineral aggregation could be identified, and their ion binding capability could be estimated as the result of CA (Figure 6, Table 1). There were two separable clusters that appeared on the edge of the calcites and/or aluminosilicates that had the highest neodymium binding capability with an average Nd content of 1460μg/g and 1140μg/g for Cluster 6 and Cluster 4, respectively (Table 1, Figure 6). The cluster related to the clayey matrix (Cluster 5) had the second highest neodymium binding capability with lower concentration value than that predicted by PMF. The results obtained by the two methods are in accordance with each other, because CA results reflect the average, while PMF results reflect the maximum uptake capacity of the clayey matrix.

For this sample, the Nd(III) equilibrium concentration was 10^{-5}M in the solution after the uptake experiment, and a total Nd load of 780μg/g was measured in the solid phase with that CA has good correlation.

3.3. Micro-XRD results

In order to verify the results obtained for the mineral phases responsible for the Nd uptake by applying multivariate methods on interleaved micro-XRF and SEM/EDX elemental maps, micro-XRD patterns were collected from several selected positions on the same sample area. When only positions representative for the clayey matrix were selected, Nd content was in good correlation with the clay mineral (illite and montmorillonite) content (Figure 7), indicating the importance of these minerals in the Nd uptake of the rock. The azimuthally integrated diffraction patterns corresponding to positions of low and high Nd content in the clayey matrix can be seen in Figure 8.

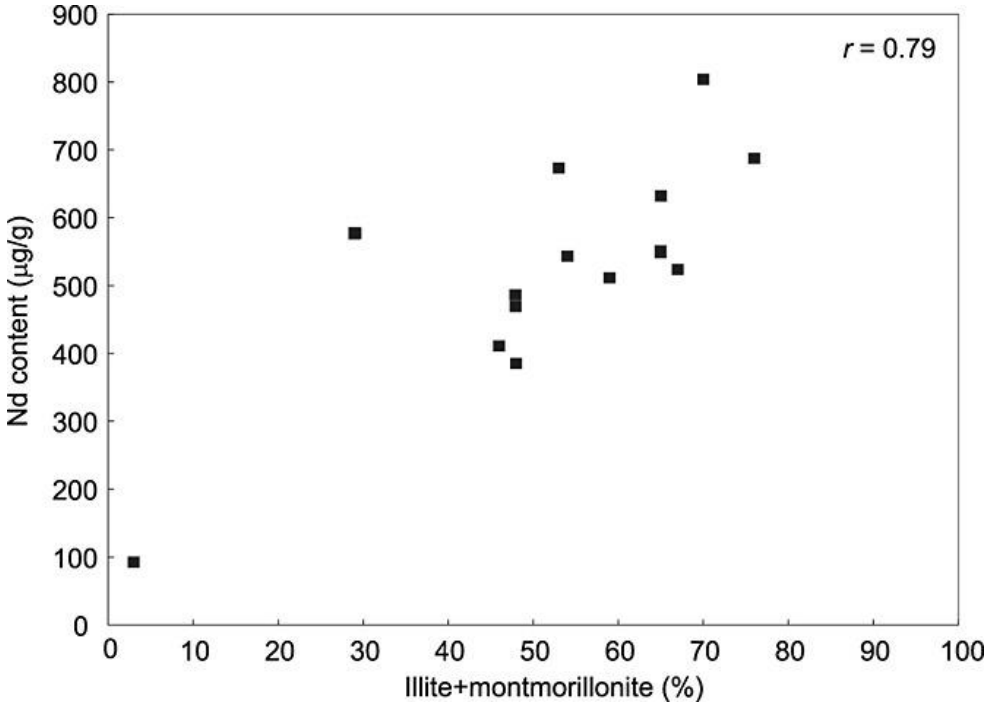

Figure 7. Results of combined microscopic X-ray fluorescence and microscopic X-ray diffraction for positions selected from the clayey matrix.

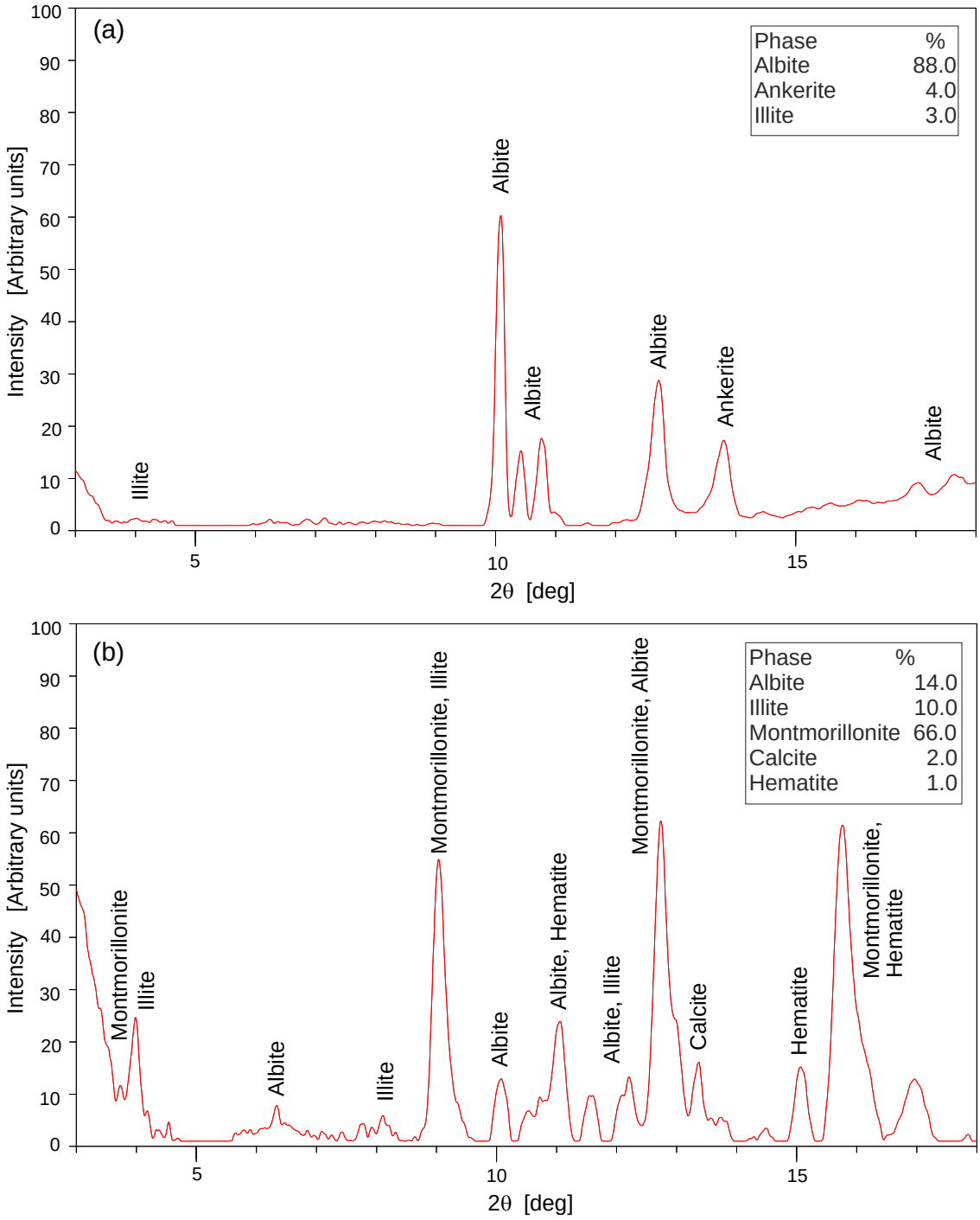

Figure 8. One-dimensional microscopic X-ray diffraction patterns for positions of (a) low and (b) high Nd content in the clayey matrix.

Table 2 contains detailed results of the semi-quantitative mineral phase composition of 13 selected positions (pixels) of the scanned area. For comparison with data obtained using micro-XRF and SEM/EDX combined with multivariate methods, the corresponding Nd concentrations, as well as CA cluster assignments and contributions to two main PMF factors, are also tabulated. Positions with calcite and albite as main mineral phases were assigned well to the corresponding clusters. Micro-XRD images could not be evaluated for pixels representative for dolomite and K-feldspar because of the presence of large single crystals.

The crystalline phase composition obtained for positions selected in the clayey matrix reflects the average composition of mineral aggregation. A strong correlation ($r = 0.91$) was observed between the contribution of PMF Factor 5 and the clay mineral content (sum of illite and montmorillonite) and all selected pixels rich in clay minerals were assigned by CA to Cluster 4.

Table 2. Results of microscopic X-ray diffraction measurements at selected positions compared with those of cluster analysis assignments (number of the clusters that the given pixel was assigned to) and positive matrix factorization factor contributions (maximum normalized for each factor) and the corresponding Nd concentrations.

Position/ pixel	Mineral phase composition [wt.%]							Nd [wt.%]	Cluster number	Factor contribution	
	Albite	Illite	Mont-morillonite	Calcite	Hematite	Jacobsite	Other			Factor 3	Factor 4
1	95						5	501	1	0.39	0.04
2	80						20	308	1	0.21	0.10
3								434	2	0.11	0.00
4								232	3	0.71	0.00
5				60	10		30	7830	4	0.54	0.04
6	40	17	34		5		4	872	5	0.06	0.38
7	23	29	25		5		18	797	5	0.07	0.48
8	42	10	33		5	5	5	723	5	0.01	0.36
9	25	11	30		5	5	24	608	5	0.01	0.32
10	48	25	17		5		5	702	5	0.01	0.32
11	23	36	20	5	5	5	6	901	5	0.09	0.39
12	41	27	15		5		12	806	5	0.08	0.37
13	15			58			27	2480	6	0.80	0.00

Micro-XRD images could not be evaluated for positions 3 and 4 because of the presence of large single crystals.

4. Conclusion

The interleaved micro-XRF and SEM/EDX elemental mapping had sufficient information to entirely identify the main mineral phases responsible for the uptake of Nd(III) ion. The presence of minerals was verified by applying micro-XRD. With the application of multivariate methods on the interleaved data set, the ion binding capability of the mineral phases could be quantified. As a result of the evaluation by PMF, Nd was found to mostly be bound to calcite and clayey matrix. With the application of CA, basically, the same results were obtained, while the differences could entirely be explained by the different mathematical approach of PMF and CA, respectively.

5. References

(1) Lázár, K.; Máthé, Z. Claystone as a Potential Host Rock For Nuclear Waste Storage In: Clay Minerals in Nature – Their Characterization Modification and Application (Eds: Valaskova, M.; Martynkova, G. S.) Budapest, Hungary, **2012**, pp. 55–80.

(2) Joint Convention on the Safety of Spent Fuel Management and on The Safety of Radioactive Waste Management, IAEA, **1997**.

(3) NEA Sorption Project Phase II: Interpretation and Prediction of Radionuclide Sorption onto Substrates Relevant for Radioactive Waste Disposal Using Thermodynamic Sorption Models, NEA, Paris, France, **2005**.

(4) Progress Report of Laboratory for Waste Management, Paul Scherrer Institute, Villigen PSI, Switzerland, **2013**.

(5) W. Miller, R. Alexander, N. Chapman, I. McKinley, J. Smellie, Natural Analogue Studies in the Geological Disposal of Radioactive Wastes, Amsterdam, Netherlands, **1994**.

(6) Mell, P.;Megyeri, J.; Riess, L.; Máthé, Z.; Csicsak, J.; Lázár, K.. Sorption of Co, Cs, Sr, and I onto Argillaceous Rock as Studied by Radiotracers. *J. Radioanal. Nucl. Ch.* **2006**, *268*, 405–410.

(7) Marques Fernandes, M.; Vér, N.; Baeyens, B. Predicting the Uptake of Cs, Ni, Co, Eu, Th and U on Argillaceous Rocks Using Sorption Models for Illite, *Appl. Geochem.* **2015**, *59*, 189-199

(8) Bradbury, M. H.; Baeyens, B. Predictive Sorption Modeling of Ni(II), Co(II), Eu(III), Th(IV) and U(VI) on MX-80 Bentonite and Opalinus Clay: A "Bottom-Up" Approach. *Appl. Clay Sci.* **2011**, *52*, 27–33.

(9) Osán, J.; Kéri, A.; Breitner, D.; Fábián, M.; Dähn, R.; Simon, R.; Török, S. Microscale Analysis of Metal Uptake by Argillaceous Rocks Using Positive Matrix Factorization of Microscopic X-Ray Fluorescence Elemental Maps. *Spectrochim. Acta B* **2014**, *91*, 12–23.

(10) Breitner, D.; Osán, J.; Fábián, M.; Zagyvai, P.; Szabó, C.; Dähn, R.; Marques Fernandes, M.; Sajó, I. E.; Máthé, Z.; Török, S. Characteristics of Uranium uptake of Boda Claystone Formation as the Candidate Host Rock of High Level Radioactive Waste Repository in Hungary. *Environ. Earth Sci.* **2015**, *73*, 209–219.

(11) Walther, C.; Denecke, M. A. Actinide Colloids and Particles of Environmental Concern. *Chem. Rev.* **2013**, *113*, 995–1015.

(12) Denecke, M. A.; Somogyi, A.; Janssens, K.; Simon, R.; Dardenne, K.; Noseck, U. Microanalysis (micro-XRF, micro-XANES and micro-XRD) of a Tertiary Sediment Using Microfocused Synchrotron Radiation. *Microsc. Microanal.* **2007**, *13*, 165–172.

(13) Kotula, P. G.; Keenan, M. R.; Michael, J. R. Automated Analysis of SEM X-ray Spectral Images: A Powerful New Microanalysis Tool. *Microsc. Microanal*. **2003**, *9*, 1–17.

(14) Isaure, M. P.; Fayard, B.; Sarret, G.; Pairis, G.; Bourguignon, S. J. Localization and Chemical Forms of Cadmium in Plant Samples by Combining Analytical Electron Microscopy and X-ray Spectromicroscopy. *Spectrochim. Acta B* **2006**, *61*, 1242–1252.

(15) Wold, S. Principal Component Analysis. *Chemometr. Intell. Lab.* **1987**, *2*, 37–52.

(16) Leea, E.; Chana, C. K.; Paatero, P. Application of Positive Matrix Factorization in Source Apportionment of Particulate Pollutants in Hong Kong. *Atmos. Environ.* **1999**, *33(19)*, 3201–3212.

(17) Tecer, L. H.; Tuncel, G.; Karaca, F.; Alagha, O.; Süren, P.; Zararsiz, A.; Kirmaz, R. Metallic Composition and Source Apportionment of Fine And Coarse Particles Using Positive Matrix Factorization in The Southern Black Sea Atmosphere. *Atmos. Res.* **2012**, *118*, 153–169.

(18) Vajna, B.; Patyi, G.; Nagy, Z.; Bódis, A.; Farkas, A.; Marosi, G. Comparison of Chemometric Methods in The Analysis of Pharmaceuticals with Hyperspectral Raman Imaging. *J. Raman Spectrosc.* **2011**, *42*, 1977–1986.

(19) Vekemans, B.; Janssens, K.; Vincze, L.; Aerts, A.; Adams, F.; Hertogen, J. Automated Segmentation of μ-XRF Image Sets. *X-Ray Spectrom.* **1997**, *26*, 333–346.

(20) Vekemans, B.; Vincze, L.; Brenker, F. E.; Adams, F. Processing of Three Dimensional Microscopic X-ray Fluorescence Data. *J. Anal. Atom. Spectrom.* **2004**, *19*, 1302–1308.

(21) Lerotic, M.; Jacobsen, C.; Schaefer, T.; Vogt, S. Cluster Analysis of Soft X-ray Spectromicroscopy Data. *Ultramicroscopy* **2004**, *100*, 35–57.

(22) Singer, D. M.; Zachara, J. M. Jr.; Brown, E. B. Uranium Speciation as a Function of Depth in Contaminated Hanford Sediments – A micro-XRF, micro-XRD and Micro- and Bulk-XAFS study. *Environ. Sci. Technol.* **2009**, *43(3)*, 630–636.

(23) Árkai, P.; Balogh, K.; Demény, A.; Fórizs, I.; Nagy, G.; Máthé, Z. Composition, Diagenetic and Post-Diagenetic Alterations of a Possible Radioactive Waste Repository Site: The Boda Albitic Claystone Formation, Southern Hungary. *Acta Geolog. Hun.* **2000**, *43*, 351–378.

(24) Varga, A.; Szakmány, G.; Raucsik, B.; Máthé, Z. Chemical Composition, Provenance and Early Diagenetic Processes of Playa Lake Deposits from the Boda Siltstone Formation (Upper Permian), SW Hungary. *Acta Geolog. Hun.* **2005**, *48*, 49–68.

(25) Varga, A.; Raucsik, B.; Szakmány, G.; Máthé, Z. Mineralogical, Petrological and Geochemical Characteristics of the Siliciclastic Rock Types of Boda Siltstone Formation. *Bull. Hungarian Geological Soc.* **2006**, *136*, 201–232.

(26) Németh, T.; Máthé, Z.; Pekker, P.; Dódony, I.; Kovács-Kis, V.; Sipos, P. Clay mineralogy of the Boda Claystone Formation (Mecsek Mts., SW Hungary). *Open Geosci.* **2016,** *8(1)*, 259-274.

(27) Ro, C.-U.; Osán, J.; Szalóki, I.; de Hoog, J.; Worobiec, A.; Van Grieken, R. A. Monte Carlo Program for Quantitative Electron-Induced X-ray Analysis of Individual Particles. *Anal. Chem.* **2003**, *75(4)*, 851–859.

(28) Vekemans, B.; Janssens, K.; Vincze, L.; Adams, F.; Van Espen, P. Analysis of X-ray Spectra by Iterative Least Squares (AXIL): New Developments. *X-Ray Spectrom.* **1994**, *23*, 278–285.

(29) Szalóki, I. Some Applications of the Fundamental Parameter Method in Energy-Dispersive X-ray Fluorescence Analysis by Isotope Excitation. *X-Ray Spectrom.* **1991**, *20*, 297–303.

(30) Piorek, S. Alloy Identification and Analysis with a Field-Portable XRF Analyzer. In X-ray Fluorescence Spectrometry: Capabilities for In Situ Analysis (Eds: Potts, P.; West, J.; Portable, M.) Cambridge, UK, **2008**, pp. 98–138.

(31) Schoonjans, T.; Silversmit, G.; Vekemans, B.; Schmitz, S.; Burghammer, M.; Riekel, C.; Brenker, F. E.; Vincze, L. Fundamental Parameter Based Quantification Algorithm for Confocal Nano-X-ray Fluorescence Analysis. *Spectrochim. Acta B* **2012**, *67*, 32–42.

(32) De Nolf, W.; Janssens, K. Micro-X-ray Diffraction and Fluorescence Tomography for the Study of Multilayered Automotive Paints. *Surf. Interface Anal.* **2010**, *42*, 411–418.

(33) Sajó, I. E.; *Powder Diffraction Phase Analytical System*, Budapest, Hungary, **2005**.

(34) Feret, F.; Authier Martin, M.; Sajo, I. Quantitative Phase Analysis of Bidi-Koum Bauxites (Guinea). *Clays Clay Minerals* **1997**, *45*, 418–427.

(35) Bondarenko, I.; Treiger, B.; Van Grieken, R.; Van Espen, P. IDAS: A Windows Based Software Package for Cluster Analysis. *Spectrochim. Acta Part B* **1996**, *51*, 441–456.

(36) Massart, D. L.; Kaufman, L. The Interpretation of Analytical Chemical Data by the Use of Cluster Analysis, Canada, **1983**.

(37) Norris, G.; Vedantham, R. *EPA Positive Matrix Factorization (PMF) 3.0. Fundamentals & Userguide*; U.S. Environmental Protection Agency Office of Research and Development, Washington, USA, **2008**.

(38) Lerotic, M.; Jacobsen, C.; Scheafer, T.; Vogt, S. Cluster Analysis of Soft X-ray Spectromicroscopy Data. *Ultramicroscopy* **2004**, *100*, 35–57.

(39) Hammer, R.; Harper, D. A. T.; Ryan, P. D. PAST: Paleontological Statistics Software Package for Education and Data Analysis. *Palaeontol. Electron.* **2001**, *4(1)*, 1–9.

(40) Alfeld, M.; Wahabzada, M.; Bauckhage, C.; Kersting, K.; Wellenreuther, G.; Falkenberg, G. Non-negative Factor Analysis Supporting the Interpretation of Elemental Distribution Images Acquired by XRF. *J. Phys.: Conf. Ser.* **2014**, *499*, 012013

CHAPTER 3:
Theoretical study:
Combined XAFS spectroscopy and *ab initio* study on the characterization of iron incorporation by montmorillonite

This chapter has been published as "Kéri, A.; Dähn, R.; Krack, M.; Churakov, S. V. Combined XAFS spectroscopy and *ab initio* study on the characterization of iron incorporation by montmorillonite. *Environmental Science and Technology*, **2017**, *51(18)*, 10585-10594."

The article in the format of the journal can be downloaded from DOI:10.1021/acs.est.7b01670 and Supporting Information.

Abstract

Iron occurs in clay minerals in both ferric and ferrous forms. Depending on its oxidation state and the environmental conditions, it can participate in redox reactions and influence the sorption processes at surfaces of clay minerals. Knowing the oxidation state and the preferential structural position of Fe^{2+} and Fe^{3+} is essential for the detailed understanding of the mechanism and kinetics of such processes. In this study, molecular dynamics (MD) calculations based on density functional theory (DFT+U) were applied to simulate the incorporated Fe in bulk montmorillonite and to explain the measured Fe K-edge X-ray absorption fine structure (XAFS) spectra. The analysis of the experimental data and simulation results suggested that iron in montmorillonite is preferentially incorporated as Fe^{3+} into the octahedral layer. The simulations showed that there is no preferential occupation of *cis*- or *trans*-sites by Fe^{2+} and Fe^{3+} in bulk montmorillonite. A very good agreement between the *ab initio* simulated and the measured XAFS spectra demonstrate the robustness of the employed simulation approach.

1. Introduction

Iron is one of the most abundant redox-active element in soils and sediments[1]. Main phases containing ferrous and ferric iron in the subsurface environment are oxides, hydroxides, and clay minerals. Since clay minerals incorporate structural iron in both ferrous $\left(Fe^{2+}\right)$ and ferric $\left(Fe^{3+}\right)$ oxidation states, iron species associated with naturally occurring clay minerals are of a great relevance for biogeochemical redox reaction, geochemical recycling of heavy metals and migration of radionuclides[1–5]. Accordingly, Fe-bearing clay minerals play a role in the main redox controlling phase in geochemical systems. They can concurrently act as electron donor for oxidative sorption of redox sensitive cations, which affect, for example, the net negative charge of the mineral structure, the hydration of smectite surfaces and the cation exchange capacity of the clay mineral[6–8]. Wet chemistry measurements, batch sorption experiments and spectroscopy studies revealed that the adsorption of ferrous iron on clay minerals are strongly depended on the structural iron concentration and its redox state. Structural iron in clay minerals has also an influence on the individual uptake characteristics of ferrous iron and other divalent ions when Fe-bearing clay minerals are present in the system[3,9–11]. The influence of the competitive sorption effects between Fe^{2+} and other relevant transition metals on their uptake characteristics remains an important issue[3].

The structure of Fe-bearing smectites can be described as layers of pseudohexagonally ordered sheets of alumina octahedra sandwiched between two opposing tetrahedral siloxane sheets[12] Fe^{2+} and Fe^{3+} mainly substitutes in the Al octahedral sheet while minor quantities of Fe^{3+} can substitute for Si in the tetrahedral sheet. One third of the octahedral sites are *trans*-symmetric and two-thirds of the octahedral sites are *cis*-symmetric with respect to the orientation of the hydroxyl (OH^{-}) groups[12,13]. Most of the Fe-bearing clay minerals belong to 2:1 type of dioctahedral smectites in which only two thirds of the possible octahedral positions are occupied[12]. Ferric and ferrous iron can occupy both the *cis*- and *trans*-sites.

A discussion about how iron is distributed between the *cis*- and *trans*-octahedral sites in 2:1 dioctahedral smectites has been going on for many years. It has been demonstrated that iron distribution in the octahedral and in the tetrahedral layer strongly depends on the total Fe content[14]. A general conclusion by Stucki[15] based on a variety of spectroscopic and structural measurements including Mössbauer- and infrared spectroscopy[16] is that the *trans*-sites are more vacant with increasing iron-content, and conversely, iron-poor clay minerals exhibit with populated *trans*-sites. The structure of the dioctahedral Fe-rich end-member, nontronite is well-studied and the relative distribution in the octahedral layer of many cations $\left(\text{e.g. } Fe^{3+}, Mg^{2+}\right)$ is quantified[5,17]. It has also been demonstrated that the structurally incorporated iron takes place in the oxidative adsorption of transition metals that can be reversible or irreversible depending on the alterations in the lattice structure of the smectite[8,17]. Much less is known about iron distribution in low (2–3%) Fe-bearing montmorillonites, such as Milos- and Wyoming-montmorillonite. According to Stucki[15] the preferred occupational site should nearly equally be distributed among the *cis*- and *trans*-sites but the quantification is still lacking[18].

The oxidation and the reduction of structural octahedral iron has been shown to be reversible in a wide range of redox conditions. Recent experimental observations demonstrated that the reversible reduction and oxidation of Fe-rich and Fe-poor clays occurs at different redox potentials[19,21]. Whereas nearly 100% oxidation and reduction efficiency is achieved for Fe-poor montmorillonite, a noticeable amount of iron remain redox inactive[19]. Electrochemical and spectroscopic analysis of the reduction and the re-oxidation cycles performed with the different Fe-bearing smectites suggested that irreversible structural changes took place in the clay structure during the first reduction or oxidation cycle[20].

Despite the large body of existing experimental work investigating the redox properties of structurally incorporated iron in clay mineral lattices, the molecular-level description is still lacking because the quantitative characterization of Fe^{2+} and Fe^{3+} in different structural position of the clay minerals remains challenging. The origin of the difficulties is two-fold: (1) X-ray adsorption fine structure (XAFS) and Mössbauer-spectroscopy are the two most widely applied tools for the spectroscopic identification of structural Fe incorporation in clay minerals[3,9,20–22]. The data analysis is often based on reference spectra for Fe^{2+} and Fe^{3+} end-members, which, however, may represent Fe in a mixed structural state. (2) Iron can unequally be distributed between *cis*- and *trans*-octahedral sites, which can barely or not at all be distinguished by these spectroscopic methods[21,22].

Significant advances in the theoretical description of the XAFS spectra made it possible to perform theoretical prediction of extended X-ray absorption fine structure (EXAFS) and X-ray absorption near edge structure (XANES) based on atomistic scale *ab initio* simulations. We have recently demonstrated that the combination of EXAFS spectroscopy and *ab initio* calculations allows a quantitative description of metal-uptake by clay minerals at the atomistic level[23]. A similar approach was applied to investigate speciation of arsenic[24,25] and silver[26] proving the applicability of this method. Studies performed on scandium and on UO_2 confirmed the successful application of the method to systems containing elements with delocalized

f– and *d*–electrons, which are known to be challenging for *ab initio* simulations[27,28]. Whereas the modelling of the EXAFS spectra has nearly become a routine, the theoretical simulation of XANES spectra for complex systems is still rare. Recent advances of the theory and computational algorithms made it possible to obtain accurate XANES spectrum of a given structure on the basis of the exact curve wave theory[29].

In this study, we demonstrate that it is possible to obtain a consistent quantitative interpretation of the measured EXAFS and XANES spectra using linear combination fit of spectra obtained from atomistic simulations. To this end, we obtained a set of *ab initio* molecular dynamic trajectories of Fe-bearing montmorillonite with different structural location of ferrous and ferric iron. We further performed a sensitivity analysis of the theoretical model parameters for the XAFS spectra simulations to evaluate the effects of the changing in the structural environment and the Fe oxidation state on the spectra. Comparing the modelling results and the experimental observations, we gained insights into the structural environment of iron. To the best of our knowledge, this is the first complete theoretical evaluation of Fe K-edge XAFS modelling performed on a Fe-bearing clay mineral system.

2. Materials and methods

2.1. Modeling setup

In our study, we considered idealized defect free tetrahedra-octahedra-tetrahedra (TOT) frames of a 2:1 dioctahedral clay with the general formula of $4\times[Al_8Si_{16}O_{40}(OH)_8]$. It is often used as the simplest structural prototype for dioctahedral clays. The simulations were performed on a single clay particle without water in the interlayer. The dimensions of the orthorhombic supercell were (18.2×20.8×15.0Å). Similar to the previous work[23,30] the cell parameter in the "*c*" direction was fixed at 15Å to minimize the interaction between the periodic images[31,32]. The incorporation of ferrous and ferric iron in the structure was considered as an exchange with the alumina in *cis*- and *trans*-octahedral position (Figure 1), respectively[33].

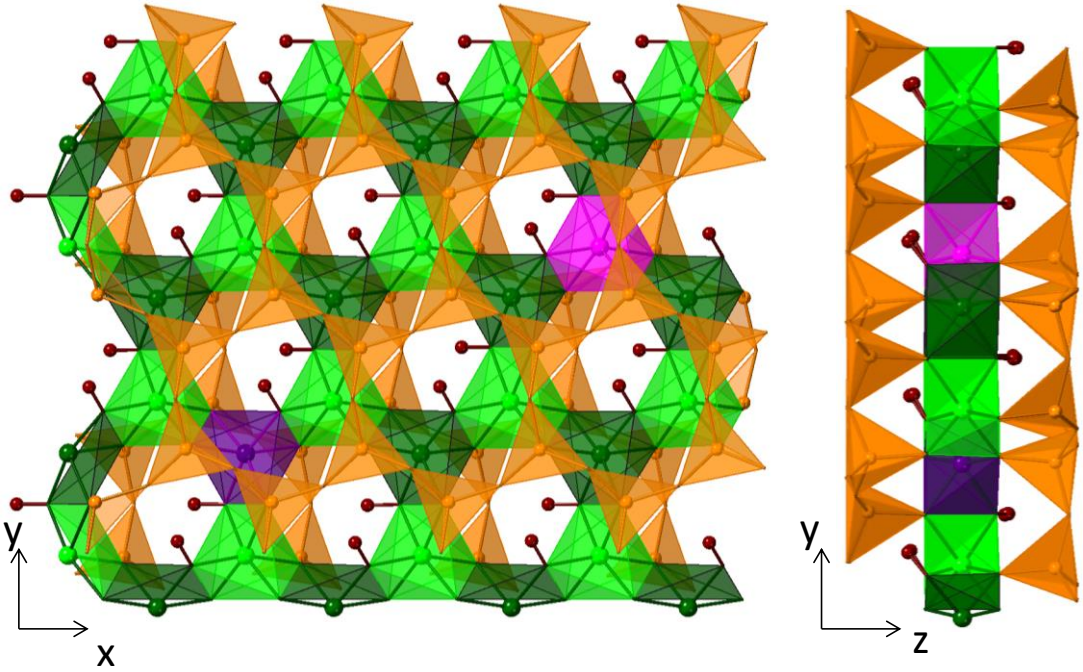

Figure 1. Views of the modeled montmorillonite with substituted iron at the *cis*- and *trans*-sites of the octahedra. The structural incorporation of Fe is illustrated as pink (magenta) octahedron at the *cis*-site and dark purple octahedral at the *trans*-site. The *cis*- and *trans*-site substitution can be distinguished by the different relative position of hydroxyl (OH^-) groups shown with red spheres. Alumina octahedra are shown in green while silica tetrahedra are orange.

2.2. *Ab initio* calculations

The spin polarized electronic structure calculations were performed based on the density functional theory (DFT) using the Gaussian Plane Wave (GPW) method as it is implemented in the QUICKSTEP module of the CP2K code[34,35]. The scalar-relativistic normconserving pseudopotentials of Goedecker, Teter and Hutter (GTH)[36,37] were applied to avoid the explicit consideration of the core electrons $\left(\text{for iron [Ne] } 3s^2\ 3p^6\ 4s^2\ 3d^6\right)$. The wave functions of the valence electrons were described by a linear combination of contracted Gaussian-type orbitals using MOLOPT basis sets optimized for the corresponding GTH pseudopotentials[38]. An auxiliary basis set of plane waves was employed to expand the electronic density using an electronic density cutoff of 1500Ry for the electronic density of states calculation and 400Ry for molecular dynamics simulations. The exchange and correlation energy was calculated using the exchange-correlation functional of Perdew, Burke and Ernzerhof (PBE)[39,40]. The simulations were performed with a multiplicity $(2S+1)_{Fe^{2+}} = 5$ for systems with a ferrous iron and $(2S+1)_{Fe^{3+}} = 6$ for systems with a ferric iron, respectively. Conventional DFT is known to underestimate the Coulomb repulsion between the localized $3d$-electrons of Fe[41]. To obtain a more accurate description of these states, the so-called DFT+U method was applied[42,43]. In this semi empirical approach, an additional potential is applied on the $3d$-states of iron (Supporting Information 1).

Born−Oppenheimer molecular dynamics (MD) simulations using a Γ-point sampling were performed within the canonical ensemble (NVT) controlled by a stochastic thermostat[44] employing an MD time step of 0.5fs. In each time step, the energy was converged to $6.3 \cdot 10^{-5}$kcal/atom. In this way, four 20ps long *ab initio* MD trajectories of montmorillonite with structural Fe^{2+} and Fe^{3+} present in *trans*- and *cis*-position were obtained. They were used to calculate thermal averaged XAFS spectra of the Fe-bearing montmorillonite.

2.3. Calculations of EXAFS and XANES spectra

The EXAFS spectra were calculated based on molecular configurations derived from the *ab initio* simulations using the FEFF 8.40 software[45,46]. For each atomic configuration, the scattering potential of the atoms were calculated self-consistently[45,47]. The amplitude reduction factor S_0^2 was set to 1.0. Multiscattering paths up to eight legs with path lengths up to 7.0Å were taken into account. The radius of the cluster for self-consistent full multiple scattering calculations was set to 5.0Å.

The thermal disorder was taken into account in two ways. In the first case, 320 molecular snapshots from MD trajectories at 300K simulating temperature separated by a 50fs time step were averaged. Here, the thermal motion of the atoms were "directly" considered. In the second "indirect" case, the static configurations derived from the initially relaxed structures were used with a Debye−Waller factor of 0.006 in the EXAFS calculations. Other parameters were set to the default values[46,48].

The calculated EXAFS spectra served as the basis for the interpretation of the experimental data. The linear combination fit to the experimental EXAFS spectra was performed according to Equation (1) after max-min normalization to the value of the first oscillation of the calculated and the measured spectra[23].

$$Q = \left\| k^3 \sum_{\mathrm{i}} a_i^2 \chi_i(k) - \chi^{\exp}(k) \right\|^2 + \left\| a_i^2 \right\|^2 \qquad (1)$$

where $\chi_i(k)$ and $\chi^{\exp}(k)$ are the calculated and the experimental EXAFS spectra, respectively. a_i^2 are the fitting parameters for the four different types of montmorillonite structures. The fitting was limited to the interval of $k\left(\text{Å}^{-1}\right) \in [3.0,9.0]$.

The theoretical prediction of XANES spectra is very challenging because of the complexity of the underlying equations, which can only be solved in an approximate way. The aim of this study was (1) to demonstrate that the quantitative approach used for the interpretation of EXAFS spectra is also applicable to XANES spectra and (2) to determine the preferred oxidation state and occupational site of iron with two independent methods. The XANES spectra were calculated based on two different theoretical approaches. The first set of the XANES spectra was obtained using the self-consistent real space multiple scattering (RSMS) method implemented in the FEFF 8.40 code[45,46]. The second set of XANES

spectra was obtained using the fully relativistic density functional theory with the local spin-density approximation (DFT-LSDA) implemented in the FDMNES code[49]. We calculated the spectra for 6.0Å large molecular clusters derived from the *ab initio* geometry optimization and MD simulations. The scattering potentials of the atoms were calculated self consistently (SCF) for each atomic configuration. For the structures obtained by geometry optimization, the XANES spectra were obtained by convolution of electronic DOS with an arctangent weighted Lorentzian as it is defined in the FDMNES software[49–51]. Other parameters were set to default values[52]. (More detailed information about the FDMNES parameter choice can be found in the Supporting Information 2.) For the data from MD simulations, well-converged XANES spectra were obtained convolving 100 instantaneous snapshots (separated by 160fs each).

The calculated XANES spectra also served as the basis for the interpretation of the experimental data after max-min normalization. The fit to the experimental XANES spectra was performed according to Equation (2), which is conceptually similar to Equation (1).

$$Q = \left\| \sum_{\mathrm{i}} b_i^2 \mu_i(E) - \mu^{\exp}(E) \right\|^2 + \left\| b_i^2 \right\|^2 \qquad (2)$$

where $\mu_i(E)$ and $\mu^{\exp}(E)$ are the calculated and experimental XANES spectra, respectively. b_i^2 are the fitting parameters for the four different type of montmorillonite structures. The fitting was limited to the interval of $E(\mathrm{eV}) \in [7110,7200]$ (the Fe K-edge is at 7112eV).

The Euclidian norm was used during the fittings as defined by the scalar product. The fit was accepted when the spectra features in the XAFS signal matched and the Q values (indicators for the fit quality) were the lowest for the given a_i^2 and b_i^2 values, respectively.

2.4. XAFS experiments

Two type of low Fe-bearing montmorillonite samples were used which show similar diversity of octahedral crystal chemistry[53]. A Milos- (Mil-) and a Wyoming-montmorillonite (SWy-)sample was prepared from the “as received” material without any physical or chemical treatment by pressing a pellet. The Fe K-edge XAFS spectra were collected at the Stanford Synchrotron Radiation Lightsource (SSRL, Menlo Park, CA) at the beamline 11−2 using a Si(220) double crystal monochromator and a Canberra 100-pixel Ge solid-state monolith detector. Higher order harmonics were rejected by detuning the monochromator by 30%. The monochromator angle was calibrated at the Fe K-edge by assigning the energy of 7112eV to the first inflection point of the K-edge absorption spectrum of Fe metal foil. XAFS data reduction was performed with the Athena/Artemis interface of the IFEFFIT software[54,55] following standard procedures[56,57].

3. Results and discussion

3.1. EXAFS spectra

The calculated Fe K-edge EXAFS spectra for montmorillonite with Fe^{2+} and Fe^{3+} located in the *cis*- and *trans*-occupational sites were obtained and compared with experimental spectrum. The statistical and thermal disorder was first taken into account directly as the MD trajectories modeled at 300K temperature served as the basis for the spectroscopic calculations (Figure 2a). In the second case, when the relaxed atomic structures at 0K were the basis for the EXAFS calculations, a global Debye−Waller factor was applied in the spectroscopic studies (Figure 2b). Although, the MD based EXAFS spectra were broadened, the spectra obtained from the relaxed geometries and the MD trajectories agree very well (Figure 2a,b).

The calculated spectra for Fe^{2+} and Fe^{3+} are clearly different in both cases. The first difference between the spectra with distinct iron ionic state is a slight shift in the first oscillation at $k \approx 4.3/4.5$ Å^{-1}. A double-bounced oscillation at $k \approx 6.1/6.6$ Å^{-1} was present only for the structures containing ferric iron. Differences could also be seen at the third oscillation $\left(k \approx 7.7/8.4 \text{ Å}^{-1}\right)$ where the shoulders were at the opposite side $\left(\text{left for } Fe^{2+}, \text{ right for } Fe^{3+}\right)$. On the other hand, iron in the *cis*- or *trans*-coordination (light and dark lines on Figure 2a and Figure 2b) turned out to have a minor effect on the obtained spectra. The spectra of Milos- and Wyoming-montmorillonite samples were similar, the only difference appeared at the double-bounced oscillation at $k \approx 6.1/6.6$Å^{-1}. Second oscillation for SWy-sample was higher.

The qualitative comparison of the calculated EXAFS spectra and the experimental ones indicate that the iron is present mainly in the Fe^{3+} form in both Milos- and Wyoming-montmorillonite. Several linear combination fits of the measured Milos- and Wyoming-montmorillonite spectra based on the theoretical one for the Fe^{2+}_{cis}, Fe^{2+}_{trans}, Fe^{3+}_{cis} and Fe^{3+}_{trans} were performed to obtain a quantitative estimation of the preferential occupational sites and the iron oxidation state. The best linear combination fits (Fit 1 in Table 1 and Table 2) obtained based on the MD trajectories and the relaxed structures are compared with the experimental data in Figure 2c−f. The best agreement (Fit 1) could be obtained for weighted spectra containing of Fe^{2+} (30−40%) and Fe^{3+} (60−70%). Iron was found to be preferentially in ferric form in both Milos- and Wyoming-montmorillonite that agreed with the assumption of earlier studies[9,53,58]. The differences in the quality of the fits between the Milos- and Wyoming-montmorillonite can be explained by the different distribution of the Fe atoms in the structure. The Fe^{3+} atoms are randomly distributed in Milos-montmorillonite, while Wyoming-montmorillonite displays an ordered iron distribution[53]. The simulations were performed at low Fe concentration without considering iron−iron clustering. The iron−iron clustering is believed to be responsible for the double-bounced oscillation at $k \approx 6.1/6.6$ Å^{-1}, therefore could not be reproduced with the applied structural model.

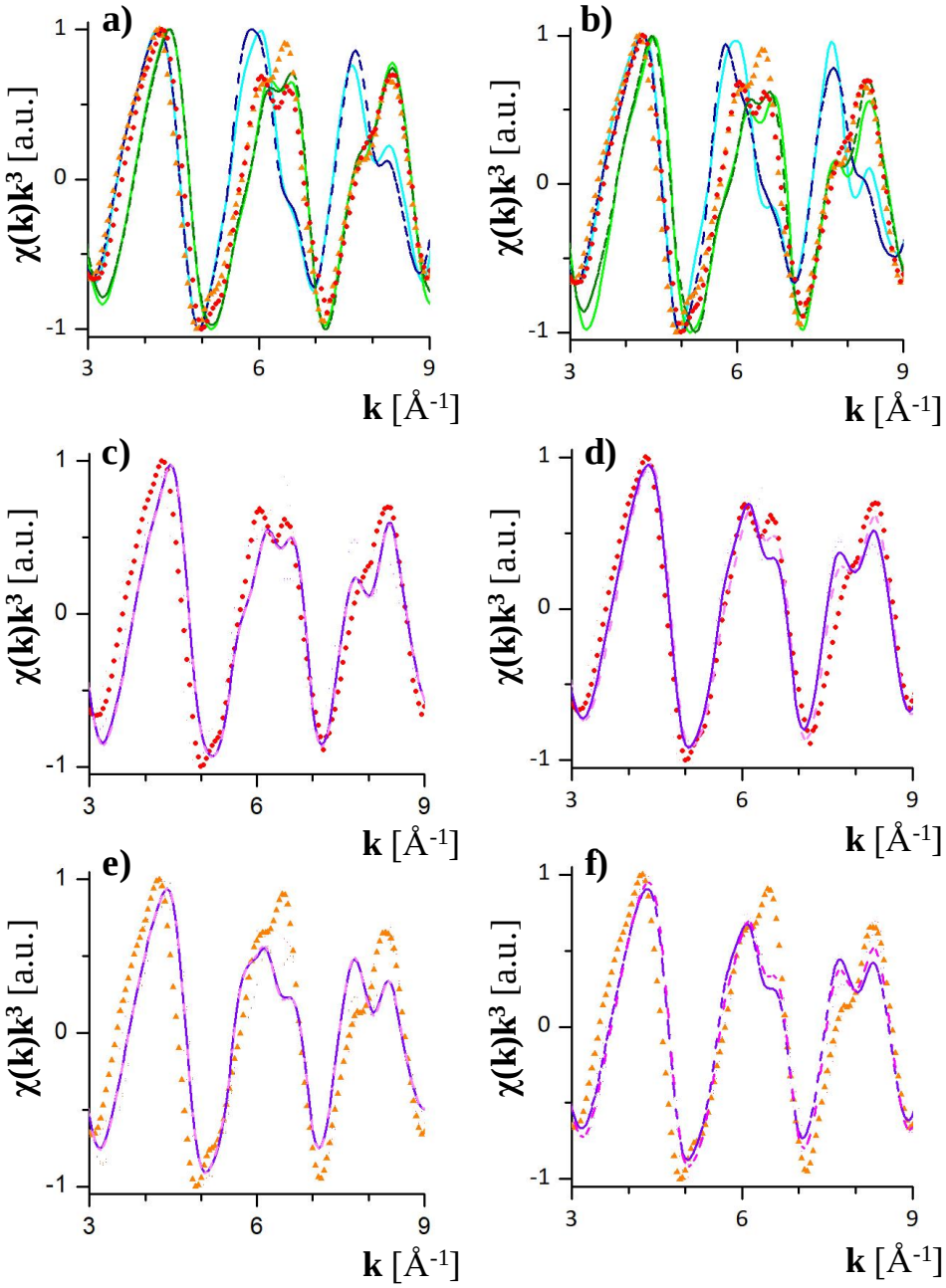

Figure 2. Experimental EXAFS spectra (red circles for Milos- and orange triangle for SWy-montmorillonite) of montmorillonite with iron incorporation and modeled EXAFS spectra (lines) of Fe incorporated in the octahedral layer of 2:1 clay. In panels a and b, blue colors correspond to the incorporated ferrous iron $\left(Fe^{2+}\right)$, while green colors represent incorporated ferric iron $\left(Fe^{3+}\right)$. The lines with lighter color represent the iron at the *cis*-site, while dashed darker lines correspond to the *trans*-occupational site. In panels c−f, the lines represent the linear combination fits, the darker purple lines show "Fit 1", while the dashed lighter pink lines correspond to the "Fit 2". Panels c and d represent fits to the Milos-montmorillonite spectra with contributions determined in Table 1, while panels e and f show linear combination fits for SWy-montmorillonite spectra with contributions determined in Table 2. The calculated EXAFS spectra for panels a, c, and e were derived from MD simulations, while in panels b, d, and f, the relaxed structures served as a basis.

Table 1. Parameters (contributions and quality (Q_{Mil})) of the EXAFS and XANES linear combination fit of incorporated iron with distinct oxidation state (Fe^{2+}/Fe^{3+}) at different occupational site (*cis*/*trans*) for Milos-montmorillonite, respectively[a]

	Basis of the EXAFS calculation	Number of the fit	**Contribution** [%] Fe^{2+} *cis*	Fe^{2+} *trans*	Fe^{3+} *cis*	Fe^{3+} *trans*	$Q_{\mathrm{Mil}}{}^{b}$ [−]
EXAFS	**MD trajectories**	"Fit 1"[a]	20	12	28	40	3.31
	Figure 2b	"Fit 2"[a]	16	16	34	34	3.33
	Relaxed structures	"Fit 1"[a]	14	18	0	68	4.49
	Figure 2d	"Fit 2"[a]	16	16	34	34	5.20
XANES	**MD trajectories**	"Fit 1"[a]	0	0	100	0	0.600
	Figure 4b	"Fit 2"[a]	0	0	50	50	0.627
	Relaxed structures	"Fit 1"[a]	0	0	100	0	0.442
	Figure 4d	"Fit 2"[a]	0	0	50	50	0.443

[a]"Fit 1" corresponds to the "best fit", while "Fit 2" is the constrained "equal site distribution fit".
[b]Q_{Mil} is calculated using Equation (1) for EXAFS and Equation (2) for XANES.

Table 2. Parameters (contributions and quality (Q_{SWy})) of the EXAFS and XANES linear combination fit of incorporated iron with distinct oxidation state (Fe^{2+}/Fe^{3+}) at Different occupational site (*cis*/*trans*) for Wyoming-montmorillonite, respectively[a]

	Basis of the EXAFS calculation	Number of the fit	**Contribution** [%] Fe^{2+} *cis*	Fe^{2+} *trans*	Fe^{3+} *cis*	Fe^{3+} *trans*	$Q_{\mathrm{SWy}}{}^{b}$ [−]
EXAFS	**MD trajectories**	"Fit 1"	36	4	19	41	8.45
	Figure 2b	"Fit 2"	20	20	30	30	8.60
	Relaxed structures	"Fit 1"	13	30	0	57	10.15
	Figure 2d	"Fit 2"	21.5	21.5	28.5	28.5	11.22
XANES	**MD trajectories**	"Fit 1"	0	0	0	100	0.582
	Figure 4b	"Fit 2"	0	0	50	50	0.603
	Relaxed structures	"Fit 1"	0	0	0	100	0.389
	Figure 4d	"Fit 2"	0	0	50	50	0.391

[a]"Fit 1" corresponds to the "best fit", while "Fit 2" is the constrained "equal site distribution fit".
[b]Q_{SWy} is calculated using Equation (1) for EXAFS and Equation (2) for XANES.

The spectra of Fe^{2+}_{cis} and Fe^{2+}_{trans} as well as the spectra of Fe^{3+}_{cis} and Fe^{3+}_{trans} show only slight differences, thus a second linear combination fit (Fit 2) was performed on the calculated structures. In this case, the total contributions of the Fe^{2+} and Fe^{3+} were kept the same, but the contributions of the different occupational sites were equalized (Table 1 and Table 2). The comparison of the fitting quality (Table 1 and Table 2) and the fitted curves (Figure 2c−f) revealed that there were only small differences between the two fits. Therefore, the preferential occupation of *cis*- or *trans*-sites by Fe^{2+} and Fe^{3+} in montmorillonite could not be determined by only comparing the calculated and the measured EXAFS spectra.

3.2. XANES spectra

Fe K-edge XANES spectra based on the RSMS approach for montmorillonite with Fe^{2+} and Fe^{3+} located in the *cis*- and *trans*-occupational sites were obtained and compared with the experimental spectrum (Figure 3). At a first glance, the simulation and the measurement results seem to agree, the characteristic shoulder at about 7140eV of the main peak is over predicted (Figure 3). A more clear difference can be seen in the pre-edge region where the experimental spectrum shows only a smooth shoulder but the RSMS calculations predict sharp pre-edges.

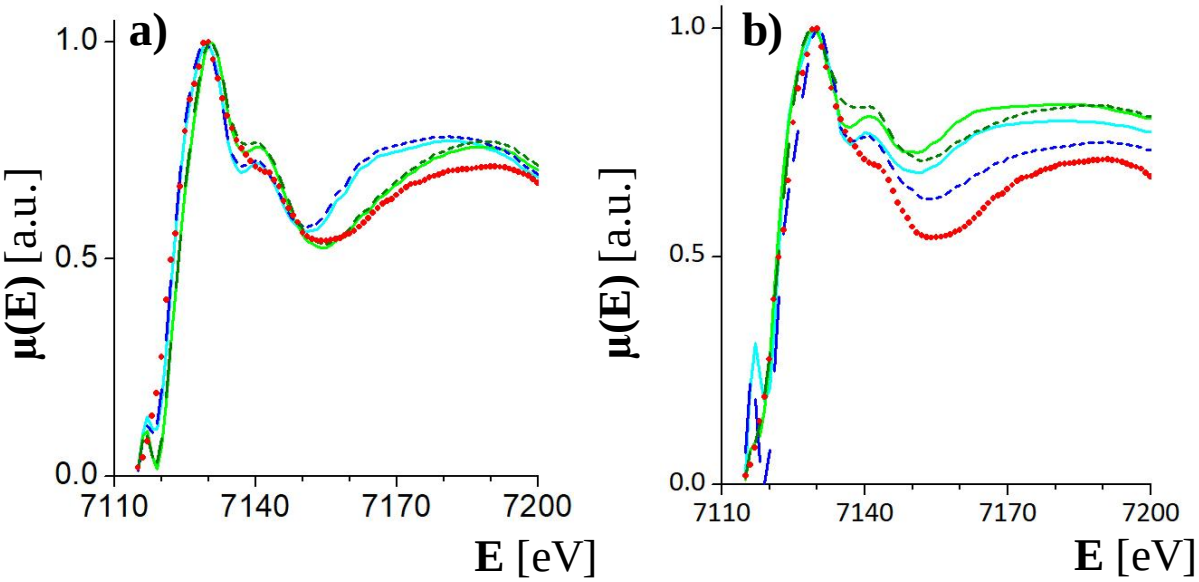

Figure 3. Experimental XANES spectrum (red circles) of Milos-montmorillonite with iron incorporation and *ab initio* XANES spectra (lines) of Fe incorporated in the octahedral layer of 2:1 clay applying FEFF 8.40 software. Blue colors correspond to the incorporated ferrous iron (Fe^{2+}) while green colors represent incorporated ferric iron (Fe^{3+}). The lighter straight lines represent the Fe at the *cis*-site, while dashed darker lines correspond to the *trans*-occupational site. The XANES spectra for panel a were derived from the MD calculations, and for panel b, the relaxed structures served as a basis.

The contradictions in the XANES spectra obtained with FEFF 8.40 software suggest that another, more sophisticated theoretical method should be applied. Therefore, we also calculated the XANES spectra based on the fully relativistic DFT-LSDA method for the four different structures with relaxed geometries using the FDMNES software[49]. The calculated spectra agreed well with both the measured XANES of the Milos- and the SWy-montmorillonite samples, however, the spectra obtained for Fe^{2+} and Fe^{3+} are clearly different (Figure 4a and Figure 4b). The shape of the first edge of the XANES spectra for Fe^{2+} and Fe^{3+} are very similar, only a small energy shift (1–2eV) can be recognized. The height of the characteristic shoulder at about 7135eV demonstrates more clearly the difference between Fe^{2+} and Fe^{3+} (Figure 4a and Figure 4b). This shoulder is also clearly seen in the experimentally measured spectra and

its height is closer to the one of Fe^{3+} (Figure 4a and Figure 4b). The structural coordination environment (*cis*- and *trans*-site) of the Fe octahedron seems to have little effect on the calculated spectra that agrees well with the EXAFS studies.

The oxidation state and the preferential occupational site of the substituted iron atoms were determined using the linear combination fit defined as in Equation (2). The data can be fitted best as a linear combination (Fit 1) of Fe^{2+}_{cis}, Fe^{2+}_{trans}, Fe^{3+}_{cis} and Fe^{3+}_{trans} (Table 1 and Table 2). The corresponding compounds of the fits agreed best within the margin of errors. The exclusive contribution of the calculated Fe^{3+}_{cis} spectrum in the linear combination fit to measured Milos-montmorillonite spectrum ensured that ferric iron is preferred in the bulk incorporation. As the XANES spectra of the SWy-montmorillonite is very similar to the Milos-montmorillonite (with a nearly identical shoulder at the right side of the first peak), the exclusive ferric iron contribution is expected. The differences can be seen in the postedge region cannot be reproduced assuming random distribution of the iron atoms in the sample.

A Fit 2 was also performed similarly to the EXAFS case when the total contributions of the Fe^{2+} and Fe^{3+} were kept the same but the contributions of the different occupational sites were equalized (Table 1 and Table 2) to test the contribution of the different occupational site. The comparison of the fitting quality (Table 1 and Table 2) and the fitted curves (Figure 4**.**c−f) revealed that there were only small differences between the two fits. Therefore, the preferential occupation of *cis*- or *trans*-sites by Fe^{2+} and Fe^{3+} in montmorillonite could not be inferred from the XAFS spectra alone.

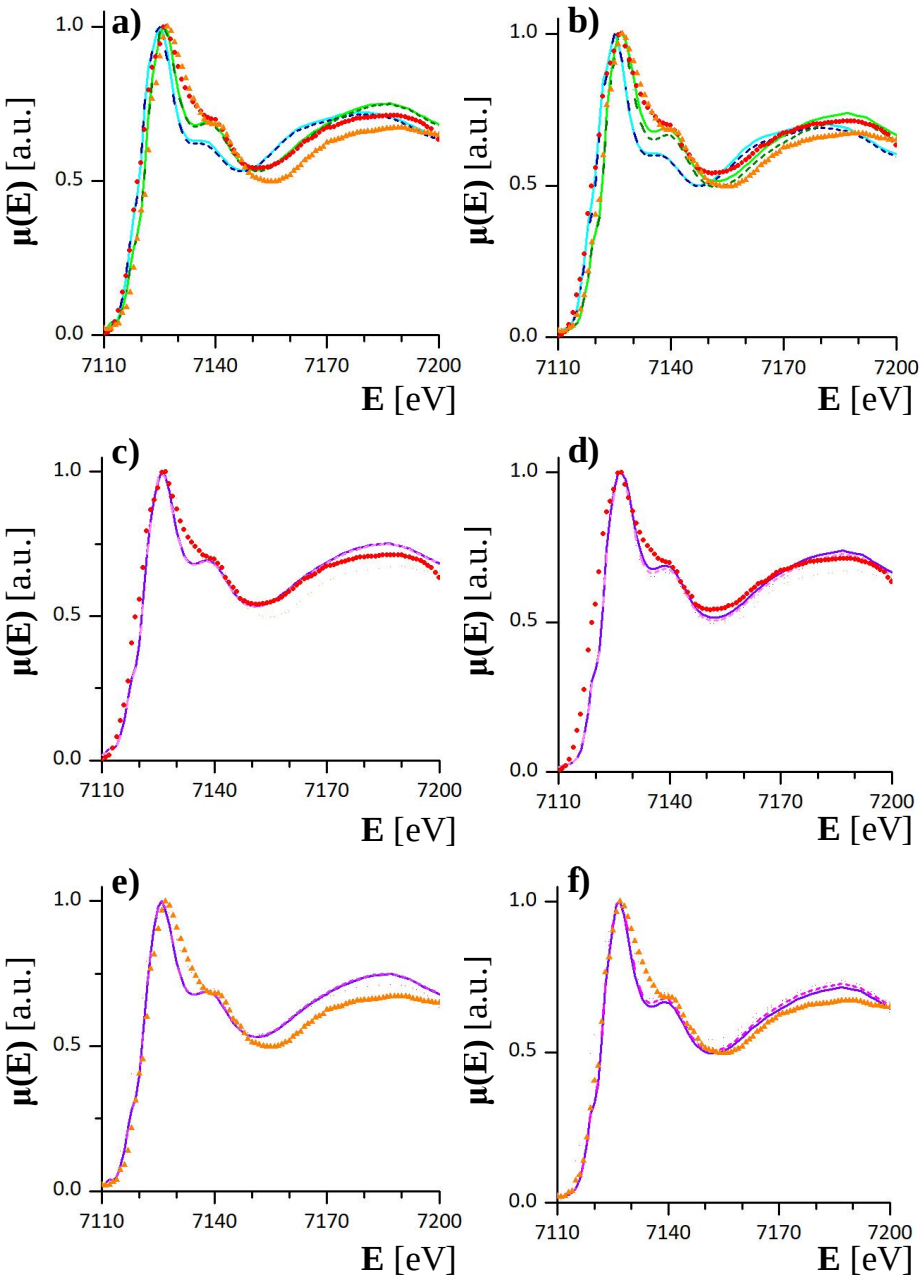

Figure 4. Experimental XANES spectra (red circles for Milos- and orange triangle for SWy-montmorillonite) of montmorillonite with iron incorporation and modeled XANES spectra (lines) of Fe incorporated in the octahedral layer of 2:1 clay. In panels a and b, blue colors correspond to the incorporated ferrous iron $\left(Fe^{2+}\right)$, while green colors represent incorporated ferric iron $\left(Fe^{3+}\right)$. The lines with lighter color represent the iron at the *cis*-site while dashed darker lines correspond to the *trans*-occupational site. In panels c–f, the lines represent the linear combination fits, the darker purple lines show Fit 1, while the dashed lighter pink lines correspond to the Fit 2. Panel c and panel d represent fits to the Milos-montmorillonite spectra with contributions determined in Table 1, while panels e and f show linear combination fit for SWy-montmorillonite spectra with contributions determined in Table 2. The calculated XANES spectra for panels a, c, and e were derived from MD simulations, while for panels b, d, and f, the relaxed structures served as a basis.

3.3. Structural position of Fe in bulk montmorillonite

The structural parameters of the relaxed structures from geometry optimization were compared with the measurement results to obtain information about the differences between the different structures (Table 3). The average Fe^{2+}–O distances of (2.13±0.03)Å are longer than the Fe^{3+}–O distances of (2.03±0.03)Å. The calculated distances are nearly identical for the *cis*- and *trans*-sites. The Fe–Al and Fe–Si distances are identical for Fe^{2+} and Fe^{3+} (Table 3). Therefore, the Fe–O shell provides only a hint about the oxidation state, whereas any conclusions about the *cis*- or *trans*-occupation based on structural data are highly speculative.

The occupancy of the *cis*- and *trans*-sites can be evaluated based on the relative energies of Fe substitution in the *cis*- and *trans*-octahedron. The calculations predict that for low Fe content investigated in this study, the relative energies of iron (both $Fe^{2+}$and Fe^{3+}) in *cis*- and *trans*-sites are equal within the uncertainties of the calculations (Table 3). This means that iron is randomly distributed between the *cis*- and *trans*-sites. The observation is consistent with the very similar structural parameters obtained in the XAFS simulations.

Table 3. Structural parameters and energy difference of bulk montmorillonite with iron incorporation derived from the *ab initio* calculations and EXAFS measurements

Structural parameters		Fe^{2+}		Fe^{3+}		EXAFS (Milos) "Fit 1"	Measurement (Milos)
		cis	*trans*	*cis*	*trans*		
Fe–O_{all}[a]	*CN* [–]	6.0 ± 0.1	6.0 ± 0.1	6.0 ± 0.1	6.0 ± 0.1	6.0 ± 0.1	5.8 ± 0.4
	R [Å]	2.14 ± 0.03	2.12 ± 0.03	2.03 ± 0.03	2.02 ± 0.03	2.05 ± 0.03	2.01 ± 0.01
Fe–O_H[b]	*CN* [–]	2.0 ± 0.1	2.0 ± 0.1	2.0 ± 0.1	2.0 ± 0.1	2.0 ± 0.1	
	R [Å]	2.08 ± 0.04	2.10 ± 0.04	2.00 ± 0.04	2.01 ± 0.04	2.03 ± 0.04	
Fe–O[c]	*CN* [–]	4.0 ± 0.1	4.0 ± 0.1	4.0 ± 0.1	4.0 ± 0.1	4.0 ± 0.1	
	R [Å]	2.14 ± 0.03	2.13 ± 0.03	2.04 ± 0.02	2.03 ± 0.02	2.07 ± 0.02	
Fe–Al	*CN* [–]	3.0 ± 0.1	3.0 ± 0.1	3.0 ± 0.1	3.0 ± 0.1	3.0 ± 0.1	2.8 ± 0.5
	R [Å]	3.04 ± 0.03	3.04 ± 0.03	3.07 ± 0.03	3.07 ± 0.03	3.06 ± 0.03	3.05 ± 0.02
Fe–Si	*CN* [–]	4.0 ± 0.1	4.0 ± 0.1	4.0 ± 0.1	4.0 ± 0.1	4.0 ± 0.1	3.8 ± 0.6
	R [Å]	3.25 ± 0.03	3.23 ± 0.03	3.24 ± 0.03	3.22 ± 0.03	3.23 ± 0.03	3.25 ± 0.03
Energy difference [kcal/mol]		**0.0 ± 0.5**		**0.0 ± 0.5**		—	—

[a] O_{all} corresponds to the all oxygen atoms in the first shell

[b] O_H corresponds to the oxygen atoms of OH^- groups in the first shell

[c] O corresponds to the oxygen atoms (not member of OH^- groups) in the first shell

A previous *ab initio* study showed the differences between ferrous and ferric iron bearing smectites investigating their structural properties (local structure of iron, hydroxyl orientations, vibration dynamics of H and Si)[59]. Our calculated structural parameters showed good agreement with the results of this study[57] the average Fe–O bond lengths (2.11Å and 2.02 Å) agreed within the uncertainty and Fe substitutions did not affect the coordination structures of the Al–O and Si–O polyhedral in neither studies[57].

4. Implication of the theoretical study in the interpretation of XAFS

This study demonstrates that the full XAFS spectra of natural montmorillonites can be obtained as a linear combination fit of theoretical *ab initio* XAFS spectra calculated based on *ab initio* MD trajectories for pure phases without any empirical adjustments of structural parameters such as bond distances or coordination. Performed linear combination analysis yields valuable information on the mechanism of structural incorporation of Fe in natural clay minerals. The comparison of two different theoretical approaches for XAS calculations (RSMS and DFT-LSDA) demonstrates that XANES calculations for elements with 3*d*-electrons largely depends on the used theory.

The differences between predictions of the two methods are significant and influence the accuracy of the quantitative data analysis. The results of the linear combination fit of XANES spectra obtained based on the DFT-LSDA approach showed best agreement with the corresponding analysis of the EXAFS spectra. The quantitative analysis of both EXAFS and XANES spectra suggest that iron is predominantly present in bulk montmorillonite in Fe^{3+} oxidation state. The experimental spectra could be fitted equally well by assuming arbitrary contribution of Fe in *cis*- and *trans*-sites or imposing equal occupation of these sites. The energy calculations suggested that at low concentrations Fe^{2+} and Fe^{3+} are equally distributed between *cis*- or *trans*-sites.

An important step toward is the better understanding of the iron uptake mechanism in the determination of relevant edge surfaces of montmorillonite. Such information will be essential for understanding the mechanism of the probable oxidative uptake of iron $\left(Fe^{2+}_{aq} \rightarrow Fe^{3+}_{surf}\right)$ by clay minerals[9]. In the best case, the comparison of the *ab initio* based XAFS calculations and the measurements will result in the determination of the oxidation state of Fe in the bulk and at the surface. The results may give insight on whether the $Fe^{2+} \rightarrow Fe^{3+}$ redox reaction occurs between the Fe atoms adsorbed on the surface and incorporated structurally into the bulk.

5. References

(1) Stucki, J. W.; Goodman, B. A.; Schwertamann, U. *Iron in Soils and Clay Minerals*. Dordrecht, Netherlands, **2012**; *vol. 217*, pp. 1−3.

(2) Ilton, E. S.; Boily, J. F.; Buck, E. C.; Skomurski, F. N.; Rosso, K. M.; Cahill, C. L.; Bargar, J. R.; Felmy, A. R. Influence of dynamical conditions on the reduction of U(VI) at the magnetite-solution interface. *Environ. Sci. Technol.* **2010**, *44*, 170−176.

(3) Soltermann, D.; Marques Fernandes, M.; Baeyens, B.; Miehé-Brendlé, J.; Dähn, R. Competitive Fe(II)-Zn(II) uptake on a synthetic montmorillonite. *Environ. Sci. Technol.* **2014**, *48*, 190−198.

(4) Leupin, O. X.; Birgersson, M.; Karnland, O.; Korkeakoski, P.; Sellin, P.; Mäder, U.; Wersin, P. *Montmorillonite Stability under near-Field Conditions, Technical Report 14-12*. Wettingen, Switzerland, **2014**, pp. 37−38.

(5) Stucki, J. W.; Golden, D. C.; Roth, C. B. Effects of reduction and reoxidation of structural iron on the surface charge and dissolution of dioctahedral smectites. *Clays Clay Miner.* **1984**, *32(5)*, 350−356.

(6) Hofstetter, T. B.; Schwarzenbach, R. P.; Haderlein, S. B. Reactivity of Fe(II) species associated with clay minerals. *Environ. Sci. Technol.* **2003**, *37*, 519−528.

(7) Hofstetter, T. B.; Neumann, A.; Schwarzenbach, R. P. Reduction of nitroaromatic compounds by Fe(II) species associated with iron rich smectites. *Environ. Sci. Technol.* **2006**, *40*, 235−242.

(8) Stucki, J. W.; Lee, K.; Zhang, L.; Larson, R. A. Effects of iron oxidation state on the surface and structural properties of smectites. *Pure Appl. Chem.* **2002**, *74(11)*, 2145−2158.

(9) Soltermann, D.; Marques Fernandes, M.; Baeyens, B.; Dähn, R.; Joshi, P. A.; Scheinost, A. C.; Gorski, C. A. Fe(II) uptake on natural montmorillonites. I. Macroscopic and spectroscopic characterization. *Environ. Sci. Technol.* **2014**, *48*, 8688−8697.

(10) Pfingsten, W.; Bradbury, M. H.; Baeyens, B. The influence of Fe(II) competition on the sorption and migration of Ni(II) in MX-80 bentonite. *Appl. Geochem.* **2011**, *26*, 1414−1422.

(11) Soltermann, D.; Baeyens, B.; Bradbury, M. H.; Marques Fernandes, M. Fe(II) uptake on natural montmorillonites. II. Surface complexation modeling. *Environ. Sci. Technol.* **2014**, *48*, 8698−8705.

(12) Guggenheim, S.; Adams, J. M.; Bain, D. C.; Bergaya, F.; Brigatti, M. F.; Drits, V. A.; Formoso, M. L. L.; Galan, E.; Kogure, T.; Stanjek, H. Summary of recommendations of nomenclature committees relevant to clay mineralogy: Report of the association international pour l'Etude des Argiles (AIPEA) nomenclature committee for 2006. *Clays Clay Miner.* **2006**, *54(6)*, 761−772.

(13) Tsipursky, S. I.; Drits, V. A. The distribution of octahedral cations in the 2:1 layers of dioctahedral smectites studied by obliquetexture electron diffraction. *Clay Miner.* **1984**, *19*, 177−193.

(14) Cardile, C. M. Structural site occupation of iron within 2:1 dioctahedral phyllosilicates studied by ^{57}Fe Mössbauer spectroscopy. *Hyperfine Interact.* **1988**, *41(1)*, 767−770.

(15) Stucki, J. W. Properties and behaviour of iron in clay mineral. In *Handbook of Clay Science* (Eds.: Bergaya, F.; Theng, B. K. G.; Lagaly, G.) **2006,** pp. 424−430.

(16) Cardile, C. M.; Johnston, J. H. ^{57}Fe Mössbauer spectroscopy of montmorillonites: A new interpretation. *Clays Clay Miner.* **1986**, *34(4)*, 307−313.

(17) Manceau, A.; Lanson, B.; Drits, V. A.; Chateigner, D.; Gates, W. P.; Wu, J.; Huo, D.; Stucki, J. W. Oxidation-reduction mechanism of iron in dioctahedral smectites: I. Crystal chemistry of oxidized reference nontronites. *Am. Mineral.* **2000**, *85*, 133−152.

(18) Tsipursky, S. I.; Drits, V. A. The distribution of octahedral cations in the 2:1 layers of dioctahedral smectites studied by obliquetexture electron diffraction. *Clay Miner.* **1984**, *19*, 177−193.

(19) Gorski, C. A.; Aeschbacher, M.; Soltermann, D.; Voegelin, A.; Baeyens, B.; Marques Fernandes, M.; Hofstetter, T. B.; Sander, M. Redox properties of structural Fe in clay minerals. 1. Electrochemical quantification of electron-donating and -accepting capacities of smectites. *Environ. Sci. Technol.* **2012**, *46*, 9360−9368.

(20) Gorski, C. A.; Klüpfel, L.; Voegelin, A.; Sander, M.; Hofstetter, T. B. Redox properties of structural Fe in clay minerals. 2. Electrochemical and spectroscopic characterization of electron transfer irreversibility in ferruginous smectite, SWa-1. *Environ. Sci. Technol.* **2012**, *46*, 9369−9377.

(21) Gorski, C. A.; Klüpfel, L. E.; Voegelin, A.; Sander, M.; Hofstetter, T. B. Redox properties of structural Fe in clay minerals: 3. Relationships between smectite redox and structural properties. *Environ. Sci. Technol.* **2013**, *47*, 13477−13485.

(22) Soltermann, D.; Fernandes, M. M.; Baeyens, B.; Dähn, R.; Miehé-Brendlé, J.; Wehrli, B.; Bradbury, M. H. Fe(II) sorption on a synthetic montmorillonite. A combined macroscopic and spectroscopic study. *Environ. Sci. Technol.* **2013**, *47*, 6978−6986.

(23) Churakov, S. V.; Dähn, R. Zinc adsorption on clays inferred from atomistic simulations and EXAFS spectroscopy. *Environ. Sci. Technol.* **2012**, *46*, 5713−5719.

(24) Ladeira, A. C. Q.; Ciminelli, V. S. T.; Duarte, H. A.; Alves, M. C. M.; Ramos, A. Y. Mechanism of anion retention from EXAFS and density functional calculations: Arsenic (V) adsorbed on gibbsite. *Geochim. Cosmochim. Acta* **2001**, *65(8)*, 1211−1217.

(25) Sherman, D. M.; Randall, S. R. Surface complexation of arsenic(V) to iron(III) (hydr)oxides: Structural mechanism from *ab initio* molecular geometries and EXAFS spectroscopy. *Geochim. Cosmochim. Acta* **2003**, *67(22)*, 4223−4230.

(26) Tsutsui, Y.; Sugimoto, K.-i.; Wasada, H.; Inada, Y.; Funahashi, S. EXAFS and *ab initio* molecular orbital studies on the structure of solvated silver(I) ions. *J. Phys. Chem. A* **1997**, *101*, 2900−2905.

(27) Bocharov, D.; Krack, M.; Kalinko, A.; Purans, J.; Rocca, F.; Ali, S. E.; Kuzmin, A. *Ab initio* molecular dynamics simulations of the Sc K-edge EXAFS of scandium triuoride. *J. Phys.: Conf. Ser.* **2016**, *712*, 012009.

(28) Bocharov, D.; Chollet, M.; Krack, M.; Bertsch, J.; Grolimund, D.; Martin, M.; Kuzmin, A.; Purans, J.; Kotomin, E. Interpretation of the U L_3-edge EXAFS in uranium dioxide using molecular dynamics and density functional theory simulations. *J. Phys.: Conf. Ser.* **2016**, *712*, 012091.

(29) Teo, B. K. EXAFS: Basic Principles and Data Analysis; Springer, **1986**, *vol. 9*, pp. 21−23.

(30) Churakov, S. V. *Ab initio* study of sorption on pyrophyllite: Structure and acidity of the edge sites. *J. Phys. Chem. B* **2006**, *110*, 4135−4146.

(31) Churakov, S. V.; Kosakowski, G. An *ab initio* molecular dynamics study of hydronium complexation in Na-montmorillonite. *Philos. Mag.* **2010**, *90(17)*, 2459−2474.

(32) Krähenbühl, F.; Stöckli, H. F.; Brunner, F.; Kahr, G.; Müller-Vonmoos, M. Study of the water-bentonite system by vapor adsorption, immersion calorimetry and X-ray techniques: I. Micropore volumes and internal surface areas, following Dubinin's theory. *Clay Miner.* **1987**, *22*, 1−9.

(33) Johnston, J. H.; Cardile, C. M. Iron substitution in montmorillonite, illite and glaucionite by ^{57}Fe Mössbauer spectroscopy. *Clays Clay Miner.* **1987**, *35(3)*, 170−176.

(34) CP2K developers group, 2000−2017. www.cp2k.org.

(35) VandeVondele, J.; Krack, M.; Mohamed, F.; Parrinello, M.; Chassaing, T.; Hutter, J. QUICKSTEP: Fast and accurate density functional calculations using a mixed Gaussian and plane waves approach. *Comput. Phys. Commun.* **2005**, *167*, 103−128.

(36) Goedecker, S.; Teter, M.; Hutter, J. Separable dual-space Gaussian pseudopotentials. Phys. Rev. B: Condens. *Matter Mater. Phys.* **1996**, *54(3)*, 1703−1710.

(37) Krack, M. Pseudopotentials for H to Kr optimized for gradientcorrected exchange-correlation functionals. *Theor. Chem. Acc.* **2005**, *114*, 145−152.

(38) VandeVondele, J.; Hutter, J. Gaussian basis sets for accurate calculations on molecular systems in gas and condensed phases. *J. Chem. Phys.* **2007**, *127*, 114105.

(39) Perdew, J. P.; Burke, K.; Ernzerhof, M. Generalized gradient approximation made simple. *Phys. Rev. Lett.* **1996**, *77(18)*, 3865−3868.

(40) Perdew, J. P.; Burke, K.; Ernzerhof, M. ERRATA: Generalized Gradient Approximation Made Simple [*Phys. Rev. Lett. 77*, 3865 (**1996**)]. *Phys. Rev. Lett.* **1997**, *78(7)*, 1396.

(41) Rollmann, G.; Rohrbach, A.; Entel, P.; Hafner, J. First-principles calculation of the structure and magnetic phases of hematite. *Phys. Rev. B: Condens. Matter Mater. Phys.* **2004**, *69*, 165107.

(42) Liechtenstein, A. I.; Anisimov, V. I.; Zaanen, J. Densityfunctional theory and strong interactions: orbital ordering in Mott-Hubbard insulators. *Phys. Rev. B: Condens. Matter Mater. Phys.* **1995**, *52(8)*, R5467−R5470.

(43) Dudarev, S. L.; Botton, G. A.; Savrasov, S. Y.; Humphreys, C. J.; Sutton, A. P. Electron-energy-loss spectra and the structural stability of nickel oxide: An LSDA+U study. *Phys. Rev. B: Condens. Matter Mater. Phys.* **1998**, *57(3)*, 1505−1509.

(44) Bussi, G.; Donadio, D.; Parrinello, M. Canonical sampling through velocity rescaling. *J. Chem. Phys.* **2007**, *126*, 014101.

(45) Ankudinov, A. L.; Ravel, B.; Rehr, J. J.; Conradson, S. D. Realspace multiple-scattering calculation and interpretation of X-ray absorption near-edge structure. *Phys. Rev. B: Condens. Matter Mater. Phys.* **1998**, *58(12)*, 7565−7575.

(46) Ankudinov, A. L.; Nesvizhskii, A. I.; Rehr, J. J. Dynamic screening effects in X-ray absorption spectra. *Phys. Rev. B: Condens. Matter Mater. Phys.* **2003**, *67*, 115120.

(47) Ankudinov, A. L.; Rehr, J. J. Theory of solid-state contributions to the X-ray elastic scattering amplitude. *Phys. Rev. B: Condens. Matter Mater. Phys.* **2000**, *62(4)*, 2437−2445.

(48) Rehr, J. J.; Ankudinov, A.; Ravel, B. User's Guide, FEFF v8.40. Seattle, USA, **2006**.

(49) Bunau, O.; Joly, Y. Self-consistent aspects of X-ray absorption calculations. *J. Phys.: Condens. Matter* **2009**, *21*, 345501.

(50) Guda, S. A.; Guda, A. A.; Soldatov, M. A.; Lomachenko, K. A.; Bugaev, A. L.; Lamberti, C.; Gawelda, W.; Bressler, C.; Smolentsev, G.; Soldatov, A. V.; Joly, Y. Optimized finite difference method for the full-potential XANES simulations: Application to molecular adsorption geometries in MOFs and metal-ligand intersystem crossing transients. *J. Chem. Theory Comput.* **2015**, *11*, 4512−4521.

(51) Amestoy, P. R.; Guermouche, A.; L'Excellent, J.-Y.; Pralet, S. Hybrid scheduling for the parallel solution of linear systems. *Parallel. Comput.* **2006**, *32(2)*, 136−156.

(52) Joly, Y. FDMNES User's Guide. Grenoble, France, **2016**; pp. 49−53.

(53) Vantelon, D.; Montarges-Pelletier, E.; Michot, L. J.; Briois, V.; Pelletier, M.; Thomas, F. Iron distribution in the octahedral sheet of dioctahedral smectites. An Fe K-edge X-ray absorption spectroscopy study. *Phys. Chem. Miner.* **2003**, *30*, 44−53.

(54) Newville, M. IFFEFFIT: interactive XAFS analysis and FEFF fitting. *J. Synchrotron Radiat.* **2001**, *8*, 322−324.

(55) Ravel, B.; Newville, M. ATHENA, ARTEMIS, HEPHAESTUS: Data analysis for X-ray absorption spectroscopy using IFEFFIT. *J. Synchrotron Radiat.* **2005**, *12*, 537−541.

(56) Teo, B. K. EXAFS: Basic Principles and Data Analysis. **1986**, *vol. 9*, pp 114−128.

(57) Koningsberger, D. C.; Prins, R. X-Ray Absorption: Principles, Applications, Techniques of EXAFS, SEXAFS and XANES. New York, USA, **1988**; *Chapter 6*, pp. 211−253.

(58) Schaefer, M. V.; Gorski, C. A.; Scherer, M. M. Spectroscopic evidence for interfacial Fe(II)–Fe(III) electron transfer in a clay mineral. *Environ. Sci. Technol.* **2011**, *45(2)*, 540−545.

(59) Liu, X.; Meijer, E. J.; Lu, X.; Wang, R. *Ab initio* molecular dynamics study of Fe-containing smectites. *Clays Clay Miner.* **2010**, *58(1)*, 89−96.

6. Supporting Information 1: Choice of the Hubbard (U_{eff}) parameter

Conventional DFT is known to underestimate the Coulomb repulsion between the localized 3*d*-electrons of Fe[S1]. In order to improve the description of these delocalized states within the DFT formalism, the so-called DFT+U method was applied[S2,S3]. This spin-polarized method combines the conventional DFT with a Hubbard-Hamiltonian. It adds a Mott-Hubbard contribution considering the on-site Coulomb repulsion and exchange function explicitly[S1,S4,S5]. The rotationally invariant total energy of the system can be determined according to Equation (S1)[S1,S3].

$$E_{\mathrm{DFT+U}} = E_{\mathrm{DFT}} + \frac{U-J}{2}\sum_{\sigma}\mathrm{Tr}[\rho^{\sigma} - \rho^{\sigma}\rho^{\sigma}] \qquad (S1)$$

where E_{DFT} is the total energy of the system calculated by using the conventional DFT method, $\frac{U-J}{2}$ is the so-called effective Hubbard parameter (hereinafter U_{eff}) and ρ_{σ} is the on-site occupancy matrix.

The U_{eff} can be determined as the difference of the value of the on-site Coulomb repulsion (U), which is characterized by a spherically averaged energy required for adding an extra d electron to an iron atom and the parameter J representing the screened exchange energy[S6]. The exact value of U_{eff} depends on the implementations and it is needed to be calibrated. Although, it can be derived from theoretical calculations based on the local spin density approximation (LSDA)[S6], we used a more pragmatic approach.

No reliable data on the electronic density of states (eDOS) or band gap information are available for Fe-bearing montmorillonite to allow a direct calibration of Hubbard parameter (U_{eff}) for the investigated system. However, it can be expected that the value of the Hubbard parameter is transferable between the iron bearing structures with octahedral coordination. Hematite (α–Fe_2O_3) and wustite (FeO) are two widely studied iron oxides with similar environment for iron as in the Fe-bearing montmorillonite. Therefore, we use published Fe 3*d* eDOS data of hematite (α–Fe_2O_3)[S7,S8] and wustite (FeO)[S9,S10] to calibrate the Hubbard parameter for the simulation with Fe-bearing montmorillonite.

The electronic density of states (eDOS) of octahedrally coordinated iron oxides such as hematite and wustite were determined for numerous U_{eff} values (Figure S1). The best agreement between the experimentally measured value for the band gap[S11,S12] and the features of the theoretically predicted eDOS[S1,S12-S14] for hematite and wustite were obtained at U_{eff} = 1.9eV. Thus, the value of the effective Hubbard parameter was fixed at 1.9eV for the further *ab initio* calculations of Fe-bearing montmorillonite.

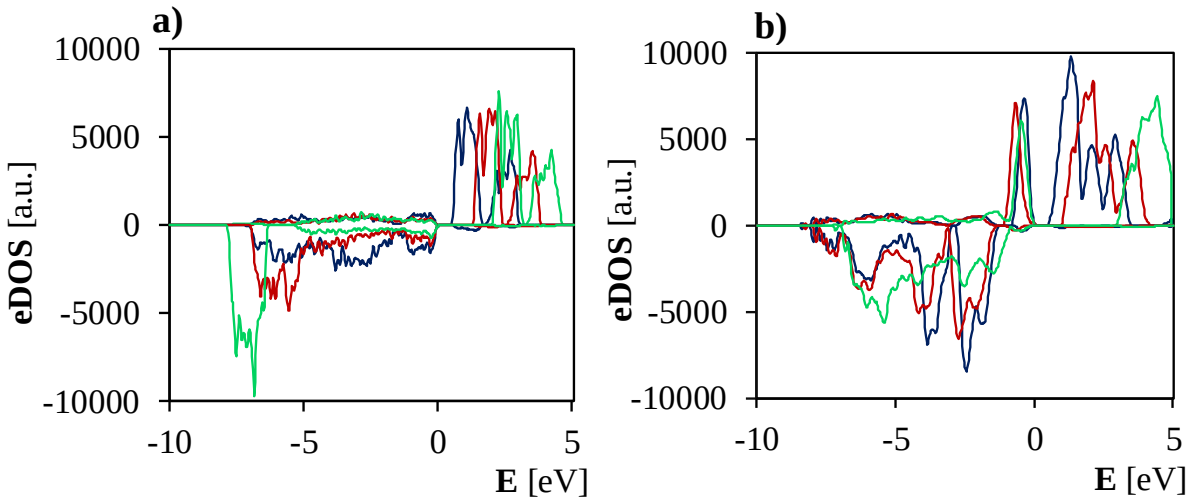

Figure S1. Fe 3*d* eDOS functions of hematite (panel a) and wustite (panel b) at three different Hubbard parameter values. Dark blue lines represents eDOS at $U_{\mathrm{eff}} = 0.0$eV, $U_{\mathrm{eff}} = 1.9$eV is marked with red lines, while $U_{\mathrm{eff}} = 4.0$eV is shown in green.

The simulations were performed in 17.2Å×17.2Å×17.2Å and 15.11Å×17.45Å×13.77Å supercells with antiferromagnetically ordered *d*-electron spins within the (111) and the (001) planes for wustite and hematite, respectively[S7,S15,S16]. The eDOS data were collected for a wide range of U_{eff} values $0.0\mathrm{eV} \leqslant U_{\mathrm{eff}} \leqslant 5.0\mathrm{eV}$. The $U_{\mathrm{eff}} = 0.0$eV calculations corresponded to the conventional density functional theory (DFT). For the initial DFT+U-based structure optimization, an auxiliary basis set of plane waves up to a 400Ry cutoff was applied. The eDOS were obtained based on these optimized atomic coordinates using a density cutoff of 1500Ry. The electronic temperature for the DOS calculation was fixed at 500K, which is between the Neel ($T_{\mathrm{N}} = 955$K) and the Morin ($T_{\mathrm{M}} = 260$K) temperatures. At these conditions hematite and wustite behave as an antiferromagnetic insulator showing only weak ferromagnetism[S7,S10].

The evolution of Fe 3*d* eDOS for upper and lower spin in hematite and wustite as the function of the Hubbard parameter is shown in Figure S1 for three different values of U_{eff} ($U_{\mathrm{eff}} = 0.0\mathrm{eV}; 1.9\mathrm{eV}; 4.0\mathrm{eV}$). The Hubbard parameter is found to have a profound influence on the electronic spectrum through the on-site Coulomb repulsion. The unoccupied Fe states were shifted to higher energies while the occupied Fe states were not changed.

The value of the band gap increased monotonically with increscent Hubbard parameter (Figure S2). The experimentally measured value of the band gap for hematite[S7] and for wustite[S9] are 2.0eV and 3.1eV, respectively. In the conventional DFT ($U_{\mathrm{eff}} = 0.0\mathrm{eV}$) calculations, the band gap values (1.4eV for hematite and 1.3eV for wustite) were underestimated. The best agreement between the experimentally measured value for the band gap[S7,S9] and the features of the theoretically predicted eDOS[S7-S10] were obtained with the value of Hubbard parameter equal to 1.9eV.

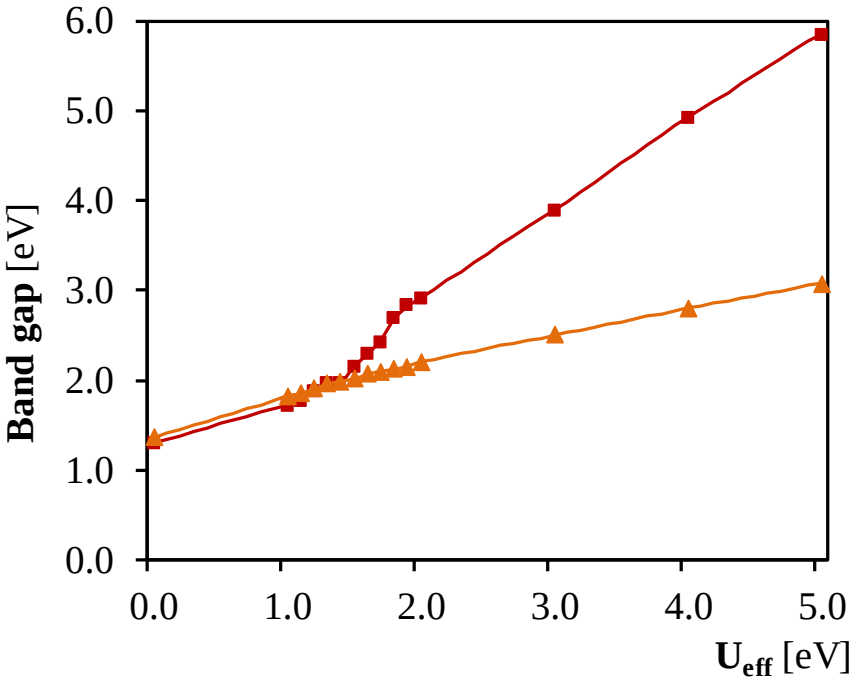

Figure S2. Band gap values of bulk systems containing Fe^{3+} (hematite) marked with orange triangles and Fe^{2+} (wustite) represented by red squares as the function of the Hubbard parameter. The lines are drawn just to guide the eyes.

The Figure S3 showed the DFT+U energy for the wustite and hematite as function of Hubbard parameter calculated based on Equation (S1). The physically acceptable values of U_{eff} must result in positive DFT+U energy, limiting the range of $U_{\text{eff}} \leqslant 2.0$eV consistent with our choice of the Hubbard parameter for further simulations. Thus, the value of the Hubbard-parameter was fixed at 1.9eV for the further *ab initio* calculations.

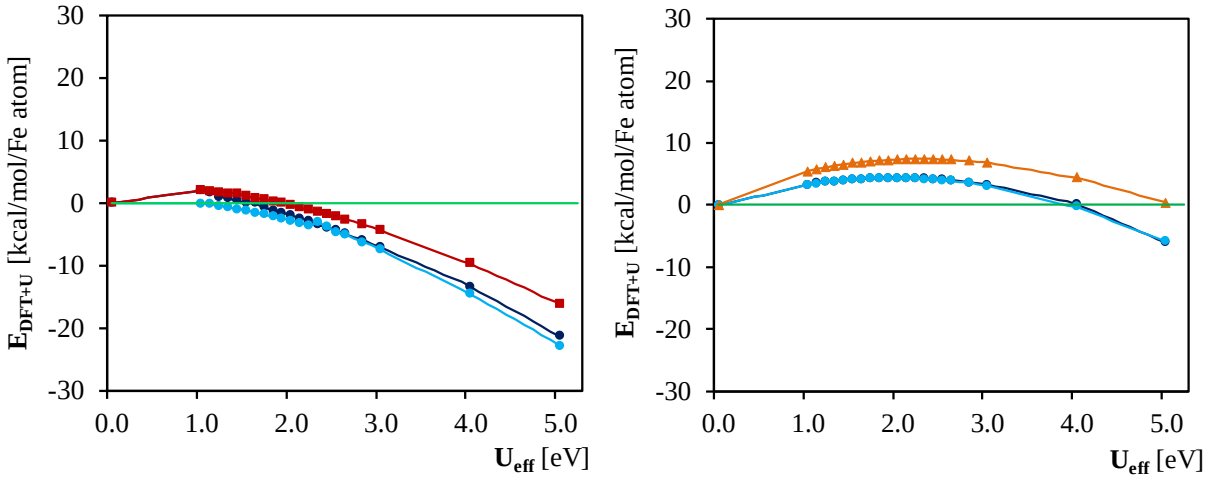

Figure S3. Relative DFT+U energy of bulk systems containing Fe^{2+} (panel a) and Fe^{3+} (panel b) as the function of the Hubbard parameter, respectively. Light blue color represents iron incorporation in bulk montmorillonite at the *cis*-site while dark blue color shows Fe at the *trans*-site. Red and orange color mark wustite and hematite, respectively. The DFT+U energies are compared to the conventional DFT one (U_{eff} = 0eV represented by constant green line). The lines are drawn just to guide the eyes.

References

(S1) Rollmann, G.; Rohrbach, A.; Entel, P.; Hafner, J. First-principles calculation of the structure and magnetic phases of hematite. *Phys. Rev. B* **2004**, *69*, 165107.

(S2) Liechtenstein, A. I.; Anisimov, V. I.; Zaanen, J. Density-functional theory and strong interactions: Orbital ordering in Mott-Hubbard insulators. *Phys. Rev. B* **1995**, *52(8)*, R5467-R5470.

(S3) Dudarev, S. L.; Botton, G. A.; Savrasov, S. Y.; Humphreys, C. J.; Sutton, A. P. Electron-energy-loss spectra and the structural stability of nickel oxide: An LSDA+U study. *Phys. Rev. B* **1998**, *57(3)*, 1505-1509.

(S4) Dorado, B.; Amadon, B.; Freyss, M.; Bertolus, M. DFT+U calculations of the ground state and metastable states of uranium dioxide. *Phys. Rev. B* **2009**, *79*, 235125

(S5) Anisimov, V. I.; Zaanen, J.; Andersen, O. K. Band theory and Mott insulators: Hubbard *U* instead of Stoner *I*. *Phys. Rev. B* **1991**, *44(3)*, 943-954

(S6) Solovyev, I. V.; Dederichs, P. H.; Anisimov, V. I. Corrected atomic limit in the local-density approximation and the electronic structure of d impurities in Rb. *Phys. Rev. B* **1994**, *50*, 16861-16871.

(S7) Rollmann, G.; Rohrbach, A.; Entel, P.; Hafner, J. First-principles calculation of the structure and magnetic phases of hematite. *Phys. Rev. B* **2004**, *69*, 165107.

(S8) Sandratskii, L. M.; Uhl, M.; Kübler, J. Band theory for electronic and magnetic properties of α–Fe_2O_3. *J. Phys. Condens. Mat.* **1996**, *8*, 983-989.

(S9) Press, M. R.; Ellis, D. E. Defect clusters in wustite $Fe_{(1-x)}O$. *Phys. Rev. B* **1987**, *35(9)*, 4438-4454.

(S10) Chou, S.-H.; Guo, J.; Ellis, D. E. Electronic structure and X-ray-absorption spectra of wustite $Fe_{(1-x)}O$. *Phys. Rev. B* **1986**, *34(1)*, 12-24.

(S11) Mochizuki, S. Electrical conductivity of α–Fe_2O_3. *Phys. Status. Solidi. A* **1977**, *41*, 591-594.

(S12) Press, M. R.; Ellis, D. E. Defect clusters in wustite $Fe_{(1-x)}O$. *Phys. Rev. B* **1987**, *35(9)*, 4438-4454.

(S13) Chou, S.-H.; Guo, J.; Ellis, D. E. Electronic structure and X-ray-absorption spectra of wustite $Fe_{(1-x)}O$. *Phys. Rev. B* **1986**, *34(1)*, 12-24.

(S14) Sandratskii, L. M.; Uhl, M.; Kübler, J. Band theory for electronic and magnetic properties of α—Fe_2O_3. *J. Phys.-Condens. Mat.* **1996**, *8*, 983-989.

(S15) Martin, G. J.; Cutting, R. S.; Vaughan, D. J.; Warren, M. C. Bulk and key surface structures of hematite, magnetite and goethite: A density functional theory study. *Am. Mineral.* **2009**, *94*, 1341-1350.

(S16) Fjellvag, H.; Hauback, B. C.; Vogt, T.; Stolen, S. Monoclinic nearly stoichiometric wüstite at low temperatures, *Am. Mineral.* **2002**, *87*, 347-349.

7. Supporting Information 2: Determination of the XANES convolutional parameters

A comprehensive Fe K-edge XANES modelling was performed on the Fe-bearing clay mineral systems to study the effect of the different convolutional parameters as it is defined in the FDMNES user manual[SS1]. The absorption spectra were calculated based on the electronic states of the relaxed structures with fixed input parameters and were convoluted by an arctangent weighted Lorentzian[SS2-SS4]. The weighting function is the following[SS1]:

$$\Gamma = \Gamma_{\mathrm{Hole}} + \Gamma_{\mathrm{m}} \cdot \left(\frac{1}{2} + \frac{1}{\pi} \arctan\left(\frac{\pi}{3} \frac{\Gamma_{\mathrm{m}}}{E_{\mathrm{Larg}}} \left(e - \frac{1}{e^2} \right) \right) \right) \qquad \textit{(SS1)}$$

where Γ_{Hole} is the core level width $\left(\Gamma_{\mathrm{Hole}} = \lim_{E \to -\infty} \Gamma\right)$, Γ_{m} is the maximum width of the final state $\left(\Gamma_{\mathrm{m}} = \lim_{E \to +\infty} \Gamma\right)$, E_{larg} is the width of the arctangent function, $e = \frac{E - E_{\mathrm{F}}}{E_{\mathrm{cent}}}$ and E_{cent} is the center energy (the difference between the deviated Fermi energy and E_{larg}) of the arctangent function[SS1].

The spectra were calculated on the basis of the four different iron substituted clay system: $\left(\mathrm{Fe}^{2+}_{cis}, \mathrm{Fe}^{2+}_{trans}, \mathrm{Fe}^{3+}_{cis}, \mathrm{Fe}^{3+}_{trans}\right)$, respectively. The relaxed atomic coordinates were recalculated putting iron atom into the center and only its 6.0Å radius environment was taken into account. The radius of the cluster for SCF was set to 6.0Å. All the four spectra were calculated at numerous different values of the convolution parameters (Figure SS1-Figure SS5). Similar calibration of the convolutional parameters on the same structures with 7.0Å radius were performed. The results showed that there are no significant differences if we increase the size of the cluster. It means that multiple scattering paths with large legs are not valued and clusters of clay minerals containing ~90 atoms are large enough for the XANES calculations.
From the convolutional parameters those values were accepted which reproduced the XANES spectroscopic features of Fe-bearing clay minerals. The first peak should be individual only slight and smooth divergence at the left side is allowed. The second peak should be smaller than the first peak and the deviation energy between the two peaks should be ~15 eV. The Fe K pre-edge was not taken into account, as unfortunately, the FDMNES code is not capable to calculate the pre-edge properly[SS3]. Table SS1 summarizes the value of the chosen convolutional parameters based on this comparison.

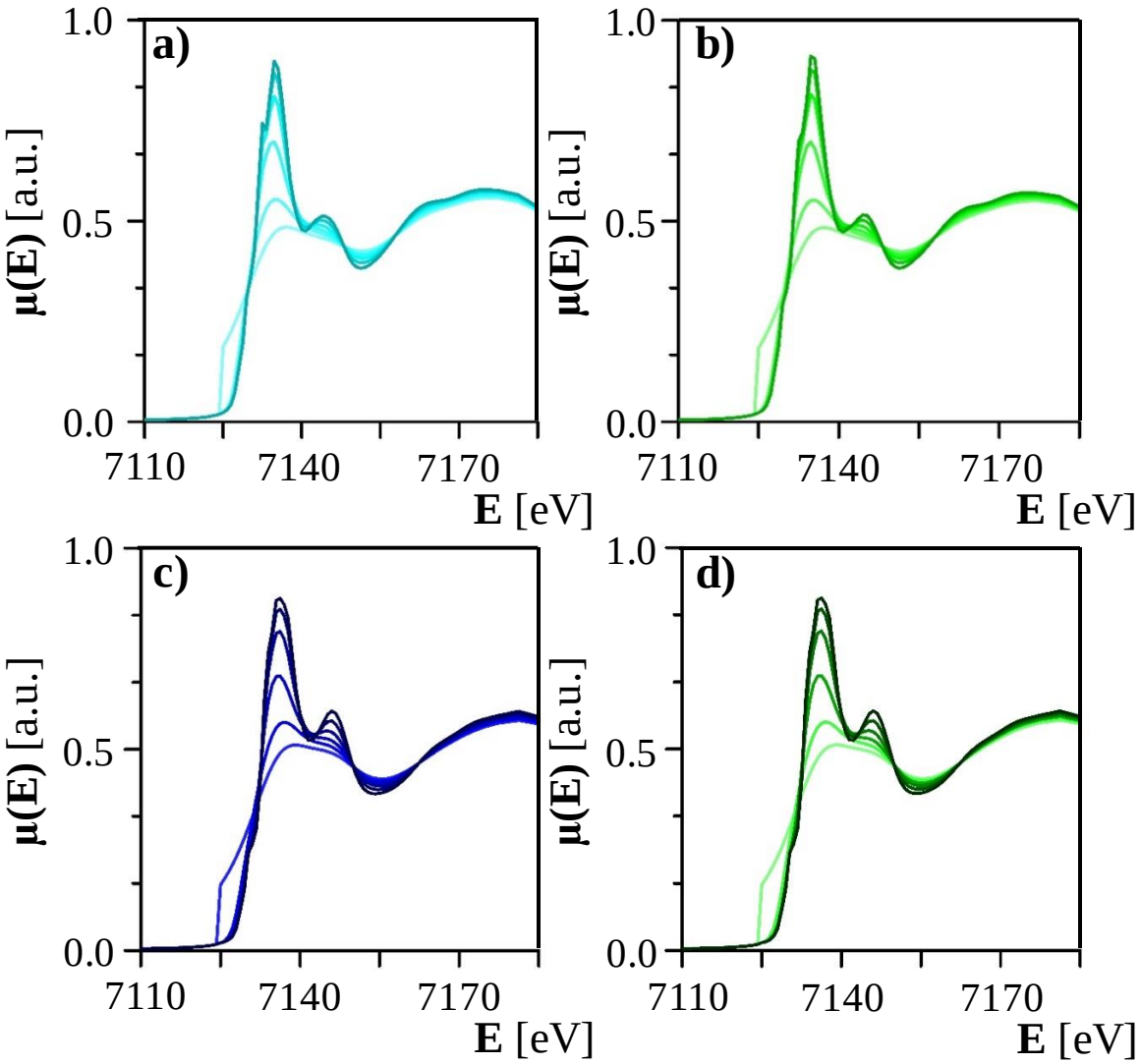

Figure SS1. The features of the XANES spectra for different E_{cent} values (lighter lines represent smaller E_{cent} values). In a) and c), spectra represent ferrous ion substitution while b) and d) correspond to ferric ion substitution. In a) and b) case, *cis*- occupational site structures served as a basis while for c) and d) the *trans*-sites. The calculations are based on 6.0Å radius size relaxed structures.

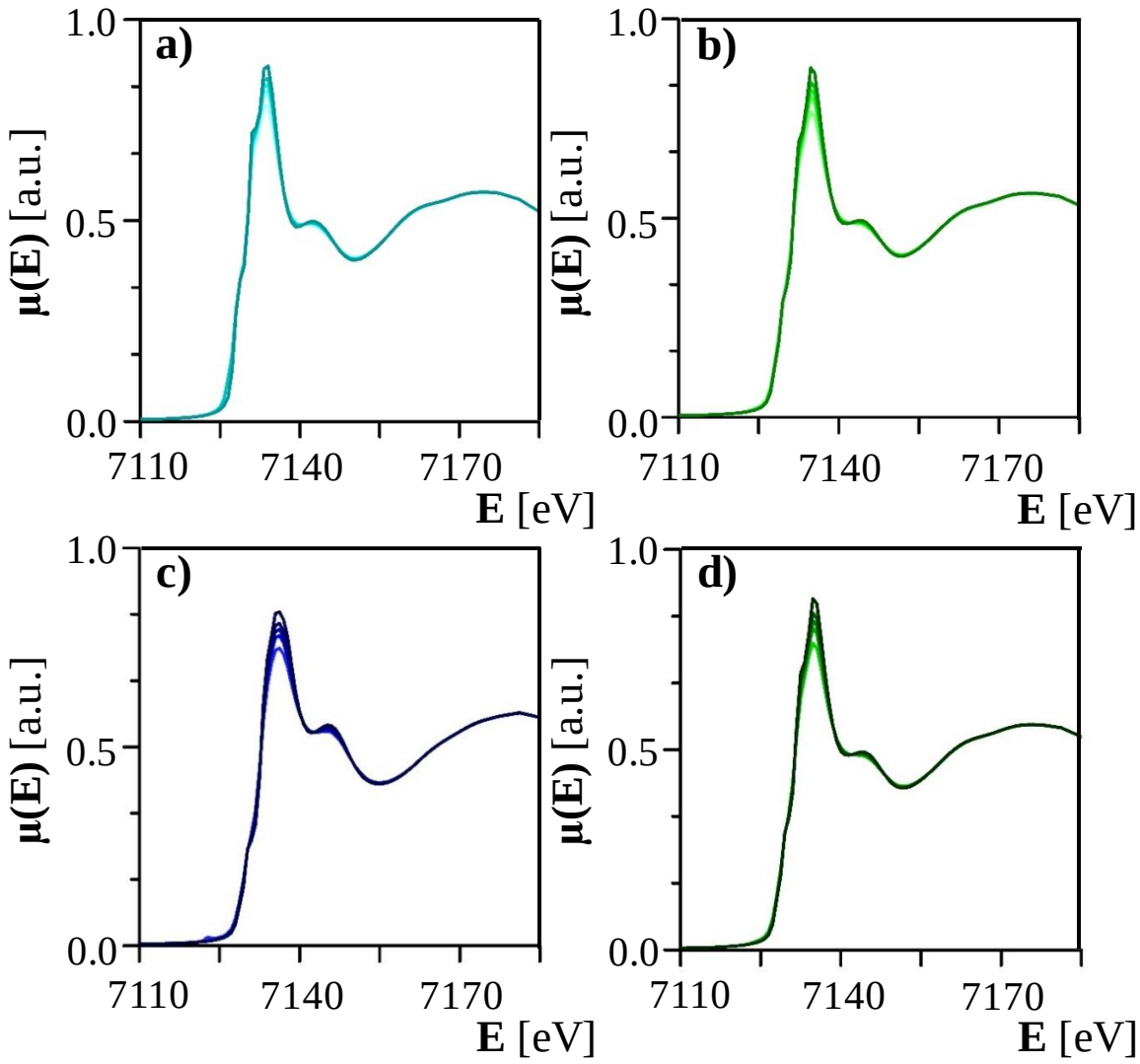

Figure SS2. The features of the XANES spectra for different E_F values (lighter lines represent smaller E_F values). In a) and c), spectra represent ferrous ion substitution, while b) and d) correspond to ferric ion substitution. In a) and b) case, *cis*- occupational site structures served as a basis while for c) and d) the *trans*-sites. The calculations are based on 6.0Å radius size relaxed structures.

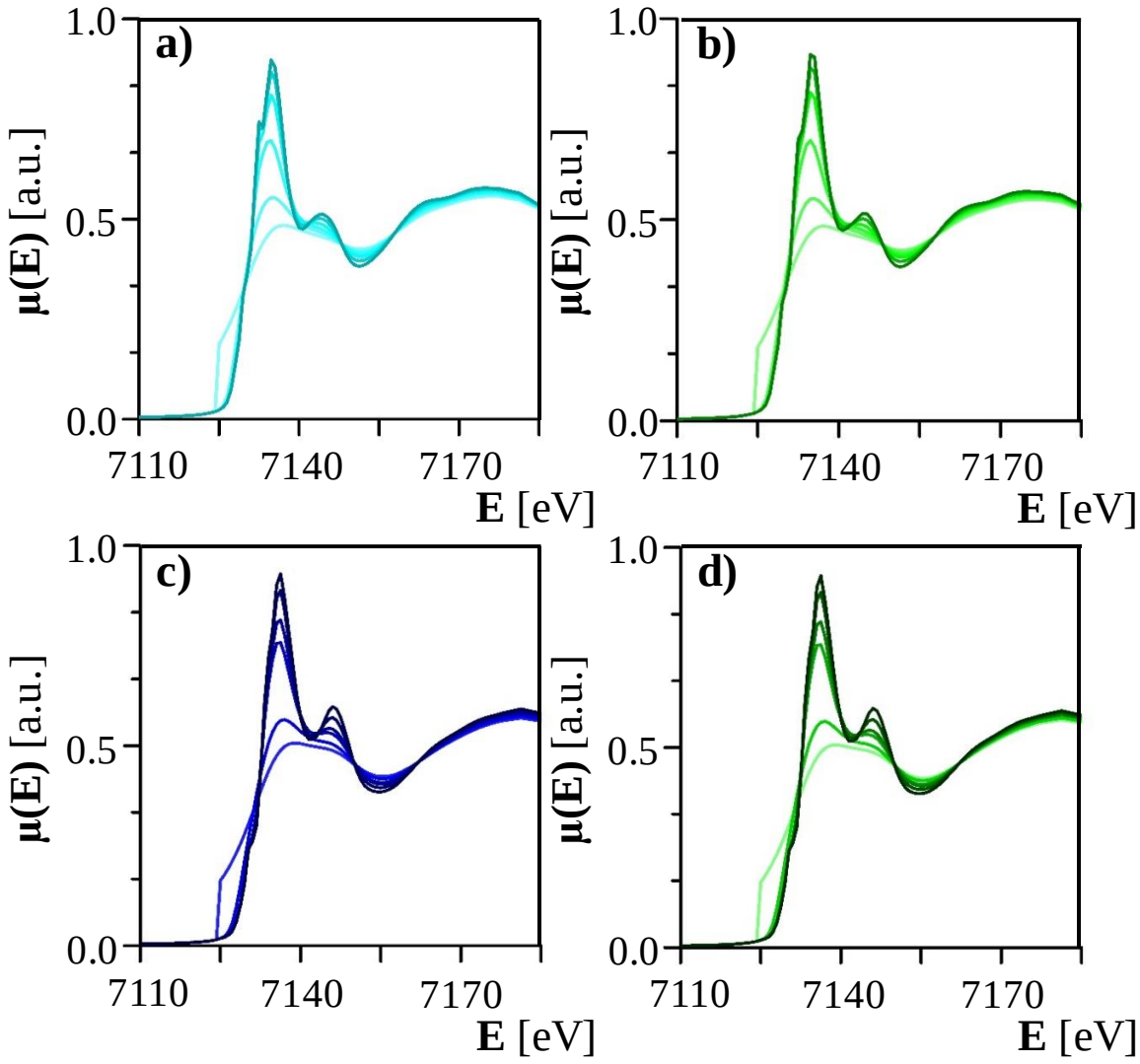

Figure SS3. The features of the XANES spectra for different E_{larg} values (lighter lines represent smaller E_{larg} values). In a) and c), spectra represent ferrous ion substitution while b) and d) correspond to ferric ion substitution. In a) and b) case, *cis*- occupational site structures served as a basis while for c) and d) the *trans*-sites. The calculations are based on 6.0Å radius size relaxed structures.

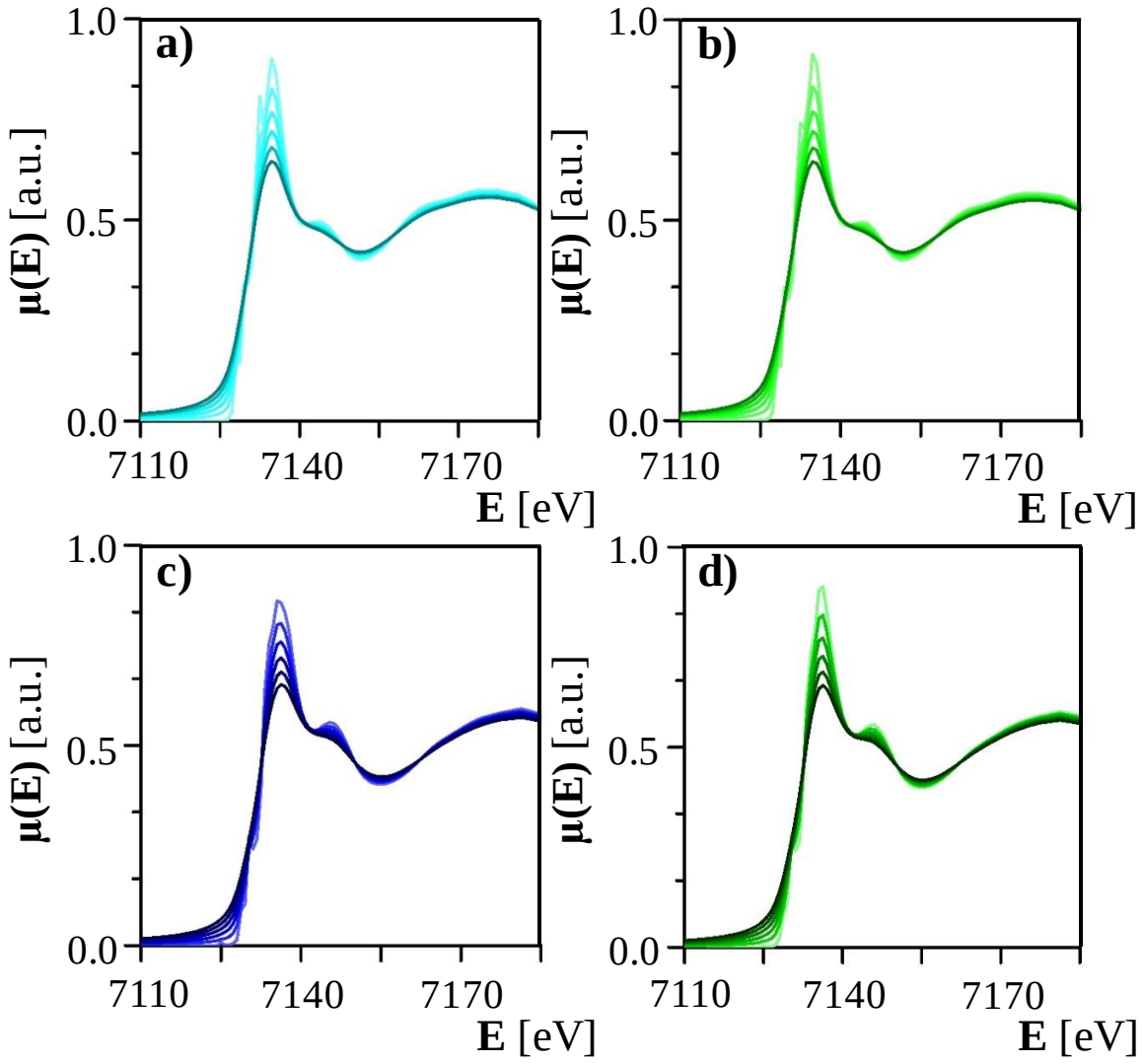

Figure SS4. The features of the XANES spectra for different Γ_m values (lighter lines represent smaller Γ_m values). In a) and c), spectra represent ferrous ion substitution while b) and d) correspond to ferric ion substitution. In a) and b) case, *cis*- occupational site structures served as a basis while for c) and d) the *trans*-sites. The calculations are based on 6.0Å radius size relaxed structures.

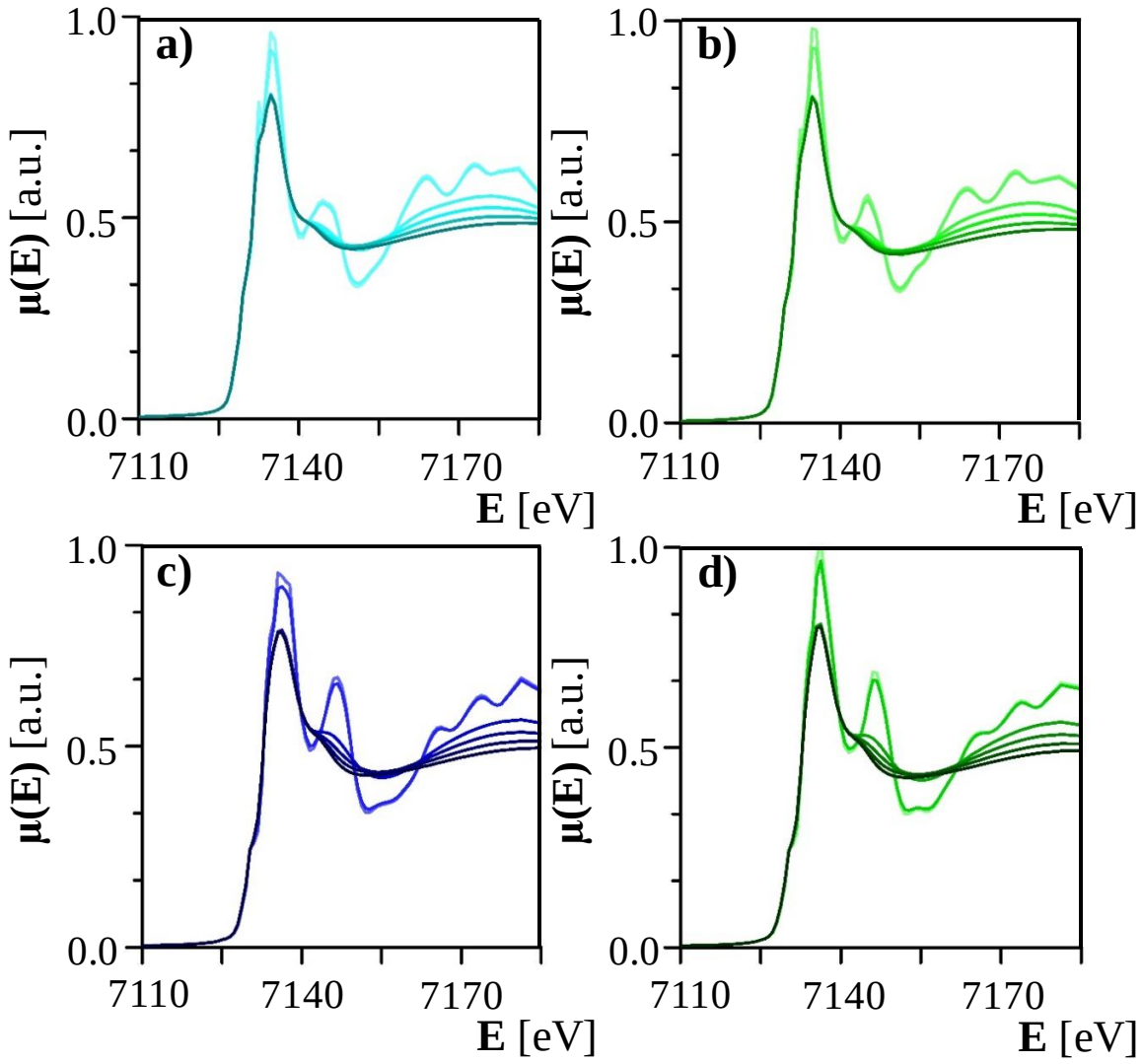

Figure SS5. The features of the XANES spectra for different Γ_{Hole} values (lighter lines represent smaller Γ_{Hole} values). In a) and c), spectra represent ferrous ion substitution while b) and d) correspond to ferric ion substitution. In a) and b) case, *cis*- occupational site structures served as a basis while for c) and d) the *trans*-sites. The calculations are based on 6.0Å radius size relaxed structures.

Table SS1. Fixed convolutional parameters of the XANES calculations

Convolution parameters	Fixed value
E_{cent}	30eV
E_F	0eV
E_{larg}	30eV
Γ_m	20
Γ_{Hole}	2

References

(SS1) Joly, Y. FDMNES User's Guide. *Institut Néel*, Grenoble, France **2016**.

(SS2) Bunau, O.; Joly, Y. Self-consistent aspects of X-ray absorption calculations. *J. Phys.-Condens. Mat.* **2009**, *21*, 345501.

(SS3) Guda, S. A.; Guda, A. A.; Soldatov, M. A.; Lomachenko, K. A.; Bugaev, A, L.; Lamberti, C.; Gawelda, W.; Bressler, C.; Smolentsev, G.; Soldatov, A. V.; Joly, Y. Optimized Finite Difference Method for the Full-Potential XANES Simulations: Application to Molecular Adsorption Geometries in MOFs and Metal-Ligand Intersystem Crossing Transients. *J. Chem. Theory. Comput.* **2015**, *11*, 4512-4521.

(SS4) Amestoy, P. R.; Guermouche, A.; L'Excellent, J.-Y.; Pralet, S. Hybrid scheduling for the parallel solution of linear systems. *Parallel. Comput.* **2006**, *32(2)*, 136-156.

CHAPTER 4:
Theoretical study:
Characterization of structural iron in smectites — an *ab initio* based XAS study

This chapter is a manuscript submitted as "Kéri, A.; Dähn, R.; Krack, M.; Churakov, S. V. Characterization of structural iron in smectites — an *ab initio* based XAS study. *Environmental Science and Technology"* on 14.04.2019

Abstract

Fe-bearing clay minerals are abundant in argillaceous rocks as redox-active structural iron may control the sorption mechanism of redox sensitive elements on the surface of clay minerals. The extent and efficiency of the redox reactions depend on the oxidation state (Fe^{2+}/Fe^{3+} ratio) and structural distribution of the substituting cations in the TOT-layer of clay minerals. Even smectites with similar structure originating from different locations might have distinct arrangement of isomorphic substitutions (e.g. individual iron or Fe–Fe pairs). In this study, the proportion of different iron distribution in Milos–, Wyoming– and Texas–montmorillonite was determined by combining X-ray absorption spectroscopy (XAS) with *ab initio* calculations. The relaxed atomic structures of the smectite models with different arrangement of individual Fe atoms and Fe–Fe/Fe–Mg clusters served as the basis for the calculations of the XAS spectra. The combination of simulation results and measured Fe K-edge XAS spectra of Wyoming–, Milos– and Texas–montmorillonites suggested that iron is present as Fe^{3+} in the octahedral sheet. Fe^{3+} in Texas–montmorillonite has a tendency to form clusters, while no definitive statement about clustering or avoidance of Fe–Fe and Fe–Mg pairs can be made for Milos– and Wyoming–montmorillonite.

1. Introduction

Iron bearing clay minerals are one of the main redox controlling phases in soils[1]. They are important sorbents for organic and metallic contaminants as heterogeneous redox reactions on clay minerals control the mobility and bioavailability of redox-sensitive elements[2–5]. Understanding the mechanisms of individual redox reactions and the iron redox cycle is important in the interpretation of geochemical modelling[1,6]. However, redox processes are inherently complex phenomena and their detailed mechanism remained purely understood[5,6]. The behavior of the Fe^{2+}/Fe^{3+} redox pairs has been studied in iron oxides (e.g. hematite[7,8], goethite[9,10]) and Fe-rich clay mineral (e.g. nontronite[4,11–14]), however, the redox processes in low Fe-bearing clay minerals (e.g. montmorillonite[3,15]) is much less understood[5]. A recent experimental study indicated that structural iron in Wyoming–montmorillonite is more accessible for an interfacial electron transfer than Texas–montmorillonite leading to the conclusion that low Fe-bearing clay minerals even with similar composition might have distinct arrangement of isomorphic substitutions[16].

The structure of Fe-bearing smectites can be described as layers of pseudo-hexagonally ordered sheets of alumina octahedral (O) sandwiched between two opposing siloxane tetrahedral (T) sheets (so called TOT-layer)[17,18]. Most of the Fe-bearing clay minerals belong to 2:1 type of dioctahedral smectites in which only two thirds of the possible octahedral positions are occupied[17]. One third of the octahedral sites are *trans*-symmetric and two thirds of the octahedral sites are *cis*-symmetric with respect to the orientation of the (OH^-) groups[17,19].

It has been demonstrated that iron distribution in the octahedral and in the tetrahedral sheet strongly depends on the total Fe content[5,20–22]. Iron mainly substitutes for Al in the octahedral sheet where it can occupy both the *cis*- and *trans*-sites[5,15,20,23,24]. It may have ordered distribution avoiding Fe–Fe or Fe–Mg pairs or it may form Fe–Fe and Fe–Mg edge sharing pairs of an octahedron[15,19,20]. Clustering usually occurs in iron rich smectites (e.g. nontronite[2,11,25–27]), but it can also be observed in iron poor clay minerals[5,15]. The structure of the dioctahedral Fe-rich end-member, nontronite is well-studied and the relative distribution in the octahedral sheet of many cations $\left(\text{e.g. } Fe^{3+}\right)$ is quantified[5,12,13,28,29]. Much less is known about iron-poor smectites despite their importance in iron redox cycle of geochemical systems.

The redox-active structural iron in clay minerals with low Fe content may control the sorption mechanism and the oxidation state of redox sensitive elements on the clay mineral surface[5,15]. The uptake of ferrous iron on clays as well as the competitive sorption between Fe^{2+} and other divalent cations present in the system greatly depend on the concentration, the redox state and the occupational site of structural iron[3,5,6,13,15,16,28,30,31]. The extent and efficiency of redox reactions depends on the specific structural environment and oxidation state of cations in the TOT-layer of clay minerals $\left(\text{e.g. } Fe^{2+}/Fe^{3+}, Mg^{2+}\right)$[5]. Due to electrostatic repulsion, Fe^{3+} forming Fe^{3+}–Fe^{2+} or Fe^{3+}–Mg^{2+} clusters are less efficient electron acceptor in the redox reaction[32]. In the best case, the phenomenon can be explained by the different structural characteristics of the montmorillonites.

X-ray absorption spectroscopy (XAS) is a widely applied tool to identify the preferred oxidation state and occupational site of iron in clay minerals[1,5,13,33]. For the quantitative interpretation, reference spectra of minerals are needed, in which the element of interest has well-characterized oxidation state. However, it is difficult to have material with pure Fe^{2+} or Fe^{3+} oxidation state because iron preferentially participates in redox-reactions leading to materials with mixed oxides[12,16,21]. Furthermore, iron can unequally be distributed between *cis*- and *trans*-octahedral sites, which can barely or not at all be distinguished only by the experimental result of the spectroscopic method[5,13,34]. Hence, it is becoming an increasingly widespread practice to calculate the extended X-ray absorption fine structure (EXAFS) based on atomistic scale *ab initio* simulations. The theoretical simulations of X-ray absorption near edge structure (XANES) spectra for complex systems are still rare. Recent advances of the theory and computational algorithms in the density functional theory with the local spin-density approximation (DFT-LSDA) based model made it possible to obtain accurate Fe K-edge XANES spectrum of a Fe-bearing structure[35,36].

In this work, we characterize the preferred oxidation state and distribution of iron in Milos–, Wyoming– and Texas–montmorillonite by modelling the measured XAS spectra of these clay minerals as a linear combination of theoretical spectra, which were obtained from *ab initio* geometry optimization calculation of Fe-bearing smectites. The effect of Fe–Fe and Fe–Mg clustering in the octahedral sheet on the XAS spectra was studied using several different dioctahedral smectite models with structural iron incorporation in the octahedral sheet.

2. Materials and methods

2.1. Modeling setup

In our study, we considered idealized defect free TOT layer of a 2:1 dioctahedral clay with the general formula of $4\cdot\left[\left(Mg_x Fe_y^{2+} Fe_z^{3+} Al_{8-x-y-z}\right)\left(Fe_n^{3+} Si_{16-n}\right)O_{40}(OH)_8\right]^{(x+y+n)-}$. It is often used as the simplest structural prototype for dioctahedral clays, where only two thirds of the cation sites in the octahedral sheet are occupied opening a possibility for two distinct structural models[17]. In the *cis*-vacant model (*cv*-model), all *trans*-octahedra are occupied and half of the *cis*- octahedra are vacant, while in the *trans*-vacant case (*tv*-model), all *trans*-octahedra are vacant and all of the *cis*-octahedra are occupied (Figure 1)[37]. Natural clay minerals can be found in both, *cis*- and *trans*-vacant forms[19,20,23].

In both models, the structural optimizations were performed on a single clay particle without water in the interlayer. The dimensions of the orthorhombic supercell were 18.2Å×20.8Å×15.0Å. Similar to previous works, the cell parameter in the "*c*" direction was fixed to 15Å to minimize the interaction between the periodic images[36–38].

The incorporation of iron in the structure was considered as a substitution for aluminum in the octahedral sheet or for silicon in the tetrahedral sheet (Figure 1). Tetrahedral iron is evidently always in the trivalent state, since Fe^{2+} has a too large ionic radius for this site[5]. In the octahedral sheet, both ferrous and ferric iron can occur. In the *tv*-model, iron is only present as *cis*-octahedral positions whereas, in the *tv*-model Fe can be present in both (*cis*- or *trans*-) octahedral positions (Figure 1). The effects of Fe–Fe clustering in the octahedral sheet was studied by replacing two Al octahedra by a Fe–Fe pair at different occupational sites (Figure 1d-g). The presence of Mg–Mg pairs as first and second neighbors produces geometrical distortions in the octahedral sheet due to the higher radius of Mg^{2+}, furthermore, the localized concentration of negative charge in the octahedral sheet would locally destabilize the structure[39,40]. Similarly, the presence of Fe^{2+}–Mg^{2+} pairs can be ruled out because of the electrostatic repulsion argument. Thus, Fe–Mg clusters were modelled to Fe^{3+}–Mg^{2+} pairs only (Figure 1h-l). In total, 26 different model structures were evaluated (Figure 1, Table 1).

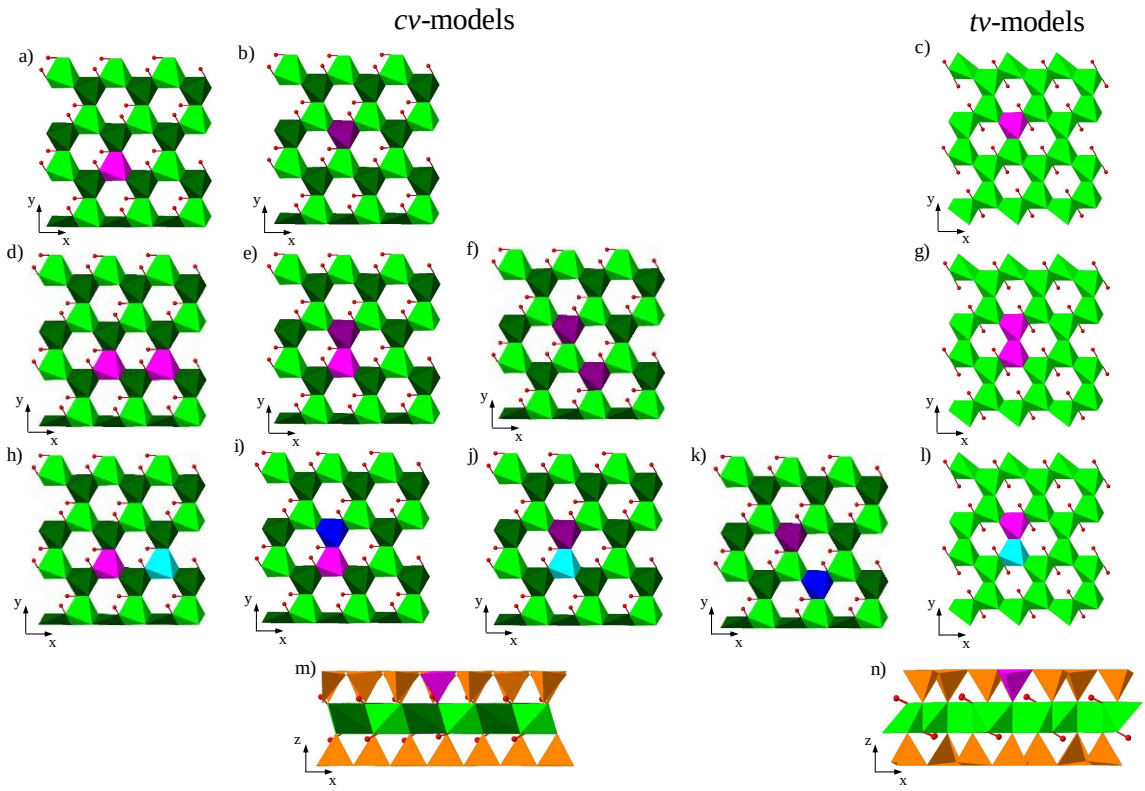

Figure 1. Schematic views of smectite models with different distribution of structural iron. Panel a-l indicate only the octahedral sheet for the sake of clarity. The structures with single iron atom per supercell corresponding to a random distribution are shown in panel a-c, configurations of Fe–Fe clusters are shown in panel d-g, while Mg–Fe clusters are shown in panel h-l. The distribution of tetrahedral iron is shown in panel m,n. *cv*-models correspond to panel a-b, d-f, h-k and m, while *tv*-models are shown in panel c, g, l and n. Silica tetrahedra are shown with orange color, while Fe, Mg and Al polyhedral (both octahedra and tetrahedra) are shown with pink, blue and green colors, respectively. *cis*-octahedra are represented with lighter, while *trans*-octahedra are marked with darker colors. The different occupational sites can be distinguished by the different relative position of the hydroxyl (OH^-) groups shown with red spheres.

Table 1. Iron incorporation model, associated short name and panels of Figure 1 in which the corresponding model structure are. Illustrated relative energy differences are calculated for structures with the same stoichiometry and total charge.

Tetrahedral/ octahedral Fe	Vacancy type	Oxidation state(s), occupational site(s) of iron(s)[a]	Short name of the model	Panel in Figure 1	Cation[a]–Cation[a] bond length[b] [Å]	Energy difference[b] [kcal/mol]
Octahedral	*cv*	Fe^{2+}_{cis}	cvOctFe2c	a)	—	0.0 ± 5.0
		Fe^{2+}_{trans}	cvOctFe2t	b)	—	-4.2 ± 5.0
	tv	Fe^{2+}_{cis}	tvOctFe2c	c)	—	-2.5 ± 5.0
	cv	Fe^{3+}_{cis}	cvOctFe3c	a)	—	0.0 ± 5.0
		Fe^{3+}_{trans}	cvOctFe3t	b)	—	0.3 ± 5.0
	tv	Fe^{3+}_{cis}	tvOctFe3c	c)	—	-5.5 ± 5.0
	cv	Fe^{2+}_{cis}–Fe^{2+}_{cis}	cvFe2cFe2c	d)	5.20 ± 0.01	0.0 ± 5.0
		Fe^{2+}_{cis}–Fe^{2+}_{trans}	cvFe2cFe2t	e)	2.93 ± 0.01	6.3 ± 5.0
		Fe^{2+}_{trans}–Fe^{2+}_{trans}	cvFe2tFe2t	f)	5.27 ± 0.01	-8.5 ± 5.0
	tv	Fe^{2+}_{cis}–Fe^{2+}_{cis}	tvFe2cFe2c	g)	3.01 ± 0.01	2.0 ± 5.0
	cv	Fe^{2+}_{cis}–Fe^{3+}_{cis}	cvFe2cFe3c	d)	5.20 ± 0.01	0.0 ± 5.0
		Fe^{2+}_{cis}–Fe^{3+}_{trans}	cvFe2cFe3t	e)	3.01 ± 0.01	0.7 ± 5.0
		Fe^{2+}_{trans}–Fe^{3+}_{cis}	cvFe2tFe3c	e)	3.05 ± 0.01	-4.1 ± 5.0
		Fe^{2+}_{trans}–Fe^{3+}_{trans}	cvFe2tFe3t	f)	5.26 ± 0.01	-3.7 ± 5.0
	tv	Fe^{2+}_{cis}–Fe^{3+}_{cis}	tvFe2cFe3c	g)	3.07 ± 0.01	-5.8 ± 5.0
	cv	Fe^{3+}_{cis}–Fe^{3+}_{cis}	cvFe3cFe3c	d)	5.21 ± 0.01	0.0 ± 5.0
		Fe^{3+}_{cis}–Fe^{3+}_{trans}	cvFe3cFe3t	e)	3.07 ± 0.01	0.1 ± 5.0
		Fe^{3+}_{trans}–Fe^{3+}_{trans}	cvFe3tFe3t	f)	5.27 ± 0.01	0.1 ± 5.0
	tv	Fe^{3+}_{cis}–Fe^{3+}_{cis}	tvFe3cFe3c	g)	3.09 ± 0.01	-6.4 ± 5.0
	cv	Fe^{3+}_{cis}–Mg^{2+}_{cis}	cvMg2cFe3c	h)	5.33 ± 0.01	0.0 ± 5.0
		Fe^{3+}_{trans}– Mg^{2+}_{cis}	cvMg2cFe3t	i)	3.11 ± 0.01	-0.1 ± 5.0
		Fe^{3+}_{cis}–Mg^{2+}_{trans}	cvMg2tFe3c	j)	3.01 ± 0.01	-1.9 ± 5.0
		Fe^{3+}_{trans}– Mg^{2+}_{trans}	cvMg2tFe3t	k)	5.24 ± 0.01	-2.9 ± 5.0
	tv	Fe^{3+}_{cis}–Mg^{2+}_{cis}	tvMg2cFe3c	l)	3.00 ± 0.01	-6.3 ± 5.0
Tetrahedral	*cv*	Fe^{3+}	cvTetFe3	m)	—	0.0 ± 5.0
	tv	Fe^{3+}	tvTetFe3	n)	—	-7.3 ± 5.0

[a]Cation corresponds to Fe^{2+}, Fe^{3+} or Mg^{2+} depending on the structure

[b]More detailed information can be found in Table S1 in the Supporting Information 1

2.2. *Ab initio* calculations

The spin polarized electronic structures calculations were performed based on the density functional theory (DFT) using the Gaussian Plane Wave (GPW) method as it is implemented in the QUICKSTEP module of the CP2K code[41,42]. The scalar-relativistic norm-conserving pseudopotentials of Goedecker, Teter and Hutter (GTH)[43,44] were applied to avoid the explicit consideration of the core electrons. For iron, the core electrons were described as [Ne] and $3s^2\ 3p^6\ 4s^2\ 3d^6$ were taken as valence electrons. The wave functions of valence electrons were described by a linear combination of contracted Gaussian-type orbitals using MOLOPT basis sets optimized for the corresponding GTH pseudopotentials[45]. An auxiliary basis set of plane waves up to 400Ry cutoff energy was employed to expand the electronic density. The exchange and correlation energy was calculated using the exchange-correlation functional of Perdew, Burke and Ernzerhof (PBE)[46]. Simulations with single iron in the (tetrahedral or octahedral) sheet were performed with a multiplicity $(2S+1)_{Fe^{2+}} = 5$ for systems with a single ferrous iron and $(2S+1)_{Fe^{3+}} = 6$ for systems with a single ferric iron, respectively. For models representing iron clustering with the same oxidation state, the multiplicity was set to $(2S+1)_{Fe^{2+}\text{—}Fe^{2+}} = (2S+1)_{Fe^{3+}\text{—}Fe^{3+}} = 1$. For Fe^{2+}–Fe^{3+} clusters, the multiplicity was set to $(2S+1)_{Fe^{2+}\text{—}Fe^{3+}} = 2$.

Conventional DFT is known to underestimate the Coulomb repulsion between the localized 3*d*-electrons of Fe[47]. In order to improve the description of these delocalized states within the DFT formalism, the so-called DFT+U method was applied[48,49]. In this semi empirical approach, an additional potential characterized by the so-called Hubbard-parameter (U_{eff}) is applied to the selected 3*d*-states of Fe. The value of U_{eff} depends on the implementation and has to be calibrated[36]. The calibration for Fe-bearing montmorillonites was performed in our previous paper[36], thus we used a fixed Hubbard-parameter with $U_{\text{eff}} = 1.9$eV value.

2.3. Calculations of EXAFS spectra

The EXAFS spectra were calculated based on molecular configurations derived from *ab initio* structure optimizations. Real space multiple scattering theory was applied as it is implemented in the FEFF 8.40 software[50]. For each atomic configuration, the scattering potential of the atoms were calculated self-consistently[50,51]. The amplitude reduction factor (S_0^2) was set to 1.0. Multi-scattering paths up to eight legs with path lengths up to 7.0Å were taken into account. The radius of the cluster for self-consistent full multiple scattering calculations was set to 5.0Å. A Debye-Waller factor of 0.006Å^2 was used to take into account the thermal and structural disorder for the static configurations. Other parameters were kept to the default values[52]. All calculated and measured spectra were normalized to the value of the first oscillation. The calculated EXAFS spectra served as the basis for the interpretation of the experimental data. The linear combination fit of the calculated to the experimental EXAFS spectra was performed according to Equation (1)[36,37].

$$Q_{\mathrm{EXAFS}} = \left(k^3 \sum_i \left(a_i^2 \chi_i(k) \right) - \chi^{\exp}(k) \right)^2 + \sum_i a_i^2 \rightarrow \min \qquad (1)$$

where $\chi_i(k)$ are the calculated and $\chi^{\exp}(k)$ is the experimental EXAFS spectra, a_i^2 are the optimized fitting parameters. The fitting was limited to the interval of $k\left(\text{Å}^{-1}\right) \in [3.0, 9.0]$[36,37]. The norm $\sum_i a_i^2$ was included in the objective function to reduce the noise of the fit. The quality of the fit is defined as Equation (1)[36,37].

2.4. XAS experiments

Four samples of low Fe-bearing montmorillonite samples were studied: one Milos– (Mil–), one Wyoming-1– (SWy1–) and two Texas– ($STx1_1$–, $STx1_2$–) montmorillonite. All the samples were prepared from the "as received" material without any physical or chemical treatment. Mil–, SWy1– and $STx1_1$–samples were prepared as a self-supporting film, in addition, from the Texas–montmorillonite, a sample was pressed into a pellet ($STx1_2$– sample). The Fe K-edge XAS spectra were collected at the Stanford Synchrotron Radiation Lightsource (SSRL, Menlo Park, CA) at beamline 11-2 using a Si(220) double crystal monochromator and a Canberra 100-pixel Ge solid-state monolith detector. The self-supporting clay films were measured with polarized extended X-ray absorption fine structure (P-EXAFS) spectroscopy at four different angles (α= 10°; 35°; 55°; 80°), where α is the angle between the electric field vector (ε) and the layer plane of the self-supporting film. In P-EXAFS, neighboring atoms along the polarization direction of the X-ray beam are preferentially probed, and atoms located in a plane perpendicular to this direction are attenuated[53]. To test the potential texture effects arising from the layered structures of the smectites, which tend to form samples having a certain degree of texture[53,54], one STx1 sample was pressed as a pellet ($STx1_2$) and measured at $\alpha = 45°$. Several scans were averaged to improve the signal to noise ratio. Higher order harmonics were rejected by detuning the monochromator by 30%. The monochromator angle was calibrated at the Fe K-edge by assigning the energy of 7112eV to the first inflection point of the K-edge absorption spectrum of Fe metal foil.

All the P-EXAFS extraction from raw data (see details in Supporting Information 2) and all the XAS data reduction was performed with the Athena/Artemis interface of IFEFFIT Software[55,56] following standard procedures. The transformation from $\chi(E)$ to $\chi(k)$ were obtained by the conversion of the abscissa using Equation (2).

$$k = \sqrt{\frac{2\mathrm{m_e}}{\hbar^2}(E - E_0)} \qquad (2)$$

where k is the wavelength, $\mathrm{m_e}$ is the electron rest mass, ħ is the reduced Planck-constant and E_0 is the edge energy. E_0 can automatically be determined by finding the first large peak of the first derivative of the $\mu(E)$ spectrum in Athena[56], however, its value was usually underestimated leading to a shift of the spectra in the k-space. Therefore, we applied an alternative approach for our models. The EXAFS spectra of the models were quantitatively compared to measured ones. To obtain the best linear combination fit for each measured sample, their $\chi(E)$ spectrum was transformed to several $\chi(k)$ spectra using different E_0 around the edge energy estimated by Athena. Afterwards, linear combination fits of each measured EXAFS spectrum based on calculated ones were performed. The EXAFS quality numbers (Q_{EXAFS}) from Equation (1) were calculated as the function of E_0 (Figure S2 in Supporting Information 2). We accepted those fits for each montmorillonite type, which had the lowest Q_{EXAFS} value.

3. Results and discussion

3.1. EXAFS spectra

The calculated Fe K-edge EXAFS spectra for *cv*- and *tv*-model with ferric iron in the tetrahedral sheet as well as Fe^{2+} and Fe^{3+} located in the *cis*- and *trans*- occupational sites in the octahedral sheet are clearly distinct (Figure 2a)[36]. The first difference between the spectra with distinct iron ionic state is a slight shift in the first oscillation at $k \sim 4.3/4.5 Å^{-1}$. A double-bounced oscillation at $k \sim 6.1/6.6 Å^{-1}$ was present only for structures containing ferric iron[36]. Differences could also be seen in the third oscillation ($k \sim 7.7/8.4 Å^{-1}$) where the shoulders are located at the opposite side (left for Fe^{2+} and right for Fe^{3+})[36]. The calculated spectra for the tetrahedral and the octahedral ferric iron clearly differ, as there is a $k \sim 0.5 Å^{-1}$ shift in the entire tetrahedral ferric iron spectrum (Figure 2a,b). Iron in the *cis*- or *trans*-coordination (light and dark lines on Figure 2a) turned out to have a minor effect on the obtained spectra. The result is consistent with energy differences (Table 1).

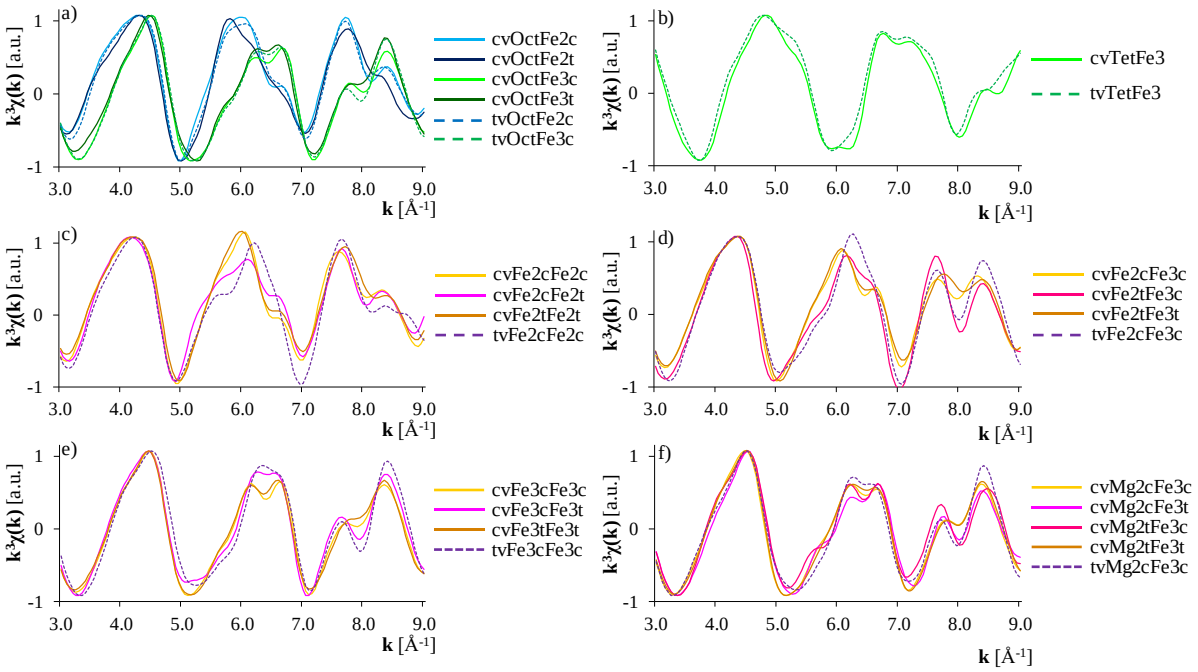

Figure 2. Modelled reference EXAFS spectra of Fe-bearing 2:1 clay minerals. In panel a and b, EXAFS spectra of single iron incorporation in the octahedral[26] and tetrahedral sheet are presented, respectively. Fe–Fe clusters are shown in panel c-e (Fe^{2+}–Fe^{2+} in panel c, Fe^{2+}–Fe^{3+} in panel d, Fe^{3+}–Fe^{3+} in panel e), while Mg^{2+}–Fe^{3+} clusters correspond to panel f. *cv*-model correspond to solid lines, while *tv*-model represented by dashed lines. A more detailed explanation about the panels can be found in Table 1.

Fourteen different EXAFS spectra representing structurally distinct Fe–Fe clusters for *cv*-models were calculated (Figure 2c-e). In general, the spectra of Fe^{2+}–Fe^{2+} clusters (Figure 2c) were similar to the spectrum of a single Fe^{2+} octahedron (individual Fe^{2+}_{cis} or Fe^{2+}_{trans} in the octahedral sheet with short name "cvOctFe2c" and "cvOctFe2t" in Figure 2a). Similarly, the spectra of Fe^{3+}–Fe^{3+} clusters (Figure 2e) showed similarity to the spectrum of a single Fe^{3+} octahedron (individual Fe^{3+}_{cis} or Fe^{3+}_{trans} in the octahedral sheet with short name "cvOctFe3c" and "cvOctFe3t" in Figure 2a). The main sign of the similarity was the matching of the first peak position ($k \sim 4.3\pm0.05$Å^{-1} for Fe^{2+} and $k \sim 4.5\pm0.05$Å^{-1} for Fe^{3+}, respectively). Other features of the EXAFS spectra of the corresponding ionic state (right shoulder at the second and the third oscillation for Fe^{2+}; double-bounced oscillation and left shoulder at the third oscillation for Fe^{3+}) showed very good agreement for Fe^{2+}_{cis}–Fe^{2+}_{cis} and Fe^{2+}_{trans}–Fe^{2+}_{trans} as well as Fe^{3+}_{cis}–Fe^{3+}_{cis} and Fe^{3+}_{trans}–Fe^{3+}_{trans} clustering models, respectively. Although, the shape and the *k* positions of the oscillations for the Fe_{cis}–Fe_{trans} clustering models remained similar, the second and the third oscillations altered. For the Fe^{2+}–Fe^{2+} clusters (Figure 2c), the second oscillation is lower and the right shoulder of it is more characteristic. In the case of Fe^{3+}–Fe^{3+} clusters (Figure 2e), the double-bounced oscillation is more flattened and the left shoulder of the third peak is higher. The spectra of Fe^{2+}–Fe^{3+} (Figure 2d) did not correspond

neither to individual Fe^{2+} ("cvOctFe2c" and "cvOctFe2t" in Figure 2a), nor to individual Fe^{3+} spectra ("cvOctFe3c" and "cvOctFe3t" in Figure 2a). The position of the first oscillation was at $k \sim 4.4 \pm 0.05 Å^{-1}$, while for the second oscillation, it varied around $k \sim 6.2 \pm 0.1 Å^{-1}$ and for the third, double-bounced oscillation the position was at $k \sim 7.70/8.5 Å^{-1}$ (Figure 2d). At the second oscillation, a right shoulder was shown, for which intensity depended on the occupational sites of the cluster. The EXAFS spectra of the *cv*-model with *cis-cis* and *trans-trans* occupational site were similar, while differences in the intensity at the second and the third oscillation could be observed for Fe^{2+}_{trans}–Fe^{3+}_{cis} (Figure 2d). The differences can be explained by the Fe–O–Fe scattering path (Table 1), which occurs only for clusters with different Fe^{2+}_{cis}–Fe^{3+}_{trans} and Fe^{2+}_{trans}–Fe^{3+}_{cis} occupational sites (Figure 1e).

The four EXAFS spectra of the Fe^{3+}–Mg^{2+} clusters for *cv*-model were very similar to the single incorporated ferric iron one (Figure 2f). Only small differences in the high of the double-bounced oscillation at $k \sim 6.30/6.65 Å^{-1}$ and of the third peak's shoulder at $k \sim 7.70 Å^{-1}$ could be observed for Fe^{3+}_{trans}–Mg^{2+}_{cis} and Fe^{3+}_{cis}–Mg^{2+}_{trans} but not for Fe^{3+}_{cis}–Mg^{2+}_{cis} and Fe^{3+}_{trans}–Mg^{2+}_{trans}. The differences (similarly to Fe–Fe clustering) can be explained by the Fe–O–Mg scattering path (Table S1 in Supporting Information 1), which occurs only for clusters with different (Fe^{3+}_{trans}–Mg^{2+}_{cis} and Fe^{3+}_{cis}–Mg^{2+}_{trans}) occupational sites (Figure 1i,j).

The corresponding EXAFS spectra of a single iron atom in the octahedral and tetrahedral position of the *cv*- and *tv*-models agreed well (Figure 2a,b). The second and the third oscillation of the spectra of Fe–Fe and Fe–Mg clusters in the *tv*-model have higher intensities than of the corresponding Fe_{cis}–Fe_{cis} and Fe_{cis}–Mg_{cis} clusters of the *cv*-models, respectively. The EXAFS spectra of Fe–Fe and Fe–Mg clusters in the *tv*-model show higher similarity to the *cv*-models representing Fe_{cis}–Fe_{trans}, Fe_{trans}–Fe_{cis} or Fe_{trans}–Mg_{cis}, Fe_{cis}–Mg_{trans} models as Fe–O–Fe and Fe–O–Mg scattering paths occur in the *tv*-models of these clusters. However, there are also differences between the *cv*- and *tv*-model. The shoulder of the second oscillation for Fe^{2+}–Fe^{2+} clusters appear at the left side of the oscillation, while the shape of the double-bound oscillation for Fe^{3+}–Fe^{3+} clusters is different. In addition, the shoulder at the second oscillation of the Fe^{2+}–Fe^{3+} cluster of the *tv*-model is lacking.

3.2. Distribution of iron in low Fe-content montmorillonites

The measured EXAFS spectra of the Milos– (Mil–), Wyoming– (SWy1–) and two Texas– ($STx1_1$– and $STx1_2$–)montmorillonites were found to be rather similar. However, several sample specific characteristic features can be seen at the second oscillation at $k \approx 6.1/6.6$ Å^{-1} and in the intensity of the left shoulder of the third oscillation (Figure 3). The differences imply distinct iron distribution in the bulk structure for Milos–, Wyoming– and Texas–montmorillonites, while no differences between the two Texas–samples prepared as self-supporting film and pellet ($STx1_1$– and $STx1_2$–) could be observed indicating that texture effects in $STx1_2$–sample can be excluded.

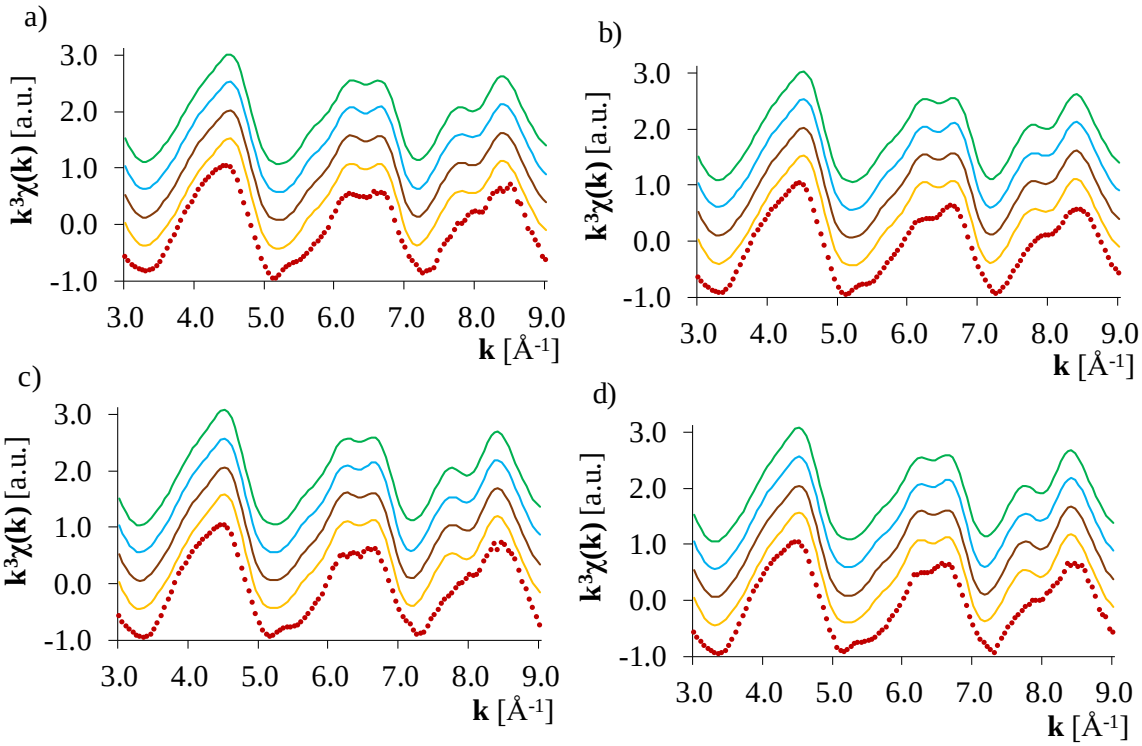

Figure 3. Experimental EXAFS spectra (red dots) with the corresponding fits (solid lines) based on the contributions shown in Table 2. In panel a, Milos-montmorillonite, in panel b, Wyoming-montmorillonite and in panel c-d, Texas- ($STx1_1$– and $STx1_2$–) montmorillonite is shown. "Fit1": yellow; "Fit2": brown; "Fit3": blue "Fit4": green

Table 2. Parameters (contributions [%] and quality [–]) of the EXAFS linear combination fit of distinct smectite models for Mil–, SWy1–, $STx1_1$– and $STx1_2$–montmorillonite

Smectite model name[a]	**Mil** [%]				**SWy1** [%]				**STx1**$_1$ [%]				**STx1**$_2$ [%]			
Fit number[b]	Fit1	Fit2	Fit3	Fit4	Fit1	Fit2	Fit3	Fit4	Fit1	Fit2	Fit3	Fit4	Fit1	Fit2	Fit3	Fit4
cvOctFe2c	<1	<1	<1	1	<1	<1	<1	<1	<1	<1	<1	<1	<1	<1	<1	<1
cvOctFe2t	<1	<1	<1	<1	<1	<1	<1	<1	<1	<1	<1	<1	<1	<1	<1	<1
tvOctFe2c	<1	<1	<1	<1	<1	<1	<1	<1	<1	<1	<1	<1	<1	<1	<1	<1
cvOctFe3c	<1	<1	7	8	16	16	23	21	4	5	10	10	8	7	13	13
cvOctFe3t	20	20	24	31	14	14	24	20	8	6	12	17	6	3	10	15
tvOctFe3c	3	3	8	10	4	4	9	9	7	8	14	15	6	7	12	15
[d]cvFe2cFe2c	<1	<1	<1	—	<1	<1	<1	—	<1	<1	<1	—	<1	<1	<1	—
[d]cvFe2cFe2t	<1	<1	<1	—	<1	<1	<1	—	<1	<1	<1	—	<1	<1	<1	—
[d]cvFe2tFe2t	<1	<1	<1	—	<1	<1	<1	—	<1	<1	<1	—	<1	<1	<1	—
[d]tvFe2cFe2c	<1	<1	<1	—	<1	<1	<1	—	<1	<1	<1	—	<1	<1	<1	—
[d]cvFe2cFe3c	<1	<1	<1	—	<1	<1	<1	—	<1	<1	<1	—	<1	<1	<1	—
[d,e]cvFe2cFe3t	—	—	—	—	—	—	—	—	—	—	—	—	—	—	—	—
[d]cvFe2tFe3c	<1	<1	<1	—	<1	<1	<1	—	<1	<1	<1	—	<1	<1	<1	—
[d]cvFe2tFe3t	6	6	8	—	<1	<1	<1	—	<1	<1	<1	—	<1	<1	<1	—
[d]tvFe2cFe3c	<1	<1	<1	—	<1	<1	<1	—	<1	<1	<1	—	<1	<1	<1	—
[d]cvFe3cFe3c	10	10	14	—	7	7	13	—	11	12	16	—	9	10	13	—
[d]cvFe3cFe3t	2	2	4	—	1	1	4	—	1	2	<1	—	8	10	11	—
[d]cvFe3tFe3t	27	27	32	—	22	22	29	—	23	23	30	—	19	18	24	—
[d]tvFe3cFe3c	3	3	4	—	<1	<1	<1	—	10	12	16	—	9	13	14	—
[d]cvMg2cFe3c	7	7	—	16	13	13	—	18	<1	<1	—	6	2	<1	—	7
[d]cvMg2cFe3t	<1	<1	—	<1	<1	<1	—	<1	<1	<1	—	<1	1	7	—	<1
[d]cvMg2tFe3c	<1	<1	—	<1	<1	<1	—	<1	<1	<1	—	<1	<1	<1	—	<1
[d]cvMg2tFe3t	19	19	—	29	22	22	—	28	21	20	—	29	20	18	—	28
[d]tvMg2cFe3c	<1	<1	—	5	1	1	—	3	12	12	—	21	8	7	—	18
cvTetFe3	<1	—	<1	<1	<1	—	<1	<1	<1	—	1	<1	1	—	3	<1
tvTetFe3	<1	—	<1	<1	<1	—	<1	<1	2	—	<1	3	2	—	<1	5
[b]$\sum Fe^{2+}$	**3**	**3**	**4**	**1**	**<1**	**<1**	**<1**	**<1**	**<1**	**<1**	**<1**	**<1**	**<1**	**<1**	**<1**	**<1**
[b]$\sum Fe^{3+}$	**97**	**97**	**96**	**99**	**100**	**100**	**100**	**100**	**100**	**100**	**100**	**100**	**100**	**100**	**100**	**100**
[c]$\sum Fe_{ordered\ tetrahedron}$	**<1**	**—**	**<1**	**<1**	**<1**	**—**	**<1**	**<1**	**2**	**—**	**1**	**3**	**3**	**—**	**3**	**5**
[c]$\sum Fe_{ordered\ octahedron}$	**94**	**94**	**92**	**95**	**97**	**97**	**96**	**97**	**75**	**74**	**82**	**77**	**70**	**63**	**73**	**77**
[c,d]$\sum$ Fe–Fe cluster	**6**	**6**	**8**	**—**	**2**	**2**	**4**	**—**	**11**	**14**	**17**	**—**	**18**	**22**	**24**	**—**
[c,d]$\sum$ Mg–Fe cluster	**<1**	**<1**	**—**	**5**	**1**	**1**	**—**	**3**	**12**	**12**	**—**	**21**	**9**	**15**	**—**	**18**
[c]$\sum Fe_{cis}$	26	26	35	40	42	42	45	51	46	50	43	51	47	49	58	53
[c]$\sum Fe_{trans}$	74	74	65	60	58	58	55	49	52	50	56	46	50	51	39	43
Q [−]	2.36	2.36	2.40	2.49	2.39	2.39	2.46	2.43	2.68	2.68	2.76	2.80	2.57	2.58	2.62	2.67

[a]Short name of the smectite models are explained in Table 1

[b]"Fit1" corresponds to "best fit", while "Fit2", "Fit3" and "Fit4" are constrained models without tetrahedral iron, Fe–Mg and Fe–Fe pairs, respectively

[c]The results were derived from the raw data written in the first "section" of the table

[d]Only *trans*-vacant (*tv*) and Fe_{cis}–Fe_{trans}, Fe_{trans}–Fe_{cis}, Fe_{trans}–Mg_{cis} and Fe_{cis}–Mg_{trans} from *cis*-vacant (*cv*) structures were considered as Fe–Fe and Fe–Mg clusters, respectively

[e]The spectra of this model was not included in the fit due to fatal error of FEFF run

The linear combination fits to the measured spectra for Mil−, SWy1−, $STx1_1$− and $STx1_2$− montmorillonite using the theoretically calculated ones as basis were performed to obtain a quantitative estimation of the preferential oxidation state and occupational sites of iron as well as the preferred type of the clustering (single Fe tetrahedron and octahedron, Fe–Fe and Fe–Mg clusters). *Cis–cis* and *trans–trans* occupational sites in the *cv*-vacant smectite models (Figure 1d,f,h,k) were considered to be structurally equivalent to individual Fe in the octahedral sheet because the two metal (Fe–Fe or Fe–Mg) ion did not influence each other valence orbital (Table S1 in Supporting Information 1). Thus, for Fe–Fe and Fe–Mg clusters in the *cv*-model, only *cis–trans* and *trans–cis* clusters were explicitly considered (Figure 1e,i,j). In the *tv*-model, Fe–Fe and Fe–Mg substitutions were considered as near neighbor clusters.

The best EXAFS linear combination fits (Figure 3a,c,e,f) indicated that iron is present almost exclusively in the Fe^{3+} form in all montmorillonite type ("Fit1" in Table 2). This result agreed well with the assumption of earlier studies[22,36]. The differences among the samples appeared in the distribution of iron. The results of linear combination fit suggested that iron has ordered distribution in Wyoming−montmorillonite, while in Milos− and Texas− montmorillonites 6–18% of iron takes part in Fe–Fe clusters ("Fit1" in Table 2). Fe–Mg clusters could provide up to 9–12% contribution in Texas−montmorillonites. Octahedral iron is equally distributed between the occupational sites in Wyoming− and Texas−samples, *trans*-site preference occurred only in Milos−montmorillonite ("Fit1" in Table 2). The energy comparison of the *cis*/*trans*-models with similar isomorphic substitutions and iron oxidation states indicated that there is no site preference in bulk smectites (Table 1).

No tetrahedral iron can be found in Milos− or in Wyoming−montmorillonite ("Fit1" in Table 2), furthermore, in $STx1_1$− and $STx1_2$−montmorillonite samples, the very low amount ~1–2% of tetrahedral iron is below the estimated absolute uncertainty (±15%)[37] for the linear combination fit ("Fit1" in Table 2). The results suggested that tetrahedral iron is negligible. To estimate the importance of tetrahedral iron for the fit quality, another fit ("Fit2") with only octahedral iron substitution models was performed for the measured EXAFS data sets. The results indicate that the exclusion of the tetrahedral iron has negligible effect on the fits of Milos− and Wyoming−montmorillonites as their "Fit2" EXAFS spectra (Figure 3a-d) and the corresponding fitting parameters (contribution and quality number) were identical (Table 2) to the previous best fits ("Fit1"). Similar conclusion could be made for Texas−montmorillonite samples as tetrahedral iron models barely influence the shape of the EXAFS spectra (little increment in the left shoulder of the second oscillation) while the quality numbers agree with the best fit results within the uncertainty. The contribution of Fe–Fe and Fe–Mg clustering models in "Fit2" is increased, while small reduction of the individual Fe in the octahedral sheet is observed.

Sensitivity analysis for Fe–Fe and Fe–Mg clustering were determined performing "Fit3" and "Fit4" without Fe–Fe and Fe–Mg pairs, respectively. The quality number of the fits show that the exclusion of Fe–Fe or Fe–Mg pairs from the fitting data set of reference spectra reduces the quality of the fit. In such a constraint fit, the contribution of the excluded clusters are redistributed among the remaining components of the fit. The omission of Fe–Fe pairs has larger effect on Milos– and Texas–samples, while the omission of Fe–Mg pairs shows more significant impact for the Wyoming-sample.

Conventional ("shell-by-shell") P-EXAFS fits were also performed on the Mil–, SWy1– and $STx1_1$–samples (Supporting Information 2). The results revealed that quite a few constrains obtained from *ab initio* calculations (e.g. coordination number of Al, Fe and first O shell, co-varying $CN_{\mathrm{Fe–O/Al/Fe/Si}}(\alpha)$ and α through a polarization parameter are necessary to reduce the number of independent fitting parameters (Supporting Information 2)[57,58]. The conventional P-EXAFS fitting results (Table S1 in Supporting Information 2) agree well with the interatomic distances and coordination numbers of relax structures containing Fe^{3+} (Table S1 in Supporting Information 1). However, the differences present in the P-EXAFS spectra of the three montmorillonite cannot be explained by using the "shell-by-shell" fit approach alone.

The XANES spectra of the different smectite models were also calculated and compared to the measured Milos–, Wyoming– and Texas–montmorillonites (Supporting Information 2). The results show that tetrahedral iron models have very different XANES spectra compared to the four measured spectra (Figure S3,S4 in Supporting Information 2). The measurement results agree well with the calculated XANES spectra containing only octahedral ferric iron (Figure S3,S4 in Supporting Information 2). However, XANES spectra turned out to be very similar for all (Figure S3 in Supporting Information 2).

4. Implication of the structural position of Fe in bulk montmorillonite

This study reveals structural differences in Fe-bearing Milos−, Wyoming− and Texas−montmorillonites. The very distinct EXAFS and XANES spectra of tetrahedral iron indicate that there is no significant amount of tetrahedral iron in low Fe-bearing smectites. Potential presence of tetrahedral iron suggested in earlier studies[5,59] cannot be confirmed on the basis of studied data.

The proportion of Fe–Fe and Fe–Mg clustering in different montmorillonite samples needs separate discussion. Depending on the total number of Fe and Mg substitutions in the sample, there is a finite probability of clusters to form in case of random (e.g. no energetically preferred interaction) distribution of Mg and Fe sites. The positive or negative deviation of EXAFS fitting results from the expectation value for a random distribution of sites will indicate an energy driven preferential cluster formation or avoidance, respectively. The probability of randomly formed cluster was evaluated by Monte Carlo simulation for the given composition of in SWy1−, STx1− and Mil−montmorillonite (Supporting Information 1). Number of Fe–Mg and Fe–Fe clusters estimated for STx1−montmorillonite from the EXAFS fit is significantly larger than the expected value for a random distribution. This result is consistent with data reported by Vantelon et al.[22] and the estimation of lattice energy for cluster formation (Table S2 in Supporting Information 1). For the Mil− and SWy1−montmorillonite, the number of clusters predicted by EXAFS is comparable with the random distribution. Taking into account the modelling uncertainties and intrinsically low amount of Fe and Mg substitutions, no definitive statement about possible slight clustering or avoidance of Fe–Fe and Fe–Mg pair can be made for Mil− and SWy1−montmorillonite based on the fitting results.

The differences in the iron distribution explain the varying Fe uptake behavior of these montmorillonites. Due to the electrostatic repulsion, ferric iron present in Fe^{3+}–Mg^{2+} clusters is a less efficient electron acceptor in the redox reaction than in Fe^{3+}–Fe^{3+} clusters or individual Fe^{3+} in the octahedral sheet. Fe^{3+}–Mg^{2+} clusters could be present in Texas−samples but not in Wyoming−montmorillonite[32]. This would explain the higher redox capacity of SWy1−montmorillonite derived from a wet chemistry and XAS spectroscopy measurement[16]. There might be certain electron small polaron hopping conduction pathways, which assist the oxidative sorption of iron $\left(Fe^{2+}_{aq} \rightarrow Fe^{3+}_{surf}\right)$. Therefore, in addition to the surface specifications (e.g. surface site, protonation scheme, inner-/outer-sphere complex), the effect of cation substitution in the bulk structure should also be studied.

Our investigations had to deal with the challenge of XAS measurements of low iron amount. Although the linear combination fit of the calculated spectra showed very good agreement with Milos−montmorillonite sample, the fit had lower quality for Wyoming− and Texas−montmorillonites. Potential explanation could be the presence of Al^{3+} substitution in the tetrahedral sheet, which were not considered in this study but have an impact on the bulk structure.

5. References

(1) Stucki, J. W.; Goodman, B. A.; Schwertamann, U. *Iron in Soils and Clay Minerals*. Dordrecht, Netherlands, **2012**, pp. 1–3.

(2) Ilgen, A. G.; Kukkadapu, R. K.; Dunphy, D. R.; Artyushkova, K.; Cerrato, J. M.; Kruichak, J. N.; Janish, M. T.; Sun, C. J.; Argo, J. M.; Washington, R. E. Synthesis and Characterization of Redox-Active Ferric Nontronite. *Chem. Geol.* **2017**, *470*, 1–12.

(3) Soltermann, D.; Marques Fernandes, M.; Baeyens, B.; Miehé-Brendlé, J.; Dähn, R. Competitive Fe(II)–Zn(II) Uptake on a Synthetic Montmorillonite. *Environ. Sci. Technol.* **2013**, *48(1)*, 190–198.

(4) Hofstetter, T. B.; Schwarzenbach, R. P.; Haderlein, S. B. Reactivity of Fe(II) Species Associated with Clay Minerals. *Environ. Sci. Technol.* **2003**, *37(3)*, 519–528.

(5) Stucki, J. W. Properties and Behaviour of Iron in Clay Minerals. In *Handbook of Clay Science*; **2006,** *Vol. 1*, pp. 423–475.

(6) Stucki, J. W. A Review of the Effects of Iron Redox Cycles on Smectite Properties. *Comptes Rendus Geosci.* **2011**, *343*, 199–209.

(7) Kerisit, S.; Rosso, K. M. Computer Simulation of Electron Transfer at Hematite Surfaces. *Geochim. Cosmochim. Acta* **2006**, *70(8)*, 1888–1903.

(8) Williams, A. G. B.; Scherer, M. M. Spectroscopic Evidence for Fe(II)–Fe(III) Electron Transfer at the Iron Oxide−Water Interface. *Environ. Sci. Technol.* **2004**, *38(18)*, 4782–4790.

(9) Alexandrov, V.; Rosso, K. M. Insights into the Mechanism of Fe(II) Adsorption and Oxidation at Fe–Clay Mineral Surfaces from First-Principles Calculations. *J. Phys. Chem. C* **2013**, *117(44)*, 22880–22886.

(10) Zarzycki, P.; Kerisit, S.; Rosso, K. M. Molecular Dynamics Study of Fe(II) Adsorption, Electron Exchange, and Mobility at Goethite (α–FeOOH) Surfaces. *J. Phys. Chem. C* **2015**, *119(6)*, 3111–3123.

(11) Gorski, C. A.; Aeschbacher, M.; Soltermann, D.; Voegelin, A.; Baeyens, B.; Marques Fernandes, M.; Hofstetter, T. B.; Sander, M. Redox Properties of Structural Fe in Clay Minerals. 1. Electrochemical Quantification of Electron-Donating and -Accepting Capacities of Smectites. *Environ. Sci. Technol.* **2012**, *46(17)*, 9360–9368.

(12) Manceau, A.; Lanson, B.; Drits, V. A.; Chateigner, D.; Gates, W. P.; Wu, J.; Huo, D.; Stucki, J. W. Oxidation-Reduction Mechanism of Iron in Dioctahedral Smectites: I. Crystal Chemistry of Oxidized Reference Nontronites. *Am. Mineral.* **2000**, *85(1)*, 133–152.

(13) Manceau, A.; Drits, V. A.; Lanson, B.; Chateigner, D.; Wu, J.; Huo, D.; Gates, W. P.; Stucki, J. W. Oxidation-Reduction Mechanism of Iron in Dioctahedral Smectites: II. Crystal Chemistry of Reduced Garfield Nontronite. *Am. Mineral.* **2000**, *85(1)*, 153–172.

(14) Hofstetter, T. B.; Neumann, A.; Schwarzenbach, R. P. Reduction of Nitroaromatic Compounds by Fe(II) Species Associated with Iron-Rich Smectites. *Environ. Sci. Technol.* **2006**, *40(1)*, 235–242.

(15) Neumann, A.; Sander, M.; Hofstetter, T. B. *Redox Properties of Structural Fe in Smectite Clay Minerals*. **2011**, pp. 361–379.

(16) Soltermann, D.; Marques Fernandes, M.; Baeyens, B.; Dähn, R.; Joshi, P. A.; Scheinost, A. C.; Gorski, C. A. Fe(II) Uptake on Natural Montmorillonites. I. Macroscopic and Spectroscopic Characterization. *Environ. Sci. Technol.* **2014**, *48(15)*, 8688–8697.

(17) Guggenheim, S.; Adams, J. M.; Bain, D. C.; Bergaya, F.; Brigatti, M. F.; Drits, V. A.; Formosso, M. L. L.; Galan, E.; Kogure, T.; Stanjek, H. Summary of Recommendations of Nomenclature Committees Relevant to Clay Mineralogy: Report of the Association Internationale Pour l'Etude Des Argiles (AIPEA) Nomenclature Committee for 2006. *Clays Clay Miner.* **2006**, *54(6)*, 761–772.

(18) Stucki, J. W.; Lee, K.; Zhang, L.; Larson, R. A. Effects of Iron Oxidation State on the Surface and Structural Properties of Smectites. *Pure Appl. Chem.* **2002**, *74(11)*, 2081–2094.

(19) Drits, V. A.; McCarty, D. K.; Zviagina, B. B. Crystal-Chemical Factors Responsible for the Distribution of Octahedral Cations over *Trans*- and *Cis*-Sites in Dioctahedral 2:1 Layer Silicates. *Clays Clay Miner.* **2006**, *54(2)*, 131–152.

(20) Wolters, F.; Lagaly, G.; Kahr, G.; Nueesch, R.; Emmerich, K. A Comprehensive Characterization of Dioctahedral Smectites. *Clays Clay Miner.* **2009**, *57(1)*, 115–133.

(21) Gates, W. P.; Slade, P. G.; Manceau, A.; Lanson, B. Site Occupancies by Iron in Nontronites. *Clays Clay Miner.* **2002**, *50(2)*, 223–239.

(22) Vantelon, D.; Montarges-Pelletier, E.; Michot, L. J.; Pelletier, M.; Thomas, F.; Briois, V. Iron Distribution in the Octahedral Sheet of Dioctahedral Smectites. An Fe K-Edge X-Ray Absorption Spectroscopy Study. *Phys. Chem. Miner.* **2003**, *30(1)*, 44–53.

(23) Tsipursky, S. I.; Drits, V. A. The Distribution of Octahedral Cations in the 2:1 Layers of Dioctahedral Smectites Studied by Oblique-Texture Electron Diffraction. *Clay Miner.* **1984**, *19(2)*, 177–193.

(24) Vantelon, D.; Pelletier, M.; Michot, L. J.; Barres, O.; Thomas, F. Fe, Mg and Al Distribution in the Octhaedral Sheet of Montmorillonites. An Infrared Study in the OH^- Bending Region. *Clay Miner.* **2001**, *36*, 360–379.

(25) Gorski, C. A.; Klüpfel, L.; Voegelin, A.; Sander, M.; Hofstetter, T. B. Redox Properties of Structural Fe in Clay Minerals. 2. Electrochemical and Spectroscopic Characterization of Electron Transfer Irreversibility in Ferruginous Smectite, SWa-1. *Environ. Sci. Technol.* **2012**, *46(17)*, 9369–9377.

(26) Gorski, C. A.; Klüpfel, L. E.; Voegelin, A.; Sander, M.; Hofstetter, T. B. Redox Properties of Structural Fe in Clay Minerals: 3. Relationships between Smectite Redox and Structural Properties. *Environ. Sci. Technol.* **2013**, *47(23)*, 13477–13485.

(27) Cashion, J. D.; Gates, W. P.; Riley, G. M. Origin of the Two Quadrupole Doublets in NAu-1 Nontronite. *J. Phys. Conf. Ser.* **2010**, *217(1)*, 012065.

(28) Stucki, J. W.; Golden, D. C.; Roth, C. B. Effects of Reduction and Reoxidation of Structural Iron on the Surface Charge and Dissolution of Dioctahedral Smectites. *Clays Clay Miner.* **1984**, *32(5)*, 350–356.

(29) Fialips, C.-I.; Huo, D.; Yan, L.; Wu, J.; Stucki, J. W. Effect of Fe Oxidation State on the IR Spectra of Garfield Nontronite. *Am. Mineral.* **2002**, *87(5–6)*, 630–641.

(30) Soltermann, D.; Baeyens, B.; Bradbury, M. H.; Marques Fernandes, M. Fe(II) Uptake on Natural Montmorillonites. II. Surface Complexation Modeling. *Environ. Sci. Technol.* **2014**, *48(15)*, 8698–8705.

(31) Neumann, A.; Petit, S.; Hofstetter, T. B. Evaluation of Redox-Active Iron Sites in Smectites Using Middle and near Infrared Spectroscopy. *Geochim. Cosmochim. Acta* **2011**, *75(9)*, 2336–2355.

(32) Rosso, K. M.; Ilton, E. S. Effects of Compositional Defects on Small Polaron Hopping in Micas. *J. Chem. Phys.* **2005**, *122(24)*, 244709.

(33) Finck, N.; Schlegel, M. L.; Dardenne, K.; Adam, C.; Kraft, S.; Bauer, A.; Robert, J.-L. Structural Iron in Smectites with Different Charge Locations. *Phys. Chem. Miner.* **2019**, DOI: 10.1007/s00269-019-01028-y

(34) Soltermann, D.; Marques Fernandes, M.; Baeyens, B.; Dähn, R.; Miehé-Brendlé, J.; Wehrli, B.; Bradbury, M. H. Fe(II) Sorption on a Synthetic Montmorillonite. A Combined Macroscopic and Spectroscopic Study. *Environ. Sci. Technol.* **2013**, *47(13)*, 6978–6986.

(35) Bunau, O.; Joly, Y. Self-Consistent Aspects of X-Ray Absorption Calculations. *J. Phys. Condens. Matter* **2009**, *21(34)*, 345501.

(36) Kéri, A.; Dähn, R.; Krack, M.; Churakov, S. V. Combined XAFS Spectroscopy and *Ab Initio* Study on the Characterization of Iron Incorporation by Montmorillonite. *Environ. Sci. Technol.* **2017**, *51(18)*, 10585–10594.

(37) Churakov, S. V.; Daehn, R. Zinc Adsorption on Clays Inferred from Atomistic Simulations and EXAFS Spectroscopy. *Environ. Sci. Technol.* **2012**, *46(11)*, 5713–5719.

(38) Churakov, S. V. *Ab Initio* Study of Sorption on Pyrophyllite: Structure and Acidity of the Edge Sites. *J. Phys. Chem. B* **2006**, *110(9)*, 4135–4146.

(39) Sainz-Diaz, C. I.; Palin, E. J.; Hernández-Laguna, A.; Dove, M. T. Octahedral Cation Ordering of Illite and Smectite. Theoretical Exchange Potential Determination and Monte Carlo Simulations. *Phys. Chem. Miner.* **2003**, *30(6)*, 382–392.

(40) Sainz-Díaz, C. I.; Timón, V.; Botella, V.; Artacho, E.; Hernández-Laguna, A. Quantum Mechanical Calculations of Dioctahedral 2:1 Phyllosilicates: Effect of Octahedral Cation Distributions in Pyrophyllite, Illite, and Smectite. *Am. Mineral.* **2002**, *87(7)*, 958–965.

(41) CP2K developers group (2002-2018): www.cp2k.org.

(42) VandeVondele, J.; Krack, M.; Mohamed, F.; Parrinello, M.; Chassaing, T.; Hutter, J. QUICKSTEP: Fast and Accurate Density Functional Calculations Using a Mixed Gaussian and Plane Waves Approach. *Comput. Phys. Commun.* **2005**, *167(2)*, 103–128.

(43) Goedecker, S.; Teter, M.; Hutter, J. Separable Dual-Space Gaussian Pseudopotentials. *Phys. Rev. B* **1996**, *54(3)*, 1703–1710.

(44) Krack, M. Pseudopotentials for H to Kr Optimized for Gradient-Corrected Exchange-Correlation Functionals. *Theor. Chem. Acc.* **2005**, *114(1–3)*, 145–152.

(45) VandeVondele, J.; Hutter, J. Gaussian Basis Sets for Accurate Calculations on Molecular Systems in Gas and Condensed Phases. *J. Chem. Phys.* **2007**, *127(11)*, 114105.

(46) Perdew, J. P.; Burke, K.; Ernzerhof, M. Generalized Gradient Approximation Made Simple. *Phys. Rev. Lett.* **1996**, *77(18)*, 3865–3868.

(47) Rollmann, G.; Rohrbach, A.; Entel, P.; Hafner, J. First-Principles Calculation of the Structure and Magnetic Phases of Hematite. *Phys. Rev. B - Condens. Matter Mater. Phys.* **2004**, *69(16)*, 165107.

(48) Liechtenstein, A. I.; Anisimov, V. I.; Zaanen, J. Density-Functional Theory and Strong Interactions: Orbital Ordering in Mott-Hubbard Insulators. *Phys. Rev. B* **1995**, *52(8)*, 5467–5471.

(49) Dudarev, S. L.; Botton, G. A.; Savrasov, S. Y.; Humphreys, C. J.; Sutton, A. P. Electron-Energy-Loss Spectra and the Structural Stability of Nickel Oxide: An LSDA+U Study. *Phys. Rev. B* **1998**, *57(3)*, 1505–1509.

(50) Ankudinov, A. L.; Ravel, B.; Rehr, J. J.; Conradson, S. D. Real-Space Multiple-Scattering Calculation and Interpretation of X-Ray-Absorption near-Edge Structure. *Phys. Rev. B* **1998**, *58(12)*, 7565–7576.

(51) Ankudinov, A. L.; Rehr, J. J. Theory of Solid-State Contributions to the X-Ray Elastic Scattering Amplitude. *Phys. Rev. B* **2000**, *62(4)*, 2437–2445.

(52) Rehr, J. J.; Ankudinov, A.; Ravel, B. *User's Guide, FEFF v.8.40*. Seeattle, USA, **2006**, pp. 66.

(53) Manceau, A.; Chateigner, D.; Gates, W. P. Polarized EXAFS, Distance-Valence Least-Squares Modeling (DVLS), and Quantitative Texture Analysis Approaches to the Structural Refinement of Garfield Nontronite. *Phys. Chem. Miner.* **1998**, *25(5)*, 347–365.

(54) Dähn, R.; Scheidegger, A. M.; Manceau, A.; Schlegel, M. L.; Baeyens, B.; Bradbury, M. H.; Morales, M. Neoformation of Ni Phyllosilicate upon Ni Uptake on Montmorillonite: A Kinetics Study by Powder and Polarized Extended X-Ray Absorption Fine Structure Spectroscopy. *Geochim. Cosmochim. Acta* **2002**, *66(13)*, 2335–2347.

(55) Newville, M. IFEFFIT: Interactive XAFS Analysis and FEFF Fitting. *J. Synchrotron Radiat.* **2001**, *8*, 322–324.

(56) Ravel, B.; Newville, M. ATHENA , ARTEMIS , HEPHAESTUS : Data Analysis for X-Ray Absorption Spectroscopy Using IFEFFIT. *J. Synchrotron Radiat.* **2005**, *12(4)*, 537–541.

(57) Dähn, R.; Baeyens, B.; Bradbury, M. H. Investigation of the Different Binding Edge Sites for Zn on Montmorillonite Using P-EXAFS – the Strong/Weak Site Concept in the 2SPNE SC/CE Sorption Model. *Geochim. Cosmochim. Acta* **2011**, *75(18)*, 5154–5168.

(58) Vespa, M.; Lanson, M.; Manceau, A. Natural Attenuation of Zinc Pollution in Smelter-Affected Soil. *Environ. Sci. Technol.* **2010**, *44(20)*, 7814–7820.

(59) Kaufhold, S.; Stucki, J. W.; Finck, N.; Steininger, R.; Zimina, A.; Dohrmann, R.; Ufer, K.; Pentrák, M.; Pentráková, L. Tetrahedral Charge and Fe Content in Dioctahedral Smectites. *Clay Miner.* **2017**, *52(1)*, 51–65.

6. Supporting Information 1

Structural parameter of the models

Bond length of Fe–O, Fe–Al, Fe–Si, Mg–O, Mg–Al, Mg–Si, Fe–Fe and Fe–Mg were calculated (Table S1) to compare structural differences between the model structures. The average Fe^{2+}–O bond length is ~2.11(±0.03)Å, while the Fe^{3+}–O corresponds ~2.02(±0.03)Å for randomly distributed octahedral iron. Average Fe–O bond distances for Fe^{2+}–Fe^{2+} clusters agree well with randomly distributed Fe^{2+} models. Fe–O bond distances in Fe^{3+}–Fe^{3+} and in Mg^{2+}–Fe^{3+} clusters models are similar to randomly distributed Fe^{3+} models. Fe^{2+}–Fe^{3+} clusters have an average of ~2.06±(0.06)Å Fe–O bond length.

Table S1. Bond length and energy difference of smectite models with iron incorporation derived from the *ab initio* calculations

Short name of the smectite model[a]	Bond length [Å]						Energy difference[f] [kcal/mol]
	Cation[b]–O_{all}[c]	Cation[b]–O[d]	Cation[b]–O_H[e]	Cation[b]–Al	Cation[b]–Si	Cation[b]–Cation[b]	
cvOctFe2c	2.11 ± 0.02	2.12 ± 0.01	2.08 ± 0.02	3.04 ± 0.04	3.23 ± 0.04	—	0.0 ± 5.0
cvOctFe2t	2.11 ± 0.03	2.10 ± 0.03	2.12 ± 0.01	3.04 ± 0.05	3.21 ± 0.07	—	-4.2 ± 5.0
tvOctFe2c	2.10 ± 0.03	2.12 ± 0.02	2.07 ± 0.03	3.03 ± 0.07	3.23 ± 0.06	—	-2.5 ± 5.0
cvOctFe3c	2.02 ± 0.03	2.04 ± 0.01	1.98 ± 0.01	3.07 ± 0.02	3.23 ± 0.04	—	0.0 ± 5.0
cvOctFe3t	2.01 ± 0.01	2.01 ± 0.01	2.01 ± 0.02	3.06 ± 0.04	3.23 ± 0.06	—	0.3 ± 5.0
tvOctFe3c	2.01 ± 0.02	2.02 ± 0.01	2.00 ± 0.01	3.06 ± 0.02	3.23 ± 0.05	—	-5.5 ± 5.0
cvFe2cFe2c	2.11 ± 0.04	2.13 ± 0.01	2.08 ± 0.04	3.03 ± 0.04	3.25 ± 0.04	5.20 ± 0.01	0.0 ± 5.0
cvFe2cFe2t	2.11 ± 0.07	2.15 ± 0.07	2.05 ± 0.07	3.07 ± 0.04	3.27 ± 0.04	2.93 ± 0.01	6.3 ± 5.0
cvFe2tFe2t	2.11 ± 0.02	2.12 ± 0.01	2.09 ± 0.02	3.03 ± 0.03	3.21 ± 0.05	5.27 ± 0.01	-8.5 ± 5.0
tvFe2cFe2c	2.11 ± 0.05	2.12 ± 0.06	2.10 ± 0.03	3.02 ± 0.12	3.26 ± 0.06	3.01 ± 0.01	2.0 ± 5.0
cvFe2cFe3c	2.07 ± 0.03	2.08 ± 0.03	2.04 ± 0.04	3.05 ± 0.04	3.24 ± 0.06	5.20 ± 0.01	0.0 ± 5.0
cvFe2cFe3t	2.06 ± 0.06	2.07 ± 0.04	2.03 ± 0.08	3.05 ± 0.05	3.24 ± 0.06	3.01 ± 0.01	0.7 ± 5.0
cvFe2tFe3c	2.06 ± 0.02	2.08 ± 0.07	2.03 ± 0.08	3.04 ± 0.05	3.23 ± 0.06	3.05 ± 0.01	-4.1 ± 5.0
cvFe2tFe3t	2.06 ± 0.03	2.07 ± 0.03	2.05 ± 0.03	3.03 ± 0.03	3.23 ± 0.06	5.26 ± 0.01	-3.7 ± 5.0
tvFe2cFe3c	2.06 ± 0.04	2.06 ± 0.05	2.05 ± 0.05	3.023 ± 0.08	3.25 ± 0.06	3.07 ± 0.01	-5.8 ± 5.0
cvFe3cFe3c	2.04 ± 0.04	2.04 ± 0.02	1.99 ± 0.02	3.06 ± 0.02	3.23 ± 0.04	5.21 ± 0.01	0.0 ± 5.0
cvFe3cFe3t	2.01 ± 0.03	2.03 ± 0.02	1.99 ± 0.02	3.07 ± 0.03	3.24 ± 0.05	3.07 ± 0.01	0.1 ± 5.0
cvFe3tFe3t	2.02 ± 0.02	2.03 ± 0.02	2.01 ± 0.02	3.06 ± 0.03	3.23 ± 0.06	5.27 ± 0.01	0.1 ± 5.0
tvFe3cFe3c	2.01 ± 0.02	2.01 ± 0.01	2.00 ± 0.02	3.05 ± 0.04	3.24 ± 0.05	3.09 ± 0.01	-6.4 ± 5.0
cvMg2cFe3c	2.05 ± 0.07	2.08 ± 0.05	2.00 ± 0.04	3.05 ± 0.10	3.22 ± 0.04	5.33 ± 0.01	0.0 ± 5.0
cvMg2cFe3t	2.04 ± 0.06	2.05 ± 0.06	2.03 ± 0.08	3.02 ± 0.03	3.20 ± 0.04	3.11 ± 0.01	-0.1 ± 5.0
cvMg2tFe3c	2.05 ± 0.07	2.07 ± 0.07	2.01 ± 0.06	3.04 ± 0.04	3.22 ± 0.03	3.01 ± 0.01	-1.9 ± 5.0
cvMg2tFe3t	2.05 ± 0.03	2.06 ± 0.03	2.02 ± 0.02	3.04 ± 0.04	3.22 ± 0.07	5.24 ± 0.01	-2.9 ± 5.0
tvMg2cFe3c	2.04 ± 0.05	2.04 ± 0.06	2.03 ± 0.02	3.03 ± 0.08	3.23 ± 0.07	3.00 ± 0.01	-6.3 ± 5.0
cvTetFe3	1.86 ± 0.02	1.86 ± 0.02	—	3.29 ± 0.06	3.10 ± 0.10	—	0.0 ± 5.0
tvTetFe3	1.86 ± 0.02	1.86 ± 0.02	—	3.29 ± 0.06	3.11 ± 0.10	—	-7.3 ± 5.0

[a]Short name of the smectite models are explained in Table 1

[b]Cation corresponds to Fe^{2+}, Fe^{3+} or Mg^{2+} depending on the structure

[c]O_{all} corresponds to the all oxygen atoms in the first shell

[d]O corresponds to the oxygen atoms (not member of OH^- groups) in the first shell

[e]O_H corresponds to the oxygen atoms of OH^- groups in the first shell

[f]Energy difference is calculated between structures with same Fe^{2+}, Fe^{3+}, Mg^{2+}, Al^{3+}, O^{2-} and OH^- numbers

The Mg–Fe and Fe–Fe distances had two distinct values: one of 3.0–3.1Å and another of 5.2–5.3Å. The first value are present in clusters of the *tv*-model (Figure 1g,l) as well as in *cis–trans* (and *trans–cis*) clusters of the *cv*-model (Figure 1e,i,j). The larger value corresponds to *cis–cis* or *trans–trans* clustering models of the *cv*-model (Figure 1d,f,h,k). The oxidation states of irons in the clustering models have only low effect on the Fe–Fe distances.

There is no difference in the Fe–Al and the Fe–Si bond length (~3.03±0.05Å and ~3.24±0.05Å) according to the iron ionic state. Furthermore, the distribution scheme (random distribution or clustering), the occupational (*cis*- or *trans*-)site of the iron and the vacancy type (*cv*- or *tv*-) of the smectite do not influence the average bond lengths. The coordination number is always 6.0 for Fe–O, 3.0 for Fe–Al and 4.0 for Fe–Si in models with octahedral iron incorporation. The bond lengths and the coordination number of Fe–O, Fe–Al and Fe–Si in the tetrahedral iron occupational model are very different from the ones with octahedral iron. The structural parameters of the smectite models agree well with earlier modelling and experimental studies[S1–S4].

The energy difference of two distinct model was calculated if the number of the different ions $\left(Fe^{2+}, Fe^{3+}, Mg^{2+}, Al^{3+}, O^{2-}, OH^{-}\right)$ were the same, respectively. The models were classified into seven group representing single Fe^{2+} or Fe^{3+} octahedron, single Fe^{3+} tetrahedron, Fe^{2+}– Fe^{2+}, Fe^{2+}–Fe^{3+}, Fe^{3+}–Fe^{3+} or Fe^{3+}–Mg^{2+} clustering models. (The groups are separated with horizontal lines in Table S1) There is no significant energy differences within the groups confirming that there is no occupational (*cis/trans*) site preference for structural iron.

There is a finite probability to form clusters in the octahedral sheet in case of random (without structural energy preference) distribution of Mg and Fe octahedral sites. The cluster formation probability of randomly distributed substitutions depends on the total concentration of Fe and Mg in the clay layer. To estimate the occurrence probability of Fe–Fe and Fe–Mg and Mg–Mg clusters, the following structural formulae[S2] were used, respectively:

Milos– (Mil–)montmorillonite: $(Si_{7.76}Al_{0.24})\left(Al_{3.00}Mg_{0.54}Fe^{2+}_{0.02}Fe^{3+}_{0.44}\right)Na_{0.79}$

Texas– (STx1–)montmorillonite: $(Si_{7.91}Al_{0.09})\left(Al_{3.12}Mg_{0.75}Fe^{3+}_{0.14}\right)Na_{0.84}$

Wyoming– (SWy1–)montmorillonite: $(Si_{7.73}Al_{0.27})\left(Al_{3.06}Mg_{0.46}Fe^{2+}_{0.03}Fe^{3+}_{0.44}\right)Na_{0.76}$

The cluster formation probability for random distribution of Mg and Fe substitutions was estimated by Monte Carlo (MC) calculations using a supercell with 64 octahedral positions. Studies by Sainz-Díaz et al.[S5,S6] indicated that Mg has a dispersion trend (avoidance of Mg–Mg pairs), thus MC simulations were performed both with and without consideration of Mg–Mg pairs. According to the MC calculations (Table S2), truly random distribution of Mg and Fe substitution shall be resulted in an approximately 1% Fe–Fe pairs and 3% Fe–Mg pairs.

Table S2. Contribution [%] of the Monte Carlo calculations and EXAFS linear combination fit of distinct smectite types for Mil–, SWy1–, STx1–montmorillonite

Clustering	Calculation mode	Mil	SWy1	STx1
Fe–Fe	MC with Mg–Mg pairs	1	1	0
	MC without Mg–Mg pairs	1	1	0
	EXAFS fitting	6	2	11–22
Fe–Mg	MC with Mg–Mg pairs	3	2	1
	MC without Mg–Mg pairs	4	3	1
	EXAFS fitting	0	1	9–15
Mg–Mg	MC with Mg–Mg pairs	2	1	3
	MC without Mg–Mg pairs	—	—	—
	EXAFS fitting	—	—	—

The deviation of EXAFS fitting results from the expected MC random distribution values will indicate preferential clustering or avoidance driven by interatomic interaction energies. The number of Fe–Mg and Fe–Fe clusters estimated for STx1–montmorillonite from the EXAFS fit is significantly larger than the expected value for a random distribution. For Mil– and SWy1–montmorillonite, the number of clusters predicted by EXAFS is comparable with the random distribution. Taking into account the modelling uncertainties and intrinsically low amount of Fe and Mg substitutions, no definitive statement about slight preferential clustering or avoidance of Fe–Fe and Fe–Mg pair can be concluded for Mil– and SWy1–montmorillonite based on the fitting results. Predicted Fe–Fe clustering in STx1–montmorillonites is in close agreement with the results of Vantelon et al.[S2].

References

(S1) Liu, X.; Meijer, E. J.; Lu, X.; Wang, R. *Ab Initio* Molecular Dynamics Study of Fe-Containing Smectites. *Clays Clay Miner.* **2010**, *58(1)*, 89–96.

(S2) Vantelon, D.; Montarges-Pelletier, E.; Michot, L. J.; Pelletier, M.; Thomas, F.; Briois, V. Iron Distribution in the Octahedral Sheet of Dioctahedral Smectites. An Fe K-Edge X-Ray Absorption Spectroscopy Study. *Phys. Chem. Miner.* **2003**, *30(1)*, 44–53.

(S3) Soltermann, D.; Marques Fernandes, M.; Baeyens, B.; Dähn, R.; Miehé-Brendlé, J.; Wehrli, B.; Bradbury, M. H. Fe(II) Sorption on a Synthetic Montmorillonite. A Combined Macroscopic and Spectroscopic Study. *Environ. Sci. Technol.* **2013**, *47(13)*, 6978–6986.

(S4) Manceau, A.; Lanson, B.; Drits, V. A.; Chateigner, D.; Gates, W. P.; Wu, J.; Huo, D.; Stucki, J. W. Oxidation-Reduction Mechanism of Iron in Dioctahedral Smectites: I. Crystal Chemistry of Oxidized Reference Nontronites. *Am. Mineral.* **2000**, *85(1)*, 133–152.

(S5) Sainz-Díaz, C. I.; Timón, V.; Botella, V.; Artacho, E.; Hernández-Laguna, A. Quantum Mechanical Calculations of Dioctahedral 2:1 Phyllosilicates: Effect of Octahedral Cation Distributions in Pyrophyllite, Illite and Smectite. *Am. Mineral.* **2002**, *87(7)*, 958–965.

(S6) Sainz-Diaz, C. I.; Palin, E. J.; Hernández-Laguna, A.; Dove, M. T. Octahedral Cation Ordering of Illite and Smectite. Theoretical Exchange Potential Determination and Monte Carlo Simulations. *Phys. Chem. Miner.* **2003**, *30(6)*, 382–392.

7. Supporting Information 2

P-EXAFS data analysis

The clay samples were measured with polarized extended X-ray absorption structure (P-EXAFS) at four different angles α, which is the angle between the electric field vector (ε) and the layer plane of the self-supporting film (α = 10°; 35°; 55°; 80°). The Fourier transforms (FT) were obtained from the $k^3\chi(k)$ functions between k = 2.5–11.5Å^{-1} using a Kaiser–Bessel window function with an apodization parameter of 1. The amplitude reduction factor was set to S_0^2 = 0.85[SS2,SS3]. All fits were performed in FT^{-1} between 1Å and 3.3Å. The numbers of degrees of freedom in the least-squares refinements were reduced by fitting all P-EXAFS spectra from the same sample together using common values for ΔE_0 (the shift between theoretical and experimental threshold energy), EXAFS distances $(R_{\mathrm{Fe}-j})$, and Debye-Waller factors (σ_j^2). The number of fit parameters was reduced further by co-varying $CN_{j,\alpha}^{\mathrm{EXAFS}}$ and α, through a polarization parameter[SS4,SS5]. The polarization parameters were calculated using β_j angles of 57° for the oxygen shell, 32° for the tetrahedral shell, and 90° for the octahedral shell[SS6,SS7]. Further details of the evaluation are described by Dähn et al.[SS5].

The Fe K-edge $k^3\chi(k)$ P-EXAFS spectra of Mil–, SWy1– and STx1$_1$–samples at four angles have a conspicuous α angular dependence (Figure S1). The intensity of the left shoulder at 5.3Å^{-1} increases with increasing α angle. In addition, the double-bounced oscillation at $k \sim$ 6.1/6.6Å^{-1} in the Milos- and Texas-samples was present at low α angle. The changes in spectral shape as the function of angle α indicate that the anisotropic coordination of Fe (i.e. the coordination environment of iron is oriented with respect to the clay layers)[SS5].

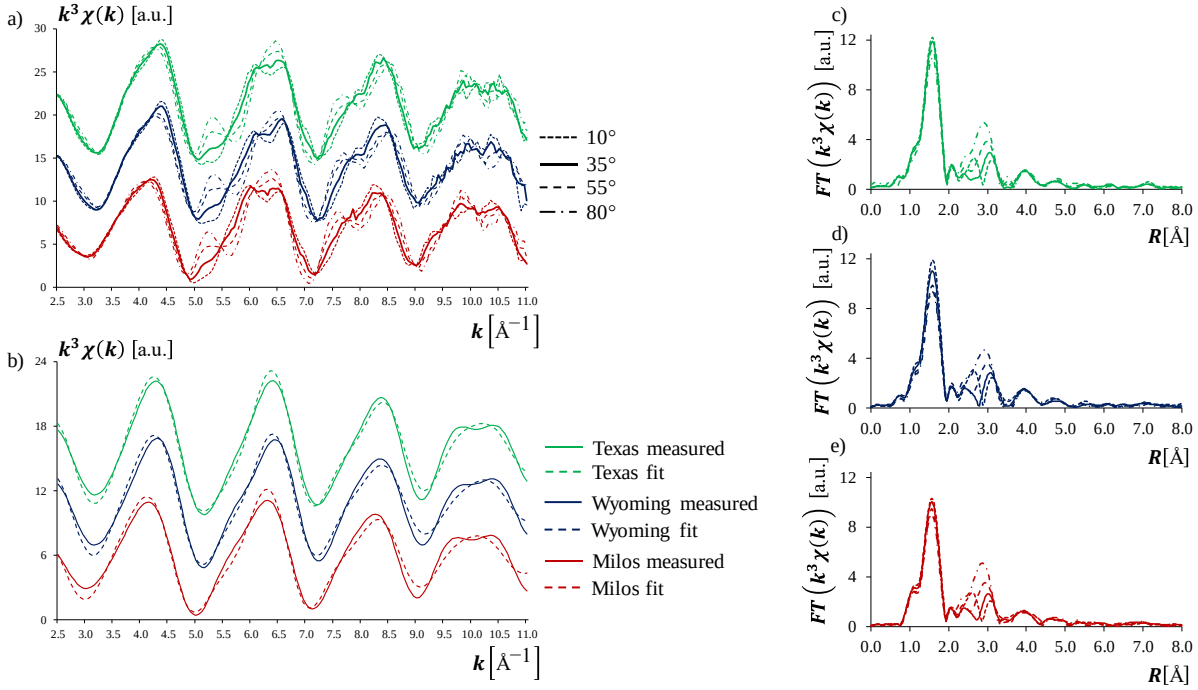

Figure SS1. Fe K-edge P-EXAFS spectra of Milos–, Wyoming– and Texas–montmorillonite (shown with red, blue and green colors, respectively). Panel a) k^3-weighted P-EXAFS measured at four different α angles (10°; 35°; 55°; 80°) of the three montmorillonite samples. Panel b) least-squares fit of FT^{-1} EXAFS data at α = 35° (Fit 3). Panel c-e) the corresponding RSFs of the four α angles of the Texas–, Wyoming– and Milos–sample, respectively.

Three different fits were performed (Table S1). Fit1 constrains the sum of coordination number Al and Fe to be fixed to 3.0. Fit2 fixes the coordination number of Si to 4.0 in addition to the constrain of Fit1. Fit3 specifies the coordination number of the first O shell was fixed to 6.0 additionally to the constrains of Fit1 and Fit2. The interatomic distances (R) and coordination numbers (CN) obtained from the fit of the experimental P-EXAFS spectra measured at α= 35° agree well with the bond length results of relaxed structure calculation (Table S1 in Supporting Information 1) when constrains described in 3) are used. The CN_{Fe}~ 1.5 value indicates the presence of Fe–Fe pairs, however, the Fourier-transformation uniform the experimental P-EXAFS spectra in the q-space erasing differences in the second oscillation (Figure S1b). The radial structure functions (RSFs) of the clay samples (Figure S1c-e) are almost identical indicating very similar bulk structure of Mil-, SWy1- and STx1-samples. Therefore, the distinct amount of Fe-Fe pairs in the bulk structure of Milos-, Wyoming- and Texas-montmorillonite cannot be determined by "shell-by-shell" (conventional) P-EXAFS fitting approach alone.

Table S1. Results from the analysis of P-EXAFS data measured at $\alpha = 35°$

	Structural parameters[a]	Fe–O_1			Fe–Al			Fe–Fe			Fe–Si			Fe–O_2			ΔE_0 [eV]	R_{fact}
		R [Å]	CN [–]	σ^2 [Å^2]	R [Å]	CN [–]	σ^2 [Å^2]	R [Å]	CN [–]	σ^2 [Å^2]	R [Å]	CN [–]	σ^2 [Å^2]	R [Å]	CN [–]	σ^2 [Å^2]		
Mil	Fit1[b]	2.01(1)	4.4(2)	0.004(1)	3.07(5)	0.004(1)	0.003(1)	3.07(2)	0.6(3)[e]	0.003(1)	3.22(1)	2.0(2)	0.003(1)	3.83(1)	4.9(5)	0.005[f]	2.99	0.01
	Fit2[c]	2.00(1)	4.0(4)	0.003(1)	3.16(14)	0.003(1)	0.010(1)	3.16(2)	1.7(2)[e]	0.010(1)	3.21(1)	4.0[f]	0.010(1)	3.82(1)	6.3(5)	0.005[f]	2.21	0.03
	Fit3[d]	2.00(1)	6.0[f]	0.007(1)	3.14(1)	0.007(1)	0.011(1)	3.14(1)	1.5(3)[e]	0.011(1)	3.20(1)	4.0[f]	0.011(1)	3.81(2)	5.8(10)	0.005[f]	1.26	0.02
SWy1	Fit1[b]	2.00(1)	4.2(3)	0.003(1)	3.15(1)	1.6(3)[e]	0.005(1)	3.15(1)	1.4(2)[e]	0.005(1)	3.21(1)	2.2(3)	0.005(1)	3.82(1)	6.3(8)	0.005[f]	6.89	0.02
	Fit2[c]	2.00(1)	4.0(4)	0.003(1)	3.17(3)	1.2(3)[e]	0.011(1)	3.17(3)	1.8(3)[e]	0.011(1)	3.20(1)	4.0[f]	0.011(1)	3.81(2)	7.2(10)	0.005[f]	6.01	0.02
	Fit3[d]	2.00(1)	6.0[f]	0.006(1)	3.15(4)	1.4(4)[e]	0.012(1)	3.15(4)	1.6(4)[e]	0.012(1)	3.19(1)	4.0[f]	0.012(1)	3.80(2)	6.4(11)	0.005[f]	5.33	0.04
STx1	Fit1[b]	2.00(1)	4.8(2)	0.003(1)	3.13(11)	1.6(3)[e]	0.004(1)	3.13(1)	1.4(2)[e]	0.004(1)	3.22(1)	2.3(2)	0.004(1)	3.83(1)	5.9(7)	0.005[f]	7.07	0.01
	Fit2[c]	2.00(1)	4.6(3)	0.003(1)	3.15(13)	1.4(2)[e]	0.010(1)	3.15(2)	1.7(2)[e]	0.010(1)	3.21(1)	4.0[f]	0.010(1)	3.82(1)	7.0(7)	0.005[f]	6.50	0.02
	Fit3[d]	2.00(1)	6.0[f]	0.005(1)	3.13(11)	1.5(3)[e]	0.010(1)	3.13(3)	1.5(3)[e]	0.010(1)	3.21(1)	4.0[f]	0.010(1)	3.81(2)	6.3(9)	0.005[f]	6.00	0.03

[a]Interatomic distance (R), coordination number (CN), Debye-Waller factor (σ^2), shift of the threshold energy (E_0), R-factor

[b]Constrains in Fit1: $CN_{Al} + CN_{Fe} = 3.0$; $\sigma^2_{Al} = \sigma^2_{Fe} = \sigma^2_{Si}$; $\sigma^2_{O_2} = 0.005$

[c]Constrains in Fit2: $CN_{Si} = 4.0$; $CN_{Al} + CN_{Fe} = 3.0$; $\sigma^2_{Al} = \sigma^2_{Fe} = \sigma^2_{Si}$; $\sigma^2_{O_2} = 0.005$

[d]Constrains in Fit3: $CN_{O_1} = 6.0$; $N_{Si} = 4.0$; $CN_{Al} + CN_{Fe} = 3.0$; $\sigma^2_{Al} = \sigma^2_{Fe} = \sigma^2_{Si}$; $\sigma^2_{O_2} = 0.005$

[e]$CN_{Al} + CN_{Fe} = 3.0$

[f]Fixed to the given value

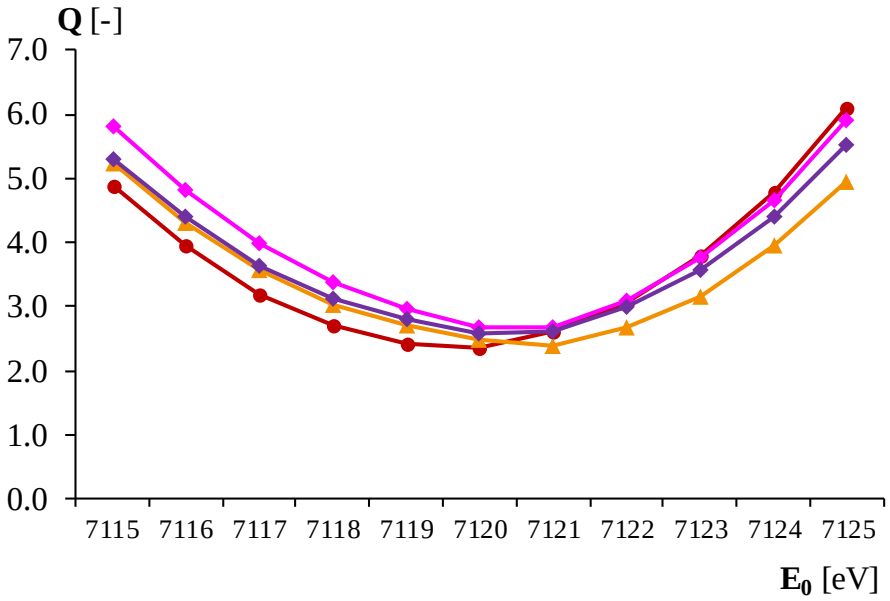

Figure SS2. Quality number (Q_{EXAFS}) derived from the linear combination fits of the calculated EXAFS spectra to the experimental spectra as the function of E_0 edge energy. Red line with dots represents fit to Mil-montmorillonite, orange line with triangles marks fit to SWy-montmorillonite, while pink and purple lines with rhombus show fits to STx_1- and STx_2-montmorillonites. The lines are drawn just to guide the eyes.

XANES calculations and comparison with measurement data

The XANES spectra were calculated based on the coordinates received from geometry optimization calculation of the different smectite models. The XANES spectra were obtained using the density functional theory with the local spin-density approximation (DFT-LSDA) as it is implemented in the FDMNES code[SS8]. They were calculated by the convolution of the electronic DOS with an arctangent weighted Lorentzian as it is defined in the FDMNES software[SS9,SS10]. The convolutional parameters, which characterize the arctangent function (the center and the width of the arctangent function, maximum width at high energy of the final state, the core level width, the Fermi level), were calibrated in our previous paper[SS1,SS8,SS11]. Based on our results, the convolutional parameters were fixed at E_{cent}= 30eV; E_{fermi}= 0eV; E_{larg}= 30eV; Γ_m= 20 eV; Γ_{hole}= 2eV[SS1]. We calculated the spectra for 6.0Å large molecular clusters derived from the relaxed structures of the *ab initio* simulations with self-consistent (SCF) scattering potentials for each atomic configuration. Other parameters were set to the default values[SS11].

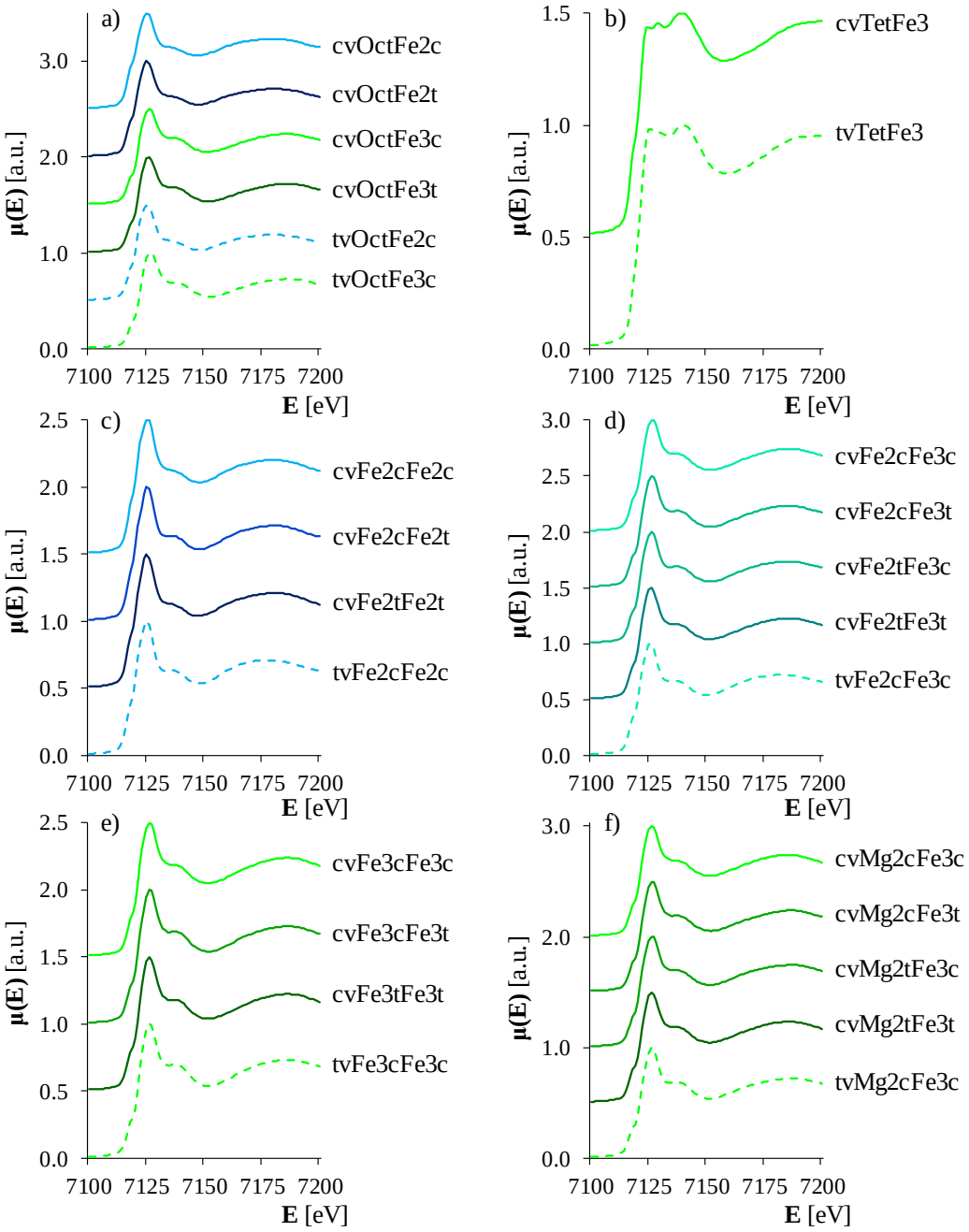

Figure SS3. Modeled XANES spectra of Fe–bearing 2:1 clay minerals. In panel a and b, XANES spectra of single iron incorporation in the octahedral[SS1] and tetrahedral sheet are presented, respectively. Fe–Fe clustering are shown in panel c-e (Fe^{2+}–Fe^{2+} in panel c, Fe^{2+}–Fe^{3+} in panel d, Fe^{3+}–Fe^{3+} in panel e), while Mg^{2+}–Fe^{3+} clustering corresponds to panel f. Blue color represents Fe^{2+}, while Fe^{3+} is marked with green color. Turquoise color in panel d represents mixed Fe^{2+}–Fe^{3+} oxidation state. *Cis*-occupational sites are marked with lighter colors, darker colors show *trans*-occupational sites, while mixed (*cis*–*trans* clustering) are represented with middle-colors, respectively. *cv*-model correspond to solid lines, while *tv*-model represented by dashed lines. A more detailed explanation about the panels can be found in Table 1.

The calculated Fe K-edge XANES spectra for *cv*- and *tv*-model with ferric iron in the tetrahedral sheet as well as Fe^{2+} and Fe^{3+} located in the *cis*- and *trans*-occupational sites in the octahedral sheet were obtained (Figure S3). The spectra of a single Fe^{2+} or Fe^{3+} octahedron are clearly different, although the shape and the peak position of the first edge is very similar (the E_0 edge energy is only 1-2eV smaller for Fe^{2+} than for Fe^{3+}). The height of the right shoulder of the first peak at about 7135eV as well as the second peak at about 7185eV clearly demonstrate the differences between Fe^{2+} and Fe^{3+} (Figure S3a)[SS1]. The oxidation state of iron specify the features of the XANES spectra not only for iron with ordered distribution but also for Fe–Fe and Mg–Fe clusters. The different cation arrangement (randomly distributed iron, Fe–Fe or Mg–Fe clustering) in the octahedral sheet, the smectite vacancy type (*cv*- and *tv*-model) and the structural coordination environment (*cis*- and *trans*-site) seemed to have little effect on the calculated XANES spectra (Figure S3a,c-f). This result agreed well with the small differences in the structural parameters (bond length, coordination number) of the consistent Fe^{2+} and Fe^{3+} incorporated smectite models (Table S1 in Supporting Information 1).

The XANES spectra of the Fe^{3+} tetrahedron in the *cv*- and in the *tv*-model (Figure S3b) were completely different from the model of randomly distributed ferric octahedron (Figure S3a). The first peak is a flattened double peak at about 7125–7140eV without a characteristic right shoulder and the higher second peak is shifted to about 7190eV.

The measurement results agree well with the calculated XANES spectra containing only octahedral ferric iron (Figure S3 and S4). The XANES spectrum of Mil-montmorillonite is shifted to a bit lower energies indicating substantial Fe^{2+} content in its bulk structure (Figure S3), which agrees well with EXAFS fitting results (Table 2). However, measured and calculated XANES spectra turned out to be very similar for all montmorillonite samples (Figure S3).

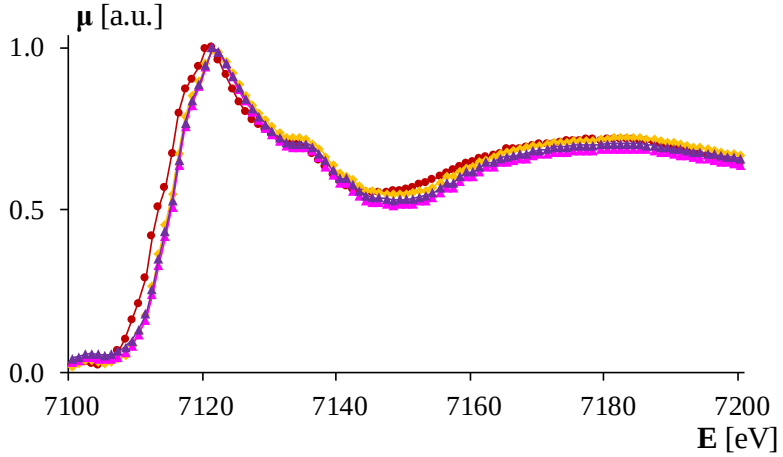

Figure SS4. Experimental XANES spectra. Red color corresponds to Milos–montmorillonite, orange color represents Wyoming–montmorillonite, while pink and purple colors show Texas– ($STx1_1$– and $STx1_2$–)montmorillonites, respectively. The lines of the corresponding colors are only to the guide the eyes.

References

(SS1) Kéri, A.; Dähn, R.; Krack, M.; Churakov, S. V. Combined XAFS Spectroscopy and *Ab Initio* Study on the Characterization of Iron Incorporation by Montmorillonite. *Environ. Sci. Technol.* **2017**, *51(18)*, 10585–10594.

(SS2) Manceau, A.; Chateigner, D.; Gates, W. P. Polarized EXAFS, Distance-Valence Least-Squares Modeling (DVLS), and Quantitative Texture Analysis Approaches to the Structural Refinement of Garfield Nontronite. *Phys. Chem. Miner.* **1998**, *25(5)*, 347–365.

(SS3) Schlegel, M. L.; Manceau, A. Evidence for the Nucleation and Epitaxial Growth of Zn Phyllosilicate on Montmorillonite. *Geochim. Cosmochim. Acta* **2006**, *70(4)*, 901–917.

(SS4) Vespa, M.; Lanson, M.; Manceau, A. Natural Attenuation of Zinc Pollution in Smelter-Affected Soil. *Environ. Sci. Technol.* **2010**, *44(20)*, 7814–7820.

(SS5) Dähn, R.; Baeyens, B.; Bradbury, M. H. Investigation of the Different Binding Edge Sites for Zn on Montmorillonite Using P-EXAFS – the Strong/Weak Site Concept in the 2SPNE SC/CE Sorption Model. *Geochim. Cosmochim. Acta* **2011**, *75(18)*, 5154–5168.

(SS6) Tsipursky, S. I.; Drits, V. A. The Distribution of Octahedral Cations in the 2:1 Layers of Dioctahedral Smectites Studied by Oblique-Texture Electron Diffraction. *Clay Miner.* **1984**, *19(2)*, 177–193.

(SS7) Schlegel, M. L.; Manceau, A.; Charlet, L.; Chateigner, D.; Hazemann, J.-L. Sorption of Metal Ions on Clay Minerals. III. Nucleation and Epitaxial Growth of Zn Phyllosilicate on the Edges of Hectorite. *Geochim. Cosmochim. Acta* **2001**, *65(22)*, 4155–4170.

(SS8) Bunau, O.; Joly, Y. Self-Consistent Aspects of X-Ray Absorption Calculations. *J. Phys. Condens. Matter* **2009**, *21(34)*, 345501.

(SS9) Guda, S. A.; Guda, A. A.; Soldatov, M. A.; Lomachenko, K. A.; Bugaev, A. L.; Lamberti, C.; Gawelda, W.; Bressler, C.; Smolentsev, G.; Soldatov, A. V.; Joly, Y. Optimized Finite Difference Method for the Full-Potential XANES Simulations: Application to Molecular Adsorption Geometries in MOFs and Metal–Ligand Intersystem Crossing Transients. *J. Chem. Theory Comput.* **2015**, *11(9)*, 4512–4521.

(SS10) Amestoy, P. R.; Guermouche, A.; L'Excellent, J.-Y.; Pralet, S. Hybrid Scheduling for the Parallel Solution of Linear Systems. *Parallel Comput.* **2006**, *32(2)*, 136–156.

(SS11) Joly, Y. *FDMNES User's Guide*. Grenoble, France, **2016**.

CHAPTER 5:
Theoretical study:
Iron adsorption on clays inferred from atomistic simulations and XAS spectroscopy

This chapter is a manuscript that is currently in preparation as "Kéri, A.; Dähn, R.; Krack, M.; Churakov, S. V. Iron adsorption on clays inferred from atomistic simulations and XAS spectroscopy."

Abstract

Iron is a ubiquitous redox–active element, which has a substantial impact on the geochemical processes in natural and engineered environments. In soils, clay minerals are the most common sorbents with variable surface structure. Iron is expected to be adsorbed in different structural forms at the edge surfaces of clay minerals. Furthermore, it might be involved in redox-reactions at the clay sites. The accurate description of Fe specialization and the probable oxidative uptake of iron $\left(Fe_{aq}^{2+} \rightarrow Fe_{surf}^{3+}\right)$ by clay minerals is fundamental in the molecular-level understanding of the mechanism. *Ab initio* structure relaxations of several different clay structures with substituted Fe^{2+}/Fe^{3+} in the bulk or at the surface site showed that the oxidative sorption of ferrous iron at the most relevant edge surfaces of Fe-bearing montmorillonite is an energetically favored process. The combination of *ab initio* simulations and X-ray absorption spectroscopy (XAS) demonstrated that not only the oxidation state of Fe determines the speciation, but also the strong/weak-site complexation has different characteristics. The quantitative interpretation of the atomistic modelling based XAS spectra measured on samples with different Fe loadings indicated a particularly complex behavior of Fe. Although, iron is mostly present in Fe^{3+} form, its extent decreases at increasing Fe loadings.

1. Introduction

Clay minerals constitute an important pool in the global iron cycle as they contain structural iron, and they can bind Fe^{2+} (ferrous iron) by surface adsorption[1,2]. Due to the distinctive chemical properties of their surfaces, there is a number of industrial applications (e.g. radioactive waste disposal), where clay minerals can be used as effective constituents of engineered (e.g. bentonite buffer) and geological barriers (e.g. argillaceous rock formation)[3,4]. Structural iron in Fe-bearing clay minerals has an influence on the individual uptake characteristics of ferrous iron[5,6], other transition[7–9] $\left(\text{e.g. } UO_2^{2+}, Tc^{7+}\right)$ and divalent[10] $\left(\text{e.g. } Zn^{2+}\right)$ ions. It is known from wet chemistry and spectroscopic experiments that ferrous iron competes with Zn^{2+} for the limited amount of binding sites of clay minerals[10]. At the same time, strong uptake of Fe traces in excess of other divalent transition metals can be explained by the possible surface-induced oxidation of the Fe^{2+} to Fe^{3+} on clay mineral surfaces[5,6,10]. The extent of the oxidative sorption processes greatly depends on the pH, the concentration of dissolved ferrous iron in the electrolyte as well as the oxidation state and the distribution of structural iron in the clay[5,6,10]. Despite the importance of the iron redox cycle and contaminant immobilization, the exact sorption mechanism of iron on clay minerals remain unclear[11]. A detailed atomistic description of iron surface complexes can ascertain the modelling of metal uptake by clay minerals in the presence of iron.

The structure of smectites can be described as layers of pseudo-hexagonally ordered sheets of alumina octahedral (O) sandwiched between two opposing siloxane tetrahedral (T) sheets (so-called TOT-layer)[12]. Most of the Fe-bearing clay minerals belong to the 2:1 type of dioctahedral smectites in which only two thirds of the possible octahedral positions are occupied[12]. One third of the octahedral sites are *trans*-symmetric and two thirds of the octahedral sites are *cis*-symmetric with respect to the orientation of the hydroxyl (OH^-) groups[12,13]. Montmorillonite is a widespread smectite (e.g. main component of bentonite), and it typically occurs in *cv*-vacant form having both *cis*- and *trans*-occupied sites[14]. The surface of clay minerals is represented by the basal plane (001) and the edges, among which (010) and (110) are the most stable ones[1,15]. While the sorption properties of the basal surface have intensively been studied by atomistic simulations[16], the reactivity of the edge surfaces is less known, because edges are difficult to isolate experimentally and challenging to model atomistically[17]. For instance, edge surfaces of montmorillonite greatly vary in reactivity because of the anisotropy of its structure (the so-called *cis*-like and *trans*-like edge surfaces) [17].

Furthermore, Fe^{2+} may form inner-sphere or outer-sphere complexes, which strongly depends on the ionic strength of ferrous iron in the electrolyte[18]. In the former case, the cation directly binds to the clay surface on one side and to a number of water molecules on the other side, whereas in outer-sphere hydration complexes, the interlayer cation is completely surrounded by water molecules[18]. Outer-sphere complexes are preferentially present at the basal site, while inner-sphere complexes are formed at the edge surfaces. Because of the conceptually different chemical environment, inner- and outer-sphere complexation can easily be differentiated by several spectroscopic techniques (e.g. EXAFS-, Mössbauer-spectroscopy). In the range near to the neutral pH, the sorption of Fe is strongly dominated by inner-sphere surface complexation at the edge sites[10,19,20]. The spectroscopic results indicated two distinct groups of edge surface binding sites[20,21]. The so-called "strong-site" $(\equiv S^{S}OH)$ complexation occur in the continuity of the Al octahedral sheet at the montmorillonite edge sites, while the so-called "weak-site" $(\equiv S^{W}OH)$ complexes show less integrity in the montmorillonite layer[20,21]. A previous *ab initio* simulation suggests that weak sites represent bidentate surface complexes attached to the octahedral sheet, whereas strong-sites correspond to the incorporation of ions at the edge surface[22]. Although, strong/weak-site complexation has different characteristics, the exact coordination environment of the two inner-sphere complexation models is still lacking[21]. In addition, previous studies showed that the sorption of ferrous iron on clay minerals cannot accurately be modeled without considering the redox properties of both the structural iron and the surface complexes[5,10].

It has been demonstrated that *ab initio* based X-ray absorption spectroscopy (XAS) is an efficient tool to interpret complex environmental structures[22–24]. In our recent works, the structural distribution of substituting cations (e.g. amount of Fe–Fe and Mg–Fe clusters) and the preferred oxidation state of iron $(Fe^{2+}/Fe^{3+}$ proportion$)$ in different montmorillonites could be identified[23,24]. Furthermore, a quantitative characterization of Zn uptake processes at the water-clay interface at the atomistic level was achieved[22].

In this work, extended X-ray absorption fine structure (EXAFS) and X-ray absorption near edge structure (XANES) spectra were interpreted using *ab initio* molecular dynamics (MD) simulations based on density functional theory (DFT+U). The linear combination fit of the calculated spectra to the experimental ones allowed for quantifying the proportion of the different sorption process at different environmental conditions.

2. Materials and methods

2.1. Modeling setup

In this study, the two most common edge surfaces of montmorillonite, namely the {110} and the {010} were investigated[25]. In order to neutralize the surface charge, OH^- groups were added manually to the surface[17,26]. The crystallographic (lattice) parameters were fixed during the simulations, while the atomic positions were relaxed. The edge surfaces of (110), $(\bar{1}\bar{1}0)$ and (010), $(0\bar{1}0)$ are not equivalent for the *cis*-vacant polymorphs of montmorillonite in contrast to *trans*-vacant phyllosilicates. To determine the energetically favored position for ferrous and ferric iron, the relaxed structures of single Fe^{2+} and Fe^{3+} incorporation in the octahedral sheet at different (bulk and surface) positions were calculated for the (110), $(\bar{1}\bar{1}0)$ (010) and $(0\bar{1}0)$ edge surfaces (Figure 1a,b). 2·2·2·7=56 different model structures (considering the orientation of the edge surfaces, Fe oxidation state and *cis*/*trans*-occupational sites) were investigated. The composition of the clay platelet in these simulations was $Al_{56}Si_{112}O_{264}(OH)_{88}$. The dimensions of the orthorhombic supercell were $a = 50.0$Å, $b = 20.8$Å, $c = 15.0$Å. Similar to previous works, the cell parameter in the a- and c-direction had larger values to reduce the interaction between the periodic images[22,23,26].

Molecular dynamics (MD) simulations were performed on clay particles representing bidentate inner-sphere Fe complexes to the octahedral sheet at the clay edge surface. Edge sites are usually saturated by chemically adsorbed water molecules[26–28], therefore trajectories from MD calculations were obtained on a single clay particle with water between the edges of clay particles. In this work, the interlayer water between basal planes of clay particles was neglected for the sake of computational efficiency as we primarily focused on Fe complexation at the edge sites of montmorillonite. Water molecules were added until the density of water in the area unoccupied by the clay framework atoms was matching 1.0g/ml.

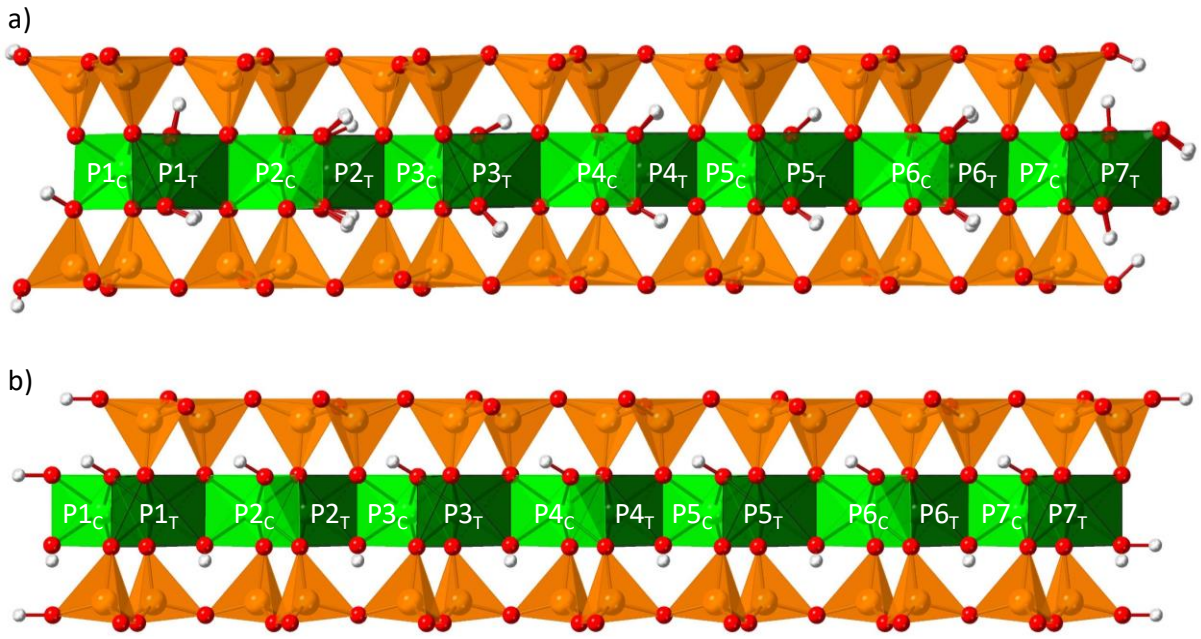

Figure 1. Views of iron substitution models. A single clay particle with (010) and (110) edge surface are shown in panel a and b, respectively. Position of iron substitution are labeled on the octahedral sheet. Alumina octahedra are shown in green, silica tetrahedra are orange, while red and grey colors correspond to oxygen and hydrogen atoms, respectively. *Cis*-octahedra are marked with light green, while dark green color corresponds to *trans*-octahedra. *Cis*- and *trans*-octahedral sites can be distinguished by the different relative position of hydroxyl (OH^-) groups. "P1" positions correspond to *cis*-like, while "P7" to *trans*-like sites.

Two iron atoms with the same oxidation state formed one-one bidentate inner-sphere strong- or weak-site Fe complexes at the two edge sites of the (010) and (110) edges, respectively (Figure 2, Table 1). The total composition of the system in these simulations was $\left[Fe_x^{2+}Fe_y^{3+}Al_{38}Si_{80}O_{184}(OH)_{72}\cdot 144H_2O\right]^{x-}$ for strong-site and $[Al_{40}Si_{80}O_{186}(OH)_{70}]^{2-}\cdot 2\left[Fe_x^{2+}Fe_y^{3+}(OH)_2(H_2O)_2\cdot 136H_2O\right]^{y+}$ for weak-site complexes with constrain $x = 0$ and $y = 2$ or $x = 2$ and $y = 0$, respectively. The cell parameters were fixed at $a = 41.4$Å, $b = 20.8$Å, $c = 10.2$Å values. (c-lattice parameter is a typical interlayer distance for dehydrated smectites[29], while parameter a was chosen large enough to avoid interaction between periodic images).

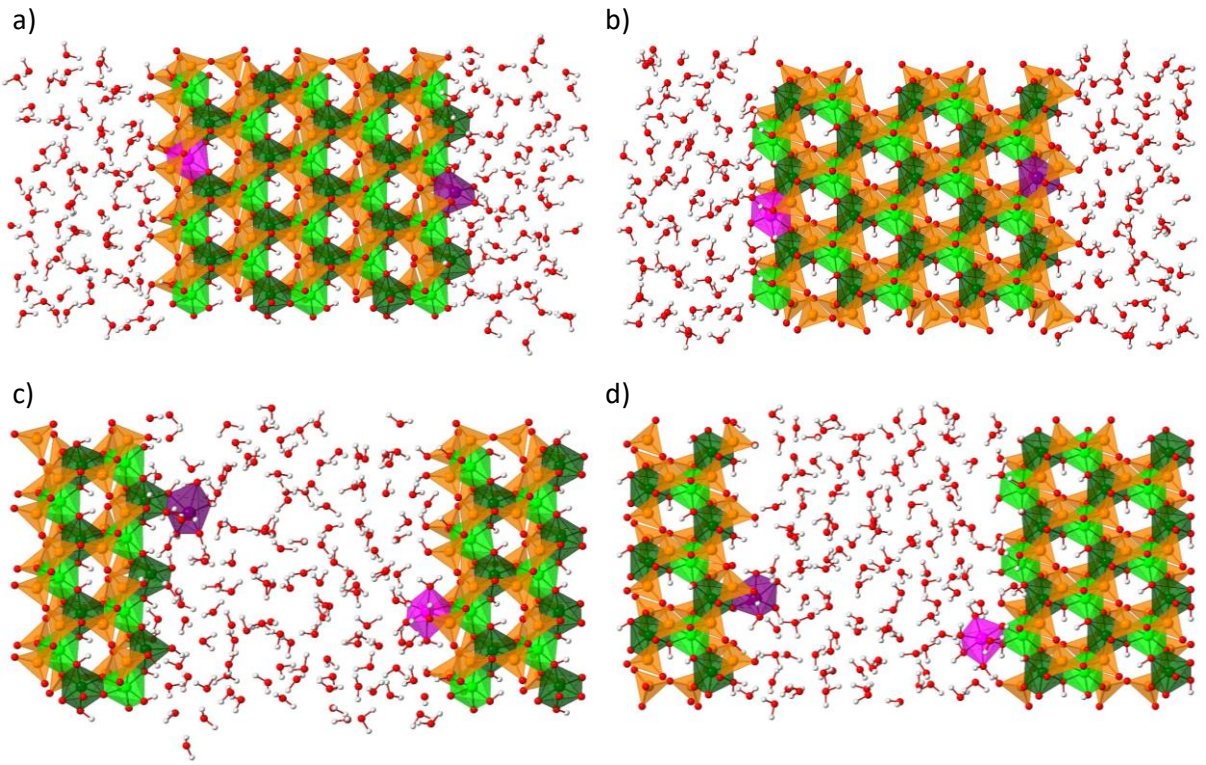

Figure 2. Views of bidentate inner-sphere sorption complexation models. The complexes referred as "strong-site" are shown in panel a and b, while structures shown in panel c and d are referred as "weak-site". In panel a and c, complexes at the (010) edge sites are shown, while view of surface complexes at the (110) edge can be seen in panel b and d. Alumina octahedra are shown in green, silica tetrahedra are orange, iron is marked with pink color, while red and grey colors correspond to oxygen and hydrogen atoms, respectively. The different octahedral occupational sites can be distinguished by the different relative position of hydroxyl (OH^-) groups (*cis*-site is marked with lighter, while *trans*-site is shown with darker colors). A more detailed explanation can be found in Table 1.

Table 1. Bidentate inner-sphere Fe complexation models, associated short names and panels of Figure 2 in which the corresponding model structures are

Edge surface	Inner-sphere complexation model	Oxidation state of iron	Surface site	Short name of the model	Panel in Figure 2
(010)	strong-site	Fe^{2+}	*cis*-like	010cSsFe2	a)
			trans-like	010tSsFe2	
		Fe^{3+}	*cis*-like	010cSsFe3	
			trans-like	010tSsFe3	
	weak-site	Fe^{2+}	*cis*-like	010cWsFe2	b)
			trans-like	010tWsFe2	
		Fe^{3+}	*cis*-like	010cWsFe3	
			trans-like	010tWsFe3	
(110)	strong-site	Fe^{2+}	*cis*-like	110cSsFe2	c)
			trans-like	110tSsFe2	
		Fe^{3+}	*cis*-like	110cSsFe3	
			trans-like	110tSsFe3	
	weak-site	Fe^{2+}	*cis*-like	110cWsFe2	d)
			trans-like	110tWsFe2	
		Fe^{3+}	*cis*-like	110cWsFe3	
			trans-like	110tWsFe3	

2.2. *Ab initio* calculations

The structure relaxations and the molecular dynamics simulations were performed based on the density functional theory (DFT) using the Gaussian plane wave (GPW) method as it was implemented in the QUICKSTEP module of the CP2K code[30–32]. The scalar-relativistic norm-conserving pseudopotentials of Goedecker, Teter and Hutter (GTH)[33,34] were applied to avoid the explicit consideration of the core electrons. The medium-core pseudopotential of iron was composed of a [Ne] core with $3s^2\ 3p^6\ 4s^2\ 3d^6$ as valance electrons. The wave functions of the valence electrons were described by a linear combination of contracted Gaussian-type orbitals using MOLOPT basis sets optimized for the corresponding GTH pseudopotentials[30]. All calculations were performed with a spin polarized implementation of the Perdew, Burke and Ernzerhof (PBE) exchange and correlation functional[35]. An empirical van der Waals (vdW) correction, PBE+D2, has been applied to improve the description of hydrogen bonding[35]. An auxiliary basis set of plane waves up to cutoff energy of 400Ry was employed to expand the electronic density. The exchange and correlation energy was calculated using the exchange-correlation functional of Perdew, Burke and Ernzerhof (PBE)[35]. An empirical van der Waals (vdW) correction PBE+D2 has been applied to improve the description of hydrogen bonding interaction[36]. A sufficiently strict convergence criterion ($\varepsilon_{SCF} = 3 \cdot 10^{-7}$) for the wave function gradients during the self-consistent field (SCF) cycle was enforced ensuring a convergence of the total energy to a similar accuracy. Simulations with single iron in the (tetrahedral or

octahedral) sheet were performed with a multiplicity $(2S+1)_{Fe^{2+}} = 5$ for systems with a single ferrous iron and $(2S+1)_{Fe^{3+}} = 6$ for systems with a single ferric iron, respectively. For models with two iron ions (with the same oxidation state), the multiplicity was set to $(2S+1)_{Fe^{2+}—Fe^{2+}} = (2S+1)_{Fe^{3+}—Fe^{3+}} = 1$.

Conventional DFT is known to underestimate the Coulomb repulsion between the 3*d*-electrons of Fe[37], which results in delocalized 3*d*-electrons. The so-called DFT+U method was applied to improve the description of these states within the DFT formalism[38,39]. This spin-polarized method augments the conventional DFT with a so-called Hubbard term, which applies an additional potential as kind of "penalty function" to the Fe 3*d*-states, selectively. The "penalty function" promotes a localization of the 3*d* electrons. In this semi-empirical approach, the value of the effective Hubbard parameter (U_{eff}) depends on the implementation and has to be calibrated[23]. The calibration for Fe-bearing montmorillonites was performed in our previous paper[23], thus we used a fixed Hubbard-parameter with $U_{eff} = 1.9$eV value.

Structures for MD calculations were first equilibrated for 9ns with 1fs time step within the canonical ensemble (NVT) as it is implemented in the LAMMPS package[40] using the classical force field ClayFF[41]. A Nose-Hoover chain of thermostats with a coupling constant of 10 fs was applied to keep the average temperature at 300K. Long-range electrostatic interactions were calculated by the Ewald summation method.

Afterwards, Born-Oppenheimer *ab initio* molecular dynamics (MD) simulations at the Γ-point (origin of the Brillouin zone) only were performed within the canonical (NVT) ensemble controlled by a stochastic thermostat through velocity rescaling (CSVR)[42] employing an MD time step of 0.5fs. In this way, eight system setups — representing different bidentate Fe complexation (strong/weak-site) with distinct oxidation state (Fe^{2+}/Fe^{3+}) at the two most relevant edge surface $((010)\text{ or }(110))$ sites of montmorillonite taking into account the anisotropy of the edge (*cis*- and *trans*-like) sites — were equilibrated for 4ps at the target temperature of 300K followed by *ab initio* MD production runs of 16ps duration.

2.3. Calculations of EXAFS and XANES spectra

The XAS spectra were obtained for each sorption model configuration based on the DFT+U MD simulations. 320 spectra for each model were calculated based on the snapshots retrieved from the MD trajectories separated by 50fs (i.e. 100 MD) time steps. All spectra belonging to the same model were then averaged in order to account for statistical and thermal disorder, straightforwardly.

The EXAFS spectra were calculated based on real space multiple scattering theory as it is implemented in the FEFF 8.40 code[43]. Multi-scattering paths up to eight legs with path lengths up to 7.0Å were taken into account. For each atomic configuration, the scattering potential of the atoms were calculated self-consistently[43,44] The radius of the cluster for self-consistent full multiple scattering calculations was set to 5.0Å. The amplitude reduction factor (S_0^2) was set to 1.0. The default values were adopted for the remaining parameters[45]. All calculated and measured spectra were normalized to the value of the first oscillation.

The XANES spectra were obtained using the density functional theory with the local spin-density approximation (DFT-LSDA) as it is implemented in the FDMNES code[46]. For each atomic configuration derived from the MD trajectories, the eDOS were first calculated with a 6.0Å cluster radius. The scattering potentials of the atoms were calculated self-consistently (SCF) with 6.0Å SCF radius. The XANES spectra were then obtained by a convolution of the eDOS with an arctangent weighted Lorentzian as it is defined in the FDMNES code[30,33]. The convolutional parameters, which characterize the arctangent function (the center and the width of the arctangent function, maximum width at high energy of the final state, the core level width, the Fermi level), were calibrated in our previous paper[23]. Based on these results[23], the convolutional parameters were fixed at E_{cent}= 30 eV; E_{fermi}= 0 eV; $\mathrm{E_{larg}}$= 30 eV; Γ_{m}= 20 eV; Γ_{hole}= 2 eV. The other input parameters were set to their default values[33]. The calculated XANES spectra also served as the basis for the interpretation of the experimental data after max-min normalization.

The calculated XAS spectra served as the basis for the qualitative and quantitative interpretation of the experimental data. The linear combination fit of the calculated EXAFS and XANES spectra served as a basis in the quantitative interpretation of experimental ones. Quantitative comparison were performed based on the quality of the fit as it is defined in Equation (1), respectively[22,23].

$$Q_{\mathrm{EXAFS}} = \left(k^3 \sum_i \left(a_i^2 \chi_i(k) \right) - \chi^{\mathrm{exp}}(k) \right)^2 + \sum_i a_i^2 \rightarrow \min \qquad (1)$$

where $\chi_i(k)$ are the calculated and $\chi^{\mathrm{exp}}(k)$ is the experimental EXAFS spectra, a_i^2 are the optimized fitting parameters.

The term $\sum_i a_i^2$ was included in the objective functions to reduce the noise of the fit. The fittings were limited to the interval of EXAFS spectroscopy to $k\left[\mathrm{Å}^{-1}\right] \in [3.0,9.0]$ to avoid mislead of noise. The fit was accepted as "best fit" (Fit1) if the indicator of quality number (Q_{EXAFS}) was the lowest.

2.4. XAFS experiments

The experimental XAS spectra evaluated in the present modelling study were taken from Baeyens et al.[47]. The EXAFS samples consisted of a synthetic iron free montmorillonite (IFM)[48,49] equilibrated for 1 week with different Fe^{2+} concentrations at pH 7 in 0.1M NaCl. The resulting Fe loadings were 6; 9; 18; 37mmol/kg respectively. Sample preparation, phase separation as well as the transfer of the wet clay pastes into the sample holders took place inside an anoxic glovebox under controlled N_2 atmosphere ($O_2 < 0.1$ppm). Further preparation procedures were similar as described by Soltermann et al.[49]. Once removed from the glovebox, the samples were immediately flash-frozen in LN2 and stored in an LN2 dewar to prevent sample oxidation. After transport to the Rossendorf Beamline at ESRF (Grenoble, France), the samples were individually removed from the LN2 dewar and transferred to a closed-cycle He cryostat operating at 10K for the XAS measurements. Measurements at 15K protect samples from oxidation and improve signal quality by reducing thermal contributions. The XAS spectra were collected in fluorescence mode at the Fe K-edge (7112.0eV) using a 13-element high-purity Ge solid state detector (Canberra) with digital signal analysis (XIA XMap). The polychromatic synchrotron beam was monochromatized using a pair of water-cooled Si(111) crystals, and higher-order harmonics were rejected by a Si mirror. Individual XAS scans were energy-calibrated against a simultaneously measured Fe foil, corrected for fluorescence dead time and averaged using SIXpack[50], while subsequent data reduction steps and shell fits were conducted using WinXAS[51].

3. Results and discussion

3.1. Preferred position of Fe^{2+} and Fe^{3+} in montmorillonite

The preferred position of Fe^{2+} and Fe^{3+} in the octahedral sheet of a clay layer was determined by comparing the total energies of the different iron incorporation models. Ferrous and ferric iron might preferentially be incorporated in the bulk ("P2-P6" positions in Figure 1) or at the surface ("P1" and "P7" positions in Figure 1). First, the preferred protonation schemes for the two idealized edge surfaces were determined. The total energies for the relaxed structures of the (010) and (110) edge configurations with different morphology were calculated and compared (Figure 3 and Table 1). The models with the lowest energy show a similar protonation scheme as found by White and Zelazny[52] for the 2:1 type dioctahedral clay at an almost neutral pH of ~7.5. Furthermore, the results of the energetic calculations indicated that there is a ~1.9kcal/mol/$Å^2$ surface energy difference between the (010) and (110) edge for the most stable models (Table 2) that controls the abundance of the surface. However, it should not have any effect on the relative stability of edge surface models with distinct Fe incorporation.

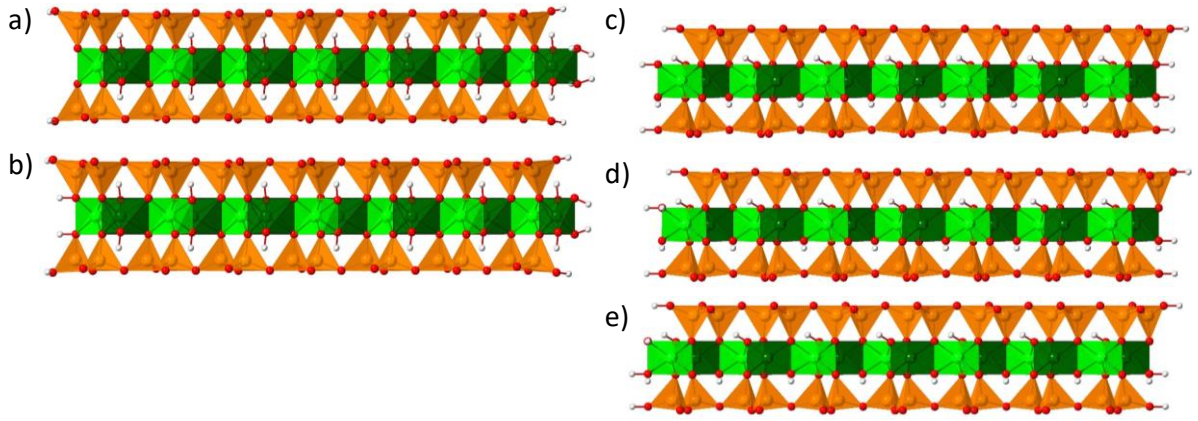

Figure 3. Different protonation schemes for the most relevant edge surfaces of montmorillonite. In panel a-b, (010) edge site is shown, while (110) edge surface present in panel c-e. The relative energy values of the models are present in Table 2. Alumina octahedra are shown in green, silica tetrahedra are orange, while red and grey colors correspond to oxygen and hydrogen atoms, respectively. *Cis*-octahedra are marked with light green, while dark green colors correspond to *trans*-octahedra. *Cis*- and *trans*-octahedral sites can be distinguished by the different relative position of the hydroxyl (OH^-) groups (*cis*-site is marked with lighter, while *trans*-site is shown with darker colors).

Table 2. Relative surface energies of the different protonation schemes plotted in Figure 3

Edge surface	Panel in Figure 3	Relative surface energy[a] [kcal/mol/Å^2]
(010)	a)	0.00
	b)	0.34
(110)	c)	-0.30
	d)	-2.43
	e)	-2.48

[a]The energies of the models are relative to the one's plotted in Figure 3a

The montmorillonite models are finite size structures with non-equivalent edge sites since there is a distinct number of oxygen ions and protons at the *cis*- and *trans*-like surface positions ("P1" and "P7" in Figure 1). To fulfill the electrostatic periodic boundary conditions, a finite interior electric field over the width of the layer evolves. A montmorillonite layer thus can be imagined as a surface dipole capacitor with a linearly decreasing/increasing potential difference in between. The explained effect is more remarkable for ferrous iron since an extra charge arising from the replacement of Al^{3+} by Fe^{2+} should be moved in the potential field.

To determine the preferred position(s) of ferrous/ferric iron in the octahedral sheet of a clay layer, the energies (Figure 4) of the (010) and (110) edge surface models with Fe^{2+} and Fe^{3+} incorporation at distinct positions were calculated as a difference relative to the energy of a structurally incorporated iron ("P4" in Figure 1), respectively. The observed monotonous trend in the relative energies of the related surface models with Fe^{2+}/Fe^{3+} incorporation is an artefact caused by the finite system size and the periodic boundary conditions. The extent of the substantive surface interaction effect can be calculated if a correction is performed considering that bulk positions ("P2-P6" in Figure 1) are equivalent. A linear fit of the energy values at bulk "P2"-"P6" positions is shown in Figure 4. The deviation from that linear fit at each position is displayed in Figure 5.

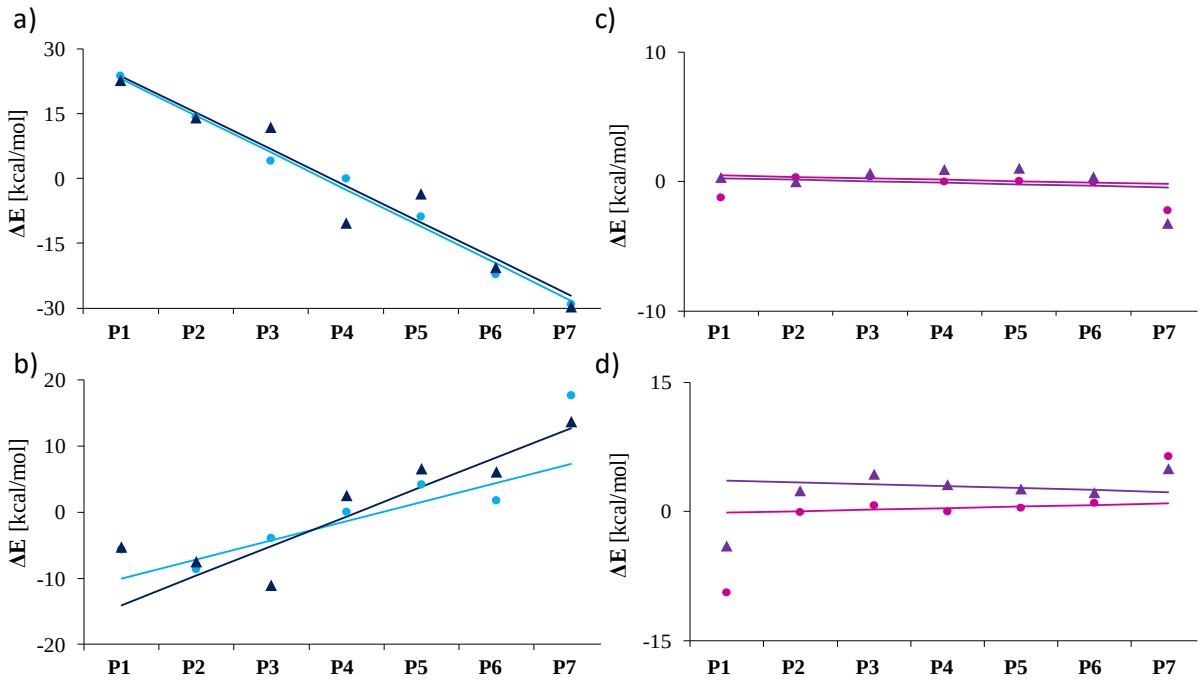

Figure 4. Relative energy of montmorillonite edge surface structures with ferrous (panel a and b) and ferric (panel c and d) iron incorporation at different octahedral positions, respectively. Diagrams in panel a and c show relative energies of (010) edge sites, while diagrams in panel b and d correspond to (110) edge surface. The energy values are calibrated for each model to middle bulk position ("P4"). The lines are linear fits to the calculated "P2-P6" energy values. Fe_{cis} is marked with lighter colors, while darker color correspond to iron at the *trans*-site. Positions of iron (e.g. "P1", "P2") are marked in Figure 1.

The relative energies for iron substitution corrected for finite size effects and the surface dipole in the periodic boundary conditions are summarized in Figure 5. The relative energies of models with ferrous iron incorporation show no clear trend (Figure 5a,b). (010) edge surface models with ferrous incorporation have the lowest energy when Fe^{2+} is at the "$P3_C$" or at the "$P4_T$" positions (Figure 5a), however, other bulk positions (e.g. "$P3_T$", "$P4_C$") have much

higher energies. The repeated *ab initio* calculations indicated that the uncertainty of the energies is about 7kcal/mol. This relatively high value implies that bulk positions for Fe^{2+} are equivalent despite the relatively high standard deviation. Furthermore, the average energy of the models with bulk Fe^{2+} incorporation has similar value as the structure with ferrous iron incorporation at the *cis*- and *trans*-like sites. The variance of the energy values for the (110) edge surface models with Fe^{2+} is also high (Figure 5b) but they also agree well within the uncertainty (7kcal/mol). In this case, however, both surface sites ("P1", "P7") have a higher energy than the average of the bulk ("P2"-"P6"). This trend indicates that Fe^{2+} prefers bulk octahedral positions in a montmorillonite layer with (110) edge surface.

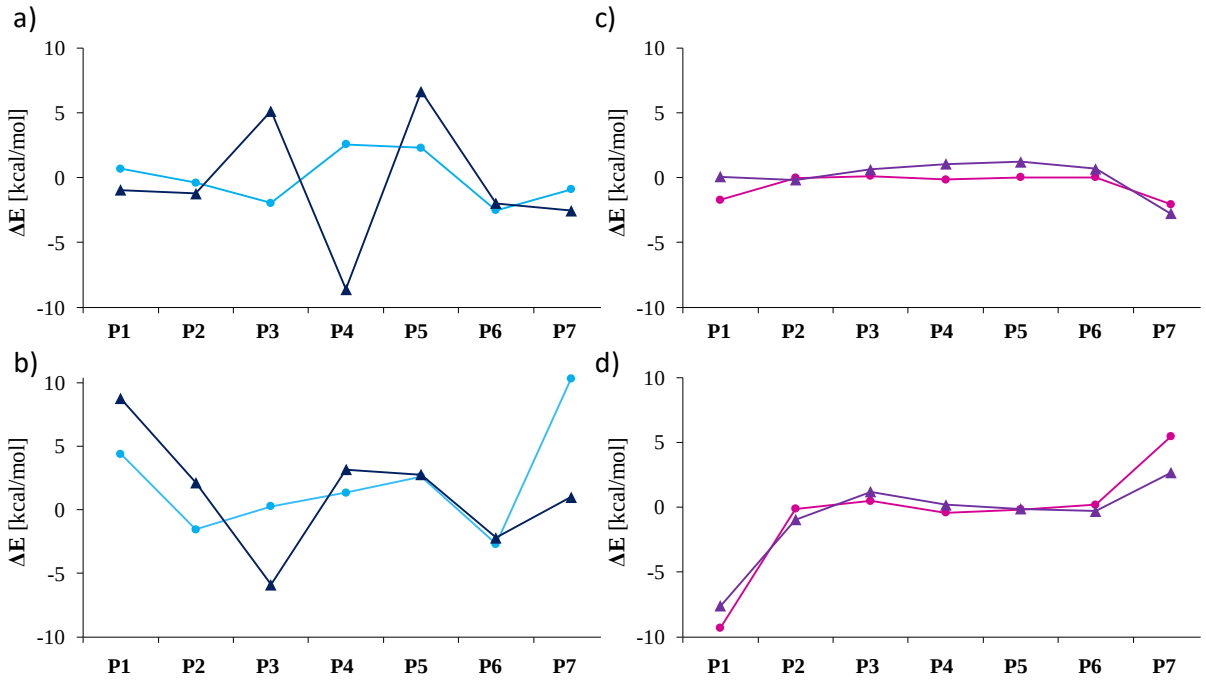

Figure 5. Relative energy for different structural position of Fe in montmorillonite structures with ferrous (panel a and b) and ferric (panel c and d) iron corrected for finite size effects, surface dipole and periodic boundary conditions. Diagrams in panel a and c show relative energies of (010) edge sites, while diagrams in panel b and d correspond to (110) edge surface. Fe_{cis} is marked with lighter colors, while darker color correspond to iron at the *trans*-site. Fe^{2+} and Fe^{3+} positions (e.g. "P1", "P2") are marked in Figure 1. Original energy values are plotted in Figure 4. The lines are drawn just to guide the eyes.

The results are more conspicuous for ferric iron. The transformed relative energies of the different iron incorporation models indicate that bulk positions are equivalent. There is no preferential occupational (*cis/trans*-)site. The energy for the (010) clay edge surface models with ferric iron incorporation (Figure 5c) at the "P2"-"P6" positions are equal to structures where Fe^{3+} occupies a surface site position ("P1" or "P7"). Ferric iron prefers a *cis*-like edge site of a montmorillonite layer with (110) edge surface as the corresponding model structure is energetically much more favorable than bulk positions ("P2"-"P6") or *trans*-like site ("P7").

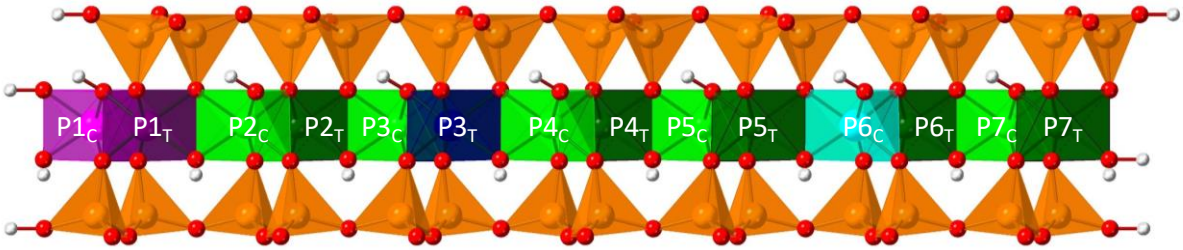

Figure 6. Preferred position for ferrous (blue color) and ferric (pink color) iron in the octahedral sheet of a montmorillonite particle with according to energetic calculations (Figure 5). Alumina octahedra are shown in green, silica tetrahedra are orange, ferrous iron is marked with blue, ferric iron with pink color, while red and grey colors correspond to oxygen and hydrogen atoms, respectively. *Cis*-octahedral positions are marked with light colors, dark colors correspond to *trans*-octahedra. *Cis*- and *trans*-octahedral sites can be distinguished by the different relative position of hydroxyl (OH^-) groups (*cis*-site is marked with lighter, while *trans*-site is shown with darker colors).

The preferred positions of Fe^{2+} and Fe^{3+} in the octahedral sheet of a montmorillonite layer indicate that the iron oxidation at the surface and the reduction in the bulk is energetically favored for the (110) edge surface (Figure 6), while such a trend is not observed for the (010) edge site. A polarization effect (the energy difference between *cis*- and *trans*-like sites) indicates a leaching of Fe^{3+} at "P7" position and its precipitation at the "P1" position. The transformed relative energy values cannot prove oxidative sorption and leaching process for clay structures with (010) edge surface as energies for these models are almost equal.

The performed *ab initio* calculations did not address the thermodynamics of the redox reaction, which depends on many environmental factors (e.g. Fe loading). In addition, iron may form weak-site inner-sphere complexes (Figure 2c,d) at the edge surfaces of the clay layer. A direct energy comparison for the strong- and weak-site models is challenging because of the different number of (e.g. Al, O, H) atoms in the modelled structures (Figure 2). The comparison of experimental and *ab initio* based XAS spectra is a promising approach to quantitatively determine the different uptake processes at the clay-water interface and to directly investigate the influence of different experimental factors (e.g. Fe concentration in the electrolyte), which are demanding to simulate.

3.2. EXAFS spectra

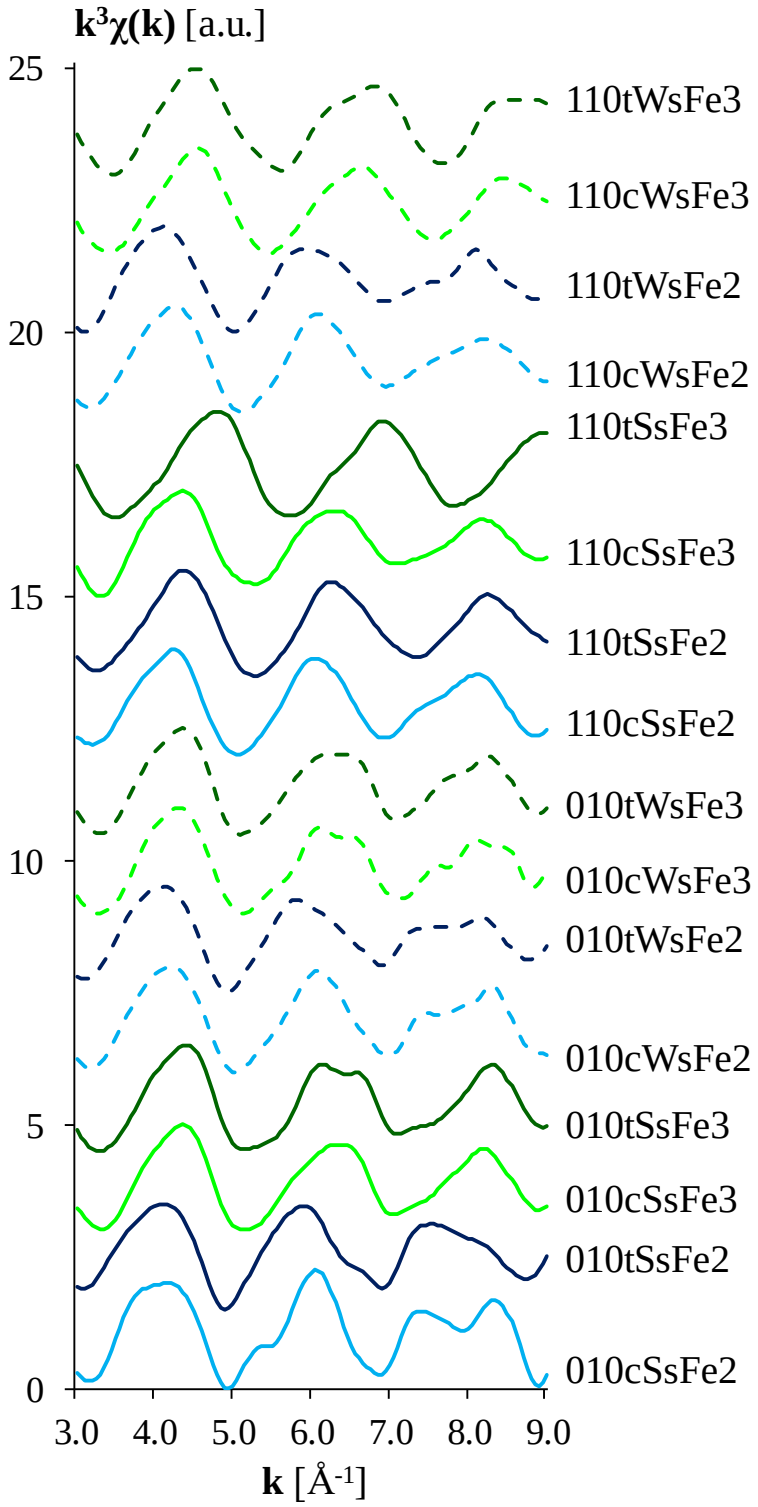

Figure 7. Theoretical EXAFS spectra of montmorillonite edge surface models representing different Fe uptake mechanisms. Blue color corresponds to Fe^{2+}, while green color indicates Fe^{3+} surface complexes. EXAFS spectra with solid lines show strong-site, while dashed lines represent weak-site complexation models. Based on the legend, a more detailed explanation can be found in Table 1.

The calculated Fe K-edge EXAFS spectra of a montmorillonite layer with Fe^{2+} or Fe^{3+} bidentate inner-sphere (strong- or weak-site) complexes at the *cis*- and *trans*-like site of the (010) and (110) edge surface were obtained, respectively. The calculated EXAFS spectra for ferrous and ferric iron are clearly different (Figure 7). The most conspicuous difference between the EXAFS spectra with distinct ionic state was a slight shift in the first oscillation at $k \sim (4.10\text{-}4.25)/(4.35\text{-}4.55)$ Å^{-1}. A similar shift is present at the second oscillation $k \sim (5.70\text{-}6.3)$ Å^{-1} for ferrous iron, $k \sim (6.0\text{-}7.0)$ Å^{-1} for ferric iron. Further differences between the Fe complexation models are difficult to distinguish based on their EXAFS spectra.

The measured EXAFS spectra of the four montmorillonite samples with increasing (from 6mmol/kg to 37mmol/kg) iron loadings were found to be rather similar, however, a few, sample specific features can be distinguished (Figure 8). The second oscillation shifts to lower k values (from $k \sim 6.6$ Å^{-1} to $k \sim 6.2$ Å^{-1}) for increasing Fe loadings (Figure 8). In addition, there is a significant shape difference in the third oscillation of EXAFS spectra (double-bounced or single oscillation with right shoulder) below and above ~30mmol/kg of iron loading (Figure 8). To quantitatively estimate the effect of the iron loading on the preferred Fe oxidation state and uptake mechanism, linear combination fits for the measured four EXAFS spectra using the theoretical spectra retrieved from the 16 *ab initio* MD trajectories were performed (Figure 8, Table 3).

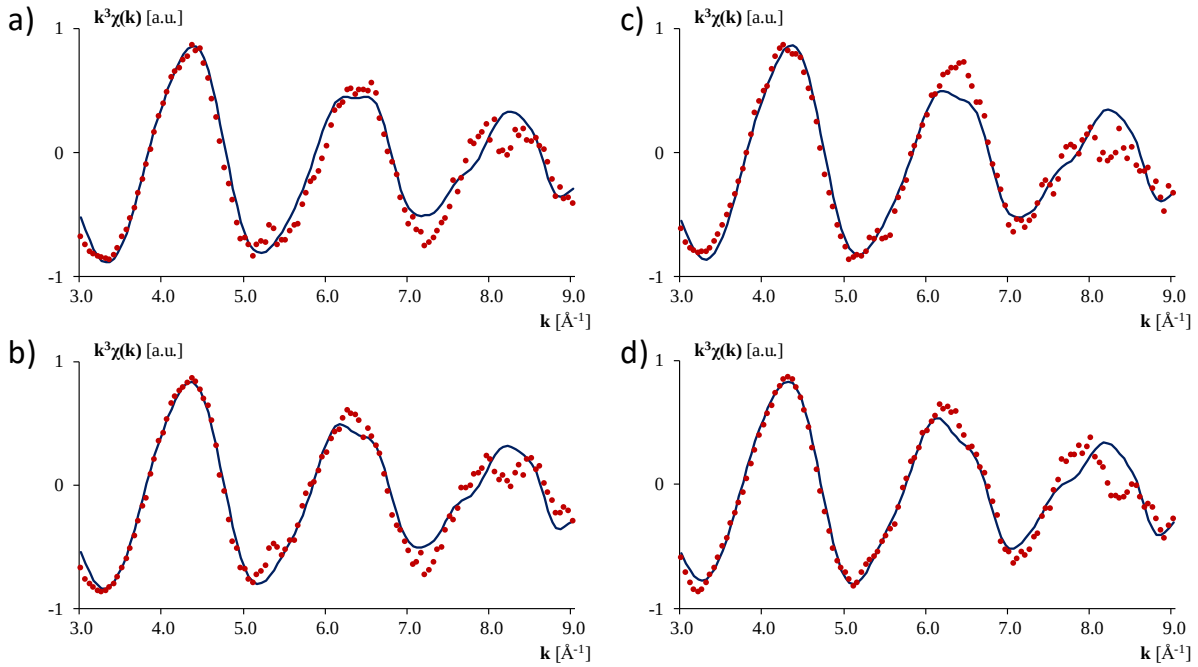

Figure 8. Experimental EXAFS spectra (red dots) with the corresponding best fits (solid lines) based on the contributions summarized in Table 3. In the panels, the measured EXAFS spectra were collected from montmorillonite samples at different Fe loadings (panel a: 6mmol/kg; panel b: 9mmol/kg; panel c: 17mmol/kg; panel d: 37mmol/kg).

Table 3. Parameters (contributions [%] and quality [–]) of the EXAFS linear combination fit of distinct smectite models for montmorillonite samples with different Fe loadings

Short name of the model[a]	**Fe loading** [mmol/kg] 6	9	18	37
010cSsFe2	<1	<1	<1	<1
010tSsFe2	<1	<1	<1	10
010cSsFe3	19	8	16	8
010tSsFe3	<1	<1	<1	<1
010cWsFe2	<1	<1	<1	9
010tWsFe2	6	<1	11	4
010cWsFe3	<1	41	<1	<1
010tWsFe3	4	22	5	2
110cSsFe2	<1	<1	<1	<1
110tSsFe2	<1	11	<1	<1
110cSsFe3	33	<1	32	32
110tSsFe3	24	4	27	22
110cWsFe2	<1	10	10	12
110tWsFe2	<1	<1	<1	<1
110cWsFe3	14	4	<1	<1
110tWsFe3	<1	<1	<1	<1
[b]$\sum \mathbf{Fe^{2+}}$	6	21	20	35
[b]$\sum \mathbf{Fe^{3+}}$	94	79	80	65
[b]$\sum \mathbf{Fe_{Ss}}$	76	70	74	73
[b]$\sum \mathbf{Fe_{Ws}}$	24	30	26	27
[b,c]$\sum \mathbf{Fe^{2+}_{Ss}}$	<1	<1	<1	10
[b,c]$\sum \mathbf{Fe^{2+}_{Ws}}$	6	21	20	25
[b,c]$\sum \mathbf{Fe^{3+}_{Ss}}$	76	70	74	63
[b,c]$\sum \mathbf{Fe^{3+}_{Ws}}$	18	8	5	2
Q [-]	3.36	2.76	3.53	3.01

[a]Short name of the smectite models are explained in Table 1

[b]The results were derived from the raw data written in the first "section" of the table

[c]The results are plotted in Figure 9

The qualitative comparison with the theoretically calculated EXAFS spectra indicates a change in the preferred oxidation state and in the uptake mechanism. The linear combination fits of the measured and calculated EXAFS spectra show that iron is mostly present in Fe^{3+} form at the strong-sites (Table 3), however, its extent is decreasing at increasing Fe loadings (Figure 9). Fe^{3+}_{Ws} exhibits a similar trend, while the extent of ferrous iron gradually increases (Table 3, Figure 9) at higher iron loadings. The results indicate that more iron is sorbed in the Fe^{2+} oxidation state at higher Fe loadings (Table 3). The proportion of the weak- and strong-site sorption mechanism remains constant (~30%:70%).

The differences between the fitted and measured EXAFS spectra can be detected, for example, at the second oscillation in Figure 8c and generally at third oscillation. The deviations can be explained by the relatively low iron loadings inducing higher background noise. The shape difference in the third oscillation of EXAFS spectra (double-bounced or single oscillation with right shoulder) below and above ~30mmol/kg of iron loading (Figure 8c,d) could not accurately be modelled. It might indicate the increased impact of outer-sphere complexation, which was not considered in the modelling.

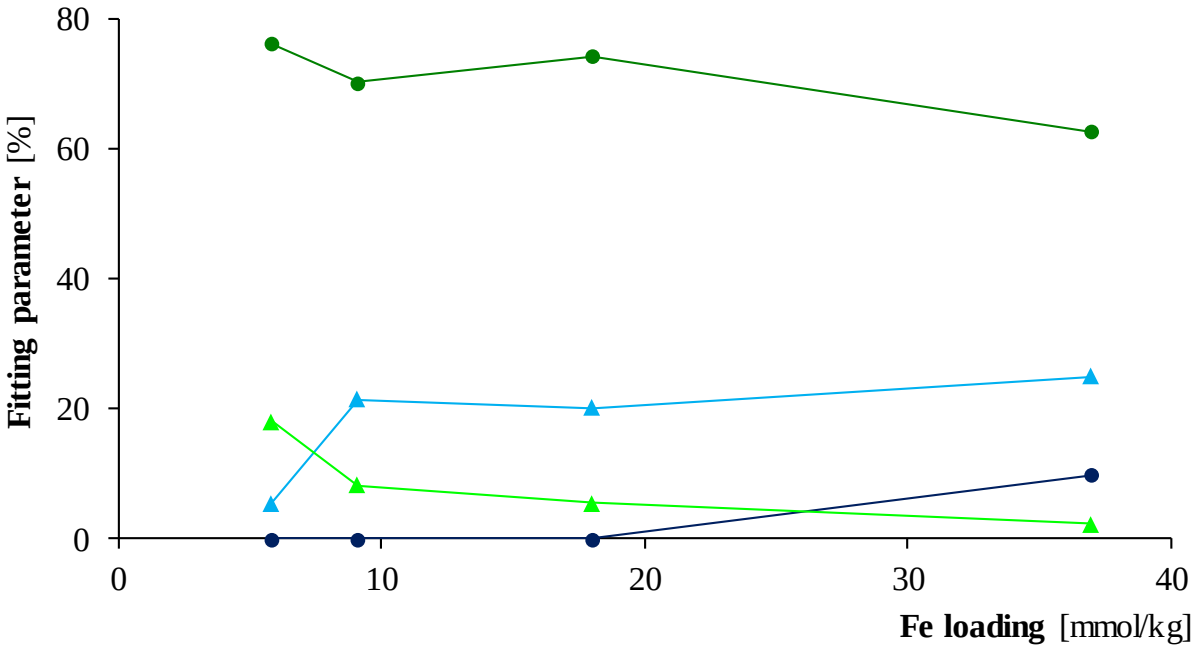

Figure 9. Contribution of the different calculated EXAFS spectra to the measured ones as the function of sorbed Fe amount. Green color represents Fe^{3+}, blue color shows Fe^{2+}. Darker colors and circles correspond to iron sorption at the strong site, while lighter colors and triangles show weak site sorption processes.

3.3. XANES spectra

XANES spectra of the 16 different uptake models were calculated and compared to measured spectra. The spectra of strong-site sorption models are clearly different from weak-site models as $\equiv S^{S}OH$ spectra have a sharper edge than $\equiv S^{W}OH$ complexes. The spectra of the "010tWsFe2" and "010tWsFe3" models show a conspicuous variation with a flattened out edge peak at about 7125–7135eV indicating perceivable structural differences (Figure 10). The shape of these two models allows the water molecules to almost completely surround the surface species, while other weak-site complexes ("010cWsFe2", "010cWsFe3", "110cWsFe2","110cWsFe3","110tWsFe2","110tWsFe3") have silica nearby (Figure 2). The spectra of ferrous and ferric iron surface complexes are similar, only the peak position of the first edge as well as the height of the right shoulder at about 7140eV show slight alteration (Figure 10). The quantitative interpretation of the modelled XANES spectra with measurement results would be difficult to interpret due to unremarkable differences between calculated ones.

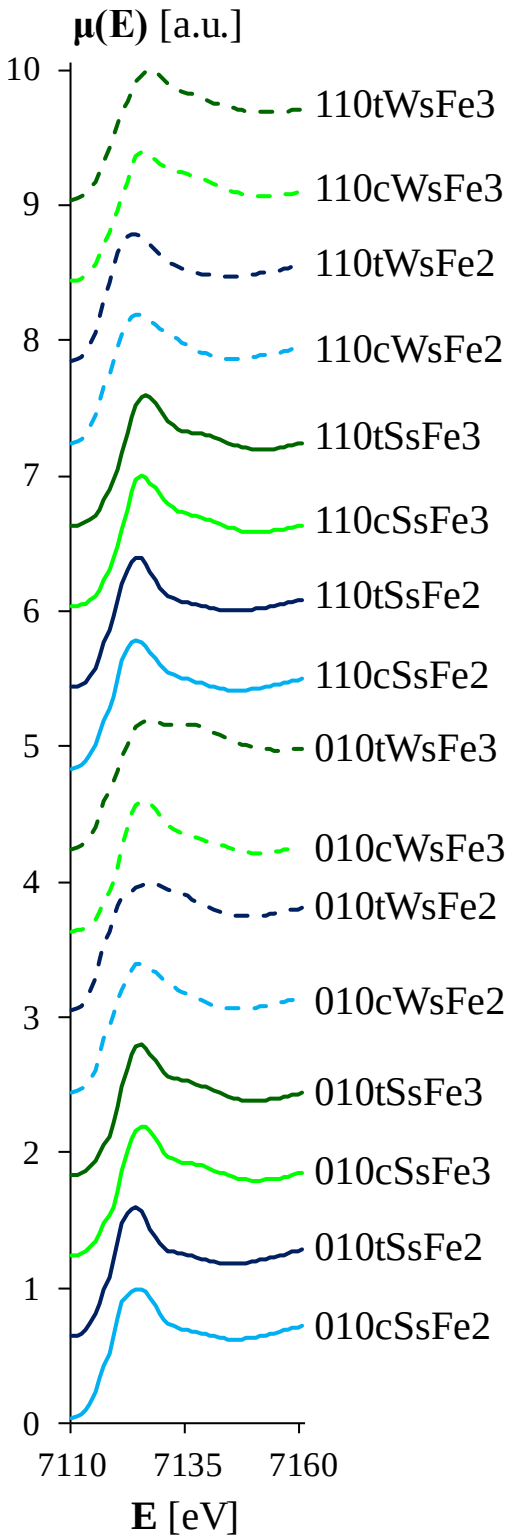

Figure 10. Theoretical XANES spectra of montmorillonite edge surface models representing different Fe uptake mechanism. Blue color corresponds to Fe^{2+}, while green color indicates Fe^{3+} complexes. XANES spectra with solid lines show incorporation of iron in the octahedral sheet, while dashed lines represents XANES spectra of inner-sphere complexes. A more detailed explanation can be found in Table 1.

4. Implication of the oxidative sorption of iron by montmorillonite

This *ab initio* study could confirm that the oxidative sorption of Fe^{2+} at the most relevant edge surface of montmorillonite is an energetically favored process. The result indicates that an electron transfer from the surface to the bulk should occurs. Rosso et al. demonstrated similar oxidative sorption processes at the edge surface of iron-oxides (e.g. hematite[53]), clay minerals (e.g. nontronite[54]) and micas[55] with high Fe-content happens. Furthermore, they calculated the kinetics of the of charge transport in the different minerals[54,56,57]. The interplay of the different electron transfer processes as Fe^{2+}/Fe^{3+} valence interchange between nearest-neighbor iron atoms via a small polaron hopping mechanism was determined and simulated. In addition, the impact of several structural defect on the electron transfer was described.

The combination of atomistic simulations and XAS spectroscopy on samples with different Fe loading showed that the sorbed amount of iron has an impact on the efficiency on the oxidative iron uptake. At higher Fe loading, larger quantities of ferrous iron remain in this oxidation state, since all possible electron donors are consumed. It explains that although strong-site Fe^{3+} complexes are present in the highest amount at the edge surface site, its extent is decreasing. In this study, iron free montmorillonite (IFM) without structural Fe^{3+} was investigated, which give rise to speculation about the possible electron donor. As no Fe^{3+} is present in the clay lattice of IFM, other reactive surface sites on IFM might induce the electron transfer between sorbed Fe^{2+} species and the clay particles[49,58]. The process may play a crucial role in the long-term mineralogical alteration of smectites into non-swelling phyllosilicates that are challenging to study experimentally. Future studies should aim a more complete description including the Fe^{2+}/clay redox cycle and the oxidative uptake mechanisms of Fe^{2+} on montmorillonite.

5. References

(1) Stucki, J. W. Properties and Behaviour of Iron in Clay Minerals. In *Handbook of Clay Science*; **2006,** *vol. 1*, pp. 423–475.

(2) Stucki, J. W.; Lee, K.; Zhang, L.; Larson, R. A. Effects of Iron Oxidation State on the Surface and Structural Properties of Smectites. *Pure Appl. Chem.* **2002**, *74(11)*, 2081–2094.

(3) Karnland, O.; Olsson, S.; Nilsson, U. *Technical Report TR-06-30: Mineralogy and Sealing Properties of Various Bentonites and Smectite-Rich Clay Materials*; Stockholm, Sweden, **2006**.

(4) Leupin, O. X.; Birgersson, M.; Karnland, O.; Korkeakoski, P.; Sellin, P.; Mader, U.; Wersin, P. *Technical Report 14-12: Montmorillonite Stability under near-Field Conditions*; Wettingen, Switzerland, **2014**, vol. 14–12.

(5) Soltermann, D.; Marques Fernandes, M.; Baeyens, B.; Dähn, R.; Joshi, P. A.; Scheinost, A. C.; Gorski, C. A. Fe(II) Uptake on Natural Montmorillonites. I. Macroscopic and Spectroscopic Characterization. *Environ. Sci. Technol.* **2014**, *48(15)*, 8688–8697.

(6) Soltermann, D.; Baeyens, B.; Bradbury, M. H.; Marques Fernandes, M. Fe(II) Uptake on Natural Montmorillonites. II. Surface Complexation Modeling. *Environ. Sci. Technol.* **2014**, *48(15)*, 8698–8705.

(7) Skomurski, F. N.; Ilton, E. S.; Engelhard, M. H.; Arey, B. W.; Rosso, K. M. Heterogeneous Reduction of U^{6+} by Structural Fe^{2+} from Theory and Experiment. *Geochim. Cosmochim. Acta* **2011**, *75(22)*, 7277–7290.

(8) Ilton, E. S.; Haiduc, A.; Moses, C. O.; Heald, S. M.; Elbert, D. C.; Veblen, D. R. Heterogeneous Reduction of Uranyl by Micas: Crystal Chemical and Solution Controls. *Geochim. Cosmochim. Acta* **2004**, *68(11)*, 2417–2435.

(9) Peretyazhko, T.; Zachara, J. M.; Heald, S. M.; Jeon, B. H.; Kukkadapu, R. K.; Liu, C.; Moore, D.; Resch, C. T. Heterogeneous Reduction of Tc(VII) by Fe(II) at the Solid-Water Interface. *Geochim. Cosmochim. Acta* **2008**, *72(6)*, 1521–1539.

(10) Soltermann, D.; Marques Fernandes, M.; Baeyens, B.; Miehé-Brendlé, J.; Dähn, R. Competitive Fe(II)–Zn(II) Uptake on a Synthetic Montmorillonite. *Environ. Sci. Technol.* **2013**, *48(1)*, 190–198.

(11) Bleam, W. F. Atomic Theories of Phyllosilicates' Quantum Chemistry, Statistical Mechanics, Electrostatic Theory, and Crystal Chemistry. *Rev. Geophys.* **1993**, *31(1)*, 51–73.

(12) Guggenheim, S.; Adams, J. M.; Bain, D. C.; Bergaya, F.; Brigatti, M. F.; Drits, V. A.; Formosso, M. L. L.; Galan, E.; Kogure, T.; Stanjek, H. Summary of Recommendations of Nomenclature Committees Relevant to Clay Mineralogy: Report of the Association Internationale Pour l'Etude Des Argiles (AIPEA) Nomenclature Committee for 2006. *Clays Clay Miner.* **2006**, *54(6)*, 761–772.

(13) Drits, V. A.; McCarty, D. K.; Zviagina, B. B. Crystal-Chemical Factors Responsible for the Distribution of Octahedral Cations over *Trans*- and *Cis*-Sites in Dioctahedral 2:1 Layer Silicates. *Clays Clay Miner.* **2006**, *54(2)*, 131–152.

(14) Kaufhold, S.; Kremleva, A.; Krüger, S.; Rösch, N.; Emmerich, K.; Dohrmann, R. Crystal-Chemical Composition of Dicoctahedral Smectites: An Energy-Based Assessment of Empirical Relations. *ACS Earth Sp. Chem.* **2017**, *1(10)*, 629–636.

(15) Liu, X.; Meijer, E. J.; Lu, X.; Wang, R. First-Principles Molecular Dynamics Insight into Fe^{2+} Complexes Adsorbed on Edge Surfaces of Clay Min. *Clays Clay Miner.* **2012**, *60(4)*, 341–347.

(16) Churakov, S. V.; Liu, X. Quantum-Chemical Modelling of Clay Mineral Surfaces and Clay Mineral–surface–adsorbate Interactions. In *Surface and Interface Chemistry of Clay Minerals* (Eds.: Schoonheydt, R., Johnston, C. T., Bergaya, F.), **2018**, pp. 49–87.

(17) Bickmore, B. R.; Rosso, K. M.; Nagy, K. L.; Cygan, R. T.; Tadanier, C. J. *Ab Initio* Determination of Edge Surface Structures for Dioctahedral 2:1 Phyllosilicates: Implications for Acid-Base for Reactivity. *Clays Clay Miner.* **2003**, *51(4)*, 359–371.

(18) Brigatti, M. F.; Galan, E.; Theng, B. K. G. Structures and Mineralogy of Clay Minerals. In *Handbook of Clay Science* (Eds.: Bergaya, F., Theng, B. K. G., Lagaly, G.), **2006**, *vol. 1*, pp. 19–86.

(19) Bradbury, M. H.; Baeyens, B. A Mechanistic Description of Ni and Zn Sorption on Na-Montmorillonite Part II: Modelling. *J. Contam. Hydrol.* **1997**, *27(3–4)*, 223–248.

(20) Bradbury, M. H.; Baeyens, B. Modelling the Sorption of Mn(II), Co(II), Ni(II), Zn(II), Cd(II), Eu(III), Am(III), Sn(IV), Th(IV), Np(V) and U(VI) on Montmorillonite: Linear Free Energy Relationships and Estimates of Surface Binding Constants for Some Selected Heavy Metals and Actinide. *Geochim. Cosmochim. Acta* **2005**, *69(4)*, 875–892.

(21) Dähn, R.; Baeyens, B.; Bradbury, M. H. Investigation of the Different Binding Edge Sites for Zn on Montmorillonite Using P-EXAFS – the Strong/Weak Site Concept in the 2SPNE SC/CE Sorption Model. *Geochim. Cosmochim. Acta* **2011**, *75(18)*, 5154–5168.

(22) Churakov, S. V.; Daehn, R. Zinc Adsorption on Clays Inferred from Atomistic Simulations and EXAFS Spectroscopy. *Environ. Sci. Technol.* **2012**, *46(11)*, 5713–5719.

(23) Kéri, A.; Dähn, R.; Krack, M.; Churakov, S. V. Combined XAFS Spectroscopy and *Ab Initio* Study on the Characterization of Iron Incorporation by Montmorillonite. *Environ. Sci. Technol.* **2017**, *51(18)*, 10585–10594.

(24) Kéri, A.; Daehn, R.; Krack, M.; Churakov, S. V. Characterisation of Structural Iron in Smectites – An *Ab Initio* Based XAS Study. *Environ. Sci. Technol.* **2018**.

(25) Bickmore, B. R.; Bosbach, D.; Michael F. H., J.; Charlet, L.; Rufe, E. In Situ Atomic Force Microscopy Study of Hectorite and Nontronite Dissolution: Implications for Phyllosilicate Edge Surface Structures and Dissolution Mechanisms. *Am. Mineral.* **2001**, *86(4)*, 411–423.

(26) Churakov, S. V. Ab Initio Study of Sorption on Pyrophyllite: Structure and Acidity of the Edge Sites. *J. Phys. Chem. B* **2006**, *110(9)*, 4135–4146.

(27) Churakov, S. V. Structure and Dynamics of the Water Films Confined between Edges of Pyrophyllite: A First Principle Study. *Geochim. Cosmochim. Acta* **2007**, *71(5)*, 1130–1144.

(28) Bergaya, F.; Lagaly, G. General Introduction: Clays, Clay Minerals, and Clay Science. In *Handbook of Clay Science: Developments in Clay Science*; (Eds.: Bergaya, F., Theng, B. K. G., Lagaly, G.), **2006,** *vol. 1*, pp. 1–18.

(29) Kraehenbuehl, F.; Stoeckli, H. F.; Brunner, F.; Kahr, G.; Mueller-Vonmoos, M. Study of the Water-Bentonite System by Vapour Adsorption, Immersion Calorimetry and X-Ray Techniques: I. Micropore Volumes and Internal Surface Areas, Following Dubinin's Theory. *Clay Miner.* **2000**, *22(1987)*, 1–9.

(30) VandeVondele, J.; Hutter, J. Gaussian Basis Sets for Accurate Calculations on Molecular Systems in Gas and Condensed Phases. *J. Chem. Phys.* **2007**, *127(11)*, 114105.

(31) CP2K developers group: www.cp2k.org.

(32) VandeVondele, J.; Krack, M.; Mohamed, F.; Parrinello, M.; Chassaing, T.; Hutter, J. QUICKSTEP: Fast and Accurate Density Functional Calculations Using a Mixed Gaussian and Plane Waves Approach. *Comput. Phys. Commun.* **2005**, *167(2)*, 103–128.

(33) Goedecker, S.; Teter, M.; Hutter, J. Separable Dual-Space Gaussian Pseudopotentials. *Phys. Rev. B* **1996**, *54(3)*, 1703–1710.

(34) Krack, M. Pseudopotentials for H to Kr Optimized for Gradient-Corrected Exchange-Correlation Functionals. *Theor. Chem. Acc.* **2005**, *114(1–3)*, 145–152.

(35) Perdew, J. P.; Burke, K.; Ernzerhof, M. Generalized Gradient Approximation Made Simple. *Phys. Rev. Lett.* **1996**, *77(18)*, 3865–3868.

(36) Grimme, S. Semiempirical GGA-Type Density Functional Constructed with a Long-Range Dispersion Correction. *J. Comput. Chem.* **2006**, *27(15)*, 1787–1799.

(37) Rollmann, G.; Rohrbach, A.; Entel, P.; Hafner, J. First-Principles Calculation of the Structure and Magnetic Phases of Hematite. *Phys. Rev. B - Condens. Matter Mater. Phys.* **2004**, *69(16)*, 165107.

(38) Liechtenstein, A. I.; Anisimov, V. I.; Zaanen, J. Density-Functional Theory and Strong Interactions: Orbital Ordering in Mott-Hubbard Insulators. *Phys. Rev. B* **1995**, *52(8)*, 5467–5471.

(39) Dudarev, S. L.; Botton, G. A.; Savrasov, S. Y.; Humphreys, C. J.; Sutton, A. P. Electron-Energy-Loss Spectra and the Structural Stability of Nickel Oxide: An LSDA+U Study. *Phys. Rev. B* **1998**, *57(3)*, 1505–1509.

(40) LAMMPS (Molecular Dynamics Simulator): lammps.sandia.gov

(41) Cygan, R. T.; Greathouse, J. A.; Heinz, H.; Kalinichev, A. G. Molecular Models and Simulations of Layered Materials. *J. Mater. Chem.* **2009**, *19(17)*, 2470.

(42) Bussi, G.; Donadio, D.; Parrinello, M. Canonical Sampling through Velocity Rescaling. *J. Chem. Phys.* **2007**, *126*, 014101.

(43) Ankudinov, A. L.; Ravel, B.; Rehr, J. J.; Conradson, S. D. Real-Space Multiple-Scattering Calculation and Interpretation of X-Ray-Absorption near-Edge Structure. *Phys. Rev. B* **1998**, *58(12)*, 7565–7576.

(44) Ankudinov, A. L.; Rehr, J. J. Theory of Solid-State Contributions to the X-Ray Elastic Scattering Amplitude. *Phys. Rev. B* **2000**, *62(4)*, 2437–2445.

(45) Rehr, J. J.; Ankudinov, A.; Ravel, B. User's Guide, FEFF v.8.40. 8.40. University of Washington, Department of Physics, Seeattle, USA, **2006**, pp. 66.

(46) Bunau, O.; Joly, Y. Self-Consistent Aspects of X-Ray Absorption Calculations. *J. Phys. Condens. Matter* **2009**, *21(34)*, 345501.

(47) Baeyens, B.; Marques Fernandes, M. Adsorption of Heavy Metals Including Radionuclides. In *Developments in Clay Science* (Eds.: Schoonheydt, R., Johnston, C. T., Bergaya, F.), **2018,** pp. 125–172.

(48) Reinholdt, M.; Miehé-Brendlé, J.; Delmotte, L.; Tuilier, M.-H.; le Dred, R.; Cortès, R.; Flank, A.-M. Fluorine Route Synthesis of Montmorillonites Containing Mg or Zn and Characterization by XRD, Thermal Analysis, MAS NMR, and EXAFS Spectroscopy. *Eur. J. Inorg. Chem.* **2001**, *2001(11)*, 2831.

(49) Soltermann, D.; Marques Fernandes, M.; Baeyens, B.; Dähn, R.; Miehé-Brendlé, J.; Wehrli, B.; Bradbury, M. H. Fe(II) Sorption on a Synthetic Montmorillonite. A Combined Macroscopic and Spectroscopic Study. *Environ. Sci. Technol.* **2013**, *47(13)*, 6978–6986.

(50) Webb, S. M. SIXPack a Graphical User Interface for XAS Analysis Using IFEFFIT. *Phys. Scr.* **2005**, *T115*, 1011–1014.

(51) Ressler, T. WinXAS: A Program for X-Ray Absorption Spectroscopy Data Analysis under MS-Windows. *J. Synchrotron Radiat.* **1998**, *5*, 118–122.

(52) Norman White, G.; Zelazny, L. W. Analysis and Implications of the Edge Structure of Dioctahedral Phyllosilicates. *Clays Clay Miner.* **1988**, *36(2)*, 141–146.

(53) Iordanova, N.; Dupuis, M.; Rosso, K. M. Charge Transport in Metal Oxides: A Theoretical Study of Hematite α–Fe_2O_3. *J. Chem. Phys.* **2005**, *122*, 144305.

(54) Alexandrov, V.; Neumann, A.; Scherer, M. M.; Rosso, K. M. Electron Exchange and Conduction in Nontronite from First-Principles. *J. Phys. Chem. C* **2013**, *117(5)*, 2032–2040.

(55) Rosso, K. M.; Ilton, E. S. Charge Transport in Micas: The Kinetics of Fe(II)/Fe(III) Electron Transfer in the Octahedral Sheet. *J. Chem. Phys.* **2003**, *119(17)*, 9207–9218.

(56) Rosso, K. M.; Dupuis, M. Electron Transfer in Environmental Systems: A Frontier for Theoretical Chemistry. *Theor. Chem. Acc.* **2006**, *116(1–3)*, 124–136.

(57) Kerisit, S.; Rosso, K. M. Kinetic Monte Carlo Model of Charge Transport in Hematite α–Fe_2O_3. *J. Chem. Phys.* **2007**, *127(12)*, 124706.

(58) Géhin, A.; Grenèche, J.-M.; Tournassat, C.; Brendlé, J.; Rancourt, D. G.; Charlet, L. Reversible Surface-Sorption-Induced Electron-Transfer Oxidation of Fe(II) at Reactive Sites on a Synthetic Clay Mineral. *Geochim. Cosmochim. Acta* **2007**, *71(4)*, 863–876.

CHAPTER 6:
Theoretical study:
First-principles study of uranyl adsorption on montmorillonite edge surfaces

This chapter is a manuscript that is currently in preparation as "Kéri, A.; Dähn, R.; Krack, M.; Churakov, S. V. First-principles study of uranyl adsorption on montmorillonite edge surfaces"

Abstract

In high-level radioactive waste disposal sites, the sorption behavior of radionuclides ($e.g.\ UO_2^{2+}$) is mostly determined by their interaction with clay mineral–water interfaces. Thus, a molecular level understanding of the sorption mechanisms is necessary. In this study, theoretical and experimental investigations were performed and compared to determine the preferred uptake mechanism of UO_2^{2+} (uranyl ion). The adsorption of uranyl at the two most relevant edge surfaces of a montmorillonite layer was investigated by using density functional theory (DFT+U). The energy comparison of the relaxed structures of various bidentate uranyl surface complexes revealed that the structural parameters of the uranyl species are essentially determined by the placement of surface chemical groups ($e.g.\ OH^-$) forming the adsorption site. Uranyl prefers to bind to the octahedral sheet of montmorillonite through two bridging oxygens or it occupies a "defect" of the clay layer. Structural Fe^{3+} (ferric iron) in the octahedral sheet of montmorillonite at the surface site increases the stability of bidentate uranium species, but it does not change the relative stability of the complexation. Although, the results of the conventional EXAFS analysis of uranium adsorbed Milos-, Wyoming- and Texas-montmorillonite is unclear, the comparison of the basic structural parameters (of U–O shell) indicates an agreement with most stable models.

1. Introduction

Clay minerals are the main constituent of the engineered and geological barriers at radioactive waste disposal repositories[1–4]. A 2:1 clay mineral, namely montmorillonite, is of particular interest, as it is the main component of the barrier material (bentonite)[1–4]. It plays an important role in the retardation and immobilization of radioactive pollutants such as uranium and other actinides[1]. The actinides are known to adsorb strongly on edge surfaces of clay minerals[2,5,6]. Sorption experiments revealed the dependence of adsorption on pH, ionic strength, uranyl (UO_2^{2+}) concentration and the presence of various ligands ($especially\ CO_3^{2-}$) in the solution[5–7].

Several experimental studies have been performed applying various measurement techniques to investigate actinide adsorption at mineral surfaces[5,6,8]. X-ray absorption spectroscopy (XAS) is a widely applied experimental method that obtains information about the averaged structural features of uranium species present on clay mineral surfaces[5,6]. It sheds light on the chemical nature of adsorption complexes (e.g. oxidation state, complexation mode, bridging ligation)[9], which can be further used in surface complexation models to ascertain the adsorption behavior of uranyl at different environmental conditions (e.g. pH, ionic strength). It could be concluded from the so far achieved results that uranyl mainly forms inner-sphere complexes at near neutral pH, while outer-sphere hydration complexes are more relevant at lower pH[5,10]. Inner- and outer-sphere complexation of uranyl ions on montmorillonite edge surfaces can easily be differentiated by various (e.g. XAS) spectroscopic

techniques[5], however, the exact coordination environment (e.g. preferred surface orientations for adsorption) is still unknown. Surface complexation models based on macroscopic sorption experiments and spectroscopic measurements could determine the adsorption behavior of uranyl on montmorillonite. The results of these simplified modelling approaches depends strongly on the chosen modelling setup (e.g. type and number of clay edge sites as well as surface species of actinides at the water–mineral interface)[7]. More reliable conclusion could be drawn based on an explicit atomistic description of the surface complexes. Furthermore, natural montmorillonite usually contains a low amount of Fe^{3+} in its bulk structure, which may control the sorption mechanism of redox sensitive actinides (like uranium) on clay mineral surfaces. Our knowledge about the impact of structural iron on actinide adsorption at the atomic level needs to be improved.

Ab initio simulations are valuable and reliable complements to experimental studies, since they provide a direct insight into the sorption species formed at mineral surfaces on the atomic scale. Modelling the adsorption of actinides is challenging because of the strong correlation of the 5*f* electrons. The application of the so-called Mott–Hubbard correction term within density functional theory (DFT), commonly referred to as DFT+U, was developed and tested for uranium-dioxide (UO_2). Applying DFT+U on UO_2 are found to produce accurate structural results and the interaction energies as compared with computationally high-level methods[11,12]. In this study, the adsorption of a uranyl ion on the (010) and the (110) edge surface of neutral montmorillonite was simulated applying the DFT+U method. The most stable surface complexation models were determined based on the comparison of the relative energies of the relaxed structures.

2. Materials and methods

2.1. Modelling setup

Montmorillonite is a 2:1 dioctahedral clay mineral consisting of two siloxane tetrahedral (T) sheets which a sandwiched, pseudo-hexagonally ordered sheet of alumina octahedral (O) where only two thirds of the available octahedral positions are occupied[13]. One third of the octahedral sites are *trans*-symmetric and two thirds of the octahedral sites are *cis*-symmetric with respect to the orientation of the hydroxyl (OH^-) groups[13,14]. Montmorillonite typically occurs in *cv*-vacant form having both *cis*- and *trans*-occupational sites[15]. In this study, the two most relevant, the (010) and the (110) edge surface sites were modelled using an idealized defect free TOT (tetrahedral-octahedral-tetrahedral) layer of a *cv*-vacant 2:1 dioctahedral clay with the general formula of $4\times[Al_8Si_{16}O_{40}(OH)_8]^0$. The anisotropy of the montmorillonite edge surface ("*cis*-like" or "*trans*-like") sites was also considered during the modelling[16].

Uranyl may form inner- or outer-sphere complexes at the surface sites of montmorillonite. In the former case, the cation directly binds to the clay surface on one side and to a number of water molecules on the other, while outer-sphere hydration complexes are completely surrounded by water molecules[5,10]. In this thesis, surface complexation was modelled at near neutral pH, thus only models of inner-sphere complexes were considered (Figure 1)[5,10]. The impact of structural iron was considered taking into account ferric iron Fe^{3+} incorporated in the octahedral sheet at the edge surface of the clay layer at the *cis*- and *trans*-octahedral positions, respectively (Figure 2)[16].

The dimensions of the orthorhombic supercell were 18.2Å × 20.8Å × 15.0Å. Similar to previous works, the cell parameter in the *c*-direction was fixed to 15Å to reduce the interaction between the periodic images[17–19]. The *ab initio* calculations were performed on a single clay particle without water in the interlayer.

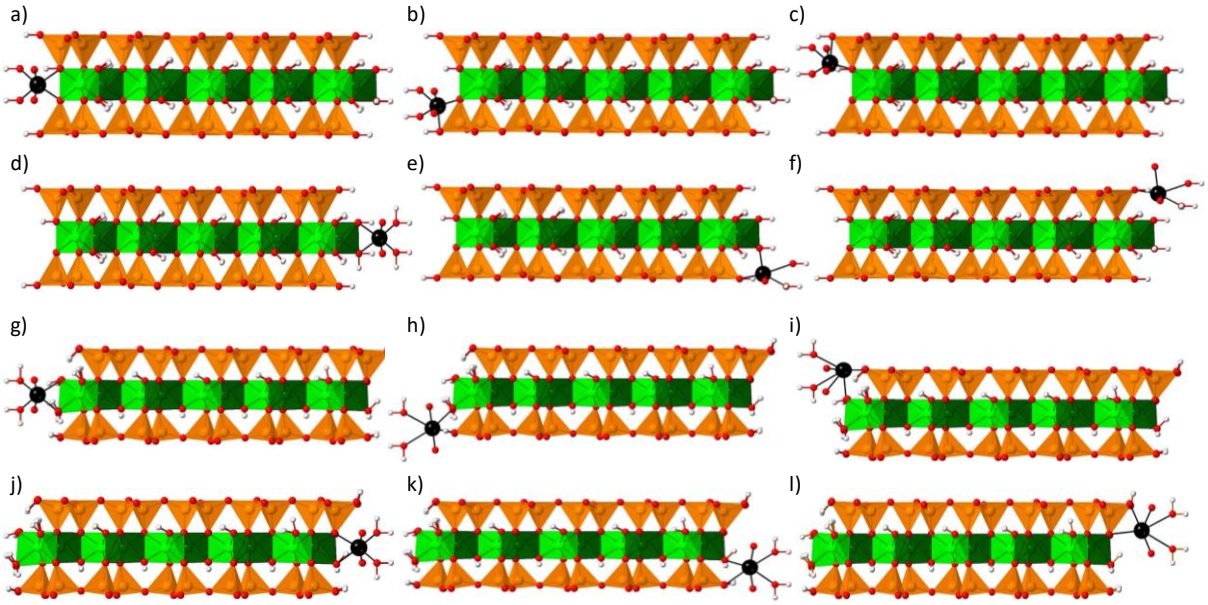

Figure 1. View of the initial model structures of the inner-sphere binuclear uranyl complexes. (010) montmorillonite edge surface is present in panel a-f, while (110) edge site is shown in panel g-l. In panel a-c and g-i, the uranyl is sorbed at the *cis*-like site, while sorption at the *trans*-like site is present in panel d-f and j-l. In panel a,d,g,j, the uranyl is attached to the octahedral sheet (two bridging oxygen from the octahedral sheet), while one of the bridging oxygen is in the octahedral, the other is in the tetrahedral sheet in panel b,c,e,f,h,i,k,l. The *cis*- and *trans*-octahedra can be distinguished by the different relative position of hydroxyl (OH^-) groups and lighter (*cis*-site) or darker (*trans*-site) colors. Alumina octahedra are shown in green, orange color corresponds to silica tetrahedra, while oxygen and hydrogen atoms are red and grey, respectively. More detailed information can be obtained from Table 1.

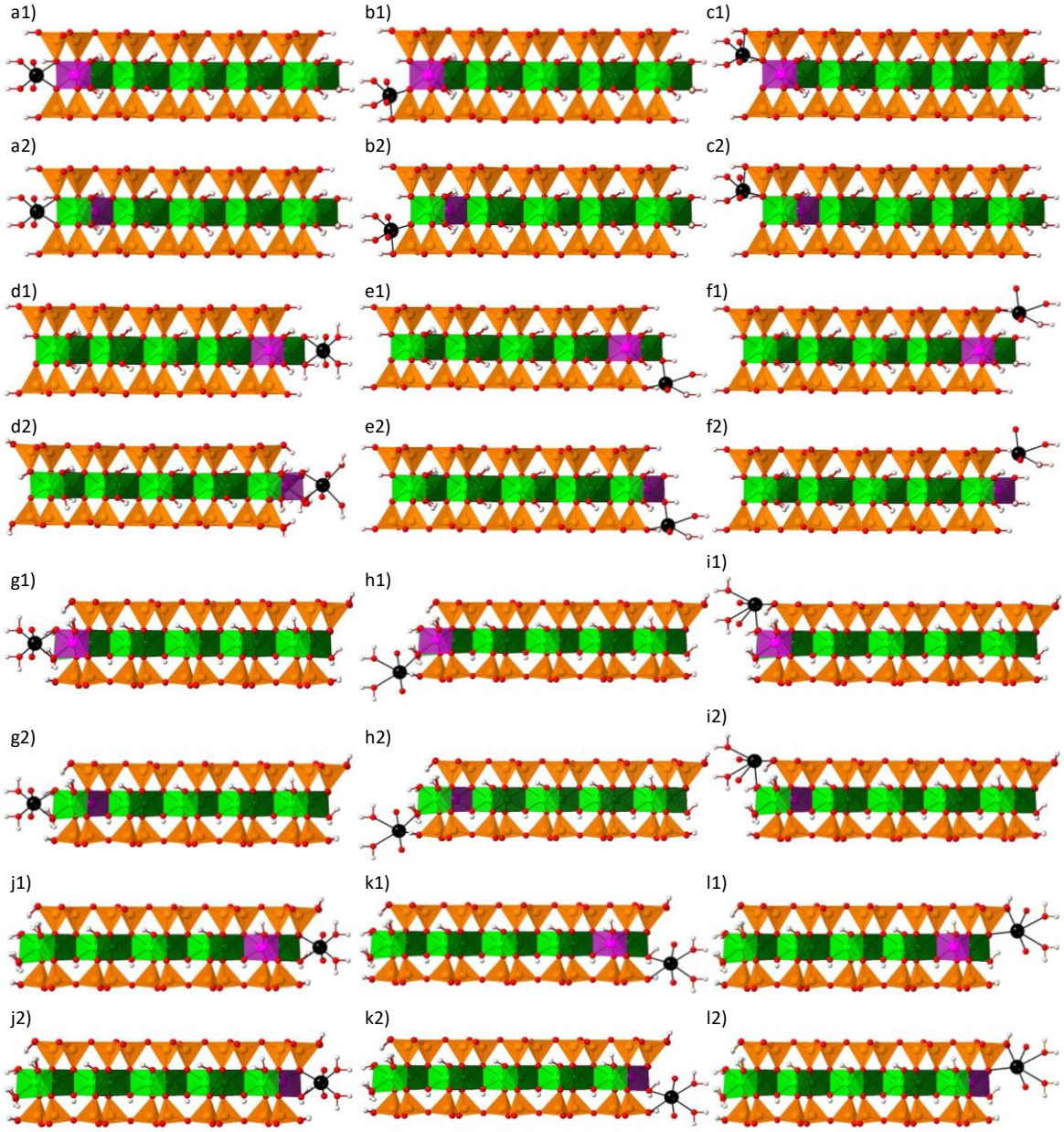

Figure 2. Views of the initial model structures of the impact of ferric iron on the inner-sphere binuclear uranyl complexes. (010) montmorillonite edge surface is present in panel a-f, while (110) edge site is shown in panel g-l. In panel a-c and g-i, the uranyl is sorbed at the *cis*-like site, while sorption at the *trans*-like site is present in panel d-f and j-l. In panel a, d, g, j, the uranyl is attached to the octahedral sheet (two bridging oxygen from the octahedral sheet), while one of the bridging oxygen is in the octahedral, the other is in the tetrahedral sheet in panel b,c,e,f,h,i,k,l. Fe^{3+} is at the *cis*- octahedral position in panels marked with label "1" (panel a1,b1,c1, etc.), while in panels with label "2" (panel a2,b2,c2, etc.), Fe^{3+} substitutes an aluminium at the *trans*-site. The *cis*- and *trans*-octahedra can be distinguished by the different relative position of hydroxyl (OH^-) groups and lighter (*cis*-site) or darker (*trans*-site) colors. Alumina octahedra are shown in green, orange color corresponds to silica tetrahedra, while oxygen and hydrogen atoms are red and grey, respectively. More detailed information can be obtained from Table 3.

2.2. *Ab initio* calculations

The *ab initio* calculations were carried out using the QUICKSTEP module of CP2K code, which employs a mixed Gaussian and plane waves basis set[20,21]. The scalar-relativistic norm-conserving pseudopotentials of Goedecker, Teter and Hutter (GTH)[22] were applied to avoid the explicit consideration of the core electrons[23]. For uranium, a medium-core pseudopotential, $[\mathrm{Xe}\ 4f^{14}\ 5d^{10}]$ with 14 valence electrons, $6s^2\ 6p^6\ 5f^3\ 6d^1\ 7s^2$, was used. The medium-core pseudopotential of iron was composed of a [Ne] core with $3s^2\ 3p^6\ 4s^2\ 3d^6$ as valance electrons. The wave functions of the valence electrons were described by a linear combination of contracted Gaussian-type orbitals using MOLOPT basis sets optimized for the corresponding GTH pseudopotentials[24]. All calculations were performed with a spin polarized implementation of the Perdew, Burke and Ernzerhof (PBE) exchange and correlation functional[25]. An empirical van der Waals (vdW) correction, PBE+D2, has been applied to improve the description of hydrogen bonding[26]. An auxiliary basis set of plane waves up to a cutoff energy of 400Ry was employed to expand the electronic density[11]. Simulations with a single U^{6+} complex at the edge surface site of montmorillonite were performed with a multiplicity $(2S+1)_{U^{6+}} = 1$. For models containing both U^{6+} complex and Fe^{3+}, the multiplicities were specified $(2S+1)_{U^{6+}\text{—}Fe^{3+}} = 6$, respectively.

Conventional DFT is known to underestimate the Coulomb repulsion between the localized 3*d*-electrons of iron and the 5*f* electrons of uranium[11,27,28]. In order to improve the description of these delocalized states within the DFT formalism, the so-called DFT+U method was applied[11,27,28]. In this semi-empirical approach, an additional potential characterized by the so-called Hubbard-parameter (U_{eff}) is applied to the selected 3*d*- and 5*f*-states of iron and uranium, respectively. The value of U_{eff} depends on the implementation and has to be calibrated[29]. For ferrous and ferric iron, the calibrations were performed on the bulk structures of two iron-oxides (wustite and hematite) in our previous paper[17], while the determination of U_{eff} for uranium was performed on the bulk and surface structure of uranium-dioxide (UO_2)[11]. Thus, fixed Hubbard-parameters with values $U_{\mathrm{eff}}^{\mathrm{iron}} = 1.9\mathrm{eV}$ and $U_{\mathrm{eff}}^{\mathrm{uranium}} = 1.98\mathrm{eV}$ were applied in this study.

2.3. XAS measurements

U L_3-edge EXAFS spectra were recorded at the Dutch Belgium Beamline (DUBBLE/BM26) at the European Synchrotron Radiation Facility (ESRF), Grenoble, France[30]. All spectra were recorded at room temperature using a Si(111) monochromator and a 9-channel monolithic Ge-solid-state detector with a sample orientation of 45° to the incident beam. Higher order harmonics were rejected with two mirrors (Si and Pt/Si). The monochromator angle was calibrated by assigning the first inflection point of the K-absorption edge spectrum of Y metal to 17038eV.

All EXAFS spectra were extracted from the raw data with the Athena interface of the IFEFFIT software[31,32]. The Fourier transforms (FT) were obtained from the $k^3\chi(k)$ functions between k = 3.2–11.3Å^{-1} using a Kaiser–Bessel window function with an apodization parameter value of 1. The FT peaks of interest were selected in the range of R = 1–4Å and fitted in reciprocal space with the Artemis interface of the IFEFFIT software. Amplitude and phase shifts functions were calculated with FEFF 8.40[33,34] using the soddyite $(UO_2)_2(SiO_4)\cdot 2H_2O$ structure[35], in which one Si was replaced by Al or Fe[7]. The amplitude reduction factor[36] (S_0^2) was set to 1.

Throughout the data analysis, which was performed on the inverse Fourier transforms (FT^{-1}) of the first and second shells, the numbers of degrees of freedom in the least-squares refinements were reduced by fixing the $CN_{U\text{-}O_{ax}}$ = 2 and linking the Debye–Waller parameters $\sigma^2_{U\text{-}O_{eq_1}}$ and $\sigma^2_{U\text{-}O_{eq_2}}$ for both shells. A global threshold energy, ΔE_0 (the shift between theoretical and experimental threshold energy), was allowed to vary during the fit, but was linked for all paths. Furthermore, $\sigma^2_{U\text{-}Al/Fe}$ was fixed to the value obtained for the U–Si fit model to avoid strong correlations. The multiple scattering (MS) path of the uranyl moiety was linked to the U–O_{ax} scattering parameters by constraining its fit parameters to values of the U–O_{ax} single scattering (SS) as described in Hudson et al.[37]. It was not possible to fit any of the experimental data using a U–U pair and/or a combination of U–U and U–Al/Si/Fe pairs. This finding suggests that no U nucleation phase formed in our sorption system under the employed reaction conditions.

3. Results and discussion

3.1. Uranyl complexation on montmorillonite edge surfaces

The relaxed structures of the different bidentate uranyl adsorption models at the two most relevant montmorillonite edge surfaces were calculated (Figure 3). The complexation models formed at the (010) edge surface (Figure 3a-f) are unstable since a water molecule initially attached to the Al octahedra at the *trans*-like site of the clay layer diffused into the interlayer. This disintegration effect cannot be seen for the (110) edge surface models indicating stable surface complexes.

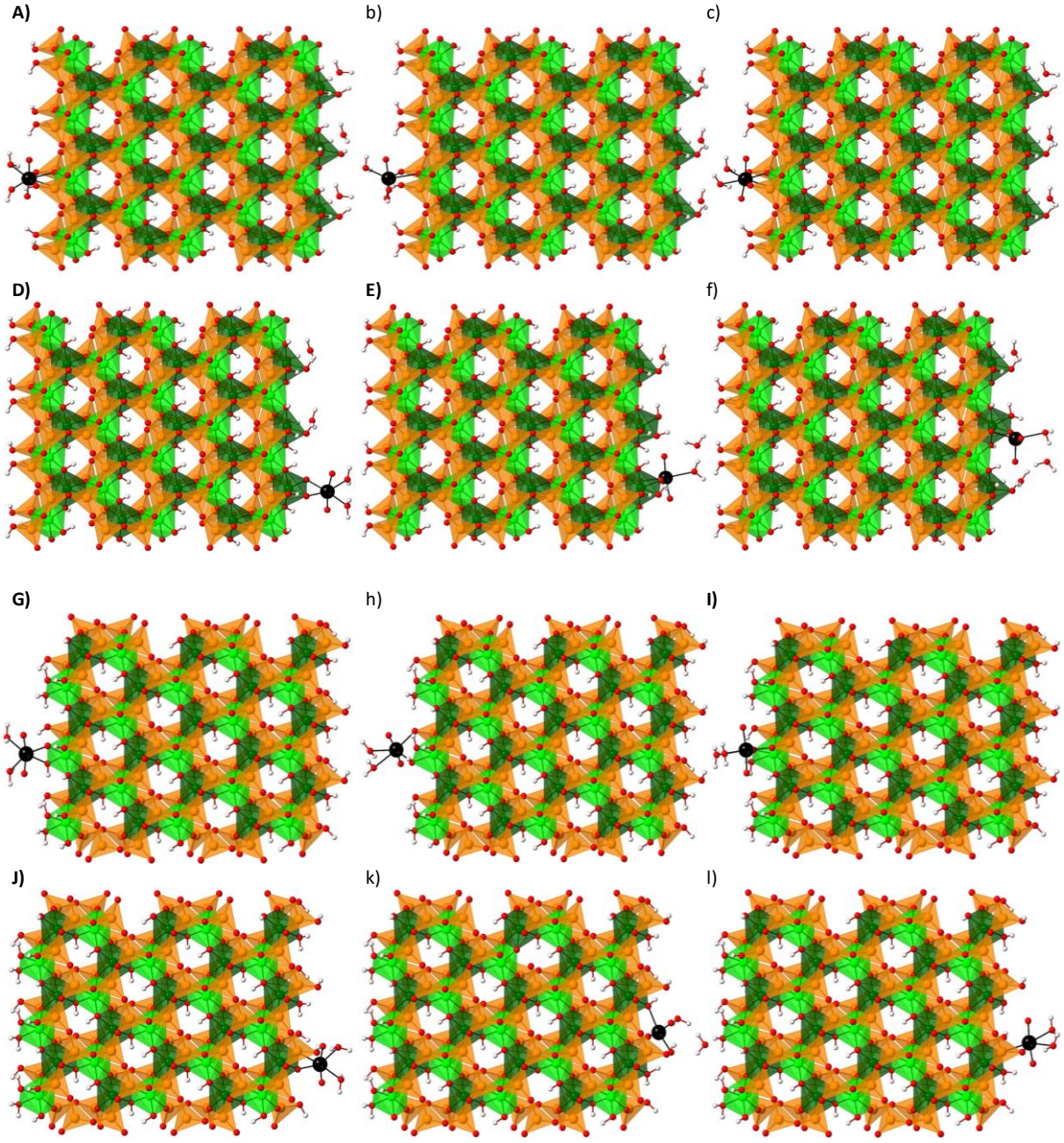

Figure 3. Relaxed structures of the inner-sphere binuclear uranyl complexes. (010) montmorillonite edge surface is present in panel a-f, while (110) edge site is shown in panel g-l. In panel a-c and g-i, the uranyl is sorbed at the *cis*-like site, while sorption at the *trans*-like site is present in panel d-f and j-l. In panel a,d,g,j, the uranyl is attached to the octahedral sheet (the two bridging oxygen are from the octahedral sheet), while one of the bridging oxygen is in the octahedral, the other is in the tetrahedral sheet in panel b,c,e,f,h,i,k,l. The *cis*- and *trans*-octahedra can be distinguished by the different relative position of hydroxyl (OH^-) groups and lighter (*cis*-site) or darker (*trans*-site) colors. Alumina octahedra are shown in green, orange color corresponds to silica tetrahedra, while oxygen and hydrogen atoms are red and grey, respectively. Based on relative energy results present in Table 1, the panels of the most stable structures are marked with bold capital letters**.**

The relative energies of the bidentate uranyl were calculated to determine the most stable adsorption complexes. The different models were categorized into sections to avoid two effects. The first effect is the difference in the energy of ideal (010) and (110) surface sites. The (010) edge site is ~30kcal/mol higher in energy compared to the (110) edge surfaces inducing an energy penalty on complexes formed at the (010) edge surface site. The other effect is caused by the anisotropy (*cis*- and *trans*-like) of an edge site. The *cis*- and *trans*-like edge surfaces have different protonation schemes (distinct number of oxygen ions and protons) and thus different surface charges. The two different surface sites form a capacitor with a potential difference. Moving a uranyl ion (a charge) from the *cis*-like site to the *trans*-like site (or in the other direction) would cost/obtain energy. To avoid the above described effects, uranyl complexes were categorized into four groups and their relative energies were calculated accordingly (Table 1).

Table 1. Relative energies of the bidentate uranyl complexes formed at the (010) and (110) edge surface sites of montmorillonite, respectively

Edge surface	Edge site of UO_2^{2+} sorption	Bridging oxygen	Short name of the model[a]	Panel[a,b]	Relative energy[c] [kcal/mol]
(010)	*cis*	oct+oct[d]	**010U6cOct**	**A)**	0.0
		oct+tet[e]	010U6cTetlow	b)	33.9
			010U6cTetup	**C)**	12.1
	trans	oct+oct[d]	**010U6tOct**	**D)**	0.0
		oct+tet[e]	**010U6tTetlow**	**E)**	-1.7
			010U6tTetup	f)	5.2
(110)	*cis*	oct+oct[d]	**110U6cOct**	**G)**	0.0
		oct+tet[e]	110U6cTetlow	h)	14.6
			110U6cTetup	**I)**	-3.6
	trans	oct+oct[d]	**110U6tOct**	**J)**	0.0
		oct+tet[e]	110U6tTetlow	k)	11.5
			110U6tTetup	l)	29.7

[a]The name and the panel of the most stable models are marked with bold (capital) letters

[b]Initial model plotted in Figure 1, relaxed structure is present in Figure 3 in the marked panel

[c]Relative energy differences (separated by horizontal lines) are calculated for structures with the same stoichiometry, total charge and montmorillonite edge surface ((010)/(110), cis/trans-like) site to which uranyl is sorbed

[d]Both (two) bridging oxygen is in the octahedral sheet

[e]One of the bridging oxygen is in the octahedral, the other is in the tetrahedral sheet

The results show that uranyl prefers to bind to the octahedral sheet through two so-called bridging oxygen atoms (Table 1, Figure 3). The "110U6cTetup" model, when uranyl binds to the (110) montmorillonite edge surface through one octahedral and one tetrahedral bridging oxygen at the "defect" of the *cis*-like site (Figure 3), has also low relative energy (Table 1).

The structural parameters (interatomic distances and coordination number) of uranium–(bridging, axial and water) oxygen agreed well for the most stable models with two octahedral bridging oxygens ("110U6cOct" and "110U6tOct" in Table 2). The only difference appeared in the U– Al and U– Si distances, which can be explained by the different morphology of the *cis*- and *trans*-like site of the (110) edge surface of montmorillonite. The U–O_b and U–O_a distances of the third most stable structure with one tetrahedral bridging oxygen ("110U6cTetup") agreed well with the other most stable models, however, higher deviation than the uncertainty could be detected for U–O_w interatomic distances (Table 2). Uranyl in the "110U6cTetup" model sits in the "defect" of the (110) clay edge surface. Thus, the surface hydroxyl groups are close to the uranyl ion. The electrostatic repulsion between surface hydroxyl groups and the water molecules attached to the uranyl ion is minimized by an increment of the U–O_w distances. The U–Al and U–Si interatomic distances remarkably varied with the structures. The shortest U–Al interatomic distances (~3.20Å) can be seen for uranyl uptake models with two octahedral bridging oxygens, while such a trend is not visible for U–Si interatomic distances. The most stable structures (with detectable U–Si interaction) have ~3.53Å long U–Si distances, the only exception is the "110U6tOct" model (~3.66Å). In this case, the uranyl affected by the hydroxyl group attached to the nearest silica pushing it farther from the montmorillonite edge surface.

The interatomic distances of the uranyl complex are determined by the edge surface site ((010)/(110), cis/trans-like) where the uranyl complex is formed, the type of the bridging oxygen atoms (two octahedral or one octahedral and one tetrahedral) and the existence of a "defect" at the surface. The comparison of various uranyl complexes at the two most relevant montmorillonite edge surfaces indicated that the structural parameters of the species are determined by the surface chemical groups (e.g. OH^-) forming the investigated clay site. For example, the deviation in the structural parameters between similar sorption models (e.g. "010U6cOct" and "010U6tOct") can be explained by the anisotropy of the edge sites. *Cis*- and *trans*-like sites have different protonation schemes (especially for the (010) edge surface) implying different arrangement of hydroxyl groups at the surface site. The uranyl complex is attached to the surface, while the repulsion force on axial and water oxygen atoms generated by surface hydroxyl groups are minimized. It indicates higher U–Al and U–Si interatomic distances.

Table 2. Structural parameters (interatomic distances and coordination numbers) of the bidentate uranium complexes formed at the two most relevant edge surfaces of montmorillonite

Short name of model[a]	Structural parameter[b]	Bond type				
		U–O_a[c]	**U–O_b**[d]	**U–O_w**[e]	**U–Al**[f]	**U–Si**[g]
010U6cOct[h]	***R*** [Å]	**1.80 ± 0.01**	**2.38 ± 0.02**	**2.36 ± 0.25**	**3.46 ± 0.01**	**3.54 ± 0.02**
	CN [-]	**2.0 ± 0.1**	**2.0 ± 0.1**	**2.0 ± 0.1**	**1.0 ± 0.1**	**2.0 ± 0.1**
010U6cTetlow	***R*** [Å]	1.81 ± 0.01	2.33 ± 0.21	2.43 ± 0.20	4.12 ± 0.01	3.02 ± 0.01
	CN [-]	2.0 ± 0.1	2.0 ± 0.1	2.0 ± 0.1	1.0 ± 0.1	1.0 ± 0.1
010U6cTetup	***R*** [Å]	1.80 ± 0.01	2.38 ± 0.08	2.57 ± 0.07	3.48 ± 0.01	3.06 ± 0.01
	CN [-]	2.0 ± 0.1	3.0 ± 0.1	2.0 ± 0.1	1.0 ± 0.1	1.0 ± 0.1
010U6tOct[h]	***R*** [Å]	**1.83 ± 0.02**	**2.16 ± 0.20**	**2.59 ± 0.03**	**3.19 ± 0.01**	**—**
	CN [-]	**2.0 ± 0.1**	**2.0 ± 0.1**	**2.0 ± 0.1**	**1.0 ± 0.1**	**0.0 ± 0.1**
010U6tTetlow[h]	***R*** [Å]	**1.81 ± 0.02**	**2.15 ± 0.06**	**2.51 ± 0.01**	**3.95 ± 0.01**	**3.53 ± 0.01**
	CN [-]	**2.0 ± 0.1**	**2.0 ± 0.1**	**1.0 ± 0.1**	**1.0 ± 0.1**	**1.0 ± 0.1**
010U6tTetup	***R*** [Å]	1.89 ± 0.11	2.06 ± 0.13	2.54 ± 0.01	3.67 ± 0.01	3.41 ± 0.01
	CN [-]	2.0 ± 0.1	2.0 ± 0.1	1.0 ± 0.1	1.0 ± 0.1	1.0 ± 0.1
110U6cOct[h]	***R*** [Å]	**1.83 ± 0.02**	**2.15 ± 0.18**	**2.56 ± 0.01**	**3.20 ± 0.01**	**—**
	CN [-]	**2.0 ± 0.1**	**2.0 ± 0.1**	**2.0 ± 0.1**	**1.0 ± 0.1**	**0.0 ± 0.1**
110U6cTetlow	***R*** [Å]	1.81 ± 0.02	2.18 ± 0.00	2.66 ± 0.09	4.12 ± 0.01	3.38 ± 0.01
	CN [-]	2.0 ± 0.1	2.0 ± 0.1	2.0 ± 0.1	1.0 ± 0.1	1.0 ± 0.1
110U6cTetup[h]	***R*** [Å]	**1.82 ± 0.01**	**2.14 ± 0.07**	**2.65 ± 0.01**	**3.54 ± 0.01**	**3.53 ± 0.01**
	CN [-]	**2.0 ± 0.1**	**2.0 ± 0.1**	**2.0 ± 0.1**	**1.0 ± 0.1**	**1.0 ± 0.1**
110U6tOct[h]	***R*** [Å]	**1.83 ± 0.02**	**2.19 ± 0.27**	**2.59 ± 0.01**	**3.22 ± 0.01**	**3.66 ± 0.01**
	CN [-]	**2.0 ± 0.1**	**2.0 ± 0.1**	**2.0 ± 0.1**	**1.0 ± 0.1**	**1.0 ± 0.1**
110U6tTetlow	***R*** [Å]	1.86 ± 0.02	2.32 ± 0.18	2.58 ± 0.00	3.54 ± 0.01	3.48 ± 0.45
	CN [-]	2.0 ± 0.1	3.0 ± 0.1	1.0 ± 0.1	1.0 ± 0.1	2.0 ± 0.1
110U6tTetup	***R*** [Å]	1.80 ± 0.03	2.27 ± 0.09	2.56 ± 0.03	4.01 ± 0.01	2.96 ± 0.01
	CN [-]	2.0 ± 0.1	2.0 ± 0.1	2.0 ± 0.1	1.0 ± 0.1	1.0 ± 0.1

[a]Short names are explained in Table 1

[b]Bond distance (R) and coordination number (CN)

[c]O_a: axial oxygen of the uranyl ion

[d]O_b: (octahedral/tetrahedral) bridging oxygen between uranyl ion and montmorillonite edge surface

[e]O_w: oxygen atom of a water molecule attached to the uranyl ion

[f]Al: aluminum in the octahedral sheet of the montmorillonite layer

[g]Si: silicon in the tetrahedral sheet of the montmorillonite layer

[h]The model name and the structural parameters of the most stable models are marked with bold letters

3.2. Impact of structural iron on the uranium complexation

The impact of structural iron on the uranium complexation was simulated by different models representing a uranyl ion sorbed at the surface of montmorillonite at the same (*cis/trans*-like) site at which Fe is incorporated (Figure 2 and Figure 4). Structural iron was always in the Fe^{3+} oxidation state and it could occupy both *cis*- and *trans*- octahedral positions (Figure 2 and Figure 4). The results indicate that ferric iron cannot stabilize the (010) edge surface of montmorillonite as water molecules at the *trans*-like site detached from the *trans*-octahedra. The (110) edge surface of the clay remain stable and models with the lowest energy are "110U6cOctFe3c", "110U6cOctFe3t", "110U6tOctFe3c", "110U6tOctFe3t", "110U6cTetupFe3c" and "110U6cTetupFe3t" (Table 3). The uranyl ion energetically prefers to bind to the octahedral sheet or to "sit" in a *cis*-like "defect" of the (110) edge surface (Table 3, Figure 4).

The structural parameters of the most stable models were compared to the corresponding structures without Fe^{3+} in the octahedral sheet ("110U6cOct", "110U6tOct", "110U6cTetup"). The uranium–oxygen interatomic distances ($U–O_a$, $U–O_b$, $U–O_w$) agree well and detectable differences could not be found for U–Al and U–Si bond length. The comparison of structural model parameters with and without structural Fe^{3+} indicates that there is no distortion in the uranyl complex or in the octahedral sheet of the montmorillonite layer due to U–Fe interaction. The results indicate that structural Fe^{3+} did not change the orientation and the relative stability of the uranium species at the surface. Uranium complexation models with low U–Fe distances (<3.6Å) are more stable than the higher ones (>5.0Å). It indicates that structural ferric iron in the octahedral sheet of montmorillonite increases the stability of bidentate uranium species.

Earlier studies revealed that montmorillonites originating from different mining sites have different structural Fe distribution. Thus, they might behave diverse transitional metal uptake mechanism. The *ab initio* calculations alone cannot reveal the differences between the possible uptake mechanisms. The comparison of the structural parameters obtained from structure relaxations and conventional EXAFS data fitting is a promising tool for first principle investigations.

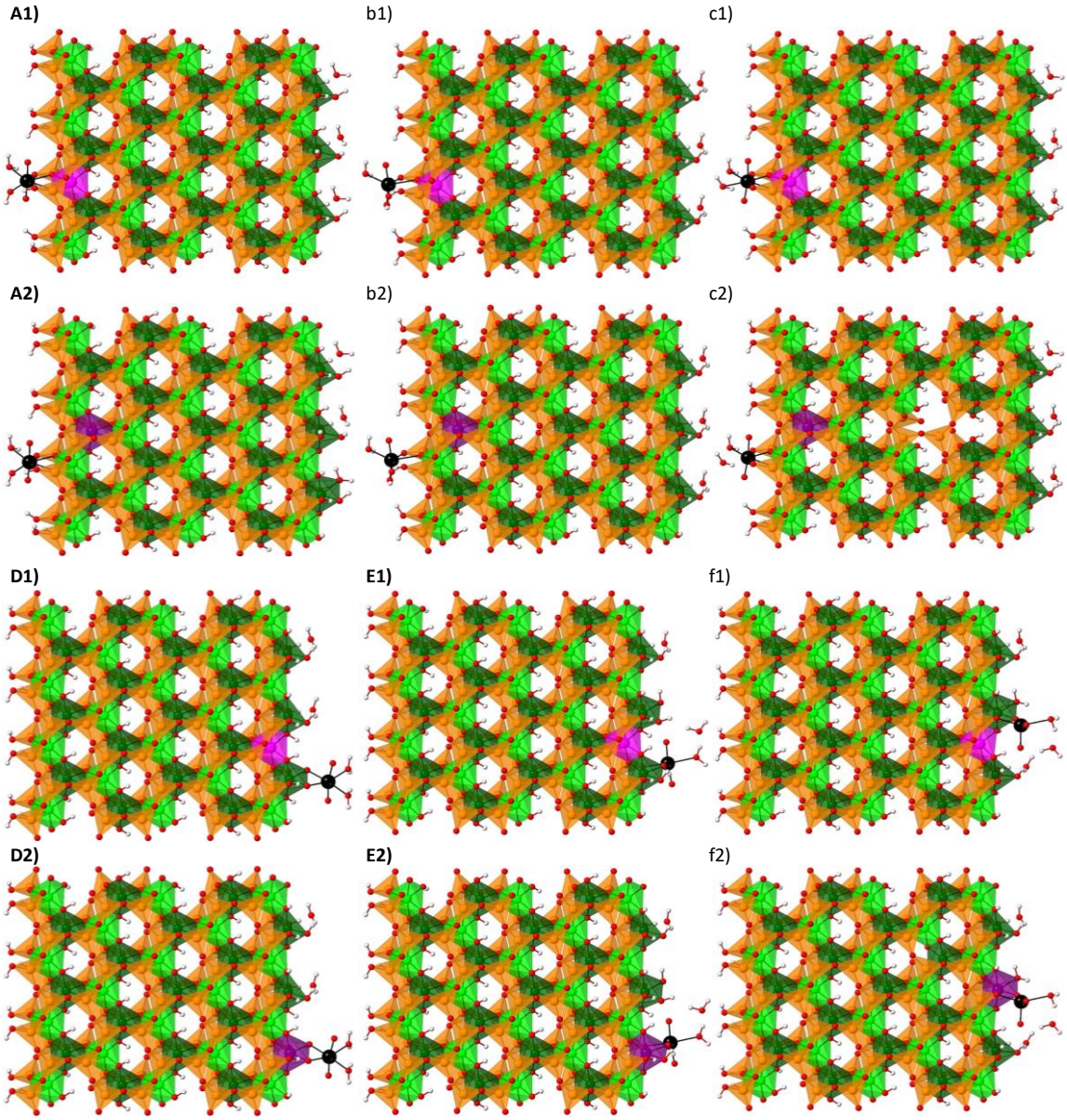

Figure 4. Relaxed structures of uranyl complexes formed at montmorillonite edge surfaces with Fe^{3+} in the octahedral sheet. (010) montmorillonite edge surface is present in panel a-f, while (110) edge site is shown in panel g-l. In panel a-c and g-i, the uranyl is sorbed at the *cis*-like site, while sorption at the *trans*-like site is present in panel d-f and j-l. In panel a, d, g, j, the uranyl is attached to the octahedral sheet (two bridging oxygen from the octahedral sheet), while one of the bridging oxygen is in the octahedral, the other is in the tetrahedral sheet in panel b,c,e,f,h,i,k,l. Fe^{3+} is at the *cis*- octahedral position in panels marked with label "1" (panel a1,b1,c1, etc.), while in panels with label "2" (panel a2,b2,c2, etc.), Fe^{3+} substitutes an aluminium at the *trans*-site. The *cis*- and *trans*-octahedra can be distinguished by the different relative position of hydroxyl (OH^-) groups and lighter (*cis*-site) or darker (*trans*-site) colors. Alumina octahedra are shown in green, orange color corresponds to silica tetrahedra, while oxygen and hydrogen atoms are red and grey, respectively. Based on relative energy results present in Table 3, the panels of the most stable structures are marked with bold capital letters.

Table 3. Relative energies [kcal/mol] of the relaxed uranium adsorption structures with Fe^{3+} incorporation in the octahedral sheet

Edge surface	Edge site of UO_2^{2+} sorption	Bridging oxygen	Occupational site of Fe^{3+}	Short name of model[a]	Panel[a,b]	Relative energy[c] [kcal/mol]
(010)	*cis*	oct+oct[d]	*cis*	**010U6cOctFe3c**	**A1)**	0.0
			trans	**010U6cOctFe3t**	**A2)**	2.1
		oct+tet[e]	*cis*	010U6cTetlowFe3c	b1)	33.6
			trans	010U6cTetlowFe3t	b2)	34.3
			cis	010U6cTetupFe3c	c1)	15.5
			trans	010U6cTetupFe3t	c2)	14.1
	trans	oct+oct[d]	*cis*	**010U6tOctFe3c**	**D1)**	0.0
			trans	**010U6tOctFe3t**	**D2)**	-3.4
		oct+tet[e]	*cis*	**010U6tTetlowFe3c**	**E1)**	-2.1
			trans	**010U6tTetlowFe3t**	**E2)**	-6.4
			cis	010U6tTetupFe3c	f1)	2.6
			trans	010U6tTetupFe3t	f2)	2.6
(110)	*cis*	oct+oct[d]	*cis*	**110U6cOctFe3c**	**G1)**	0.0
			trans	**110U6cOctFe3t**	**G2)**	4.6
		oct+tet[e]	*cis*	110U6cTetlowFe3c	h1)	14.6
			trans	110U6cTetlowFe3t	h2)	18.5
			cis	**110U6cTetupFe3c**	**I1)**	-7.1
			trans	**110U6cTetupFe3t**	**I2)**	0.2
	trans	oct+oct[d]	*cis*	**110U6tOctFe3c**	**J1)**	0.0
			trans	**110U6tOctFe3t**	**J2)**	-5.3
		oct+tet[e]	*cis*	110U6tTetlowFe3c	k1)	11.1
			trans	110U6tTetlowFe3t	k2)	11.2
			cis	110U6tTetupFe3c	l1)	28.3
			trans	110U6tTetupFe3t	l2)	28.0

[a]The name and the panel of the most stable models are marked with bold (capital) letters

[b]Initial model plotted in Figure 1, relaxed structure is present in Figure 3 in the marked panel

[c]Relative energy differences (separated by horizontal lines) are calculated for structures with the same stoichiometry, total charge and montmorillonite edge surface ((010)/(110), *cis/trans*-like) site to which uranyl is sorbed

[d]Both (two) bridging oxygen is in the octahedral sheet of the montmorillonite layer

[e]One of the bridging oxygen is in the octahedral, the other is in the tetrahedral sheet of the montmorillonite layer

Table 4. Structural parameters (interatomic distances and coordination numbers) of the bidentate uranium complex models with ferric iron incorporation in the octahedral sheet of (010) montmorillonite edge surface

Short name of model[a]	Structural parameter[b]	Bond type					
		U–O_a[c]	**U–O_b**[d]	**U–O_w**[e]	**U–Fe**[f]	**U–Al**[g]	**U–Si**[h]
010U6cOctFe3c[i]	***R*** [Å]	**1.81 ± 0.01**	**2.36 ± 0.02**	**2.35 ± 0.24**	**3.48 ± 0.05**	**—**	**3.57 ± 0.02**
	CN [-]	**2.0 ± 0.1**	**2.0 ± 0.1**	**2.0 ± 0.1**	**1.0 ± 0.1**	**0.0 ± 0.1**	**2.0 ± 0.1**
010U6cOctFe3t[i]	***R*** [Å]	**1.81 ± 0.01**	**2.38 ± 0.02**	**2.36 ± 0.25**	**5.57 ± 0.05**	**3.45 ± 0.05**	**3.54 ± 0.03**
	CN [-]	**2.0 ± 0.1**	**2.0 ± 0.1**	**2.0 ± 0.1**	**1.0 ± 0.1**	**1.0 ± 0.1**	**2.0 ± 0.1**
010U6cTetlowFe3c	***R*** [Å]	1.81 ± 0.01	2.31 ± 0.14	2.43 ± 0.18	4.15 ± 0.05	—	3.01 ± 0.05
	CN [-]	2.0 ± 0.1	2.0 ± 0.1	2.0 ± 0.1	1.0 ± 0.1	0.0 ± 0.1	1.0 ± 0.1
010U6cTetlowFe3t	***R*** [Å]	1.81 ± 0.01	2.33 ± 0.21	2.43 ± 0.19	6.14 ± 0.05	4.10 ± 0.05	3.02 ± 0.05
	CN [-]	2.0 ± 0.1	2.0 ± 0.1	2.0 ± 0.1	1.0 ± 0.1	1.0 ± 0.1	1.0 ± 0.1
010U6cTetupFe3c	***R*** [Å]	1.80 ± 0.01	2.38 ± 0.07	2.55 ± 0.04	3.52 ± 0.05	—	3.08 ± 0.05
	CN [-]	2.0 ± 0.1	3.0 ± 0.1	2.0 ± 0.1	1.0 ± 0.1	0.0 ± 0.1	1.0 ± 0.1
010U6cTetupFe3t	***R*** [Å]	1.80 ± 0.01	2.38 ± 0.07	2.59 ± 0.04	5.56 ± 0.05	3.46 ± 0.05	3.07 ± 0.05
	CN [-]	2.0 ± 0.1	3.0 ± 0.1	2.0 ± 0.1	1.0 ± 0.1	1.0 ± 0.1	1.0 ± 0.1
010U6tOctFe3c[i]	***R*** [Å]	**1.83 ± 0.02**	**2.16 ± 0.21**	**2.58 ± 0.03**	**5.49 ± 0.05**	**3.18 ± 0.05**	**—**
	CN [-]	**2.0 ± 0.1**	**2.0 ± 0.1**	**2.0 ± 0.1**	**1.0 ± 0.1**	**1.0 ± 0.1**	**0.0 ± 0.1**
010U6tOctFe3t[i]	***R*** [Å]	**1.83 ± 0.02**	**2.16 ± 0.17**	**2.56 ± 0.02**	**3.20 ± 0.05**	**—**	**—**
	CN [-]	**2.0 ± 0.1**	**2.0 ± 0.1**	**2.0 ± 0.1**	**1.0 ± 0.1**	**0.0 ± 0.1**	**0.0 ± 0.1**
010U6tTetlowFe3c[i]	***R*** [Å]	**1.81 ± 0.02**	**2.15 ± 0.06**	**2.50 ± 0.01**	**5.12 ± 0.05**	**3.94 ± 0.05**	**3.51 ± 0.05**
	CN [-]	**2.0 ± 0.1**	**2.0 ± 0.1**	**1.0 ± 0.1**	**1.0 ± 0.1**	**1.0 ± 0.1**	**1.0 ± 0.1**
010U6tTetlowFe3t[i]	***R*** [Å]	**1.81 ± 0.02**	**2.14 ± 0.04**	**2.50 ± 0.01**	**3.98 ± 0.05**	**—**	**3.54 ± 0.05**
	CN [-]	**2.0 ± 0.1**	**2.0 ± 0.1**	**1.0 ± 0.1**	**1.0 ± 0.1**	**0.0 ± 0.1**	**1.0 ± 0.1**
010U6tTetupFe3c	***R*** [Å]	1.89 ± 0.11	2.05 ± 0.14	2.54 ± 0.01	4.81 ± 0.05	3.68 ± 0.05	3.41 ± 0.05
	CN [-]	2.0 ± 0.1	2.0 ± 0.1	1.0 ± 0.1	1.0 ± 0.1	1.0 ± 0.1	1.0 ± 0.1
010U6tTetupFe3t	***R*** [Å]	1.89 ± 0.11	2.06 ± 0.15	2.52 ± 0.01	3.67 ± 0.05	—	3.45 ± 0.05
	CN [-]	2.0 ± 0.1	2.0 ± 0.1	1.0 ± 0.1	1.0 ± 0.1	0.0 ± 0.1	1.0 ± 0.1

[a]Short names are explained in Table 3

[b]Bond distance (R) and coordination number (CN)

[c]O_a: axial oxygen of the uranyl ion

[d]O_b: (octahedral/tetrahedral) bridging oxygen between uranyl ion and montmorillonite edge surface

[e]O_w: oxygen atom of a water molecule attached to the uranyl ion

[f]Fe: ferric iron in the octahedral sheet of the montmorillonite layer

[g]Al: aluminum in the octahedral sheet of the montmorillonite layer

[h]Si: silicon in the tetrahedral sheet of the montmorillonite layer

[i]The model name and the structural parameters of the most stable models are marked with bold letters

Table 5. Structural parameters (interatomic distances and coordination numbers) of the bidentate uranium complex models with ferric iron incorporation in the octahedral sheet of (110) montmorillonite edge surface

Short name of model[a]	Structural parameter[b]	Bond type					
		U–O_a[c]	**U–O_b**[d]	**U–O_w**[e]	**U–Fe**[f]	**U–Al**[g]	**U–Si**[h]
110U6cOctFe3c[i]	***R*** [Å]	**1.83 ± 0.01**	**2.15 ± 0.14**	**2.58 ± 0.02**	**3.24 ± 0.05**	**—**	**—**
	CN [-]	**2.0 ± 0.1**	**2.0 ± 0.1**	**2.0 ± 0.1**	**1.0 ± 0.1**	**0.0 ± 0.1**	**0.0 ± 0.1**
110U6cOctFe3t[i]	***R*** [Å]	**1.83 ± 0.01**	**2.16 ± 0.17**	**2.59 ± 0.02**	**5.38 ± 0.05**	**3.21 ± 0.05**	**—**
	CN [-]	**2.0 ± 0.1**	**2.0 ± 0.1**	**2.0 ± 0.1**	**1.0 ± 0.1**	**1.0 ± 0.1**	**0.0 ± 0.1**
110U6cTetlowFe3c	***R*** [Å]	1.80 ± 0.01	2.17 ± 0.01	2.66 ± 0.07	4.09 ± 0.05	—	3.42 ± 0.05
	CN [-]	2.0 ± 0.1	2.0 ± 0.1	2.0 ± 0.1	1.0 ± 0.1	0.0 ± 0.1	1.0 ± 0.1
110U6cTetlowFe3t	***R*** [Å]	1.81 ± 0.02	2.18 ± 0.01	2.66 ± 0.07	5.81 ± 0.05	4.14 ± 0.05	3.38 ± 0.05
	CN [-]	2.0 ± 0.1	2.0 ± 0.1	2.0 ± 0.1	1.0 ± 0.1	1.0 ± 0.1	1.0 ± 0.1
110U6cTetupFe3c[i]	***R*** [Å]	**1.82 ± 0.01**	**2.14 ± 0.06**	**2.62 ± 0.02**	**3.52 ± 0.05**	**—**	**3.59 ± 0.05**
	CN [-]	**2.0 ± 0.1**	**2.0 ± 0.1**	**2.0 ± 0.1**	**1.0 ± 0.1**	**0.0 ± 0.1**	**1.0 ± 0.1**
110U6cTetupFe3t[i]	***R*** [Å]	**1.82 ± 0.01**	**2.14 ± 0.07**	**2.62 ± 0.01**	**5.12 ± 0.05**	**3.55 ± 0.05**	**3.53 ± 0.05**
	CN [-]	**2.0 ± 0.1**	**2.0 ± 0.1**	**2.0 ± 0.1**	**1.0 ± 0.1**	**1.0 ± 0.1**	**1.0 ± 0.1**
110U6tOctFe3c[i]	***R*** [Å]	**1.82 ± 0.02**	**2.19 ± 0.27**	**2.57 ± 0.03**	**5.48 ± 0.05**	**3.20 ± 0.05**	**3.68 ± 0.05**
	CN [-]	**2.0 ± 0.1**	**2.0 ± 0.1**	**2.0 ± 0.1**	**1.0 ± 0.1**	**1.0 ± 0.1**	**1.0 ± 0.1**
110U6tOctFe3t[i]	***R*** [Å]	**1.82 ± 0.02**	**2.19 ± 0.22**	**2.55 ± 0.03**	**3.24 ± 0.05**	**—**	**3.68 ± 0.05**
	CN [-]	**2.0 ± 0.1**	**2.0 ± 0.1**	**2.0 ± 0.1**	**1.0 ± 0.1**	**0.0 ± 0.1**	**1.0 ± 0.1**
110U6tTetlowFe3c	***R*** [Å]	1.86 ± 0.02	2.33 ± 0.18	2.58 ± 0.01	4.03 ± 0.05	3.70 ± 0.23	3.16 ± 0.05
	CN [-]	2.0 ± 0.1	3.0 ± 0.1	1.0 ± 0.1	1.0 ± 0.1	2.0 ± 0.1	1.0 ± 0.1
110U6tTetlowFe3t	***R*** [Å]	1.86 ± 0.04	2.32 ± 0.17	2.56 ± 0.01	3.56 ± 0.05	3.94 ± 0.15	3.17 ± 0.05
	CN [-]	2.0 ± 0.1	3.0 ± 0.1	1.0 ± 0.1	1.0 ± 0.1	2.0 ± 0.1	1.0 ± 0.1
110U6tTetupFe3c	***R*** [Å]	1.80 ± 0.03	2.26 ± 0.11	2.56 ± 0.00	5.19 ± 0.05	4.02 ± 0.05	2.95 ± 0.05
	CN [-]	2.0 ± 0.1	2.0 ± 0.1	2.0 ± 0.1	1.0 ± 0.1	1.0 ± 0.1	1.0 ± 0.1
110U6tTetupFe3t	***R*** [Å]	1.80 ± 0.02	2.26 ± 0.05	2.54 ± 0.02	4.03 ± 0.05	—	2.97 ± 0.05
	CN [-]	2.0 ± 0.1	2.0 ± 0.1	2.0 ± 0.1	1.0 ± 0.1	0.0 ± 0.1	1.0 ± 0.1

[a]Short names are explained in Table 3

[b]Bond distance (R) and coordination number (CN)

[c]O_a: axial oxygen of the uranyl ion

[d]O_b: (octahedral/tetrahedral) bridging oxygen between uranyl ion and montmorillonite edge surface

[e]O_w: oxygen atom of a water molecule attached to the uranyl ion

[f]Fe: ferric iron in the octahedral sheet of the montmorillonite layer

[g]Al: aluminum in the octahedral sheet of the montmorillonite layer

[h]Si: silicon in the tetrahedral sheet of the montmorillonite layer

[i]The model name and the structural parameters of the most stable models are marked with bold letters

4. Implication of uranium adsorption on montmorillonite

The uranium uptake mechanisms of three montmorillonite samples originating from different mining sites (Milos, Wyoming, Texas) were studied by comparing the results of *ab initio* calculations and conventional EXAFS data fit. During the conventional EXAFS data analysis, the interatomic distances (R) could vary. Coordination numbers (CN) could change with respect to the initially guessed values (except for $U–O_1$ in Table 6). Six shells were fitted ($U–O_1$, $U–O_2$, $U–O_3$, U–Fe, U–Al, U–Si) but the Debye-Waller factor (σ^2) for the Fe, Al, and Si shells was fixed to $0.007 Å^2$ to reduce the number of fitting parameters. Furthermore, the fitted EXAFS data were obtained in three different ways using (1) only the Si shell, (2) the Al and Si shells or (3) the Fe and Si shells. The corresponding interatomic distances and coordination numbers from the conventional EXAFS fit (Table 6) and from the *ab initio* calculations (Table 2, Table 4, Table 5) were compared. The R and CN values of the $U–O_1$ shell (R ~ 1.77 Å; CN = 2.0 in Table 6)were almost equal to the theoretically calculated $U–O_a$ (axial oxygen) distances (R ~ 1.80 Å; CN = 2.0 in Table 2, Table 4, Table 5). Moreover, the interatomic distances of the $U–O_2$ shell (R ~ 2.23 Å in Table 6) agreed within the uncertainty to the $U–O_b$ (bridging oxygen) values (R ~ 2.17 Å in Table 2, Table 4, Table 5). Remarkable differences can be noticed between structural parameters of the experimental $U–O_3$ (R ~ 2.43 Å; CN ~ 4.0 in Table 6) and theoretically calculated $U–O_w$ (R ~ 2.58 Å; CN ~ 2.0 in Table 2, Table 4, Table 5) shells. The differences can be explained by the lack of additional water molecules in the interlayer, which would increase the coordination number and may decrease the interatomic distances.

The interatomic distances and coordination number for Al and Si shells varied R_{Al} ~ 3.15…3.64Å; R_{Si} ~ 3.08…3.64Å; CN_{Al} ~ 0.3…0.8; CN_{Al} ~ 0.5…1.2 (Table 6). The best agreement between the fitted and theoretically calculated results (Table 2) could be obtained when only a Si shell was applied (Fit1, Fit4 and Fit6 in Table 6). In these cases, however, the Al and Fe shells were excluded, which contradicts to the results of the *ab initio* calculations ($CN_{Al/Fe}$ = 1.0 in Table 2, Table 4, Table 5).

The U–Fe and U–Si structural parameters of EXAFS fits on Texas-montmorillonite samples (Fit3 in Table 6) mismatched with the calculated results of the most stable structures (Table 4 and Table 5), while no convergence of the fit could be obtained for Milos- and Wyoming-montmorillonite samples. The results indicate that the interpretation of conventional EXAFS data analysis is very challenging and uncertain. Moreover, it includes constrains which are hard to determine (e.g. σ^2 for U–Al and U–Si). Therefore, a direct comparison of experimental and modelling results is necessary.

Table 6. Structural parameters derived from conventional EXAFS fits for uranyl ions sorbed on Mil-, SWy- and STx-montmorillonite

Sample	Fit number	Structural parameter	Bond type						ΔE_0	R_{fact}
			U–O_1	U–O_2	U–O_3	U–Fe	U–Al	U–Si		
STx	Fit1	R [Å]	1.76 ± 0.01	2.23 ± 0.03	2.42 ± 0.03	—	—	3.64 ± 0.01	2.46	0.01
		CN [ ]	2.0[f]	3.7 ± 0.7	3.3 ± 0.9	—	—	0.9 ± 0.4		
		σ^2 [Å^2]	0.003 ± 0.001	0.008 ± 0.004	0.008 ± 0.004	—	—	0.007[f]		
	Fit2	R [Å]	1.77 ± 0.01	2.24 ± 0.04	2.43 ± 0.03	—	3.15 ± 0.1	3.64 ± 0.07	2.00	0.02
		CN [ ]	2.0[f]	3.5 ± 0.9	3.8 ± 1.2	—	0.3 ± 0.5	0.7 ± 0.6		
		σ^2 [Å^2]	0.003 ± 0.001	0.008 ± 0.005	0.008 ± 0.005	—	0.007[f]	0.007[f]		
	Fit3	R [Å]	1.76 ± 0.01	2.25 ± 0.04	2.45 ± 0.03	3.44 ± 0.05	—	3.08 ± 0.06	1.80	0.02
		CN [ ]	2.0[f]	4.0 ± 1.0	4.2 ± 1.2	0.4 ± 0.3	—	0.5 ± 0.4		
		σ^2 [Å^2]	0.003 ± 0.001	0.003 ± 0.005	0.003 ± 0.005	0.007[e]	—	0.007[f]		
SWy	Fit4	R [Å]	1.77 ± 0.01	2.23 ± 0.04	2.43 ± 0.03	—	—	3.63 ± 0.06	2.71	0.01
		CN [ ]	2.0[f]	3.8 ± 1.0	3.5 ± 1.2	—	—	1.0 ± 0.4		
		σ^2 [Å^2]	0.003 ± 0.001	0.009 ± 0.005	0.009 ± 0.005	—	—	0.007[f]		
	Fit5	R [Å]	1.77 ± 0.01	2.24 ± 0.04	2.43 ± 0.03	—	3.14 ± 0.05	3.63 ± 0.06	2.29	0.02
		CN [ ]	2.0[f]	4.0 ± 1.0	3.8 ± 1.2	—	0.3 ± 0.3	0.7 ± 0.4		
		σ^2 [Å^2]	0.003 ± 0.001	0.010 ± 0.005	0.010 ± 0.005	—	0.007[f]	0.007[f]		
Mil	Fit6	R [Å]	1.77 ± 0.01	2.21 ± 0.04	2.39 ± 0.03	—	—	3.61 ± 0.06	2.71	0.02
		CN [ ]	2.0[f]	3.1 ± 1.0	4.3 ± 1.2	—	—	0.6 ± 0.4		
		σ^2 [Å^2]	0.003 ± 0.001	0.010 ± 0.005	0.010 ± 0.005	—	—	0.007[f]		
	Fit7	R [Å]	1.77 ± 0.01	2.22 ± 0.04	2.40 ± 0.03	—	3.18 ± 0.05	3.60 ± 0.06	2.12	0.02
		CN [ ]	2.0[f]	3.8 ± 1.0	3.5 ± 1.2	—	0.4 ± 0.3	0.4 ± 0.4		
		σ^2 [Å^2]	0.003 ± 0.001	0.010 ± 0.005	0.010 ± 0.005	—	0.007[f]	0.007[f]		

[a]Montmorillonite originating from different locations: Milos- (Mil-), Wyoming- (SWy-), Texas- (STx-)montmorillonite
[b]The fit was performed with Si shell
[c]The fit was performed with Al and Si shells
[d]The fit was performed with Fe and Si shells
[e]Bond distance (R), coordination number (CN) and Debye-Waller factor (σ^2)
[f]The variable was fixed to the written value

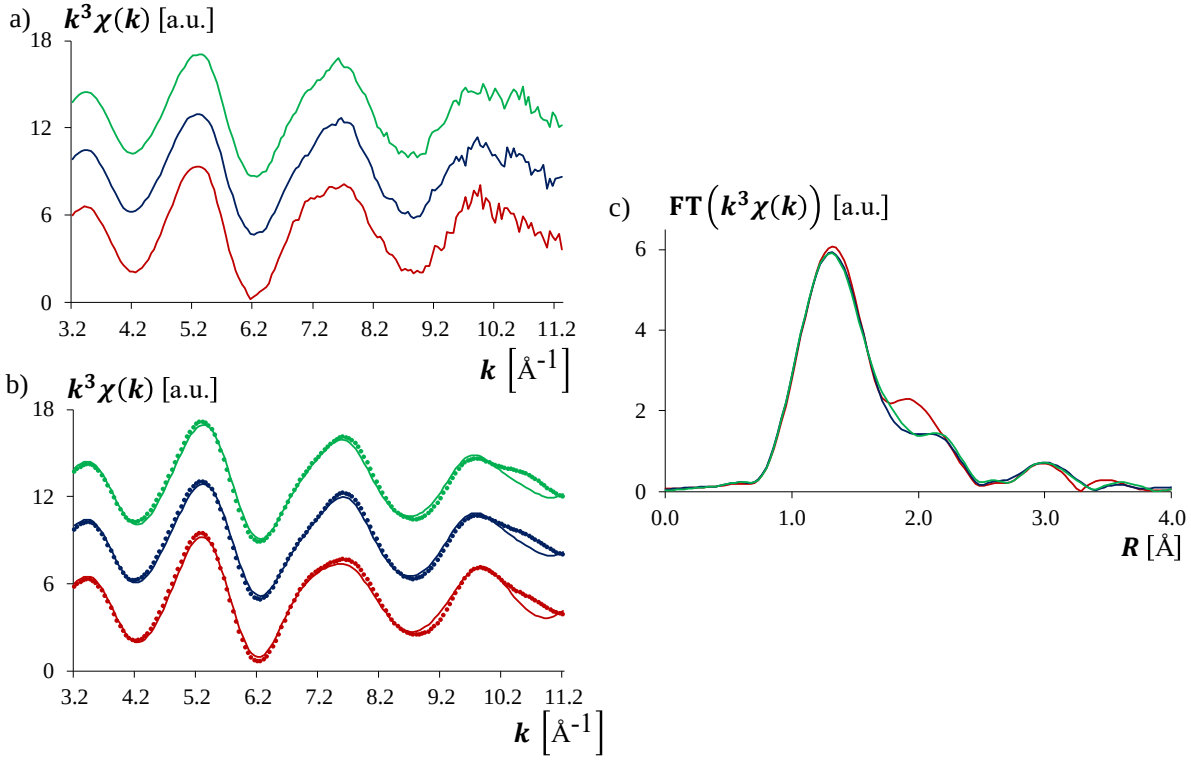

Figure 5. U L_3-edge P-EXAFS spectra of Milos–, Wyoming– and Texas–montmorillonite (shown with red, blue and green colors, respectively). k^3-weighted P-EXAFS spectra of the three montmorillonite samples measured at $\alpha = 35°$ angle is shown in panel a. Least-squares fit of FT^{-1} EXAFS data is present in panel b, while the corresponding RSFs of the Texas–, Wyoming– and Milos–sample is shown in panel c.

It has been demonstrated by Bocharov et al.[38] that experimental U L_3-edge EXAFS spectra can be interpreted by theoretically calculated, *ab initio* molecular dynamics (MD) simulations based spectra. Furthermore, with the recent advances in X-ray absorption near edge structure (XANES) spectroscopy, the direct comparison of experimental and theoretical XANES spectra is possible. The MD and XANES calculations are computationally expensive, thus only the most promising complexation models should further be investigated. This *ab initio* study determined the energetically preferred uptake mechanisms on which subsequent studies can focus.

5. References

(1) Kremleva, A.; Krüger, S.; Rösch, N. Uranyl Adsorption at Solvated Edge Surfaces of 2:1 Smectites. A Density Functional Study. *Phys. Chem. Chem. Phys.* **2015**, *17(20)*, 13757–13768.

(2) Bradbury, M. H.; Berner, U.; Curti, E.; Hummel, W.; Kosakowski, G.; Thoenen, T. *Technical Report 12-01: The Long Term Geochemical Evolution of the Nearfield of the HLW Repository*. Wettingen, Switzerland, **2014**.

(3) Baeyens, B.; Thoenen, T.; Bradbury, M. H.; Marques Fernandes, M. *Technical Report 12-04: Sorption Data Bases for Argillaceous Rocks and Bentonite for the Provisional Safety Analyses for SGT-E2.* Villigen PSI, Switzerland, **2014**.

(4) Leupin, O. X.; Birgersson, M.; Karnland, O.; Korkeakoski, P.; Sellin, P.; Mader, U.; Wersin, P. *Technical Report 14-12: Montmorillonite Stability under near-Field Conditions.* Wettingen, Switzerland, **2014**.

(5) Catalano, J. G.; Brown, G. E., J. Uranyl Adsorption onto Montmorillonite: Evaluation of Binding Sites and Carbonate Complexation. Geochim. *Cosmochim. Acta* **2005**, *69(12)*, 2995–3005.

(6) Sylwester, E. R.; Hudson, E. A.; Allen, P. G. The Structure of Uranium(VI) Sorption Complexes on Silica, Alumina, and Montmorillonite. Geochim. *Cosmochim. Acta* **2000**, *64(14)*, 2431–2438.

(7) Marques Fernandes, M.; Baeyens, B.; Dähn, R.; Scheinost, A. C.; Bradbury, M. H. U(VI) Sorption on Montmorillonite in the Absence and Presence of Carbonate: A Macroscopic and Microscopic Study. *Geochim. Cosmochim. Acta* **2012**, *93*, 262–277.

(8) Baumann, N.; Brendler, V.; Arnold, T.; Geipel, G.; Bernhard, G. Uranyl Sorption onto Gibbsite Studied by Time-Resolved Laser-Induced Fluorescence Spectroscopy (TRLFS). *J. Colloid Interface Sci.* **2005**, *290(2)*, 318–324.

(9) Denecke, M. A. Actinide Speciation Using X-Ray Absorption Fine Structure Spectroscopy. *Coord. Chem. Rev.* **2006**, *250(7–8)*, 730–754.

(10) Brigatti, M. F.; Galan, E.; Theng, B. K. G. Structures and Mineralogy of Clay Minerals. In *Handbook of Clay Science* (Eds.: Bergaya, F., Theng, B. K. G., Lagaly, G.) **2006**, *Vol. 1*, pp. 19–86.

(11) Krack, M. On the Ground State Electronic Structure of Uranium Dioxide. *Phys. Scr.* **2015**, *90(9)*, 094014.

(12) Rabone, J.; Krack, M. A Procedure for Bypassing Metastable States in Local Basis Set DFT+U Calculations and Its Application to Uranium Dioxide Surfaces. *Comput. Mater. Sci.* **2013**, *71*, 157–164.

(13) Guggenheim, S.; Adams, J. M.; Bain, D. C.; Bergaya, F.; Brigatti, M. F.; Drits, V. A.; Formosso, M. L. L.; Galan, E.; Kogure, T.; Stanjek, H. Summary of Recommendations of Nomenclature Committees Relevant to Clay Mineralogy: Report of the Association Internationale Pour l'Etude Des Argiles (AIPEA) Nomenclature Committee for 2006. *Clays Clay Miner.* **2006**, *54(6)*, 761–772.

(14) Drits, V. A.; McCarty, D. K.; Zviagina, B. B. Crystal-Chemical Factors Responsible for the Distribution of Octahedral Cations over *Trans*- and *Cis*-Sites in Dioctahedral 2:1 Layer Silicates. *Clays Clay Miner.* **2006**, *54(2)*, 131–152.

(15) Kaufhold, S.; Kremleva, A.; Krüger, S.; Rösch, N.; Emmerich, K.; Dohrmann, R. Crystal-Chemical Composition of Dicoctahedral Smectites: An Energy-Based Assessment of Empirical Relations. *ACS Earth Sp. Chem.* **2017**, *1(10)*, 629–636.

(16) Bickmore, B. R.; Rosso, K. M.; Nagy, K. L.; Cygan, R. T.; Tadanier, C. J. Ab Initio Determination of Edge Surface Structures for Dioctahedral 2:1 Phyllosilicates: Implications for Acid-Base for Reactivity. *Clays Clay Miner.* **2003**, *51(4)*, 359–371.

(17) Kéri, A.; Dähn, R.; Krack, M.; Churakov, S. V. Combined XAFS Spectroscopy and *Ab Initio* Study on the Characterization of Iron Incorporation by Montmorillonite. *Environ. Sci. Technol.* **2017**, *51(18)*, 10585–10594.

(18) Churakov, S. V.; Daehn, R. Zinc Adsorption on Clays Inferred from Atomistic Simulations and EXAFS Spectroscopy. *Environ. Sci. Technol.* **2012**, *46(11)*, 5713–5719.

(19) Churakov, S. V. Ab Initio Study of Sorption on Pyrophyllite: Structure and Acidity of the Edge Sites. *J. Phys. Chem. B* **2006**, *110(9)*, 4135–4146.

(20) CP2K developers group: www.cp2k.org.

(21) VandeVondele, J.; Krack, M.; Mohamed, F.; Parrinello, M.; Chassaing, T.; Hutter, J. QUICKSTEP: Fast and Accurate Density Functional Calculations Using a Mixed Gaussian and Plane Waves Approach. *Comput. Phys. Commun.* **2005**, *167(2)*, 103–128.

(22) Goedecker, S.; Teter, M.; Hutter, J. Separable Dual-Space Gaussian Pseudopotentials. *Phys. Rev. B* **1996**, *54(3)*, 1703–1710.

(23) Krack, M. Pseudopotentials for H to Kr Optimized for Gradient-Corrected Exchange-Correlation Functionals. *Theor. Chem. Acc.* **2005**, *114(1–3)*, 145–152.

(24) VandeVondele, J.; Hutter, J. Gaussian Basis Sets for Accurate Calculations on Molecular Systems in Gas and Condensed Phases. *J. Chem. Phys.* **2007**, *127(11)*, 114105.

(25) Perdew, J. P.; Burke, K.; Ernzerhof, M. Generalized Gradient Approximation Made Simple. *Phys. Rev. Lett.* **1996**, *77(18)*, 3865–3868.

(26) Grimme, S. Semiempirical GGA-Type Density Functional Constructed with a Long-Range Dispersion Correction. *J. Comput. Chem.* **2006**, *27(15)*, 1787–1799.

(27) Rollmann, G.; Rohrbach, A.; Entel, P.; Hafner, J. First-Principles Calculation ofthe Structure and Magnetic Phases of Hematite. *Phys. Rev. B Condens. Matter Mater. Phys.* **2004**, *69(16)*, 165107.

(28) Dudarev, S. L.; Nguyen Manh, D.; Sutton, A. P. Effect of Mott-Hubbard Correlations on the Electronic Structure and Structural Stability of Uranium Dioxide. *Philos. Mag. B* **1997**, *75(5)*, 613–628.

(29) Anisimov, V. I.; Zaanen, J.; Andersen, O. K. Band Theory and Mott Insulators: Hubbard *U* Instead of Stoner *I*. *Phys. Rev. B* **1991**, *44(3)*, 943–954.

(30) Nikitenko, S.; Beale, A. M.; van der Eerden, A. M. J.; Jacques, S. D. M.; Leynaud, O.; O'Brien, M. G.; Detollenaere, D.; Kaptein, R.; Weckhuysen, B. M.; Bras, W. Implementation of a Combined SAXS/WAXS/QEXAFS Set-up for Time-Resolved in Situ Experiments. *J. Synchrotron Radiat.* **2008**, *15(6)*, 632–640.

(31) Newville, M. IFEFFIT: Interactive XAFS Analysis and FEFF Fitting. *J. Synchrotron Radiat.* **2001**, *8*, 322–324.

(32) Ravel, B.; Newville, M. ATHENA , ARTEMIS , HEPHAESTUS : Data Analysis for X-Ray Absorption Spectroscopy Using IFEFFIT. *J. Synchrotron Radiat.* **2005**, *12(4)*, 537–541.

(33) Rehr, J. J.; Mustre de Leon, J.; Zabinsky, S. I.; Albers, R. C. Theoretical X-Ray Absorption Fine Structure Standards. *J. Am. Chem. Soc.* **1991**, *113(14)*, 5135–5140.

(34) Ankudinov, A. L.; Ravel, B.; Rehr, J. J.; Conradson, S. D. Real-Space Multiple-Scattering Calculation and Interpretation of X-Ray-Absorption near-Edge Structure. *Phys. Rev. B* **1998**, *58(12)*, 7565–7576.

(35) Demartin, F.; Gramaccioli, C. M.; Pilati, T. The Importance of Accurate Crystal Structure Determination of Uranium Minerals. II. Soddyite $(UO_2)_2(SiO_4).2H_2O$. *Acta Crystallogr. Sect. C* **1992**, *48(1)*, 1–4.

(36) Hennig, C.; Reich, T.; Dähn, R.; Scheidegger, A. M. Structure of Uranium Sorption Complexes at Montmorillonite Edge Sites. *Radiochim. Acta* **2002**, *90(9)*, 653–657.

(37) Hudson, E. A.; Allen, P. G.; Terminello, L. J.; Denecke, M. A.; Reich, T. Polarized X-Ray Absorption Spectroscopy of the Uranyl Ion: Comparison of Experiment and Theory. *Phys. Rev. B* **1996**, *54(1)*, 156–165.

(38) Bocharov, D.; Chollet, M.; Krack, M.; Bertsch, J.; Grolimund, D.; Martin, M.; Kuzmin, A.; Purans, J.; Kotomin, E. Interpretation of the U L_3 -edge EXAFS in uranium dioxide using molecular dynamics and density functional theory simulations. *J. Phys. Conf. Ser.* **2016**, *712*, 012091.

CHAPTER 7:
Conclusions and Outlook

Conclusions and Outlook

X-ray absorption spectroscopy (XAS) is an element specific analytical tool for the qualitative and quantitative characterization of the short-range structural environment of chemical elements present at high to trace concentration in mineral phases, solutions and at mineral surfaces. The technique is widely applied for the characterization of heavy and transition metal retention in natural and engineered environment. Clay minerals are the most common sorbents in soils and subsurface sedimentary rocks. Due to their complex surface structure, the adsorbed heavy and transition metal species can be present in different structural forms. A particularly complex behavior of redox sensitive elements is expected as the cation uptake may be accompanied by redox reactions at the mineral surfaces. Iron is an abundant and ubiquitous redox-sensitive element in soils and rocks, thus Fe^{2+}/Fe^{3+} (ferrous/ferric iron) is one of the most important redox couple. The structural characterization of this redox-active element present in trace concentration in the bulk structure of clay minerals and at their surface sites is of paramount importance. However, the quantitative XAS data analysis is challenging for such complex systems where the analyzed element is present in several structural forms and in mixed oxidation states. Obtaining reliable experimental reference spectra is demanding due to the complexity and variability of the bulk and surface structure of clay minerals.

In this thesis, a multi-disciplinary approach combining *ab initio* calculations and X-ray absorption spectroscopy (XAS) techniques was further developed to determine the preferred oxidation state of iron, its occupational site in the bulk structure and the different Fe and U species at the most relevant clay mineral edge sites. The combination of the theoretical and experimental approach provided a quantitative description of structural iron and metal-uptake by clay minerals. The methodological work demonstrated that not only extended X-ray absorption fine structure (EXAFS) but also X-ray absorption near edge structure (XANES) spectra are useful references for the interpretation of the experimental results.

It could be shown that in the bulk structure of smectites, the preferred oxidation state of iron is Fe^{3+}, while it is equally distributed between the *cis*- and *trans*- octahedral sites. Montmorillonites of different origin (Milos, Wyoming and Texas) show differences in their experimental EXAFS spectra implying distinct (individual Fe, Fe–Fe or Mg–Fe clustering) arrangements of isomorphic ferric iron substitution in the octahedral sheet. The obtained atomic scale information raises the question why the typology of these smectites is so different and whether it is in connection with the geological features (e.g. rock basin type, extent of diagenesis) of the montmorillonite deposits.

The investigation of the uptake mechanism of iron on montmorillonite at the atomistic level allows a determination of the energetically favored positions for ferrous and ferric iron. Several former experimental studies speculate on the oxidative Fe uptake. The *ab initio* calculations performed in this thesis indicated the relative stability of ferric iron at the "*cis*-like" (110) surface site and the energetically preferred position of ferrous iron in the bulk octahedral sheet of a clay layer. The results imply that the oxidative sorption of ferrous iron as the result of an electron transfer (ET) from the surface into the bulk is an energetically favored process.

This thermodynamic assumption was not tested since describing the interaction of Fe^{2+} with smectites is challenging, which is not only due to the influence of the smectite-specific redox activity but also due to the concentration dependent uptake of ferrous iron. *Ab initio* based EXAFS and XANES reference spectra were applied for the interpretation of XAS spectra measured on samples with different Fe loadings to determine the oxidation state of sorbed iron and to find the most relevant bidentate inner-sphere Fe complexation structures. The results indicate that iron is mostly present in Fe^{3+} form, however, its concentration is decreasing at increasing Fe loadings. The effect can be explained by the limited number of structurally incorporated ferric iron. When all the available structural Fe^{3+} have been consumed in the electron transfer reactions, oxidative sorption cannot proceed anymore leaving the further sorbed species in the Fe^{2+} oxidation state. The oxidative sorption has been shown to be feasible, but this study does not address the detailed mechanism of the electron transfer reaction at the montmorillonite-water interface speculated in experimental studies. Such a complex process would deserve a separate investigation elucidating the sorption behavior of ferrous iron in complex natural systems. The activation barriers for the interfacial ET reaction between adsorbed Fe^{2+} and structural Fe^{3+} species for iron-oxides (e.g. hematite[6], magnetite[7]) and for Fe-rich clay minerals (e.g. nontronite[1]) were calculated using the so-called small polaron hopping (SPH) approach. In this method, the initial and final states correspond to two polaron centers with an extra electron localized on an iron atom. The ET activation barrier is determined by locating an intersection point on the nuclear reaction coordinate between the initial- and final-state parabolic potential energy surfaces of the energy profile for the electron migration path[1]. Although, the electron transport in transition metal oxides is known experimentally to involve tightly bound charge carriers, low mobility and thermal activation, the SPH approach could give an appropriate description[1,6]. A SPH study performed on micas (sheet silicates) studied the effects of compositional defects on ET in the octahedral sheet[8]. A similar SPH study on the most relevant smectite models representing the different natural montmorillonites (with distinct arrangements of isomorphic Fe^{3+} substitution in the octahedral sheet) would give a great opportunity to at least theoretically describe the differences in their ferrous iron uptake. This particularly interesting study may give an answer what the impact of other substituents (e.g. Mg^{2+} in the octahedral and Al^{3+} in the tetrahedral sheet) is.

In this thesis, iron sorption was modelled on montmorillonite at near neutral environmental conditions (pH ~7), where the sorption of Fe^{2+} is pH-independent and the interfacial Fe^{2+}–Fe^{3+} electron transfer is expected to predominantly occur on the edge sites but not exclusively[1–3]. An investigation suggested a strong pH-dependence of the Fe^{2+} surface complexation at higher pH[4]. With increasing Fe loading and at higher pH, not only inner-sphere but also outer-sphere complexation should be taken into account enhancing the complexity of the atomistic modelling. Dehydroxylation of surface hydroxyl groups and the sorption of cations $\left(\text{e.g. } Na^{+}, Ca^{2+}\right)$ at the planar sites counter-balance the charge deficit resulting from the reduction of structural ferric iron[5]. The former process may play a crucial role in the long-

term mineralogical alteration of smectites into non-swelling Fe-bearing phyllosilicates that are challenging to study experimentally. Atomistic scale calculations are an efficient tool to investigate the rearrangement of surface OH^- groups and to determine which parameters (e.g. substituting cations, pH) influence and at what extent.

The combined use of the *ab initio* based and the experimentally measured XAS spectra is a novel approach, which needs further improvement to reduce the relatively high (±15%) estimated uncertainties due to the indirect comparison of the models and the low signal-to-noise ratio of the measured XAS spectra caused by the low content of the measured element. Modelling clay structures and their transitional metal uptake mechanism often results in models with almost equal coordination number and interatomic distances, which have necessarily almost identical XAS spectra (e.g. for Fe at *cis*- and *trans*-octahedral positions in the bulk structure of smectites). In this study, systematic errors arising from correlations between similar models were determined by comparing the results of the unconstrained and at least one constrained fit as well as evaluating the *ab initio* calculations (e.g. energy comparison of similar structures). The uncertainties of the calculated contribution can be reduced by measuring well-characterized samples (e.g. with a specific oxidation state). The task is challenging because transitional metals might occur in more than one oxidation state (e.g. Fe^{2+}/Fe^{3+}) and the undesirable reduction/oxidation of the element should be avoided.

The theoretical simulation of XANES spectra for complex systems is still rare. Recent advances of the theory and computational algorithms made it possible to obtain accurate XANES spectrum of a given structure on the basis of the exact curve wave theory[9]. The comparison of the real space multiple scattering (RSMS) and the density functional theory with the local spin-density approximation (DFT-LSDA) in XANES calculations demonstrated that these theoretical XAS studies for elements with 3*d*-electrons largely depends on the applied theory. Furthermore, the choice of the exchange-correlation functional affects the electron energy level diagram, especially in the vicinity of the HOMO−LUMO gap[9,10]. The pre-edge structures prior to the Fe K-edge contains useful information about the weak transitions below the absorption edge[11]. Pre-edge features can be observed for first row transition metals arise from 1*s* to 3*d* transition as long as its 3*d* orbital is not fully occupied[11]. Although the 1*s* to 3*d* transition is forbidden by dipole selection rules, it is nevertheless observed because of the 3*d*–4*p* orbital mixing as well as direct quadrupolar coupling[11]. The structure of the absorption site distorts from a centrosymmetric geometry when the 1*s* to 3*d* transition increases[11]. The process can be utilized as a tool indicating the improvement of the 3*d*–4*f* mixing[11]. The currently available exchange-correlation functionals (Hedin- Lundquist, Perdew and Wang and X-alpha) in the DFT-LSDA approach are capable to predict XANES spectrum around the Fe K-edge and above it, but they inappropriately model the pre-edge region[9]. It is the aim of the DFT-LSDA future development to implement other possibilities (e.g. hybrid functionals with different exchange contributions), which can accurately describe the pre-edge features[9]. Experimental XANES data were collected with 0.5eV resolution, which is sufficient for qualitative analyses, but not for a quantitative comparison of calculated and measured pre-edge features.

The release and mobility of the uranyl ion $\left(UO_2^{2+}\right)$ into the bio- and geosphere is highly relevant for high-level radioactive waste (HLW) repositories. In the presented first-principles study, the energetically preferred bidentate inner-sphere uranyl complexes were determined and their structural parameters were compared to conventional EXAFS data analysis. Structural Fe^{3+} in the octahedral sheet of montmorillonite at the surface site increases the stability of bidentate uranium species. The theoretically calculated results and basic structural data of U–O shell derived from EXAFS experiments agreed well for montmorillonite samples and for the most stable uranyl complexation models, however, the result of the conventional EXAFS fit is unclear for the Al, Si and Fe shells. The applied atomistic models were simplified, as they did not include water molecules beyond the first coordination shell of the uranyl complexes. A more accurate description of the sorption process can be obtained when interlayer and interparticle (pore) water molecules are considered. In addition, the expected high Fe^{2+} concentrations in the interstitial pore waters of the near and far fields in radioactive waste repository concepts might have a significant influence on the sorption behavior of UO_2^{2+} through redox reactions. UO_2^{2+} might participate in redox reaction with dissolved or sorbed ferrous iron or structurally incorporated ferric iron. The uptake mechanism of uranyl ion is also affected by other key solution parameters, such as pH, ionic strength, exchangeable cation composition and the presence or absence of CO_2, however, their influence and extent was not considered in this study. The direct comparison of *ab initio* molecular dynamics (MD) based theoretically calculated XAS spectra and experimental results should be performed to gain a more comprehensive understanding of the interfacial reactivity of redox-active Fe-bearing clay minerals by considering different reducing agents, the effects of solution chemistry and the possible structural rearrangements of the clay mineral accompanying ET processes.

Understanding the sorption processes on a single mineral phase is necessary but not sufficient in the safety analysis of HLW disposal sites. Clay formations are highly heterogeneous on the micro-scale and the sorption of Fe^{2+} and UO_2^{2+} on one of the mineral phases might significantly be influenced by other key parameters. For example, cavity filling minerals play an important role in the uptake of uranium on samples originating from the Boda Claystone Formation where secondary mineralization around the carbonate filled veins and vugs was observed[12]. In addition, uranium binds in the same quantity to the clayey matrix (containing clay minerals and nanometer size hematite crystals)[13]. X-ray fluorescence (XRF) spectroscopy combined with mathematical approaches was capable to estimate the uptake capacity of the different mineral phases in the micro-meter scale, but it cannot individually determine the role of clay minerals and nanometer size hematite crystals[13]. *Ab initio* based XAS study on the samples is a promising approach to quantify the effect of the different mineral phases for the uptake of uranium, further on, of other relevant transition metals and radionuclides.

Knowing the sorption mechanism on the atomistic level is the first step in the upscaling procedure where the local pore diffusion coefficients can be derived from MD simulations for specific local environments such as the interlayer or edge regions of clay particles[14]. The profound microscopic understanding of complex clay systems is fundamental for modelling on pore and continuum scale.

References

(1) Alexandrov, V.; Rosso, K. M. Insights into the Mechanism of Fe(II) Adsorption and Oxidation at Fe–clay Mineral Surfaces from First-Principles Calculations. *J. Phys. Chem. C* **2013**, *117(44)*, 22880–22886.

(2) Latta, D. E.; Neumann, A.; Premaratne, W. A. P. J.; Scherer, M. M. Fe(II)–Fe(III) Electron Transfer in a Clay Mineral with Low Fe Content. *ACS Earth Sp. Chem.* **2017**, *1(4)*, 197–208.

(3) Neumann, A.; Olson, T. L.; Scherer, M. M. Spectroscopic Evidence for Fe(II)-Fe(III) Electron Transfer at Clay Mineral Edge and Basal Sites. *Environ. Sci. Technol.* **2013**, *47(13)*, 6969–6977.

(4) Soltermann, D.; Marques Fernandes, M.; Baeyens, B.; Dähn, R.; Joshi, P. A.; Scheinost, A. C.; Gorski, C. A. Fe(II) Uptake on Natural Montmorillonites. I. Macroscopic and Spectroscopic Characterization. *Environ. Sci. Technol.* **2014**, *48(15)*, 8688–8697.

(5) Neumann, A.; Sander, M.; Hofstetter, T. B. Redox Properties of Structural Fe in Smectite Clay Minerals. In *ACS Symposium Series*, **2011**, pp. 361–379.

(6) Rosso, K. M.; Smith, D. M. A.; Dupuis, M. An *Ab Initio* Model of Electron Transport in Hematite (α–Fe_2O_3) Basal Planes. *J. Chem. Phys.* **2003**, *118(14)*, 6455–6466.

(7) Skomurski, F. N.; Kerisit, S.; Rosso, K. M. Structure, Charge Distribution, and Electron Hopping Dynamics in Magnetite (Fe_3O_4) (100) Surfaces from First Principles. *Geochim. Cosmochim. Acta* **2010**, *74(15)*, 4234–4248.

(8) Rosso, K. M.; Ilton, E. S. Effects of Compositional Defects on Small Polaron Hopping in Micas. *J. Chem. Phys.* **2005**, *122(24)*, 244709.

(9) Guda, S. A.; Guda, A. A.; Soldatov, M. A.; Lomachenko, K. A.; Bugaev, A. L.; Lamberti, C.; Gawelda, W.; Bressler, C.; Smolentsev, G.; Soldatov, A. V.; Joly, Y. Optimized Finite Difference Method for the Full-Potential XANES Simulations: Application to Molecular Adsorption Geometries in MOFs and Metal–ligand Intersystem Crossing Transients. *J. Chem. Theory Comput.* **2015**, *11(9)*, 4512–4521.

(10) Droghetti, A.; Alfè, D.; Sanvito, S. Assessment of Density Functional Theory for Iron(II) Molecules across the Spin-Crossover Transition. *J. Chem. Phys.* **2012**, *137(12)*, 124303.

(11) Manceau, A.; Lemouchi, C.; Rovezzi, M.; Lanson, M.; Glatzel, P.; Nagy, K. L.; Gautier-Luneau, I.; Joly, Y.; Enescu, M. Structure, Bonding, and Stability of Mercury Complexes with Thiolate and Thioether Ligands from High-Resolution XANES Spectroscopy and First-Principles Calculations. *Inorg. Chem.* **2015**, *54(24)*, 11776–11791.

(12) Osán, J.; Kéri, A.; Breitner, D.; Fábián, M.; Dähn, R.; Simon, R.; Török, S. Microscale Analysis of Metal Uptake by Argillaceous Rocks Using Positive Matrix Factorization of Microscopic X-Ray Fluorescence Elemental Maps. *Spectrochim. Acta Part B At. Spectrosc.* **2014**, *91*, 12–23.

(13) Kéri, A.; Osán, J.; Fábián, M.; Dähn, R.; Török, S. Combined X-Ray Microanalytical Study of the Nd Uptake Capability of Argillaceous Rocks. *X-Ray Spectrom.* **2016**, *45(1)*, 54–62.

(14) Churakov, S. V.; Gimmi, T. Up-Scaling of Molecular Diffusion Coefficients in Clays: A Two-Step Approach. *J. Phys. Chem. C* **2011**, *115(14)*, 6703–6714.

Declaration of consent

on the basis of Article 28 para. 2 of the RSL05 phil.-nat.

Name, First Name: Kéri, Annamária Gabriella
Matriculation Number: 15-131-030
Study program: Earth Sciences
Title of the thesis: Mechanism of metal uptake by clay minerals — X-ray spectroscopy and molecular modelling study
Supervisors: Prof. Dr. Sergey V. Churakov
Dr. Rainer Dähn
Dr. Matthias Krack

I declare herewith that this thesis is my own work and that I have not used any sources other than those stated. I have indicated the adoption of quotations as well as thoughts taken from other authors as such in the thesis. I am aware that the Senate pursuant to Article 28. RSL Phil.-nat. 05 is authorized to revoke the title awarded on the basis of this thesis.

For the purposes of evaluation and verification of compliance with the declaration of originality and the regulations governing plagiarism, I hereby grant the University of Bern the right to process my personal data and to perform the acts of use this requires, in particular, to reproduce the written thesis and to store it permanently in a database, and to use said database, or to make said database available, to enable comparison with future theses submitted by others.

Bern, 19.04.2019.

Kéri Annamária

Annamária Gabriella Kéri